



UiT The Arctic University of Norway

Faculty of Science and Technology

Department of Physics and Technology

Dielectric nanoantennas and metasurfaces for optical trapping

Md Rabiul Hasan

A dissertation for the degree of Philosophiae Doctor – September 2023

Abstract

Analysis of biological nanoparticles in medical sciences is very promising, as it can reveal groundbreaking information about disease mechanisms, potentially leading to innovative and more effective treatment strategies. The existing methods used for analyzing biological nanoparticles come with several limitations, involving extensive sample preparation, and giving limited information about the nanoparticles. Optical tweezers combined with Raman spectroscopy is an analytical technique that has opened new possibilities for chemical analysis of biological nanoparticles. Currently used Raman optical tweezers are restricted to capturing Raman spectra from a single or a few nanoparticles and a large number of measurements are necessary to obtain valid statistics, giving low throughput analysis. Thus, development of new techniques is necessary for high-throughput chemical analysis of biological nanoparticles.

The presented thesis uses numerical simulation to investigate two types of dielectric nanostructures for on-chip optical trapping and Raman spectroscopy. The aim is to find a suitable structure for high throughput analysis of multiple extracellular vesicles (EVs), a type of biological nanoparticle released from various cells. The technique relies on using the near-visible laser to trap and excite Raman scattering from the EVs. First, a low-quality factor optical nanoantenna is investigated to find the most suitable material for optical trapping of EVs. The design parameters of the nanoantennas are optimized for maximum field enhancement. The optimized designs are then used for investigating optical trapping of various nanoparticles. The temperature increase around nanoantennas with absorbing dielectric materials and corresponding thermally induced flow are also presented. The nanoantennas can be used to trap quantum dots (QDs) and polystyrene (PS) beads up to a 40 nm diameter but are not found suitable for the trapping of EVs. Then, a silicon nitride (Si_3N_4) metasurface with tilted bars is numerically investigated, which supports a high-quality factor quasi-bound state in the continuum (quasi-BIC). The field enhancement is very high at the quasi-BIC resonance. It gives a significant Raman enhancement at the excitation wavelength and can be used to trap EVs with a modest input power but the size of the EVs is limited to 70 nm in diameter. The influence of trapped EVs on the quasi-BIC and trapping potential is studied. Finally, a metasurface design is presented, which consists of two parallel bars and a cylindrical disk. This gives a larger tip-to-tip gap, which can be used to trap EVs with a diameter up to 200 nm. The influence of the ellipticity of the bars on fabrication tolerances is explored and found to decrease for lower ellipticity, i.e., more circular, bars.

Acknowledgements

I begin this acknowledgement with utmost gratitude to my Creator, who has bestowed upon me countless blessings and opportunities that have led to the completion of this PhD thesis.

I find myself deeply indebted to my supervisor, Olav Gaute Hellestø. His mentorship, support, and motivation has served as the foundation upon which my PhD journey has been built. I consider myself exceptionally lucky to have such a friendly and helpful person as my supervisor.

I am also profoundly grateful to my co-supervisor, fellow researchers, colleagues, and friends who have contributed to this journey in countless ways. Special thanks go to Marek for his work on metasurface fabrication and his help in building the experimental setups. I have been fortunate to work alongside some motivated individuals who have not only enriched my academic experience but also provided a welcoming and supportive environment.

I am grateful to the Department of Physics and Technology for the state-of-the-art facilities, resources, and opportunities that have played a critical role in the development of this work.

I would like to thank Habib and Henock for their support in the early days of my PhD when I was struggling to adjust to a new environment.

Lastly, I am deeply indebted to my family for their unwavering love, encouragement, and support throughout my academic pursuits. Their sacrifices and belief in me have been a constant source of inspiration and motivation.

List of publications and author contributions

Peer reviewed articles

Paper I

M. R. Hasan, and O. G. Hellesø, “Dielectric optical nanoantennas,” *Nanotechnology*, vol. 32, no. 20, pp. 202001, Feb. 2021.

Author contributions: Md Rabiul Hasan performed the modelling, simulation, and data analysis. Md Rabiul Hasan wrote the initial draft and Olav Gaute Hellesø finalized it before submission. Both authors contributed to revise the manuscript.

Paper II

M. R. Hasan, and O. G. Hellesø, “Materials for dielectric nanotweezers in the near-visible region,” *ACS Applied Optical Materials*, vol. 1, no. 4, pp. 832-842, March 2023.

Author contributions: Md Rabiul Hasan conceived the idea, performed all simulations and data analysis. Md Rabiul Hasan wrote the initial draft and Olav Gaute Hellesø finalized it before submission. Both authors contributed to revise the manuscript.

Paper III

M. R. Hasan, and O. G. Hellesø, “Metasurface supporting quasi-BIC for optical trapping and Raman-spectroscopy of biological nanoparticles,” *Optics Express*, vol. 31, no. 4, pp. 6782-6795, 2023.

Author contributions: Md Rabiul Hasan conceived the idea, performed all simulations and data analysis. Olav Gaute Hellesø contributed to derive equations. Md Rabiul Hasan wrote the initial draft and Olav Gaute Hellesø finalized it before submission. Both authors contributed to revise the manuscript.

Paper IV

M. R. Hasan, and O. G. Hellesø, “Influence of ellipticity on quasi-BIC in metasurface with parallel bars and a disk,” manuscript submitted to *IEEE Photonics Technology Letters*.

Author contributions: Md Rabiul Hasan conceived the idea, performed all simulations and data analysis. Both authors contributed to the initial draft and finalized it before submission.

Conferences

M. R. Hasan, and O. G. Helleø, “Trapping of biological nanoparticles by quasi-bound state in the continuum,” NanoPlasm, Italy, June 2022. (Oral presentation)

M. R. Hasan, M. Vlk, and O. G. Helleø, “Simulation of trapping by quasi-bound state in the continuum,” Electro-Optic Meeting, Trondheim, Norway, September 2022. (Poster presentation)

M. R. Hasan, and O. G. Helleø, “Trapping of biological nanoparticles by quasi-BIC metasurfaces,” TNNN conference, Vestfold, Norway, June 2023. (Poster presentation)

Contents

Abstract.....	i
Acknowledgements.....	iii
List of publications and author contributions	v
1 Introduction	1
1.1 Why optical trapping combined with Raman spectroscopy?	1
1.2 Project setting and aims of the Thesis.....	2
1.3 Organization of the Thesis and the publications.....	3
2 Methods for analysis of biological particles	5
2.1 Biological particles and why analyze them?	5
2.2 Methods for analysis of biological particles.....	6
2.2.1 Size distribution	6
2.2.2 Transmission electron microscopy.....	7
2.2.3 Flow cytometry.....	8
2.2.4 Fluorescence microscopy.....	9
2.2.5 Raman spectroscopy and surface-enhanced Raman spectroscopy.....	10
2.2.6 Raman tweezers microspectroscopy	11
2.3 Motivation for new methods	12
3 Fundamental concepts	13
3.1 Optical trapping and forces on a particle.....	13
3.2 Raman scattering and Raman spectroscopy	18
3.3 The finite element method.....	21
4 Dielectric nanoantennas for on-chip optical trapping	23
4.1 On-chip optical trapping and Raman spectroscopy.....	24
4.2 Plasmonic versus dielectric nanoantennas	26
4.3 Simulation of mode volume and Q-factor.....	27
4.4 Field enhancement and Raman enhancement factor.....	29
4.5 Joule heating	30
4.6 Thermally induced flow.....	32
4.7 Dielectric nanotweezers in the near-visible	33
4.8 Outline of set-ups for trapping and Raman spectroscopy of nanoparticles ...	37

5	Quasi-bound states in the continuum in metasurfaces	41
5.1	Dielectric metasurfaces.....	41
5.2	Bound states in the continuum (BICs)	43
5.3	Theory of high-Q quasi-BICs in dielectric metasurfaces.....	46
5.4	Dielectric metasurfaces with quasi-BIC as nanotweezers	49
5.5	Dielectric quasi-BIC metasurface with parallel bars and a disk	52
5.6	Fabrication of quasi-BIC metasurfaces.....	55
5.7	Experimental setup for measurement of reflectance spectrum from metasurfaces.....	56
6	Conclusions and future work	59
6.1	Conclusions	59
6.2	Future work	61
	Bibliography	63
	Included publications	71
7.1	Paper I.....	71
7.2	Paper II	95
7.3	Paper III	109
7.4	Paper IV.....	133

Dedicated to the memory of my loving mother

CHAPTER 1

Introduction

1.1 Why optical trapping combined with Raman spectroscopy?

Optical trapping has revolutionized the study of biological systems and has led to breakthroughs in fields such as cell biology and biophysics [1]. Optical trapping, also known as optical tweezers, is a technique that uses a focused laser beam to trap and manipulate small particles in three dimensions. Arthur Ashkin was awarded the Nobel Prize in 2018 for his groundbreaking invention of optical tweezers. This technique enables the holding and moving of microscopic objects, such as cells [2] and bacteria [3], with great accuracy and precision, allowing for experiments to be performed that would otherwise be impossible. Raman spectroscopy, on the other hand, is a powerful analytical technique that provides chemical composition and molecular structure of a sample by analyzing the scattered light. This technique is based on the Raman effect, a phenomenon in which the incident light is scattered by a molecule, resulting in a change in frequency and energy [4]. C.V. Raman was awarded the Nobel Prize in Physics in 1930 for the discovery of the Raman effect.

In recent years, there has been growing interest in combining optical trapping with Raman spectroscopy [5-7] to analyze functional cells and individual biological particles and gain deeper insights into their molecular structures and subcellular constituents. Raman spectroscopy is a non-destructive technique that does not require any labeling of the sample to be studied. However, Raman scattering is weak. Thus, the signal must be acquired for a period (e.g., seconds to minutes) and the particle should preferably be separated from any objects giving a Raman background. Optical trapping allows for the manipulation and immobilization of microscopic particles without direct physical contact. Thus, combining the two methods

enables label-free analysis of the sample, which make them ideal for observing live cells and other biological particles [2, 8]. Another advantage of this combined approach is that it requires minimal sample preparation, needing only the separation and cleaning of particles to be analyzed.

Raman spectroscopy typically acquires multiple Raman spectra from a sample and averages them to improve the signal-to-noise ratio (SNR) [9]. This is particularly useful when dealing with weak Raman signals. Averaging spectra collected from various spatial locations on the sample results in a spectrum that represents the average properties of the sample across those locations. This may lead to a loss of spatial information, particularly in samples with heterogeneous compositions. Besides, a sample may contain different molecules with similar vibrational frequencies that makes it challenging to distinguish them in the acquired spectra. By combining optical trapping with Raman spectroscopy, individual particles can be trapped, enabling the acquisition of Raman spectra from a single entity. As a result, the acquired spectra provide detailed information about the specific particle being analyzed, rather than averaging the properties across multiple particles.

An on-chip approach, using planar structures can offer a compact and multifunctional trapping system integrated on a single chip [10]. This chip can contain multiple trapping locations, allowing for the trapping of individual particles, while simultaneously collecting Raman scattering from each location. The process can be made continuous by automating the chip with microfluidics. The microfluidic devices can be designed with multiple chambers, each capable of manipulating particles for a designated trapping location. Some methods have been investigated for parallel trapping and Raman spectroscopy of multiple particles simultaneously [11, 12] and this thesis will study novel on-chip approaches for this.

1.2 Project setting and aims of the Thesis

This thesis is part of a Research Council of Norway (RCN) funded project, “On-chip Raman-spectroscopy of extracellular vesicles” which aims to develop high throughput methods for chemical analysis of extracellular vesicles (EVs). The main focus of the project is to use optical waveguides to trap multiple EVs simultaneously and collect Raman spectra from them. However, dielectric nanoantennas and metasurfaces are studied in this thesis instead of optical waveguides. They are considered as possible alternatives to optical waveguides to trap and combine with Raman spectroscopy for analyzing single or multiple nanoparticles at the near-visible wavelength of 785 nm.

The integration of Raman spectroscopy with optical trapping using nanoantennas and metasurfaces can make it possible to investigate smaller objects. This is particularly of interest for the analysis of biological nanoparticles. Trapping of biological nanoparticles is challenging using conventional optical tweezers as the focal spot is diffraction limited. The primary goal of this thesis is to investigate suitable methods for trapping and Raman spectroscopy of multiple nanoparticles in parallel, aiming for high-throughput analysis of nanoparticles using a single excitation wavelength. A near-visible wavelength of 785 nm is considered, as it is most commonly used for Raman spectroscopy. The idea is to achieve multiple field-enhancement zones, or 'hotspots,' where a single nanoparticle is optically trapped at each hotspot, and Raman scattering is excited. Focus is given on dielectric materials because of limitations with surface-enhanced Raman scattering (SERS). The main issue with SERS arises from the variability of surface enhancements at different locations in the substrate. This is due to the strong dependence of the SERS signal on the location of a particle relative to the substrate, leading to an overall SERS spectrum that may appear distorted and often challenging to interpret. An additional goal is to investigate dielectric nanostructures capable of minimizing Joule heating at 785 nm.

Numerical simulations of two distinct types of dielectric nanostructures are performed using COMSOL Multiphysics. The first nanostructure is a low-Q (quality factor) resonant nanoantenna. The field enhancement in the nanoantenna gap is relatively low, but it gives enhancement of signal both at the excitation wavelength of 785 nm and at the Raman emission wavelengths. The second nanostructure involves a dielectric resonant metasurface that supports a high-Q quasi-bound state in the continuum (quasi-BIC) resonance at 785 nm. The metasurface can give very high field enhancement at the excitation wavelength but there is no enhancement at the emission wavelengths. The metasurface has been fabricated and an experimental setup established for its characterization. Reflectance measurements to observe resonances in the metasurface are currently in progress.

1.3 Organization of the Thesis and the publications

Chapter 2 gives a brief overview of existing methods for investigating biological particles. Chapter 3 presents the fundamentals of optical forces and Raman scattering. A brief description of the finite element method (FEM) which is used by COMSOL Multiphysics is included. Chapter 4 focuses on nanoantennas, with the theoretical background of near-field enhancement, Joule heating, heat-induced flow, and Raman enhancement. The key findings of Paper I and II are also discussed in this chapter. In Chapter 5, the physics behind quasi-BICs is presented,

along with a discussion of the main results found in Paper III and IV. This chapter also includes some scanning electron microscope (SEM) images of the fabricated samples, and the experimental setup for measuring the reflectance from the metasurface is presented. Chapter 6 summarizes the main results presented in this thesis and provides recommendations for future research. At the end of the thesis, three published articles and an article under review are included.

Paper I is a topical review article focusing on dielectric nanoantennas. It covers the properties and performance characteristics of nanoantennas, provides an overview of recent developments in the field, and highlights some selected applications. Paper II studies different dielectric materials for a bowtie nanoantenna to minimize Joule heating at 785 nm. This paper also presents optimization results of the bowtie configuration for maximum field enhancement. The bowtie nanoantenna is proposed for optical trapping and Raman spectroscopy of individual nanospheres (diameter of 15-40 nm). Paper III includes simulation results for a Si_3N_4 quasi-BIC metasurface to trap multiple EVs (diameter of 30-70 nm) simultaneously at 785 nm using low input intensity. The unit cell of this metasurface consists of two tilted elliptical bars. The interplay between the quasi-BIC and the trapped nanoparticles is studied and its influence on the trapping performance is investigated. Paper IV investigates a modified design of the Si_3N_4 quasi-BIC metasurface with two parallel elliptical bars and a cylindrical disk. The design parameters of the metasurface are optimized to maximize the fabrication tolerances and to trap EVs with a diameter up to 200 nm.

CHAPTER 2

Methods for analysis of biological particles

2.1 Biological particles and why analyze them?

Biological particles can exhibit some of the properties of life, such as growth, reproduction, metabolism, and response to stimuli, and are composed of one or more molecules or macromolecules [13]. Examples of biological particles include viruses, bacteria, extracellular vesicles (EVs), liposomes, cells, and protein aggregates [14, 15]. Analyzing the properties and functions of these particles are important as they can provide information about fundamental cellular activities such as cell signaling, metabolism, and gene regulation. This may help to better understand the root causes of many diseases and to develop more effective treatments. For example, there has been considerable interest in the chemical analysis of EVs [16-18], the topic of the RCN project, which this thesis is part of. EVs are bilayer membrane vesicles released from various cells, which are known to play a crucial role in intercellular communication by exchange of proteins, lipids, and genetic material between cells [19]. It has been shown that increased plasma levels of EVs is linked to several diseases, such as atherosclerosis, diabetes, cancer, arterial cardiovascular diseases, and venous thromboembolism (VTE) [20]. The majority of clinical VTE events cannot be adequately predicted based on the current knowledge of pathogenesis and risk factors. Therefore, identification of new risk factors is necessary that can assist in delivering targeted treatment to reduce VTE incidents. Moreover, microorganisms and pathogenic bacteria also release EVs, which can play an important role in antibiotic treatment [21] and infection process [22]. EVs are heterogeneous in nature and analyzing a limited number of them may hide their important features. Therefore, mass-screening of EVs is necessary to gain new knowledge about causes

and states of diseases, which may ultimately lead to development of more effective treatments and prevention strategies for diseases.

2.2 Methods for analysis of biological particles

Currently there are several methods used to analyze biological particles such as measurement of size distribution [23], transmission electron microscopy [24], flow cytometry [25], and fluorescence microscopy [26, 27], in addition to chemical/biological methods [28]. A brief overview of each method, along with their respective advantages and disadvantages, is presented in this section. While these methods are relevant for studying biological particles, they are not used in this thesis.

2.2.1 Size distribution

Measurement of size distribution is a technique widely used to study various biological particles such as proteins, virus-like particles, vesicles, and cells in a liquid suspension [29]. Nanoparticle tracking, dynamic light scattering, and laser diffraction are commonly used terms and approaches for measuring the size distribution using commercial instruments. All these approaches rely on directing a laser beam onto a sample containing particles and measuring light scattered from them. The fluctuation of the scattered light provides information about the size distribution of the particles. An example of size distribution measurement of biological particles by nanoparticle tracking analysis is shown in figure 2.1. The data collected show size distribution of liposomes (figure 2.1(a)) and EVs derived from human urine (figure 2.1(b)) [14]. Measurement of size distribution is a fast method, which can determine size distribution of particles within a low sample volume and allows high-throughput analysis. This method is, according to [30], suitable for particles with size ranging from sub-nanometer to several micrometers. However, this seems optimistic, as particles with diameter 50 nm, 100 nm, and 200 nm are hardly separated in figure 2.1(a). Also, the presence of large particles in the sample can dominate the scattered light signal, making it difficult to accurately measure small particles. The technique is not efficient for size measurement of non-spherical particles. Furthermore, they do not provide information about chemical composition of particles.

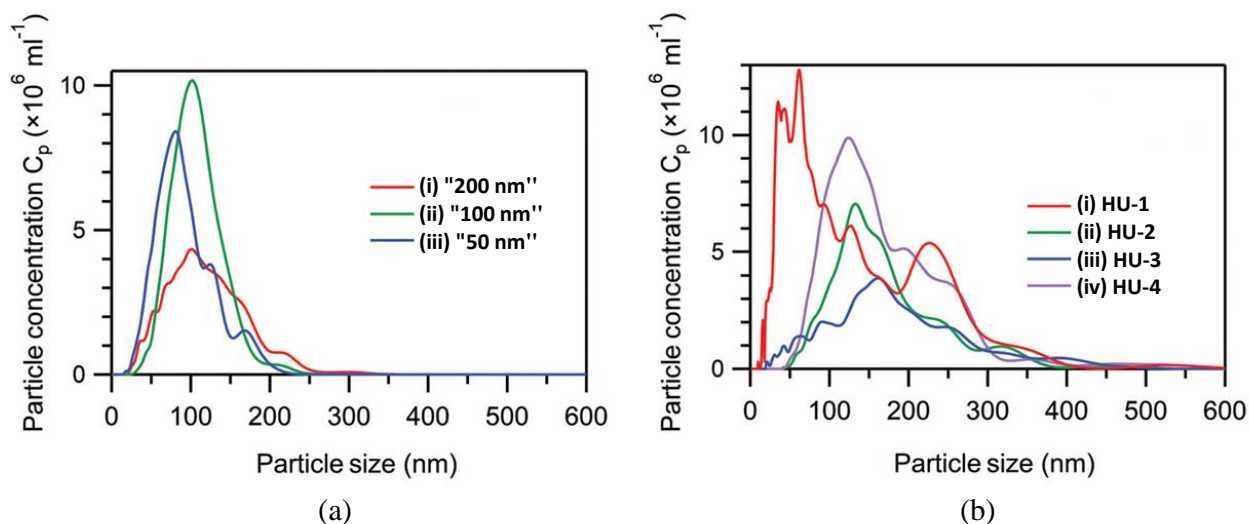


Figure 2.1: Size distribution of biological particles measured from (a) liposomes of various sizes and (b) EVs from human urine with different sizes using nanoparticle tracking analysis with NanoSight LM10 apparatus (Malvern Panalytical, UK). Reproduced from ref. [14].

2.2.2 Transmission electron microscopy

Transmission electron microscopy (TEM) is an imaging technique that utilizes a beam of electrons to create a highly magnified image of cells, viruses, proteins, and other biological particles. This method can provide high-resolution images of the particles, revealing their size and shape at the nanometer scale [31]. TEM images of 100 nm and 50 nm size liposomes, and various sizes of EVs from human urine are shown in figure 2.2 [14]. This method can be combined with other analytical techniques such as energy-dispersive X-ray spectroscopy (EDS) to determine chemical composition of the particles.

There are a number of limitations of TEM. It requires a thin sample (typically less than 100 nm) to ensure electron transmission, which can be time-consuming to prepare. Due to the small field of view of TEM, only a small portion of the sample can be observed at a time, which gives low throughput. Moreover, a biological sample may be damaged due to the interaction with the electron beam. Furthermore, samples must be completely dry and fixed with chemicals before being placed into the microscope, which can cause changes or artifacts when studying biological samples.

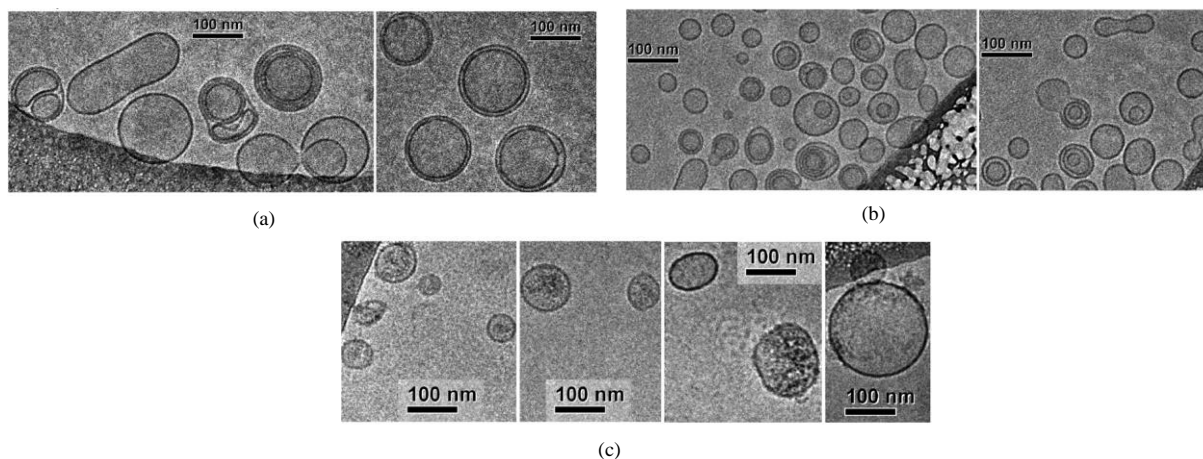


Figure 2.2: TEM images of (a) 100 nm and (b) 50 nm liposomes, and (c) various sizes exosomes from human urine. Reproduced from ref. [14].

2.2.3 Flow cytometry

Flow cytometry is a powerful technique for analyzing and quantifying the physical and chemical properties of cells or particles in a fluid suspension. Particles are suspended in a fluid stream and typically passed one-by-one through a laser beam. As the cells interact with the laser, they scatter light and emit fluorescence if they are labeled with fluorescent markers. The scattered light and fluorescence emission provide information about the size, shape, and characteristics of the particles [32]. By labeling the cells with fluorescent antibodies or dyes that bind to specific molecules, flow cytometry can be used to measure the expression of surface markers, intracellular proteins, and other molecules within the cells. Figure 2.3(a) shows differentiation of various subpopulations of human blood, which was obtained using a commercial flow cytometer (Beckman Coulter FC500) [33]. Figure 2.3(b) shows the number of CD4⁺ cell count in human blood. The blood cells are stained with monoclonal Alexa Fluor 488-labeled anti-human CD4 antibody to count the CD4⁺ cells using the Beckman Coulter FC500 flow cytometer [33].

Flow cytometry can analyze thousands of particles per second, making it suitable for high-throughput analysis of particles. Flow cytometry requires fluorescent labeling, which can be challenging for nanoparticles and provide information about only one or few chemical compounds present in the particle. Moreover, this technique is primarily designed for analyzing particles in suspension, and adherent cells often require extra steps to be detached and processed before analysis.

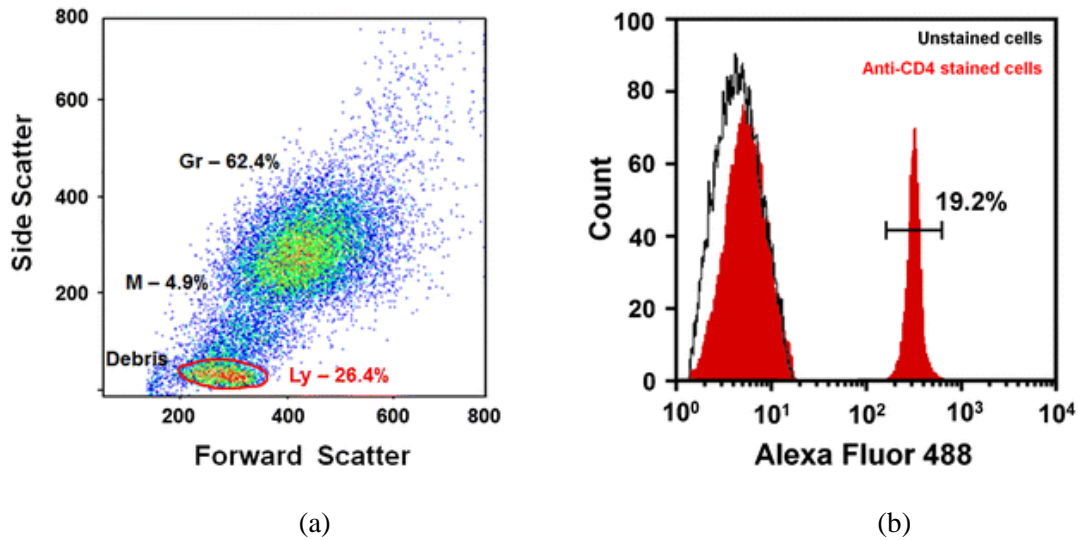


Figure 2.3: (a) Identification of different subpopulations of human blood using a commercial Beckman Coulter FC500 flow cytometer. Percentages of granulocytes (Gr), monocytes (M), and lymphocytes (Ly) are shown in forward versus side scatter plot. (b) CD4+ cell count in human blood using the Beckman Coulter FC500 flow cytometer. Reproduced from ref. [33].

2.2.4 Fluorescence microscopy

Fluorescence microscopy is an optical imaging technique that utilizes the properties of fluorescence to visualize specific structures or molecules within cells, or other biological particles [34]. It involves the use of fluorophores, which are molecules that can absorb light at a specific wavelength and emit light at a longer wavelength. The sample is labeled with fluorophores, either directly or through the use of fluorescent antibodies or other binding molecules. When illuminated with the appropriate excitation light, the fluorophores emit light, which is detected and imaged by the microscope. For instance, figure 2.4 shows characterization of red blood cells labeled with different fluorescent dyes [35]. Fluorescence microscopy allows for the specific visualization of target molecules by using fluorophore-labeled probes or simultaneous visualization of multiple targets by using different fluorophores with non-overlapping emission spectra.

Fluorescence microscopy has several limitations. It requires labelling of samples with fluorophores that can be time-consuming and may alter the biological properties of the sample, as for flow cytometry. Moreover, poor sample preparation in fluorescence microscopy can lead to high background noise, poor signal-to-noise ratio, and loss of important cellular structures. Furthermore, fluorescent dyes used in these techniques can be damaged by the excitation light, leading to photobleaching of the fluorescence signal over time. Fluorescence microscopy has a

medium throughput, which is higher than that of TEM, but lower than flow cytometry and size measurement techniques.

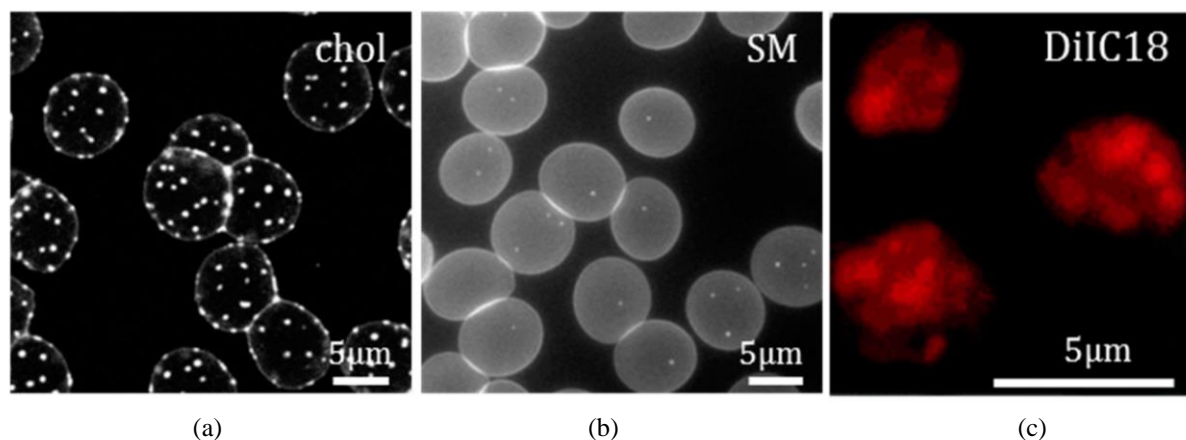


Figure 2.4: Fluorescence microscopy images of (a, b) red blood cells labeled with theta-D4-mCherry and boron-dipyrromethene-sphingomyelin, respectively and (c) platelets labeled with DiI C18. Reproduced from ref. [35].

2.2.5 Raman spectroscopy and surface-enhanced Raman spectroscopy

Recently, Raman spectroscopy has emerged as a useful technique for analyzing biological specimens such as blood cells [36], EVs [18], and tumor cells [37]. One of the key advantages of Raman spectroscopy over the above-mentioned methods is that it can provide detailed information about the chemical composition of particles without any labeling of the sample. The method can analyze live cells without altering their natural state, as opposed to TEM. The intensity of the Raman scattering signal is extremely weak, typically several orders of magnitude weaker than the incident laser light used to excite the sample. Surface-enhanced Raman spectroscopy (SERS) is a technique that can amplify Raman scattering by placing a sample onto a roughened metallic surface, where the local electromagnetic field is strongly enhanced due to the excitation of surface plasmon resonances [38]. This results in a large increase in the Raman scattering cross-section, allowing for the detection of very small amounts of the sample molecule. The interest in SERS for the analysis of biomolecules and nanosized bioparticles is large and substantial efforts have been made to achieve a giant SERS enhancement, making it possible to detect single molecules [39]. Among the various applications of SERS are characterization of antibiotic resistance [40] and pathogenic bacteria [41]. The main limiting factor of SERS is that SERS signals can be highly variable, depending on the properties of the metal substrate, distance between the molecule and the SERS substrate, and the adsorption sites of the analyte molecules [42]. This leads to a fragmented, distorted, and often difficult-to-interpret SERS vibrational spectrum. Only molecules attached to or

incorporated into the particle's membrane can be detected and analyzed due to the short range of the field enhancement. Moreover, SERS requires a clean and well-defined metal surface to obtain reliable signals. Any contamination or surface modification can affect the SERS signals, making it difficult to obtain reproducible and quantitative data.

2.2.6 Raman tweezers microspectroscopy

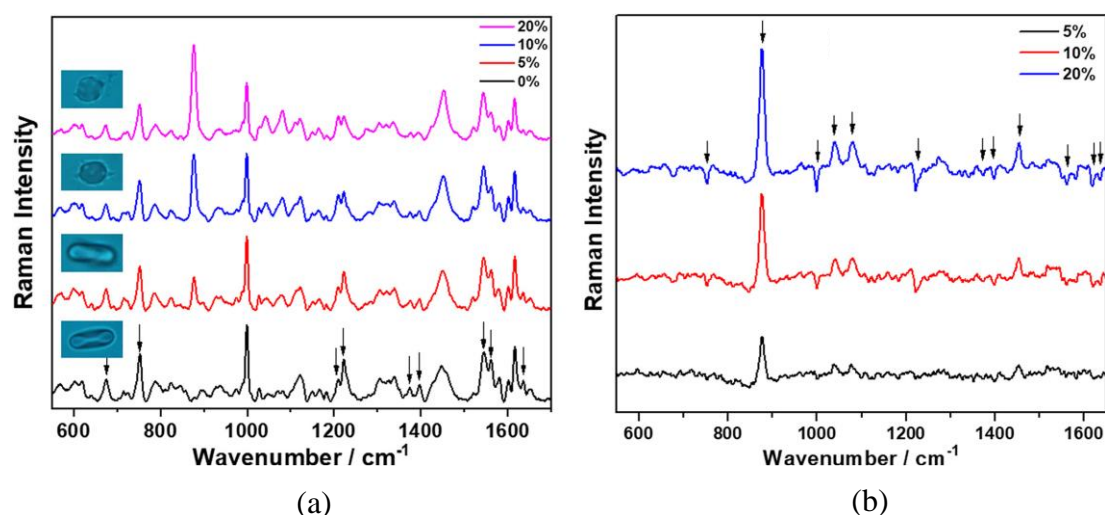


Figure 2.5: (a) Average Raman spectra of RBC with different ethanol concentrations. Images of trapped RBC suspended in different ethanol concentrations are shown in the inset. (b) Difference spectra obtained for three ethanol concentrations relative to 0% ethanol. Reproduced from ref. [7].

Optical trapping combined with Raman spectroscopy, known as Raman tweezers microspectroscopy, is a non-contact and label-free technique that combines Raman spectroscopy with optical tweezers to study individual particles. The main idea of this technique is to use the same laser beam for optical trapping of particles and exciting Raman scattering from them. Raman tweezers microspectroscopy using a single laser beam has been reported to characterize different solids [43-45] and biological particles [6, 7, 14, 46, 47]. A recent work has shown that it can distinguish alcohol-treated cells and healthy cells [7], as reproduced here in figure 2.5(a). The Raman spectra of cells treated with ethanol are noticeably distinct from those of healthy cells, as demonstrated by the difference spectra for three concentrations of ethanol shown in figure 2.5(b). In other articles, the biomolecular composition of trapped EVs has been investigated using Raman tweezers microspectroscopy [14, 17, 47]. In addition to studies using a single laser, some have used one wavelength for trapping and a different wavelength for Raman excitation [5, 48]. Furthermore, counter-propagating beams have been used to trap solid and biological particles [49-51]. On-chip approaches for optical trapping and

Raman spectroscopy of microparticles were also demonstrated using optical waveguides [10, 52, 53]. As Raman tweezers microspectroscopy relies on measuring average Raman spectra of a small number of particles, the process must be repeated to accumulate sufficient data for statistical analysis. This technique thus provides low throughput as it allows the analysis of only a single particle or a few particles at the same time. Raman tweezers microspectroscopy is primarily used in research, but it has potential for application in a variety of industries, such as pharmaceuticals, biotechnology, environmental science, and materials science.

2.3 Motivation for new methods

This thesis focuses on exploring new methods for analyzing chemical compositions of biological nanoparticles such as extracellular vesicles (EVs). The analysis performed with current techniques provides only limited information about the size, and the chemical compositions of nanoparticles. Besides, some methods require complex sample preparation, potentially altering the physical and chemical properties of the biological nanoparticles. Similarly, a method that only captures Raman spectra from one nanoparticle or a few nanoparticles at the same time requires a large number of measurements to obtain reliable statistics. This results in low throughput analysis of the nanoparticles. Therefore, the development of new techniques is crucial to obtain high throughput by analyzing multiple nanoparticles in parallel. Optical trapping combined with Raman spectroscopy, using dielectric nanoantennas or quasi-BIC metasurfaces, is as a promising approach, as it offers several advantages over conventional techniques. These nanostructures provide multiple trapping hotspots, where a single nanoparticle can be trapped at each hotspot, thus enabling high-throughput analysis of the nanoparticles. The nanostructures are fabricated on a single chip and can be integrated with microfluidics for automating the analysis system.

CHAPTER 3

Fundamental concepts

In this chapter, the fundamental concepts used throughout the thesis are presented. First, the origin of optical forces acting on a particle is introduced. Two different scenarios are considered: forces in the dipole approximation and beyond the dipole approximation. An introduction to the Maxwell stress tensor (MST) is given, as it is used to compute optical forces for the works presented. The fundamental physics of Raman scattering and its application to Raman spectroscopy is presented. Finally, a brief overview of the finite element method (FEM) is given, which is used to perform simulations of nanostructures using COMSOL Multiphysics.

3.1 Optical trapping and forces on a particle

Light (photons) carries both linear and angular momentum, which produces optical forces and torques on objects through momentum transfer. The ability of light to exert optical forces was reported in 1901, while the trapping of micrometer-sized particles using a laser was first demonstrated by A. Ashkin in 1970 [54]. It was demonstrated that a single, tightly focused laser beam, now known as *optical tweezers*, can trap microscopic particles near the focal point of the laser beam. The basic experimental setup for optical tweezers is straightforward: a single continuous wave (CW) laser beam is directed into an optical microscope and focused by a high numerical aperture (NA) objective lens to create a diffraction-limited spot, where a particle becomes trapped. Since the first demonstration of optical tweezers, they have been used to capture and handle diverse small objects, spanning from dielectric and metallic particles to atoms, molecules, viruses, and living cells. The research literature on optical tweezers is extensive and some review papers can be found in [55-60].

Upon interacting with a light beam, an object experiences momentum and forces exerted by the light. Depending on the size of the trapped object relative to the incident wavelength, these

forces can be described in several ways. In the following, the dipole approximation and the rigorous Maxwell stress tensor are described.

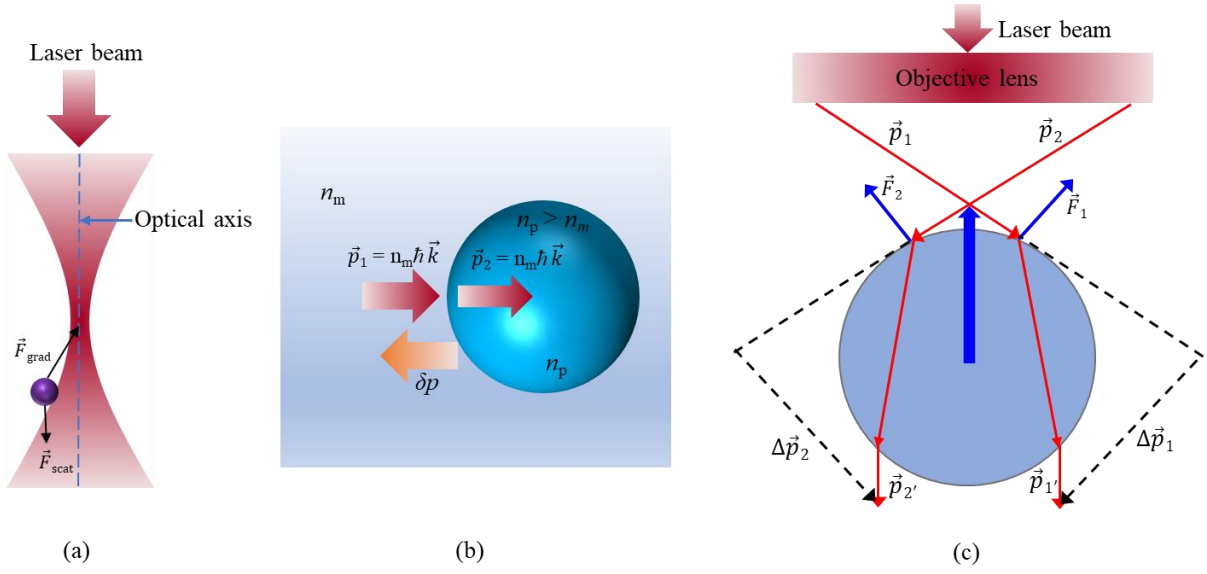


Figure 3.1: (a) Schematic illustration of single-beam optical tweezers, (b) illustration of the momentum transfer of photons impinging perpendicularly on a particle, and (c) ray optics picture of the origin of gradient force \vec{F}_{grad} . Adapted from ref. [61].

Forces in the dipole approximation: When the size of the trapped particle is significantly smaller than the wavelength of the trapping laser (Rayleigh particle), the interaction between the particle and the light field can be described using the dipole approximation [62]. Under this approximation, when the Rayleigh particle encounters a beam, it acts like an electric point dipole that oscillates with the incident electric field. The oscillating dipole experiences a time-averaged force which is given by [63]:

$$\langle \vec{F} \rangle = \underbrace{\frac{1}{4} \text{Re}(\alpha_p) \nabla |\vec{E}|^2}_{\vec{F}_{\text{grad}}} + \underbrace{\frac{\sigma(\alpha_p)}{2c} \text{Re}(\vec{E} \times \vec{H}^*) + \sigma(\alpha_p) c \nabla \times \left(\frac{\epsilon_0}{4\omega i} \vec{E} \times \vec{E}^* \right)}_{\vec{F}_{\text{scat}}} \quad (3.1)$$

where α_p is the polarizability of the particle, ϵ_0 is the vacuum permittivity, and c is the speed of light in vacuum. The incident electromagnetic field is given by \vec{E} and \vec{H} , and has a frequency ω . In equation (3.1), the first term denotes the optical gradient force \vec{F}_{grad} , which is proportional to the real part of the polarizability of the particle and the gradient of the field intensity. This is a conservative force that pulls the particle towards the highest intensity region of the beam (focus), as shown in figure 3.1(a). For a Rayleigh particle, the polarizability can be found from the following expression [64]:

$$\alpha_p = \frac{\alpha_0}{1 - i\alpha_0 k_0^3 / 6\pi\epsilon_0} \quad (3.2)$$

where $k_0 = 2\pi/\lambda$ is the free-space wavenumber of the trapping laser beam, λ is the wavelength of the beam, and the static Clausius-Mossotti polarizability α_0 is given by [64]:

$$\alpha_0 = 4\pi n_m^2 \varepsilon_0 r^3 \left(\frac{n_p^2 - n_m^2}{n_p^2 + 2n_m^2} \right) \quad (3.3)$$

where n_m is the refractive index of the medium surrounding the particle, n_p is the refractive index of the particle, and r is the particle radius.

Using the first order approximation, i.e., $\alpha_0 \approx \alpha_p$, the gradient force \vec{F}_{grad} becomes,

$$\langle \vec{F}_{\text{grad}} \rangle = \pi n_m^2 \varepsilon_0 r^3 \left(\frac{n_p^2 - n_m^2}{n_p^2 + 2n_m^2} \right) \nabla |\vec{E}|^2 \quad (3.4)$$

The second and the third term in equation (3.1) jointly represent the scattering force \vec{F}_{scat} . This is a nonconservative force which is proportion to the total cross-section of the particle, $\sigma(\alpha_p)$. The radiation pressure force, represented by the second term, propels the particle along the direction of the Poynting vector (figure 3.1(a)). The third term is the spin curl force which originates from an irregular distribution of the spin density of the light field. The total particle cross-section is the sum of the scattering cross section σ_{scat} and the absorption cross-section σ_{abs} .

$$\sigma(\alpha_p) = \sigma_{\text{scat}} + \sigma_{\text{abs}} \quad (3.5)$$

where σ_{scat} and σ_{abs} are given by [62]:

$$\sigma_{\text{scat}}(\alpha_p) = \frac{k^4}{6\pi\varepsilon_0^2} |\alpha_p|^2 \quad (3.6)$$

$$\sigma_{\text{abs}}(\alpha_p) = \frac{k}{\varepsilon_0} \text{Im}(\alpha_p). \quad (3.7)$$

For a plane wave with intensity I_0 and Poynting vector \mathbf{S} , the spin curl force becomes zero. Also, for a small non-absorbing particle, $\sigma_{\text{abs}}(\alpha_p) = 0$ and σ_{scat} is given by [63]:

$$\sigma_{\text{scat}}(\alpha_p) = \frac{128\pi^5 r^6}{3\lambda^4} \left(\frac{n_p^2 - n_m^2}{n_p^2 + 2n_m^2} \right)^2. \quad (3.8)$$

Therefore, the scattering force \vec{F}_{scat} can be expressed as [63]:

$$\langle \vec{F}_{\text{scat}} \rangle = \frac{\sigma_{\text{scat}}}{c} I_0 \mathbf{S} = \frac{128\pi^5 r^6}{3c\lambda^4} \left(\frac{n_p^2 - n_m^2}{n_p^2 + 2n_m^2} \right)^2 I_0 \mathbf{S}. \quad (3.9)$$

When \vec{F}_{scat} becomes strong, it counteracts the effect of \vec{F}_{grad} by pushing the particle in the propagation direction and destabilizes the optical trap. Therefore, for stable trapping, \vec{F}_{grad} must

exceed \vec{F}_{scat} . In this thesis, the size of the trapped particle is significantly smaller (10 to 200 nm in diameter) than the wavelength of the trapping beam (785 nm). Therefore, the optical forces acting on these particles, as discussed in Chapter 4 and 5, can be determined using the dipole approximation.

Forces beyond the dipole approximation: When the particle size is comparable to or larger than the trapping laser wavelength, the dipole approximation is invalid and cannot be used to describe the optical forces. The particle now acts as a refractive object. The forces acting on the particle can be described using ray optics for particles significantly larger than the wavelength. Figure 3.1(b) shows momentum of photons propagating in a medium with refractive index n_m , which is given by [65]:

$$\vec{p}_1 = n_m \hbar \vec{k} \quad (3.10)$$

The photons cross the particle with refractive index $n_p > n_m$ and undergoes a change of momentum to:

$$\vec{p}_2 = n_p \hbar \vec{k} \quad (3.11)$$

According to Newton's second law, the rate of change of momentum produces a force. Thus, the force acting on the particle is given by:

$$\vec{F} = \frac{\delta \vec{p}}{\delta t} = \frac{\delta}{\delta t} \hbar \vec{k} (n_p - n_m) \quad (3.12)$$

Figure 3.1(c) uses ray optics to illustrate the origin of gradient force \vec{F}_{grad} . The individual rays emitted from the laser are refracted as it enters and exits the particle. The refraction changes the direction of the light (red arrows), which implies a change in the momentum of photons. According to the momentum conservation law, any change in momentum of the photons must be compensated by an equivalent and opposite change in momentum of the particle. The changes in momentum $\Delta \vec{p}_1$ and $\Delta \vec{p}_2$ create forces \vec{F}_1 and \vec{F}_2 on the particle (blue arrows). The vector sum of the two forces gives a force \vec{F}_{grad} (backward blue arrow) that pulls the particle to the focus. Similarly, rays reflected by the particle produce scattering force \vec{F}_{scat} that pushes the particle in the direction of incident light (not shown here). Stable trapping occurs when there is an equilibrium between the opposing forces.

For a particle that cannot be considered as a point dipole, the optical force exerted on it can be determined using a numerical simulation of the field and applying rigorously the Maxwell stress

tensor (MST). This is a widely used method and it is correct for objects with arbitrary shape, size, and refractive index. When an object interacts with an electromagnetic field, the total time-averaged optical force $\langle \vec{F} \rangle$ exerted on an object can be determined by integrating the stress tensor over an arbitrary surface S enclosing the object [66]:

$$\langle \vec{F} \rangle = \oint_{\delta S} \langle \vec{T}(\vec{r}, t) \rangle \cdot \hat{n}(\vec{r}) dS \quad (3.13)$$

where $\vec{T}(\vec{r}, t)$ is the Maxwell stress tensor, and $\hat{n}(\vec{r})$ is the outward-pointing unit normal vector to the surface S . The time-averaged stress tensor is given by [62]:

$$\langle \vec{T}(\vec{r}, t) \rangle = \frac{1}{2} \text{Re} \left[\varepsilon_0 \varepsilon_r \vec{E} \vec{E}^* + \mu_0 \mu_r \vec{H} \vec{H}^* - \frac{1}{2} \left(\varepsilon_0 \varepsilon_r |\vec{E}|^2 + \mu_0 \mu_r |\vec{H}|^2 \vec{I} \right) \right] \quad (3.14)$$

which is a rank-2 tensor, represented by a 2-dimensional 3×3 matrix in cartesian coordinates. The components are given by:

$$\vec{T} = \begin{bmatrix} T_{xx} & T_{xy} & T_{xz} \\ T_{yx} & T_{yy} & T_{yz} \\ T_{zx} & T_{zy} & T_{zz} \end{bmatrix},$$

with $T_{xx} = \varepsilon_0 \varepsilon_r \left(E_x^2 - \frac{E^2}{2} \right) + \mu_0 \mu_r \left(H_x^2 - \frac{H^2}{2} \right)$

$$T_{yy} = \varepsilon_0 \varepsilon_r \left(E_y^2 - \frac{E^2}{2} \right) + \mu_0 \mu_r \left(H_y^2 - \frac{H^2}{2} \right)$$

$$T_{zz} = \varepsilon_0 \varepsilon_r \left(E_z^2 - \frac{E^2}{2} \right) + \mu_0 \mu_r \left(H_z^2 - \frac{H^2}{2} \right)$$

$$T_{xy} = \varepsilon_0 \varepsilon_r E_x E_y + \mu_0 \mu_r H_x H_y \quad (3.15)$$

$$T_{xz} = \varepsilon_0 \varepsilon_r E_x E_z + \mu_0 \mu_r H_x H_z$$

$$T_{yx} = \varepsilon_0 \varepsilon_r E_x E_y + \mu_0 \mu_r H_x H_y$$

$$T_{yz} = \varepsilon_0 \varepsilon_r E_y E_z + \mu_0 \mu_r H_y H_z$$

$$T_{zx} = \varepsilon_0 \varepsilon_r E_x E_z + \mu_0 \mu_r H_x H_z$$

and $T_{zy} = \varepsilon_0 \varepsilon_r E_y E_z + \mu_0 \mu_r H_y H_z$.

Furthermore, \vec{I} is the identity matrix, ε_0 is the vacuum permittivity, μ_0 is the vacuum permeability, ε_r is the relative permittivity and μ_r is the relative permeability of the surrounding medium. The force acting on a homogeneous and inelastic particle is solely dependent on the

electric and magnetic fields present on the surface S of the particle. As the Maxwell stress tensor considers both the incident and scattered fields (figure 3.2), the force calculations can be performed without explicitly solving the scattering problem for the particle involved. In this thesis, the Maxwell stress tensor is used to determine the optical force on different particles in nanoantennas and quasi-BIC metasurfaces, as discussed in chapters 4 and 5, respectively.

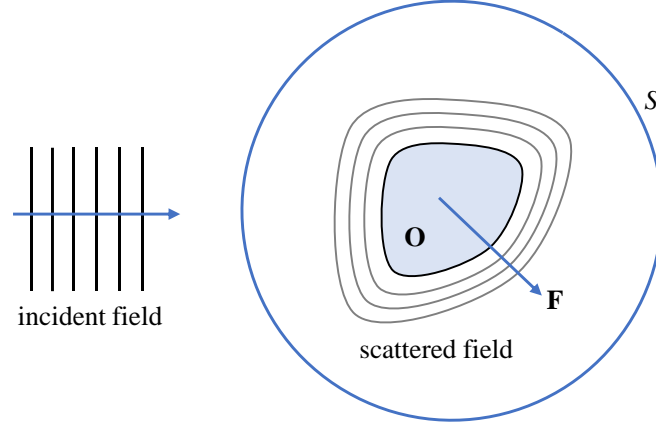


Figure 3.2: Field induced force on an object O calculated on the surface boundary S . Adapted from ref. [62].

Trapping potential: Once the optical force acting on a particle is determined, the trapping potential can be calculated by integrating the force in one dimension, such as along the z -axis. Mathematically, the trapping potential $U(z_0)$ is given by the following expression:

$$U(z_0) = - \int_{\infty}^{z_0} \langle F_z(z) \rangle \cdot dz \quad (3.16)$$

where z_0 is the reference point. As z approaches infinity, the trapping potential tends to zero.

3.2 Raman scattering and Raman spectroscopy

Raman scattering, named after the famous scientist C.V. Raman, is a phenomenon in which a small fraction of incident light is scattered by a molecule. Raman scattering occurs when a photon interacts with a molecule, causing a temporary distortion in the electron cloud of the molecule, which leads to a change in the vibrational or rotational energy levels of the molecule. This interaction results in three possible outcomes, which can be described by the Jablonski diagram shown in figure 3.3. First, a photon interacts with a molecule, raising it to a virtual energy state. The molecule may return to its original state while releasing a photon with the same energy as the incoming photon. This is an elastic process known as Rayleigh scattering, in which the wavelength of the incident photon and the scattered photon remains the same. Second, a molecule in the ground state is excited to a virtual state and relax back to a vibrational state, emitting a photon with less energy than the incoming photon. This is called Stokes

scattering, where the scattered photon exhibits a longer wavelength than the incident photon. Third, a molecule already in a vibrational state is stimulated to a higher virtual state and revert to the ground state, emitting a photon with higher energy than the incoming photon. This is known as anti-Stokes scattering, where the emitted photon possesses a shorter wavelength than the incoming photon. Both Stokes and anti-Stokes scattering are inelastic scattering. The difference between the incident wavelength and the scattered wavelength is called the Raman shift. This also represents the difference in energy between the incident light and the Raman scattered light and is proportional to the vibrational energy of the molecule. For Raman scattering to occur in a molecule, there must be a change in the polarizability of the molecule during the scattering process. This change can occur due to a change in the molecular vibrational state, which leads to a change in the distribution of electrons within the molecule. The strength of the Raman scattering is directly proportional to the change in polarizability of the molecule.

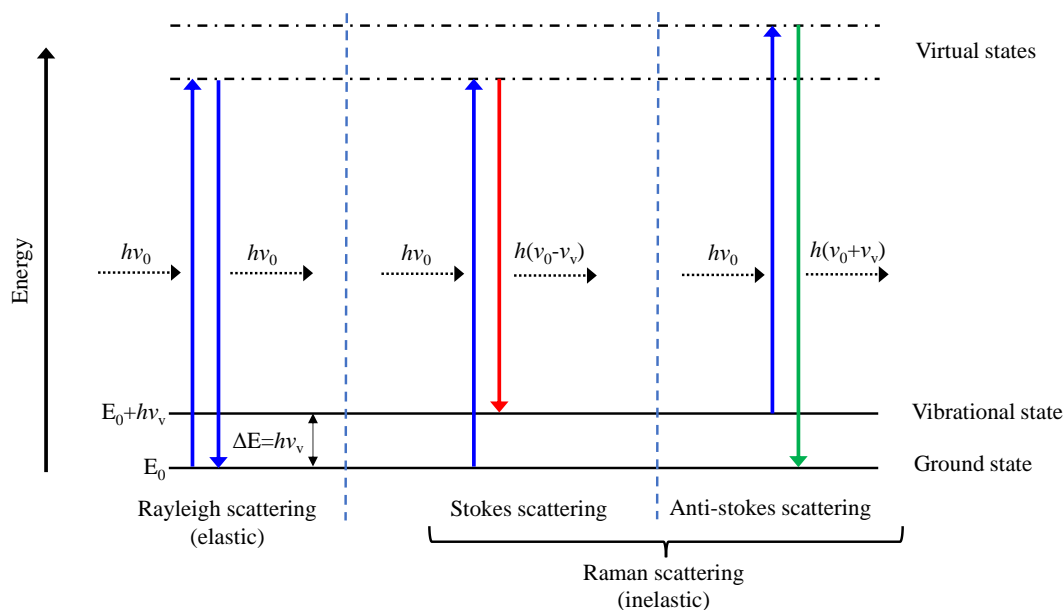


Figure 3.3: Jablonski diagram showing quantum energy transitions when a molecule is excited by a photon with energy $h\nu_0$ where ν_0 is the frequency of the incident photons. Here, ΔE represents a difference in the vibrational or rotational energy levels.

In Raman spectroscopy, a monochromatic light source, often a laser, illuminates the sample, and the scattered light is measured by a spectrometer. The intensity of the inelastically scattered light at different Raman shifts is plotted, which is known as the Raman spectrum. A schematic of a Raman spectrum is shown in figure 3.4 showing Stokes and anti-Stokes shift relative to the incident laser wavelength. Raman shift $\Delta\tilde{\nu}$ is typically measured in wavenumbers (cm^{-1}),

reciprocal of the wavelength. The conversion between wavelength and wavenumber is given by:

$$\Delta\tilde{\nu}(\text{cm}^{-1}) = \left(\frac{1}{\lambda_0(\text{nm})} - \frac{1}{\lambda_1(\text{nm})} \right) \times \frac{(10^7 \text{ nm})}{(\text{cm})}. \quad (3.17)$$

with λ_0 is wavelength of the incident laser, and λ_1 is the wavelength of the Raman scattering. The Raman spectrum contains peaks corresponding to the vibrational modes of molecules present in the sample. These peaks are the unique fingerprints for specific molecules, allowing identification of the molecular constituents within the sample. The width of the peaks in a Raman spectrum can provide information about the crystallinity of a material. Sharper and narrower peaks in the Raman spectrum are associated with crystalline materials, while broader and less well-defined peaks are indicative of amorphous materials. The intensity of the peaks in a Raman spectrum can give information about the concentration of the substance in the sample.

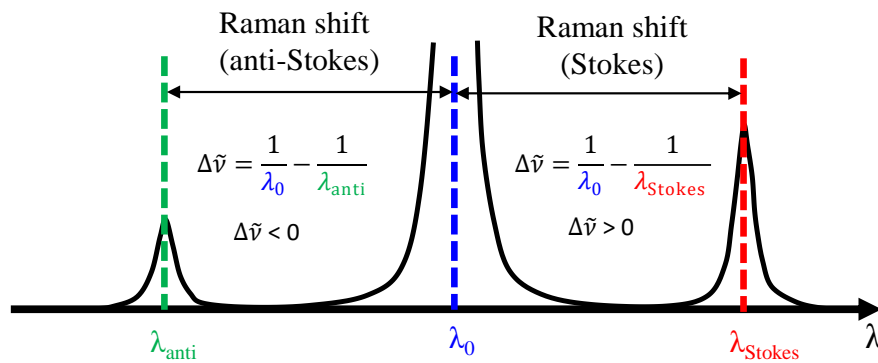


Figure 3.4: Stokes and anti-Stokes Raman shift determined from Stokes and anti-Stokes wavelengths with respect to incident laser wavelength. $\Delta\tilde{\nu}$ is positive for Stokes shift and is negative for anti-Stokes shift.

In Raman spectroscopy, Stokes scattering is typically more intense than anti-Stokes scattering at thermal equilibrium because most molecules are in the ground vibrational state. Thus, there is a higher probability for Stokes scattering than for anti-Stokes scattering. For this reason, the Stokes shift is typically measured in Raman spectroscopy. As the temperature increases, more molecules have enough thermal energy to be in an excited vibrational state. This means that the probability of an anti-Stokes scattering event increases, which in turn results in an increase in the intensity of the anti-Stokes lines. The temperature dependence of the intensity ratio between Stokes and anti-Stokes Raman scattering is described by the Boltzmann distribution. The intensity of a Stokes line (I_{Stokes}) and an anti-Stokes line (I_{anti}) is related to the temperature by [67]:

$$\frac{I_{\text{stokes}}}{I_{\text{anti}}} = \exp\left[\frac{h\nu_b}{kT}\right] \quad (3.18)$$

where h is Planck's constant, ν_b is the frequency of the vibrational mode, k is Boltzmann's constant, and T is the absolute temperature.

3.3 The finite element method

The laws of physics governing space- and time-dependent problems are typically expressed through partial differential equations (PDEs). For many geometries and problem types, these PDEs cannot be solved analytically. To address this challenge, approximation techniques such as the finite element method (FEM) or the finite difference time domain (FDTD) are employed. COMSOL Multiphysics is a powerful simulation software that employs the finite element method to solve complex physics-based problems. In COMSOL, users can generate physics-based models using a computer-aided design (CAD) graphical interface. The software allows users to define material properties and specify boundary conditions for the problem at hand. Once the model is set up, the FEM solver discretizes the problem domain into smaller, simpler elements called finite elements. The behavior of these elements is described using mathematical equations, and the global system of equations is assembled from these individual element equations. The assembled system of equations is then solved to obtain the approximate solution to the original PDEs.

In COMSOL, meshing is a crucial step in the simulation process, as it defines how the geometry of the problem is discretized into smaller elements. COMSOL provides different types of meshes to suit different problem geometries and physics. For instance, tetrahedral elements are suitable for most 3D geometries while triangular elements are used for 2D problems. Defining the mesh size is important to correctly resolve the simulation domains. For simulation of high refractive index nanostructures at visible wavelengths, a dense mesh is required to obtain accurate results. To illustrate how the mesh size affects the simulation results, a silicon disk nanoantenna is simulated in air (figure 3.5). The maximum mesh element size is varied by changing a scaling factor S according to mesh size = $\lambda/(nS)$. The simulation wavelength λ is 785 nm, and n is the refractive index of the disk. A small scaling factor gives coarse mesh, as shown in figure 3.5(a) with a scaling factor $S = 3$. On the other hand, increasing the scaling factor results in a dense mesh, which is shown in figure 3.5(b) for a scaling factor $S = 7$. Figure 3.5(c) shows the maximum electric field enhancement in the silicon nanoantenna as a function of scaling factor. The maximum of the field enhancement fluctuates for smaller scaling factors,

and it becomes flat when the scaling factor exceeds 7, indicating that this gives a sufficiently dense mesh to get an accurate result.

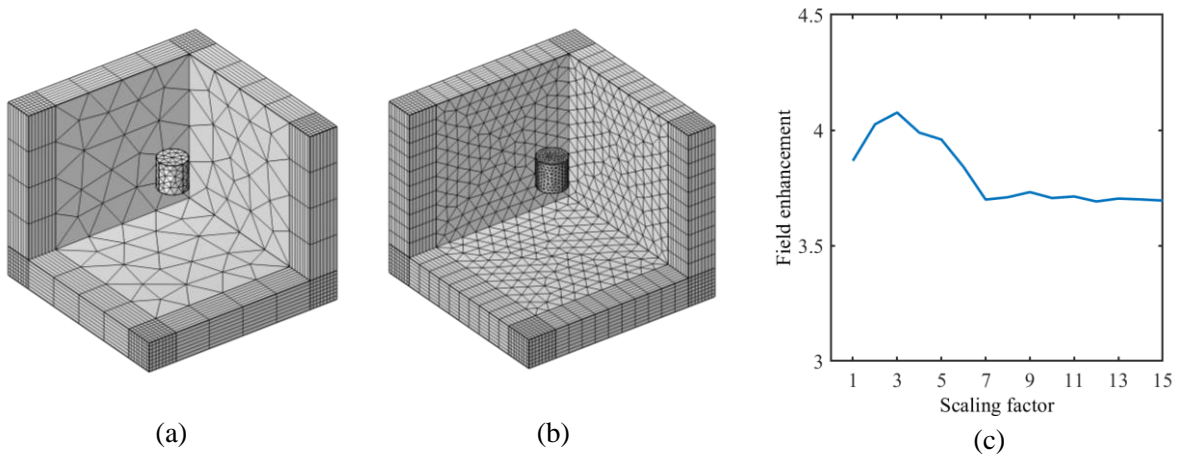


Figure 3.5: Meshing of a silicon disk nanoantenna surrounded by air with scaling factor of (a) $S = 3$ and (b) $S = 7$, respectively. (c) Maximum electric field enhancement as function of scaling factor. In the simulation, the refractive indices of air, and silicon are set to 1 and 3.7, and the wavelength is 785 nm.

Various boundary conditions can be used in COMSOL simulations. A perfectly matched layer (PML) is an artificial absorbing boundary condition, which is typically added around the simulation domain to absorb the outgoing waves and prevent them from reflecting back into the simulation domain. In chapter 4, dielectric nanoantennas are simulated using PML boundary conditions around the nanoantennas. A scattering boundary condition (SBC) can also serve as a non-reflective layer; however, PML typically provides more accurate results at the expense of some extra mesh elements. In addition, perfect electric conductor (PEC) and perfect magnetic conductor (PMC) are used to take advantage of symmetry in a problem, allowing only to simulate a portion of the geometry. This reduces the complexity of the problem and the computational resources required but limits the study to one polarization of the field. If a structure is periodic and infinitely large, periodic boundary conditions (PBCs) can be employed to determine the response of the entire structure. These boundary conditions are applied to a smaller part of the structure, known as the unit cell, rather than the entire structure, thereby reducing the computational memory requirements and simulation time. PBCs are used to simulate quasi-BIC metasurfaces, as presented in Chapter 5.

CHAPTER 4

Dielectric nanoantennas for on-chip optical trapping

The conventional techniques discussed in Chapter 2 for analyzing nanoparticles suffer from numerous limitations, with one major drawback being their off-chip nature. This chapter focuses on a chip-based method for optical trapping and Raman spectroscopy of nanoparticles. Section 4.1 provides an overview of various existing methods, discussing their limitations when operating at near-visible wavelengths. It is argued for the use of dielectric nanoantennas in this chapter, given their ability to combine optical trapping and Raman spectroscopy. This approach can readily be extended to simultaneous analysis of multiple nanoparticles using an array of nanoantennas on a single chip and using a single trapping beam.

Optical nanoantennas provide a means to manipulate light on the subwavelength scale. They confine light beyond the diffraction limit and provide a small mode volume. These properties have enabled a wide range of applications. While plasmonics is an established field in nanophotonics, dielectric nanoantennas are considered the next frontier. In section 4.2, some advantages of dielectric nanoantennas over plasmonic nanoantennas are discussed. This chapter includes two papers. Paper I is a review article on dielectric optical nanoantennas. It presents important optical properties of dielectric nanoantennas with some recent applications. New simulations of a silicon dimer are included in the article and discussed in this chapter to show the relationship between mode volume, Q-factor, and Purcell factor.

This chapter also includes definitions and explanations of important parameters and physics of dielectric nanoantennas that are relevant to optical trapping and Raman spectroscopy, such as field enhancement, Raman enhancement, Joule heating, and convective flow. Paper II presents

simulations of these properties in dielectric nanoantennas using various modules in COMSOL Multiphysics.

4.1 On-chip optical trapping and Raman spectroscopy

On-chip optical trapping can be described as a technique that involves trapping and manipulating particles on and with a chip. This approach provides several advantages over traditional optical trapping methods. One advantage of on-chip trapping is the miniaturization of the trapping system, which facilitates trapping with a very small sample volume. Moreover, the chips can be designed with a number of trapping sites for simultaneous trapping of many particles, enabling high-throughput analysis. Several on-chip methods have been explored to trap and manipulate particles. Waveguides are one of the most promising on-chip platforms. For example, a silicon slot waveguide was demonstrated for on-chip trapping of 100 nm polystyrene nanoparticles at 1550 nm, as shown in figure 4.1(a) and (b) [68]. Moreover, on-chip trapping and transport of particles were experimentally demonstrated at 1070 nm using rib waveguides [69, 70]. These structures are capable of trapping a single or a few particles at once, but the wavelengths used are not suitable for Raman spectroscopy, as the range of high sensitivity spectrometers is limited to ≤ 1050 nm. Photonic crystal cavities are another example of an on-chip approach for optical trapping. A silicon photonic crystal cavity was demonstrated to trap 48 nm and 62 nm nanoparticles at 1550 nm (figure 4.1(c)) [71]. This structure is also not applicable for Raman spectroscopy, as silicon is not transparent for wavelengths < 1100 nm.

Optical nanoantennas as a platform for optical trapping and Raman spectroscopy has been proposed in recent years. These nanostructures, typically made of metallic or dielectric nanostructures, can confine, and manipulate light at the nanoscale, leading to enhanced light-matter interactions. Raman spectroscopy and plasmonic trapping has been demonstrated in different plasmonic nanoantenna configurations [72-74]. For instance, optical trapping and manipulation of 300 nm polystyrene beads were experimentally demonstrated using a gold diabolo nanoantenna, as shown in figure 4.1(d) and (e) [75]. Plasmonic nanostructures have also been investigated to combine optical trapping of nanoparticles and simultaneously collect their SERS spectra using a single trapping beam [76, 77]. Numerous works have shown that on-chip SERS can amplify the Raman by 10^7 to 10^{12} [78], which has enabled analysis of single biomolecules. A limitation of on-chip SERS is that the SERS enhancement can be highly sensitive to the size and shape of the nanostructured metallic surface, which can lead to variability and reduced reproducibility between different SERS substrates. Trapping and

Raman spectroscopy of biological particles using plasmonic nanostructures is also limited due to Joule heating.

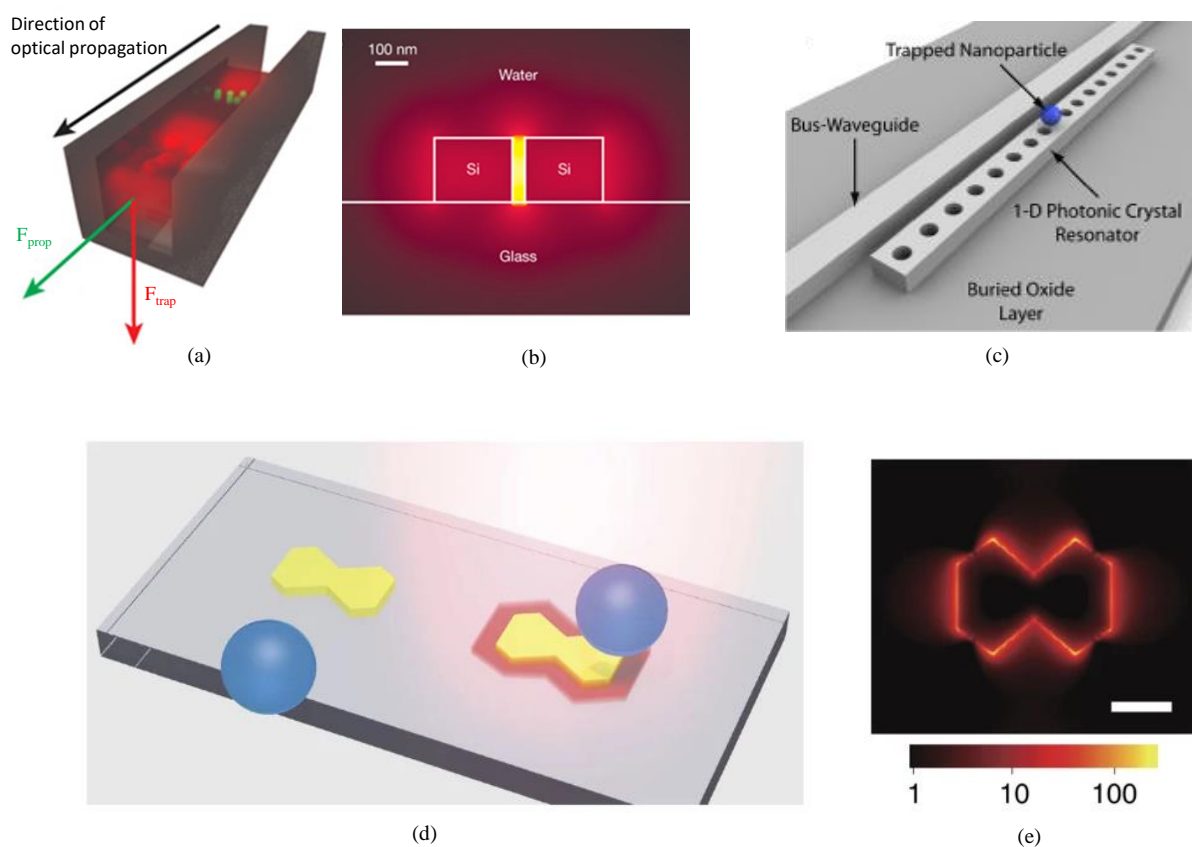


Figure 4.1: (a) Schematic of an on-chip optical trapping using a silicon slot waveguide and (b) high-intensity slot mode showing the trapping region. Reproduced from ref. [68]. (c) Nanoparticle trapping by a 1-D silicon photonic crystal resonator. Reproduced from ref. [71]. (d) Schematic of a gold diabolo nanoantenna on a glass substrate and (e) simulated electric field enhancement in the nanoantenna. Reproduced from ref. [75].

The limitations of the existing on-chip approaches can be mitigated using dielectric nanoantennas. They provide lower field enhancement than plasmonic nanoantennas but produce less heating when using low-loss dielectrics. This reduces the risk of flow-induced forces and damaging temperature-sensitive biological nanoparticles. The design parameters of dielectric nanoantennas can be optimized to achieve maximum field enhancement at near-visible wavelengths, allowing Raman spectroscopy to be performed using the trapping laser. Dielectric nanoantennas have recently been demonstrated to trap single nanoparticles [79, 80]. It has also been shown that the near-field enhancement of a single nanoantenna provides significant enhancement of the Raman scattering, enabling Raman spectroscopy of individual nanoparticles [81, 82]. An array of dielectric nanoantennas can be fabricated on a single chip

and simultaneously excited by a single beam, as described in section 4.8. This is advantageous for high-throughput analysis of multiple nanoparticles.

4.2 Plasmonic versus dielectric nanoantennas

Optical nanoantennas are nanoscale structures designed for enhanced light-matter interactions on the subwavelength scale. They function similarly to radio frequency antennas but operate at optical frequencies, usually in the visible or near-infrared range. Optical nanoantennas can interact with light, concentrate it within a narrow mode volume, and enhance local electromagnetic fields. Plasmonic and dielectric nanoantennas represent two distinct classes of optical nanoantennas which have enabled a broad range of applications in nanophotonics [83-85]. Plasmonic nanoantennas are made of metals, specifically gold, silver, or aluminum. These materials can show resonances in response to an incident field supported by collective oscillations of the conduction electrons near the surface of the metal, which is known as surface plasmons. These plasmon resonances provide control and manipulation of light at the nanoscale. The simplest and most common resonance mode supported in plasmonic nanoantennas is the dipole mode. This mode occurs when the conduction electrons are displaced from their equilibrium position (figure. 4.2(a)), creating a net charge separation between the electrons and the positively charged ions. This creates an oscillating dipole moment in the particle, with the electron cloud and the positive ions oscillating back and forth.

On the other hand, dielectric nanoantennas are made of low-loss dielectric materials such as silicon, titanium dioxide, silicon nitride, gallium arsenide and so on. They rely on Mie resonances, a phenomenon where light interacts with the induced electric and magnetic dipoles in the dielectric nanoparticles. One of the distinguishing properties of dielectric nanoantennas is their ability to support both magnetic and electric resonances, a feature that is uncommon in plasmonic nanoantennas due to the vanishing fields inside the metallic structures. The generation of resonant magnetic dipole moments in dielectric nanoantennas can be attributed to the interaction between incident light and the circular displacement current of the electric field (figure. 4.2(b)). High refractive index dielectric nanoantennas provide greater flexibility in designing nanoantennas with specific resonant properties. Some dielectric materials are compatible with CMOS fabrication processes, enabling high-volume fabrication and their integration into lab-on-a-chip systems. Moreover, dielectric nanoantennas show various optical properties including directional emission, enhanced electric fields, Fano resonances, high Purcell factor, small mode volume etc. By harnessing these unique properties in dielectric

nanoantennas, new research directions and a diverse range of applications have emerged. This is described in the next section and in paper I.

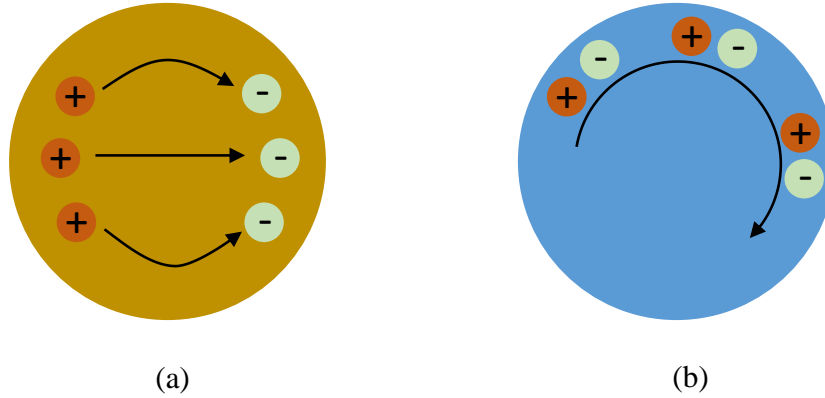


Figure 4.2: Schematic diagram showing (a) the fundamental dipole mode in a metallic nanoparticle (arrow indicates plasmon dipole moment) and (b) the fundamental magnetic dipole mode in a dielectric nanoparticle (arrow indicates circular displacement current). Adapted from ref. [86].

4.3 Simulation of mode volume and Q-factor

The mode volume determines the spatial distribution of light in a tightly confined spot within a dielectric nanoantenna. The Q-factor of a nanoantenna is a measure of its ability to store and sustain energy in a resonant mode. In this section, simulation results of mode volume and Q-factor for a spherical dimer are summarized. These results are taken from paper I. A dimer is considered, as shown in figure 4.3(a). The dimer consists of two silicon spheres with radius 150 nm and separated by a small gap. The surrounding medium is air. The nanoantenna is excited by a plane wave with electric field polarized along the x -axis and propagating along the z -axis, as shown in figure 4.3(a). The mode volume V_m is defined as:

$$V_m = \frac{\int \varepsilon(\vec{r}) |\vec{E}(\vec{r})|^2 dV}{\text{Max}(\varepsilon(\vec{r}) |\vec{E}(\vec{r})|^2)} \quad (4.1)$$

where $\vec{E}(\vec{r})$ is the position dependent electric field and $\varepsilon(\vec{r})$ is the dielectric constant. As shown in figure 4.3(b), the simulated mode volume in air ($n = 1$) is extremely small, with a value $< 0.005 (\lambda/n)^3$ at $\lambda = 1100$ nm. The small mode volume creates a nanoscale hotspot, enabling the trapping of nanoparticles smaller than the diffraction limit. Using the procedures and equations given in section 2.2 of paper I, the scattering spectrum of the dimer nanoantenna is obtained. The Q-factor is calculated from the scattering spectrum, considering the fundamental magnetic dipole (MD) resonance giving the highest Q-factor. The scattering spectra for other resonances are broader than the MD resonance, showing a lower Q-factor. The simulated Q-

factor varies from low to moderate (3 to 16) for a gap varying from 5 to 300 nm, which is shown in figure 4.3(b).

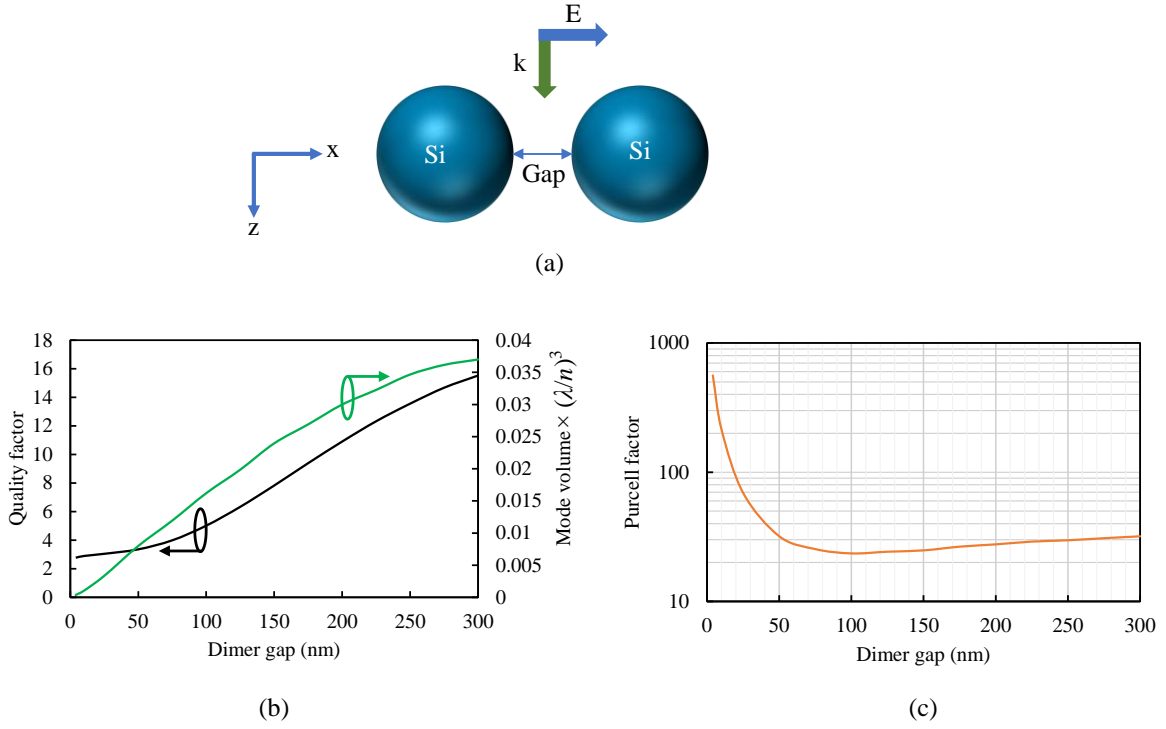


Figure 4.3: (a) Schematic of a silicon spherical dimer simulated for determining mode volume and Q-factor at $\lambda = 1100$ nm. The radius of the spheres is 150 nm. The incident field is a plane wave polarized along the x -axis and propagating along the z -axis. (b) Simulated Q-factor and mode volume as a function of the dimer gap and (c) corresponding Purcell factor at 1100 nm. Adapted from figure 10 of paper I.

The Purcell factor F_p is another important parameter of dielectric nanoantennas, which quantifies the efficiency of quantum emitters. This parameter is studied in paper I, as it contributes to enhancement of fluorescence and Raman scattering. The Purcell factor strongly depends on mode volume and Q-factor of the nanoantennas and is given by:

$$F_p = \frac{3}{4\pi^2} \left(\frac{\lambda}{n}\right)^3 \frac{Q}{V_m} \quad (4.2)$$

It is thus proportional to the ratio of the Q-factor and the mode volume of the nanoantenna. The Purcell factor as a function of dimer gap is shown in figure 4.3(c) at $\lambda = 1100$ nm. A small gap leads to a sharp increase in the Purcell factor as the mode volume is reduced. On the other hand, the Purcell factor is almost constant for a gap larger than 50 nm. While the simulation of the Purcell factor is not directly relevant for the aims of this thesis, it is nonetheless related with Raman scattering. Essentially, a Raman-active molecule near a nanoantenna with a high Purcell factor can exhibit increased Raman scattering due to more efficient coupling between the emitter and the resonant modes of the nanoantenna.

4.4 Field enhancement and Raman enhancement factor

The field enhancement of a nanoantenna refers to the ability of a nanoantenna to intensify an electric or magnetic field due to resonance. Electric field enhancement, represented by $|\mathbf{E}|/|\mathbf{E}_0|$, is the ratio of the absolute value of the local electric field in the presence of a nanoantenna ($|\mathbf{E}|$) to the absolute value of the electric field without the nanoantenna ($|\mathbf{E}_0|$). Similarly, magnetic field enhancement is represented by $|\mathbf{H}|/|\mathbf{H}_0|$, where $|\mathbf{H}|$ is the absolute value of the local magnetic field in the presence of a nanoantenna ($|\mathbf{H}|$) to the absolute value of the magnetic field without the nanoantenna ($|\mathbf{H}_0|$). The field enhancement in a nanoantenna typically relies on its shape, size, the refractive index of the material, and the excitation wavelength [87]. High refractive index dielectric materials produce a stronger light-matter interaction, which gives a larger field enhancement compared to low-index dielectrics. Thus, high-index materials are normally preferred if they also have low absorption at the design wavelength. Electric and magnetic field enhancement maps for a silicon disk nanoantenna at 785 nm are shown in figure 4.4. The simulated electric and magnetic field enhancements are ~ 3.6 and ~ 5.9 , respectively, in the xy plane at $z = 75$ nm (see color bars).

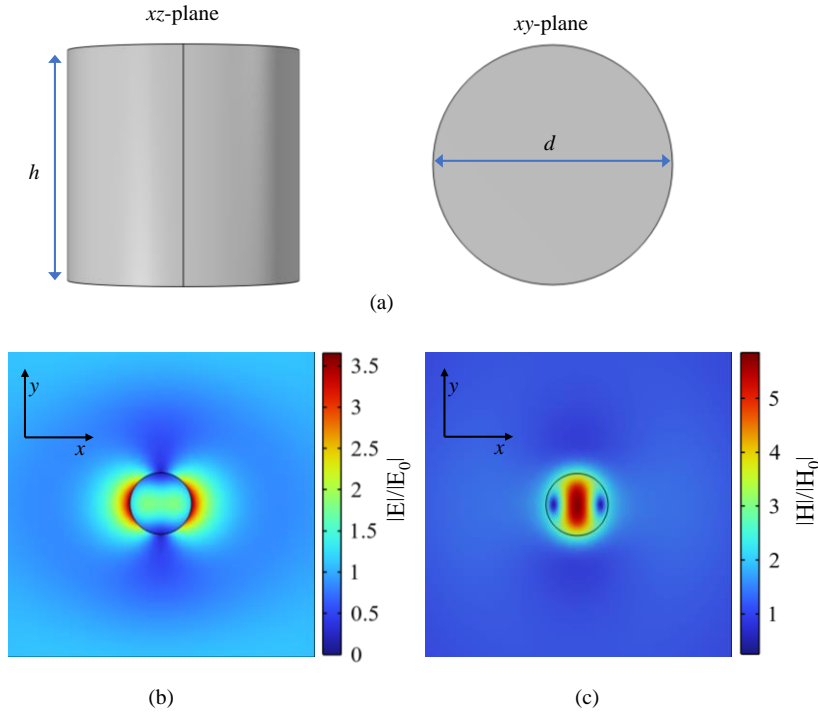


Figure 4.4: (a) Geometry of a silicon cylindrical disk nanoantenna. The simulated disk has a diameter $d = 200$ nm, height $h = 200$ nm, and is surrounded by air. The incident field is polarized along the x -axis and propagating along the z -axis. Profile of (b) electric field enhancement $|\mathbf{E}|/|\mathbf{E}_0|$ and (c) magnetic field enhancement $|\mathbf{H}|/|\mathbf{H}_0|$ at $\lambda = 785$ nm. The field profiles are taken in the xy plane at $z = 75$ nm.

When a molecule is located near a nanoantenna, the Raman scattering from the molecule is enhanced. The Raman enhancement factor arises from the enhancement of both the incident and scattered fields. The incident electric field intensity is enhanced by the nanoantenna by a factor $|\mathbf{E}|^2/|\mathbf{E}_0|^2$ at the excitation wavelength. The scattered field is enhanced by a factor $|\mathbf{E}_{\text{emission}}|^2/|\mathbf{E}_0|^2$ at the Raman-shifted wavelengths λ_{Raman} . Therefore, the overall enhancement factor for the Raman scattered intensity is:

$$EF_{\text{Raman}} = \left| \frac{E}{E_0} \right|^2 \times \left| \frac{E_{\text{emission}}}{E_0} \right|^2 \quad (4.3)$$

For dielectric nanoantennas, the Q-factor is usually very low. As a result, the field enhancement at both the excitation wavelength and the Raman-scattered wavelengths can be considered approximately equal, with $\left| \frac{E}{E_0} \right| \approx \left| \frac{E_{\text{emission}}}{E_0} \right|$. Hence, the Raman enhancement factor EF_{Raman} scales with the fourth power of the local field enhancement [81]:

$$EF_{\text{Raman}} \approx \left| \frac{E}{E_0} \right|^4. \quad (4.4)$$

4.5 Joule heating

Joule heating is the process of generating heat in a material through the absorption of light. When light interacts with a material, part of its energy is absorbed and converted into thermal energy, leading to an increase in temperature. The extent of Joule heating depends on nanoantenna material properties, such as absorption coefficient, thermal conductivity, and the intensity of the incident light [88]. The temperature distribution surrounding a nanoantenna can be described by the heat diffusion equation [89]:

$$\rho(\vec{r})C(\vec{r}) \frac{\partial T(\vec{r}, t)}{\partial t} = \kappa(\vec{r}) \nabla^2 T(\vec{r}, t) + q(\vec{r}) \quad (4.5)$$

where ρ is the density, C is the specific heat, κ is the thermal conductivity of the nanoantenna material, and T refers to the reference temperature. In equation (4.5), the left-hand term represents the rate of change of total thermal energy. The first right-hand term indicates spatial variation of temperature due to conduction, and the second term $q(\vec{r})$ represents the heat source density.

A rigorous method for determining $q(\vec{r})$ is possible using COMSOL Multiphysics by coupling the wave optics module with the heat transfer module. The position-dependent electric field distribution surrounding the dielectric nanoantenna is determined by solving the wave vector equation in COMSOL:

$$\nabla \times (\nabla \times \vec{E}) - k_0^2 \varepsilon(\vec{r}) \vec{E} = 0 \quad (4.6)$$

where \vec{E} denotes the total field, which is the sum of the incident and scattered electric fields, $k_0 = 2\pi/\lambda$ is the wavenumber of free space, and $\varepsilon(\vec{r})$ is the complex permittivity of the nanoantenna material. The heat source density $q(\vec{r})$ represents electromagnetic losses in the nanoantenna due to light dissipation, which is the sum of resistive and magnetic losses:

$$q(\vec{r}) = Q_r(\vec{r}) + Q_m(\vec{r}) \quad (4.7)$$

where $Q_r(\vec{r})$ is the resistive losses and is determined in COMSOL using the following expression [90]:

$$Q_r(\vec{r}) = \frac{1}{2} \text{Re}[\vec{J}^*(\vec{r}) \cdot \vec{E}(\vec{r})] = \frac{\omega}{2} \text{Im}(\varepsilon) |\vec{E}(\vec{r})|^2 \quad (4.8)$$

where $\vec{J}^*(\vec{r})$ is the complex conjugate of the current density, $\vec{E}(\vec{r})$ is the position dependent complex electric field, ω is the angular frequency of the incident field, and $\text{Im}(\varepsilon)$ is the imaginary part of the complex permittivity of the nanoantenna material. The right-hand term in equation (4.8) shows that heat dissipation in the nanoantenna is proportional to the square of the absolute value of the complex electric field.

The magnetic loss $Q_m(\vec{r})$ is calculated using the following equation [88]:

$$Q_m(\vec{r}) = \text{Re} \left[\frac{i\omega}{2} (\vec{B}(\vec{r}) \cdot \vec{H}^*(\vec{r})) \right] \quad (4.9)$$

where $\vec{B}(\vec{r})$ is the magnetic flux density and $\vec{H}^*(\vec{r})$ is the complex conjugate of the magnetic fields. For a dielectric nanoantenna, the induced magnetic loss is very small and thus is often neglected from the calculation.

The simulated heat source density $q(\vec{r})$ is put into equation (4.5), which gives a temperature increase distribution surrounding the nanoantenna. The generated total heat power Q is found by integrating the heat source density over the volume of the nanoantenna.

$$Q = \int_V q(\vec{r}) dV. \quad (4.10)$$

This is the case for a transparent substrate, where the nanoantenna is the only heat source. However, in the presence of an absorbing substrate, the contribution of the substrate in the total heat power Q must be considered. This can be taken into account by integrating equation (4.10) over the part of the absorbing substrate that is illuminated.

4.6 Thermally induced flow

As mentioned in the previous section, absorption of light generates a local increase of temperature in the nanoantenna. This results in a large temperature gradient that may lead to thermophoresis and thermal convection of fluid. Thermophoresis is a phenomenon in which particles in a fluid move from a region of higher temperature to a region of lower temperature and typically happens due to a temperature gradient. Thermal convection, often referred to as natural convection, occurs when a fluid moves due to changes in mass density caused by temperature differences. This movement is driven by buoyancy forces that flows radially upward. The hot fluid cools down by exchanging heat with the non-heated walls of a microfluidic chamber. After cooling, the water flows back to the nanoantenna structure, creating a convective flow pattern, as shown in figure 4.5. Thermally induced convection can be determined using COMSOL Multiphysics by coupling the heat transfer in solids and fluids module with the laminar flow module. The software provides a comprehensive way to study the temperature-dependent behavior of fluid dynamics within the system. When there are only small temperature differences in a flow, it can generally be treated as incompressible, implying that the density of the water remains constant or nearly constant. For the studied nanoantennas, the profile of fluid convection is governed by the Navier-Stokes equation [91]:

$$\rho_0 \frac{\partial \vec{u}(\vec{r})}{\partial t} + \rho_0 \vec{u}(\vec{r}) (\nabla \cdot \vec{u}(\vec{r})) = -\nabla p(\vec{r}) + \mu \nabla^2 \vec{u}(\vec{r}) + \vec{f} \quad (4.11)$$

where ρ_0 is the temperature dependent fluid density at a reference pressure, $p(\vec{r})$ is the pressure, $\vec{u}(\vec{r})$ is the velocity field, and μ is the viscosity of fluid. On the left-hand side of equation (4.11), the first term indicates the rate of change of total linear momentum, and the second term signifies the rate of change of momentum due to convection. On the right-hand side, the first term represents the pressure force, the second term is the rate of change of momentum caused by viscous transfer, and the final term \vec{f} corresponds to the body force per unit volume.

The force term \vec{f} can be estimated using the Boussinesq approximation. This method is widely used for solving non-isothermal flows and is accurate when density changes are small (incompressible flow). This approximation considers the temperature dependence of the density by imposing a buoyance force term due to the temperature increase [92]:

$$\vec{f} = \rho_0 \beta(T) [T(\vec{r}) - T_0] \vec{g} \quad (4.12)$$

where $\beta(T)$ is the temperature dependent thermal expansion coefficient of the fluid, $T_0 = 293.15$ K is the reference temperature, and \vec{g} is the gravitational acceleration. By numerically solving the equations from (4.11) to (4.13) in COMSOL, the velocity fields due to convection can be determined.

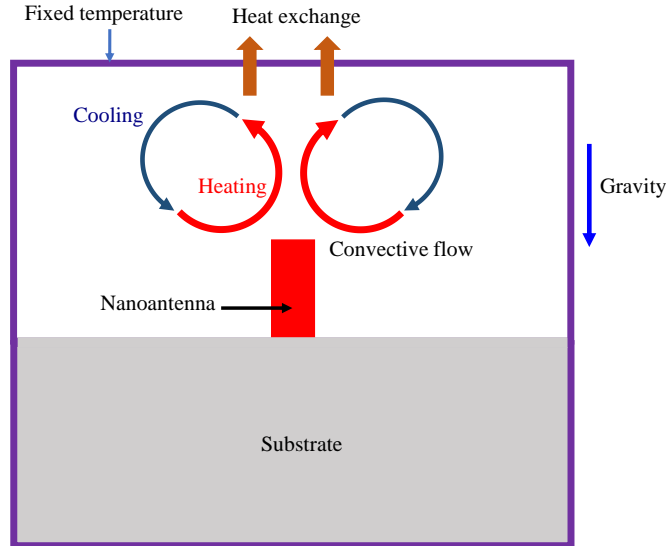


Figure 4.5: Convective flow pattern around a dielectric nanoantenna. The nanoantenna acts a heat source while the absorption in the fluid is considered negligible.

4.7 Dielectric nanotweezers in the near-visible

This section serves as an introduction to paper II with some more details and explanations of the main results relevant for trapping and Raman spectroscopy of EVs. As outlined in section 4.1, most on-chip approaches for optical trapping are restricted to near-infrared wavelengths. This is a challenge for Raman spectroscopy since silicon photodetectors are sensitive up to approximately 1050 nm. Plasmonic nanoantennas have demonstrated their ability for combining optical trapping with Raman spectroscopy, but they suffer from excessive Joule heating. In this section, dielectric nanoantennas are proposed as nanotweezers operating at the near-visible wavelength of 785 nm, aiming to mitigate the heating effect. The trapping performance of different dielectric materials is numerically studied to identify suitable materials for the optical trapping of nanoparticles. Various modules of COMSOL Multiphysics are used for the simulation of near fields, distribution of temperature increase, convective flow, and optical forces, as described in the previous sections.

A schematic of the proposed nanotweezer based on a bowtie dielectric nanoantenna is shown in figure 4.6. The bowtie is formed by two equilateral triangles on a substrate, with a gap of 50 nm between them. The simulations are performed for four different dielectric materials, which

are multilayer tungsten disulfide WS_2 , silicon Si, gallium phosphide GaP, and silicon nitride Si_3N_4 . Among these materials, tungsten disulfide ($n = 4.37 + 0.0136i @ 785 \text{ nm}$), and silicon ($n = 3.7 + 0.0025i @ 785 \text{ nm}$) possess very high refractive indices with some absorption. Gallium phosphide ($n = 3.2 @ 785 \text{ nm}$) exhibits a high refractive index and silicon nitride has a medium index ($n = 2.02 @ 785 \text{ nm}$) but both are transparent. The purpose of studying a variety of materials is to investigate how their refractive indices influence field enhancement and heating around the nanoantennas. It is worth noting that the triangles and the substrate are made from the same material. This is less common in the literature, as low-index substrates such as silica and glass are commonly used. Tungsten disulfide and silicon possess high thermal conductivity, thus can be used as good heat sinks. For gallium phosphide and silicon nitride nanoantennas, using a similar material provides a simplified fabrication process. The substrate materials considered here have higher refractive indices than silica and glass, giving an increased field enhancement, as discussed in section 3.1 of paper II.

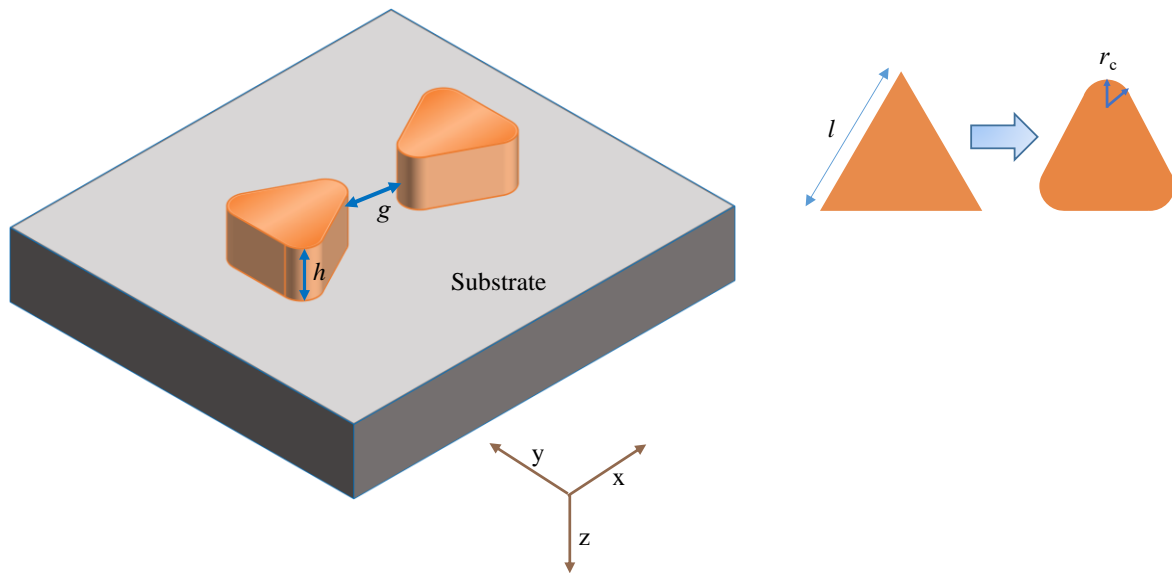


Figure 4.6: Schematic of a dielectric bowtie nanoantenna, consisting of a pair of equilateral triangles separated by a gap $g = 50 \text{ nm}$, height h , sidelength l , and placed on top of a substrate. Rounded corners of the triangles, with a radius of curvature $r_c = 30 \text{ nm}$, are shown in the right panel. The nanoantenna is excited by a plane wave polarized along the x -axis and propagating along the z -axis and $\lambda = 785 \text{ nm}$.

The nanoantennas are excited by a plane wave, with electric field polarized along the x -axis and propagating along the z -axis. Using COMSOL simulations, the dimensions of the bowtie nanoantennas are optimized to obtain maximum field enhancement in the middle of the gap, as shown in figure 4.7. For the high refractive index dielectrics, the maximum field enhancement in the middle of the 50 nm gap exceeds 5 at the wavelength of 785 nm . Using equation (4.3),

the Raman enhancement factor is calculated, which exceeds 10^3 for the high index dielectrics (figure 5 of paper II). Using a transparent substrate with a low refractive index, such as silica ($n = 1.461 @ 785 \text{ nm}$), glass ($n=1.5 @ 785 \text{ nm}$), or quartz ($n = 1.541 @ 785 \text{ nm}$), results in a slightly lower field enhancement compared to a substrate using the same material for the structure and the nanoantenna. This is shown for the silicon nanoantenna in figure 4(d) of paper II.

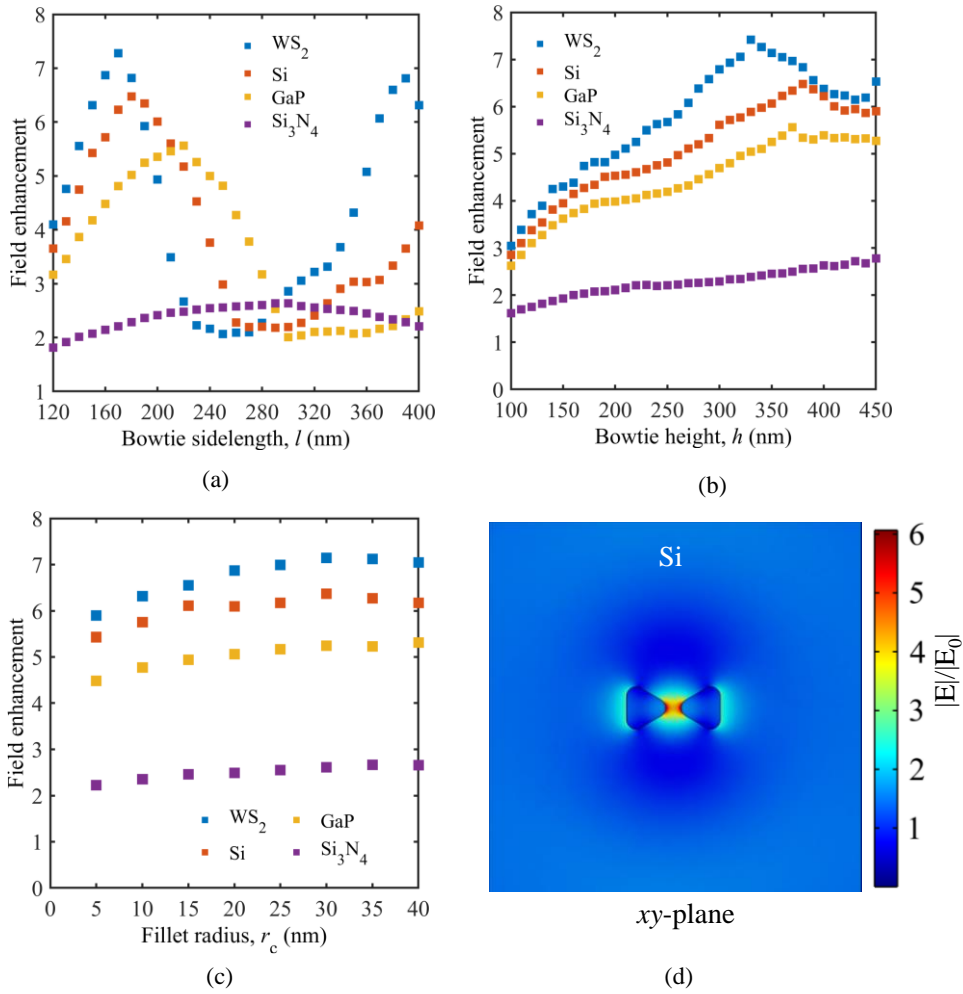


Figure 4.7: Electric field enhancement as a function of (a) sidelength l , (b) height h , and (c) fillet radius r_c at 785 nm in tungsten disulfide, silicon, gallium phosphide, and silicon nitride nanoantennas with gap of 50 nm. (d) Electric field enhancement profile in the xy -plane at the mid-height of the bowtie for the silicon nanoantenna.

Tungsten disulfide and silicon nanoantennas produce a local temperature increase due to absorption of light. The power absorbed by the triangles and substrate is determined by the equations described in section 4.5, and this absorbed power acts as a heat source for the thermal simulation in COMSOL. For an input intensity of $1 \text{ mW}/\mu\text{m}^2$, the maximum temperature increase in multilayer tungsten disulfide and silicon nanoantennas is 0.8 and 0.14 K, respectively (figure 6(a) and (b) in paper II). The high thermal conductivity of silicon (148 W

$\text{K}^{-1}\text{m}^{-1}$) and tungsten disulfide ($142 \text{ W K}^{-1}\text{m}^{-1}$) effectively takes away the generated heat through the substrate, thus giving a relatively low temperature increase. With a silica substrate, the temperature increase is approximately 2.3 K for the same input intensity (figure 6(c) in paper II). The very low thermal conductivity of silica ($1.38 \text{ W K}^{-1}\text{m}^{-1}$) prevents the diffusion of heat through the substrate, causing a rise in temperature. Gallium phosphide and silicon nitride are transparent at 785 nm, thus they do not heat up unless there are impurities in the material.

The generated heat in the tungsten disulfide and silicon nanoantennas results in a convective flow. Convection of fluid is simulated in COMSOL laminar flow module using the equations in section 4.6 with a water chamber height of $15 \mu\text{m}$. For an input intensity of $1 \text{ mW}/\mu\text{m}^2$, the peak fluid velocity around tungsten disulfide and silicon nanoantennas is 0.12 and 0.023 nm/s (figure 7 of paper II). Moreover, the force due to the fluid velocity is simulated, but is found to be extremely weak compared to the optical force. For stable trapping, a significant increase in input intensity is required, which will consequently lead to an increase in temperature and fluid velocity. However, in this scenario, the force due to fluid velocity does not increase substantially. Thus, the flow does not move the trapped particle away from the hotspot.

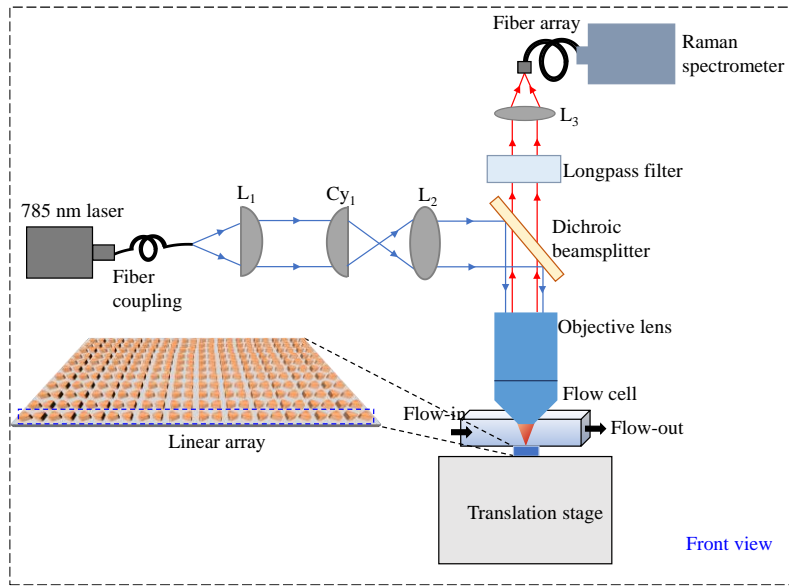
As discussed in section 3.1, the gradient of the localized field intensity produces a force that pulls a nanoparticle towards the hotspot where it is optically trapped (figure 3.1). Three different nanoparticles, namely quantum dots (QDs), polystyrene (PS) beads, and EVs, are considered in this work for the simulation of optical forces using the Maxwell stress tensor. The optical force with a high index silicon nanoantenna is higher than for low index silicon nitride, as expected due to the higher field enhancement for the silicon nanoantenna (figure 8(a) and (b) of paper II). Moreover, the optical force on a QD is comparatively higher than on an EV, due to the high refractive index of the QDs ($n = 2.49$ vs. $n = 1.39$ for EVs). The trapping potential is found using equation (3.16) and the z -position of the nanoparticle is varied from 30 to 500 nm. For tungsten disulfide, silicon, and gallium phosphide nanoantennas used to trap 40 nm diameter QDs, the trapping potential depths are $1.4 k_{\text{B}}T$, $1 k_{\text{B}}T$, and $0.8 k_{\text{B}}T$, respectively, for an input intensity of $1 \text{ mW}/\mu\text{m}^2$. To achieve stable trapping, the trapping potential must be at least $10 k_{\text{B}}T$. Consequently, for high refractive index nanoantennas, an input intensity $> 10 \text{ mW}/\mu\text{m}^2$ is necessary to trap QDs. For stable trapping of PS beads and EVs, an even higher input intensity is required.

The RCN project aims to trap and analyze EVs at 785 nm. The simulation results shown in paper II suggest that using the proposed dielectric nanoantennas to trap EVs will be extremely challenging. The limiting factors include the need for very high input intensities to achieve

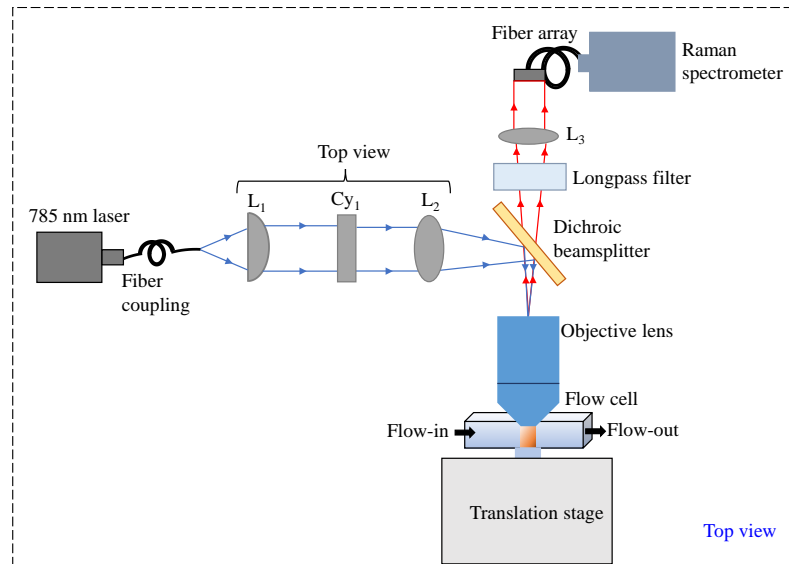
stable trapping and thus a significant temperature increase around the nanoantennas. For absorbing materials such as multilayer tungsten disulfide and silicon, input intensities of 121 and 161 mW/ μm^2 , respectively, are required to trap an EV of 40 nm diameter. These intensities are achievable, but the corresponding temperature increases are substantial, nearly 96 K and 22 K, respectively. Therefore, these materials are not suitable for trapping of EVs. The input intensities required for gallium phosphide and silicon nitride nanoantennas are 217 and 1030 mW/ μm^2 , respectively. While the intensity required for gallium phosphide is high, yet achievable, silicon nitride requires an extremely high input intensity. Therefore, gallium phosphide emerges as the only alternative material for trapping EVs due to its high refractive index and transparency at 785 nm. However, the fabrication process for gallium phosphide is challenging, as it is not a standard material for CMOS fabrication. On the other hand, silicon is far more common and sets the benchmark for CMOS fabrication. The silicon nanoantenna is suitable for trapping QDs, requiring only a moderate input intensity and resulting in a low temperature increase. To conclude, none of the investigated materials are suitable for the RCN project which this thesis is part of.

4.8 Outline of set-ups for trapping and Raman spectroscopy of nanoparticles

Paper II considers the trapping of a single nanoparticle. However, simultaneous trapping of multiple nanoparticles is feasible using a nanoantenna array placed on a single substrate. Figure 4.8 shows an outline of a suggested experimental setup for trapping and Raman spectroscopy of multiple nanoparticles using a linear array of bowtie nanoantennas. Initially, the output beam from the fibre is collimated using lens L_1 . Then a cylindrical lens Cy_1 focuses it into a line on the back aperture of an objective lens, as shown in the top view. Observing from the front, the beam appears to be collimated on the back aperture of this objective lens. The objective lens focuses the beam when viewed from the front and collimates the beam when looked from the top, thus resulting in a line focus on the linear array. The position of the chip is optimized such that the corresponding focused line covers a linear array of bowties. The focused line excites the nanoantennas and creates a field enhancement in individual bowtie gaps, which act as hotspots for the optical trapping of nanoparticles. Ideally, one nanoparticle is trapped at each hotspot. The same laser beam is used to excite Raman scattering by nanoparticles. The Raman signal is captured by the objective lens. When viewed from the top, the captured beam is collimated towards the coupling lens L_3 . However, the same beam appears focused when observed from the front. A long-pass filter is used to eliminate Rayleigh scattered light, passing only Stokes Raman wavelengths.



(a)



(b)

Figure 4.8: Outline of an experimental setup for on-chip trapping and Raman spectroscopy of multiple nanoparticles using a bowtie nanoantenna array. Front and top view of the setup are shown in (a) and (b), respectively.

The Raman scattered light is then focused onto the entrance aperture of a bundle of single mode (SM) fibers. Each SM fiber in the stack corresponds to a different trapping location along the focused line on the linear array. The bundle of fibers transfers the light to a multichannel spectrometer. Each SM fiber is connected to a different input channel of the spectrometer. The light from each channel is diffracted by a grating, and the resulting spectra are imaged onto a CCD detector with a motorized translation stage. The focused line scans the next linear array,

and the process is repeated to acquire spectra from new trapping locations. The chip can be integrated with a microfluidic device, which utilizes a flow-in process to deliver nanoparticles to the trapping region. Once the nanoparticles are trapped and the Raman scattering data are collected, a flow-out process can be initiated to remove the particles from the trapping sites. This process facilitates the cleaning and preparation of the trapping sites for the next batch of nanoparticles, making the trapping process continuous.

The set-ups outline here has not been made. The optical design must be optimized and reviewed, particularly regarding the lenses and the fibre array, if the set-ups is to be made.

CHAPTER 5

Quasi-bound states in the continuum in metasurfaces

In the previous chapter, an on-chip approach for optical trapping and Raman spectroscopy of nanoparticles was discussed using dielectric nanoantennas. For stable trapping of EVs, the required input intensity was very high, which in turn produced a significant temperature increase around the nanoantennas. To mitigate these issues, this chapter presents another on-chip approach based on quasi-bound states in the continuum (quasi-BICs) in low-index dielectric metasurfaces. Section 5.1 gives a short introduction to metasurfaces with examples of some previous works. A brief overview of BICs and the theory of high-Q quasi-BICs in dielectric metasurfaces is presented in section 5.2 and 5.3, respectively. This chapter contains two papers: paper III and paper IV. Section 5.4 is based on paper III, where the main results of the studied quasi-BIC metasurfaces are presented. Paper IV investigates simulations of quasi-BIC metasurfaces with parallel bars and a cylindrical disk for larger tip-to-tip gaps, which are presented in section 5.5. This chapter includes some scanning electron microscope (SEM) images of the fabricated metasurfaces. Finally, an experimental setup is described for measuring the reflectance from quasi-BICs. This setup has been made in collaboration with Dr. Marek Vlček and used to test some samples.

5.1 Dielectric metasurfaces

Metasurfaces are structured surfaces composed of a periodic array of subwavelength-scale ‘meta-atoms’. Meta is a prefix of Greek origin that means ‘beyond’, which indicates that these surfaces have properties and capabilities that go beyond those of natural surfaces. Meta-atoms are small and are the fundamental building blocks of metasurfaces. They are often known as unit cell of a metasurface. The incident electromagnetic waves interact with the subwavelength

meta-atoms to impart phase changes or amplitude modulation, which allows to control the propagation, polarization, and phase of light. These features have opened up new possibilities in fields such as imaging, sensing, and optical communications [93, 94]. In recent years, metasurfaces have become an integral component of flat optics, which enable the development of highly efficient and compact optical devices.

Dielectric metasurfaces are made from low-loss dielectric materials. Typical materials used are silicon, titanium dioxide, silicon nitride, gallium arsenide, and aluminum gallium arsenide. Unlike their metallic counterparts, dielectric metasurfaces made of highly transparent materials can control the phase of light without absorption losses, making them extremely efficient for light manipulation. Depending on the specific application, various configurations of dielectric metasurfaces have been investigated, as shown in recent review articles [85, 95, 96]. Figure 5.1 shows two examples of dielectric metasurfaces.

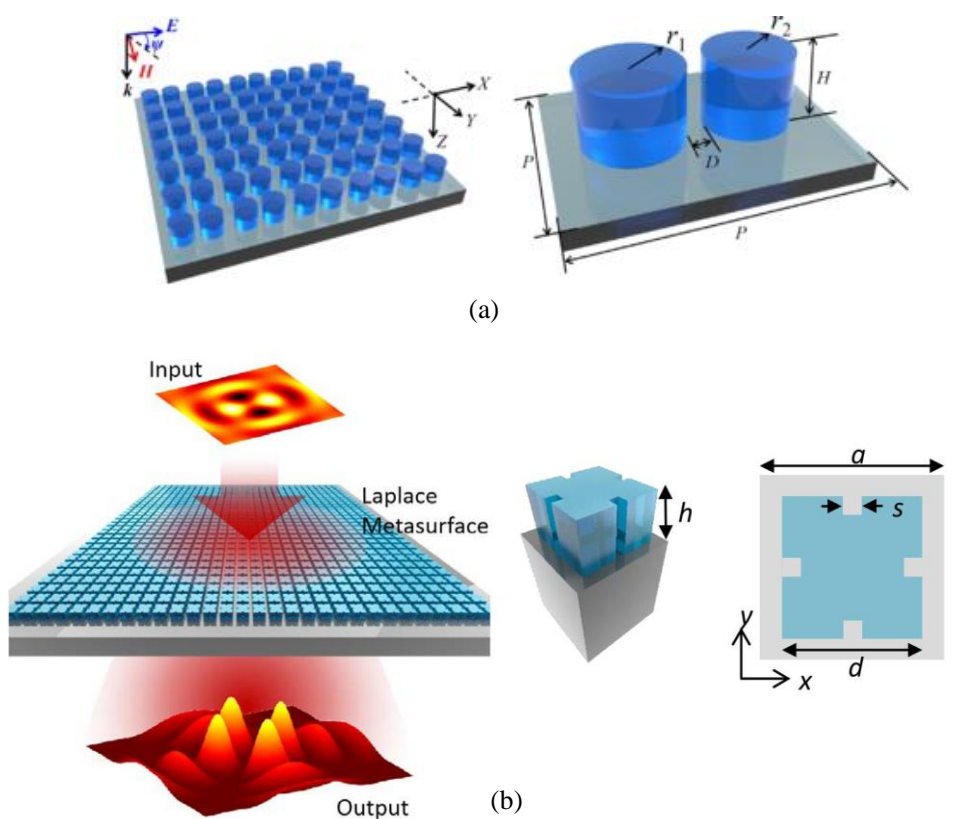


Figure 5.1: Examples of dielectric metasurfaces. (a) Schematic diagram of a metasurface with a periodic array of silicon nanodisk dimers arranged in a square lattice. The unit cell is shown in the right panel. Reproduced from ref. [97]. (b) Dielectric metasurface consisting of a periodic arrangement of square unit cells with four square voids at the centers of all edges. Reproduced from ref. [98].

5.2 Bound states in the continuum (BICs)

A quantum system typically contains two distinct types of states, which are separated in energy. The first type is the regular bound states which support discrete sets of localized propagating modes (shown in blue color in figure 5.2). The second type is the delocalized states having a continuum of propagating solutions. States inside the continuum spectrum couple with extended waves and are known as resonance leaky states (green color in figure 5.2). Apart from these states, exotic states known as bound states in the continuum (BICs) may exist in a quantum system. BICs are peculiar states of light that possess discrete energies similar to the bound states, but they coexist within the continuum spectrum of the system. They remain perfectly localized in space with no leakage losses (red color in figure 5.2).

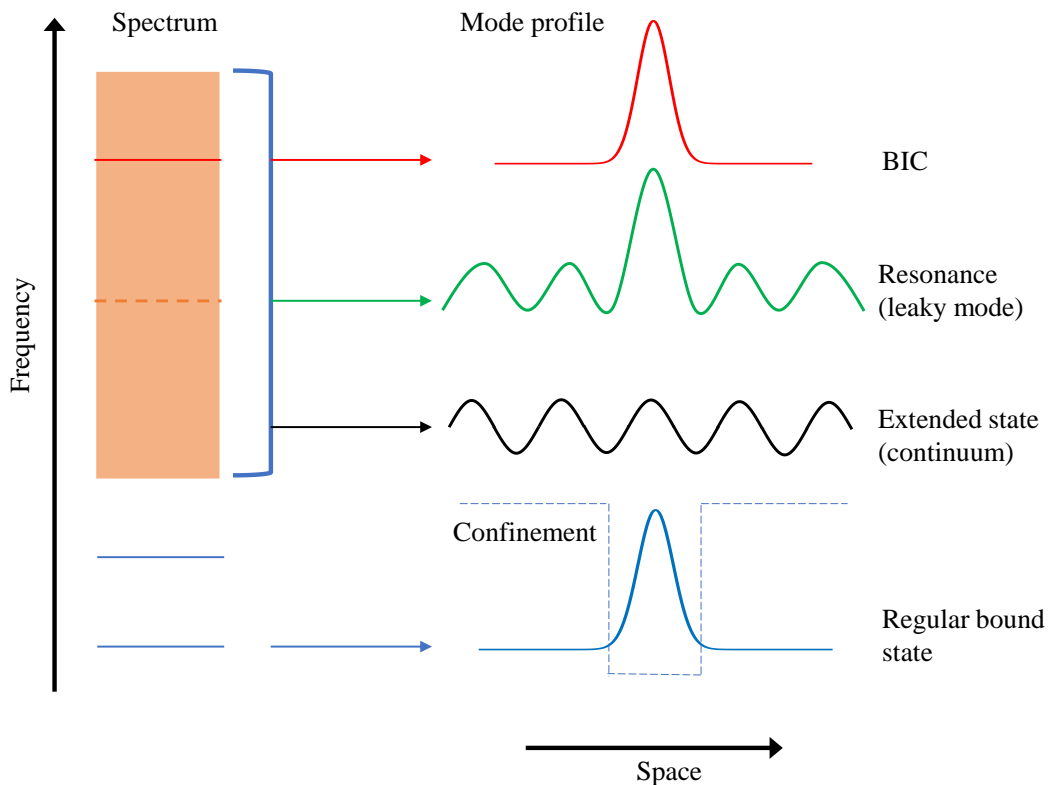


Figure 5.2: Illustration of different states supported in a quantum system and their mode profiles: regular bound states, extended states, leaky resonances and BICs. Adapted from ref. [99].

The concept of BICs was introduced by Neumann and Wigner in 1929 [100]. The concept was formulated purely mathematically based on the Schrödinger equation and has never been realized in that form in practical systems. Since the initial proposal, BICs were first experimentally observed in acoustic and water waves [101, 102]. In these systems, BICs occur when the scattered or radiated waves interfere destructively with each other in such a way that certain discrete states within the continuum become bound, resulting in a perfect confinement

inside the system. The theoretical concept of BICs was first introduced in optics in 2008 [103] and was experimentally demonstrated in optical waveguides in 2011 [104]. Over the past decade, BICs have been investigated in various nanophotonic systems [99, 105]. They are mainly classified into two categories. The first type is symmetry-protected BICs, which are formed when the spatial symmetry of the resonant state is incompatible with the in-plane symmetry of the radiating channels. In an earlier work by Parker, symmetry-protected BIC was experimentally demonstrated in acoustic waveguides with parallel plates [106]. Besides, periodic structures such as gratings, photonic crystal slabs, and metasurfaces can exhibit symmetry-protected BICs [105]. In these periodic structures, BICs rely on the time-reversal and the in-plane symmetry, and they can be found in high symmetry points. An example of symmetry-protected BICs in a photonic crystal slab is shown in Fig. 5.3 (a-c). The slab supports a symmetry-protected BIC in the symmetry point Γ (figure 5.3(c)). The second type is the resonance-trapped BICs (also known as accidental BICs), which originate from the complete destructive interference through the tuning of structural parameters of the system. The resonance-trapped BICs can be categorized into two main groups: Fabry-Pérot BICs and Friedrich-Wintgen BICs. Fabry-Pérot BICs rely on two similar resonances from two cavities coupled through a single radiation channel and a schematic is shown in figure 5.3(d). A resonant cavity provides a unity reflectance near the resonance frequency ω_0 as a result of the destructive interference between the direct transmission and the resonant radiation. Two such resonant structures can make a pair of perfect mirrors that trap light between them. BICs are generated when the resonance frequency ω_0 or the gap d between the two cavities is tuned such that the sum of the round-trip phase shifts ψ becomes an integer multiple of 2π (figure 5.3(d)). On the other hand, Friedrich-Wintgen BICs are based on two different resonances within an identical cavity. Referring to the figure 5.3(d), Friedrich-Wintgen BICs can arise when the cavities exhibit different resonance wavelengths $\omega_{1,2}$ and radiation rates $\gamma_{1,2}$. This happens when the two cavities are far apart or with no separation ($d = 0$). Friedrich-Wintgen BICs appear close to the frequency crossings of the uncoupled resonances. Structures supporting different BICs and their properties have been recently reviewed in [99].

A true BIC shows an infinite Q-factor, and it cannot be observed in the transmittance/reflectance spectrum. However, a true BIC never exists due to finite size of the structures, material absorption, and structural imperfections [107]. Thus, a true BIC is transformed into a resonant state that closely resembles the original BIC and have a finite, but very high, Q-factor. This is known as quasi-BIC, which is visible as a narrow peak in the

reflectance spectrum and can be used in practical applications. In recent years, quasi-BICs have been proposed for applications such as sensing, imaging, lasing, optical trapping, and on-chip communications, as recently reviewed in [105].

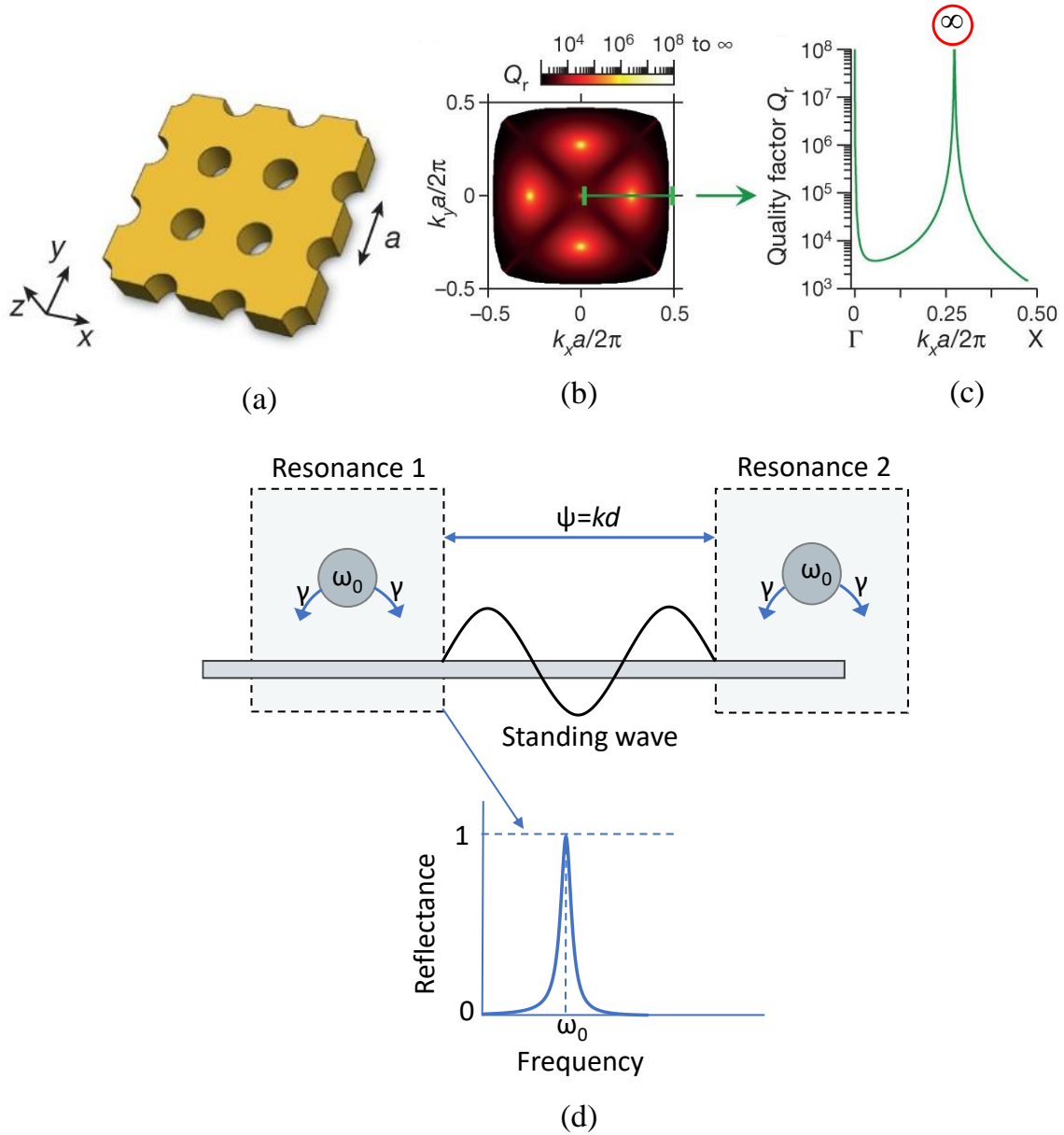


Figure 5.3: Illustration of various types of BICs. (a) Schematic of a photonic crystal slab supporting BICs and (b-c) mapping of the radiative quality factor of the lowest TM-like band in the continuum. Two BICs are found at wavevectors $k_x = 0$ and $k_x a/2\pi = 0.27$, respectively. The first BIC arises at the Γ point due to symmetry of the photonic crystal and the second BIC is obtained through parameter tuning. Reproduced from ref. [108]. (d) A schematic illustration of Fabry-Pérot BIC. Two identical resonators with a resonance frequency ω_0 coupled into a single radiation channel. Waves can be trapped between the two resonances when the round-trip phase shift ψ is an integer multiple of 2π . Adapted from ref. [99].

5.3 Theory of high-Q quasi-BICs in dielectric metasurfaces

Dielectric metasurfaces with various configurations can support symmetry protected quasi-BICs [109, 110]. One common configuration is a metasurface consisting of a periodic array, with a unit cell containing a pair of elliptical bars [111, 112]. By tailoring the shape and orientation of the bars, a quasi-BIC resonance can be achieved. Moreover, this design provides a high field enhancement on the tips of the bars, making it suitable for optical trapping. This will be discussed in the following section, together with a theoretical presentation in terms of electric dipoles.

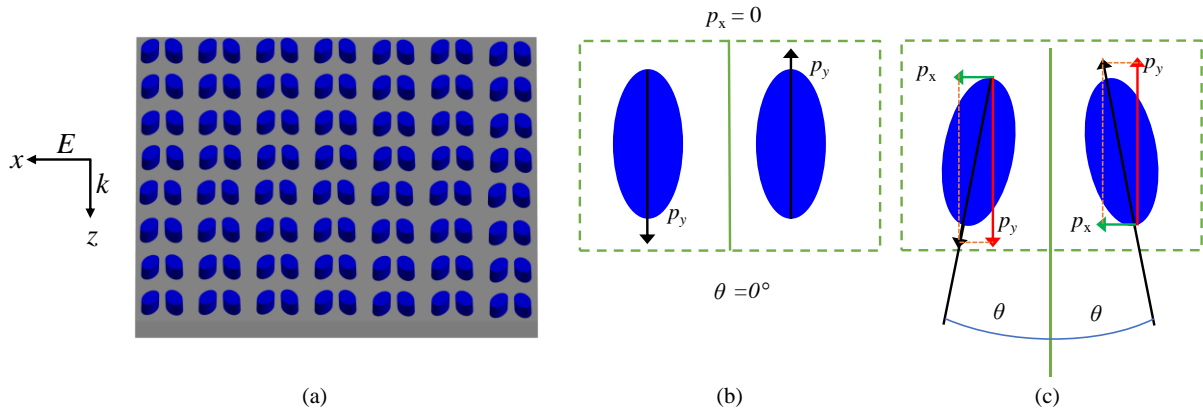


Figure 5.4: (a) Schematic diagram of a silicon nitride metasurface consisting of a periodic array. The unit cell consists of a pair of ellipses with a tilt angle θ . The diagram shows the electric dipole moments in the meta-atoms for (b) $\theta = 0^\circ$ and (c) $\theta = 10^\circ$. The components p_x and p_y are the dipole moments along the x -direction and y -direction, respectively. The metasurface is excited by a plane wave polarized along the x -axis and propagating along the z -axis.

A schematic diagram of the metasurface investigated in paper III is shown in figure 5.4 (a). The metasurface consists of a periodic array of elliptical meta-atoms and the unit cell is made of a pair of elliptical bars. To understand how the proposed metasurface supports true and quasi-BIC, the dipole moment in each meta-atom is considered, as illustrated in figure 5.4 (b) and (c). First, a true BIC scenario is presented. An incident plane wave with x -polarization induces inverse electric dipole moments in the meta-atoms, as indicated by the block arrows in figure 5.4 (b). Each dipole moment can be decomposed into p_x and p_y , where p_x is the x -component and p_y is the y -component of the dipole moment. For $\theta = 0^\circ$, the dipole moment in the meta-atoms only has p_y components which are parallel but in opposite directions. As the dipoles are opposing each other, out-coupling to the plane wave is completely prohibited and a true BIC exists. If the in-plane symmetry of the metasurface is broken by introducing a tilt angle θ , the true BIC (infinite Q-factor) is transformed into a quasi-BIC (finite Q-factor). As shown in figure 5.4 (c) for $\theta = 10^\circ$, the dipole moment has both p_x and p_y components, where p_y is the dominant

component. Again, the components p_y of the meta-atoms cancels each other and the out-coupling of p_y to the plane wave is forbidden. This suppresses radiative losses significantly, thereby contributing to a high Q-factor. The non-zero p_x components give radiative losses by out-coupling to the incident plane wave. For a small θ , the overall contribution of p_x on the total dipole moment is weak compared to p_y , thereby the quality factor of the quasi-BIC resonance becomes large.

In the following, a general relationship between Q-factor and tilt angle θ is deduced, which is related to the results shown in paper III and IV. The theory is based on ref. [111]. The meta-atoms are assumed lossless. The incident x -polarized plane wave generates forward and backward scattering, which are related to non-zero dipole moment p_x by the following expressions:

$$E_f = E_i + \frac{i\omega\eta}{2A} p_x \quad (5.1)$$

$$E_b = \frac{i\omega\eta}{2A} p_x \quad (5.2)$$

where E_f is the forward scattered field, E_b is the backward scattered field, E_i is the x -polarized incident plane wave, ω is the angular frequency, η is the wave impedance of the surroundings, and A is the area of the unit cell. The dipole moment p_x can be written as:

$$p_x = i2Iu \sin\theta / \omega \quad (5.3)$$

with u being the normalized dipole moment of a single meta-atom. I is the frequency-dependent current amplitude that captures the resonant characteristic and can be expressed as:

$$I = \frac{E_i u \sin\theta}{Z} \quad (5.4)$$

where Z is the effective impedance of the meta-atom considering mutual interactions among all meta-atoms. The effective impedance in a single resonance can be resembled with an RLC circuit:

$$Z = -i\omega L - \frac{1}{i\omega C} + R \quad (5.5)$$

where R is the effective resistance, L is effective inductance, and C is the effective capacitance. Here, the effective resistance R solely contributes to the radiative losses. The energy conservation law requires that,

$$|E_i|^2 = |E_f|^2 + |E_b|^2 \quad (5.6)$$

Substituting E_f and E_b into equation (5.6) give:

$$|E_i|^2 = \left| E_i + \frac{i\omega\eta}{2A} p_x \right|^2 + \left| \frac{i\omega\eta}{2A} p_x \right|^2 \quad (5.7)$$

Putting the expression of p_x and I into equation (5.7), we can write:

$$|E_i|^2 = \left| E_i - \frac{\eta E_i u^2 \sin^2 \theta}{AZ} \right|^2 + \left| -\frac{\eta E_i u^2 \sin^2 \theta}{AZ} \right|^2 \quad (5.8)$$

Eliminating E_i and simplifying the equation (5.8), we get:

$$\frac{\eta u^2 \sin^2 \theta}{A \operatorname{Re}(Z)} = 1 \quad (5.9)$$

Now, using $\operatorname{Re}(Z) = R$, the following relationship between the effective resistance R and the tilt angle θ is obtained:

$$R = \frac{\eta u^2 \sin^2 \theta}{A} \quad (5.10)$$

The Q-factor of a RLC circuit is given by the following expression:

$$Q = \frac{1}{R} \sqrt{L/C} \quad (5.11)$$

The inductance L and the capacitance C do not change significantly for a small tilt angle θ , thus equation (5.8) indicates $Q \propto 1/\sin^2 \theta$. This suggests that the Q-factor increases drastically when tilt angle θ is reduced. A generalized asymmetry parameter α (here $\alpha = \sin \theta$) can be defined according to the structure considered and ranges from 0 to 1 [107]. It has been shown that the Q-factor is related to this asymmetry parameter by $Q \propto \alpha^{-2}$ [107, 109].

The frequency dependence of quasi-BIC in symmetry-breaking structures can be rigorously described by a Fano-type resonance [113]. The resonance curve is fitted to the following Fano lineshape function to extract the Q-factor [114, 115]:

$$R_{\text{Fano}}(\omega) = \left| a_1 + ia_2 + \frac{b}{\omega - \omega_0 + i\gamma} \right|^2 \quad (5.12)$$

where a_1 , a_2 , and b represent the fitting parameters, ω_0 denotes the central resonance frequency, and γ indicates the overall damping rate of the resonance. From a Fano lineshape fitting to the reflectance curve, the Q-factor is determined by $Q = \omega_0/2\gamma$.

5.4 Dielectric metasurfaces with quasi-BIC as nanotweezers

This section discusses the main results from Paper III and shows how quasi-BIC metasurfaces can be used for optical trapping and Raman spectroscopy of EVs. A recent work has proposed the use of silicon quasi-BIC metasurfaces for trapping of nanoparticles at 1550 nm [115]. As discussed in the previous chapter, Raman spectroscopy at this wavelength is not practical, and silicon metasurfaces are not suitable for near-visible wavelengths due to high absorption. In this section, a silicon nitride metasurfaces is proposed to avoid absorption at 785 nm. Paper III includes simulation of field enhancement, Q-factor, mode volume, and Raman enhancement factor using COMSOL Multiphysics. Furthermore, simulations of optical trapping for EVs are presented, and the influence of these EVs on the trapping performance is investigated. In this section, a summary of these simulations is given.

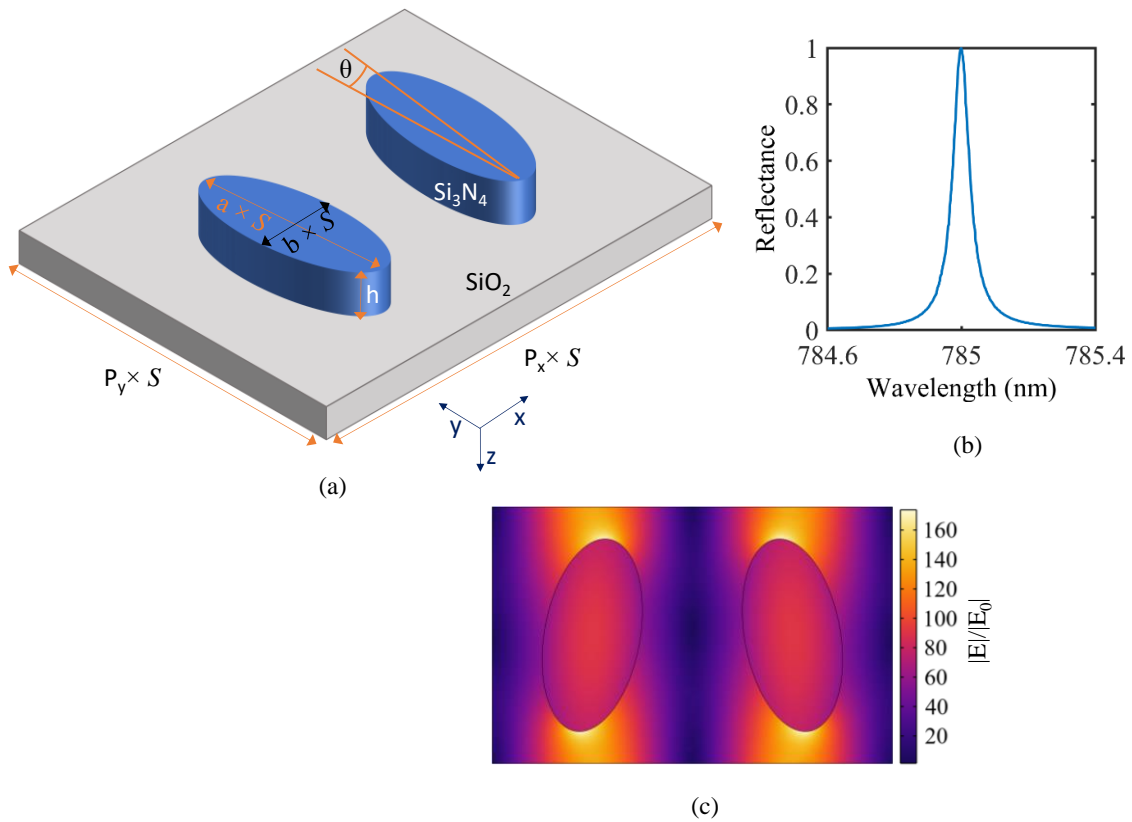


Figure 5.5: (a) Schematic of the unit cell with design parameters. The parameters are: $P_x = 522$ nm, $P_y = 336$ nm, $a = 255$ nm, $b = 125$ nm, $S = 1$, and $h = 230$ nm, giving a quasi-BIC resonance at 785 nm as shown in (b). (c) Field enhancement profile in the xy plane at the mid-height of the bar. The metasurface is excited by a plane wave polarized along the x -axis and propagating along the z -axis.

The unit cell of the proposed metasurface with geometrical parameters is shown in figure 5.5 (a). It consists of two identical silicon nitride elliptical bars situated on a silica substrate. These materials are chosen because they are transparent at 785 nm, hence heating can be avoided.

Previously, dielectric metasurfaces have been studied for different applications in the near infrared (NIR) [107, 115] and mid-IR wavelengths [111]. The metasurface presented in Paper III is tuned to operate at a near-visible wavelength of 785 nm, enabling the combination of optical trapping and Raman spectroscopy. As discussed in section 5.3, using a tilt angle for the bars breaks the symmetry of the structure, resulting in the transformation of a true BIC into a quasi-BIC. A tilt angle of 10° is chosen, as this can be easily controlled during fabrication. A smaller tilt angle would provide a higher Q-factor (discussed in section 5.3), but it would also complicate the fabrication process. The relationship between tilt angle θ and Q-factor has not been studied as it is well known. Periodic boundary conditions are set on the faces of the unit cell, thus making the metasurface into an infinite array of unit cells.

The metasurface is excited by a plane wave polarized along the x -axis and propagating along the z -axis. For the optimized design parameters (caption of figure 5.5), a reflectance peak is found at 785 nm, which corresponds to a quasi-BIC resonance (figure 5.5 (b)). The reflectance spectrum is fitted with a Fano lineshape, equation (5.12), giving a Q-factor of 1.3×10^4 . The metasurface shows a high electric field enhancement at the resonance wavelength (figure 5.5 (c)). On the bar tips, the enhancement is 178 and it decreases to 138 in the middle of gap (edge of figure 5.5(c)). Compared to the field enhancement in dielectric and plasmonic nanoantennas, this enhancement is several times higher. This is advantageous for optical trapping of nanoparticles using a low input power. Besides, a number of these hotspots can be obtained in the proposed metasurfaces (two per unit cell). When an EV is trapped in the hotspot, the incident beam can be used to excite Raman scattering. At the excitation wavelength, the Raman enhancement factor is approximately $138^2 \approx 2 \times 10^4$, which is a result of strong intensity enhancement in the gap. On the other hand, there is no enhancement at the emission wavelength, as the field enhancement beyond the resonance wavelength is approximately 1 (figure 3 of paper III).

The metasurface shows very small mode volume, about $0.03 \times (\lambda/n_{\text{water}})$, considering one trapping location. This is because of an extreme localization of the field to the gaps between the bars. With the presence of a trapped nanoparticle, a slight variation is found both in the Q-factor and mode volume (supplementary file of paper III). The resonance wavelength of the metasurface is sensitive to variations of the design parameters. The resonance wavelength varies linearly with the scaling factor S , while the variation is less pronounced when changing the height of the bar h (figure 4 of paper III). The field enhancement in the gap for different bar heights is studied in paper III and it was found that the enhancement for thin bars is significantly

higher than for thick bars (figure 5 of paper III). A physical explanation for this is that the mode field stretches into the substrate, as the bar height is reduced. This makes the mode less affected by the asymmetry of the bars, which increases the field enhancement.

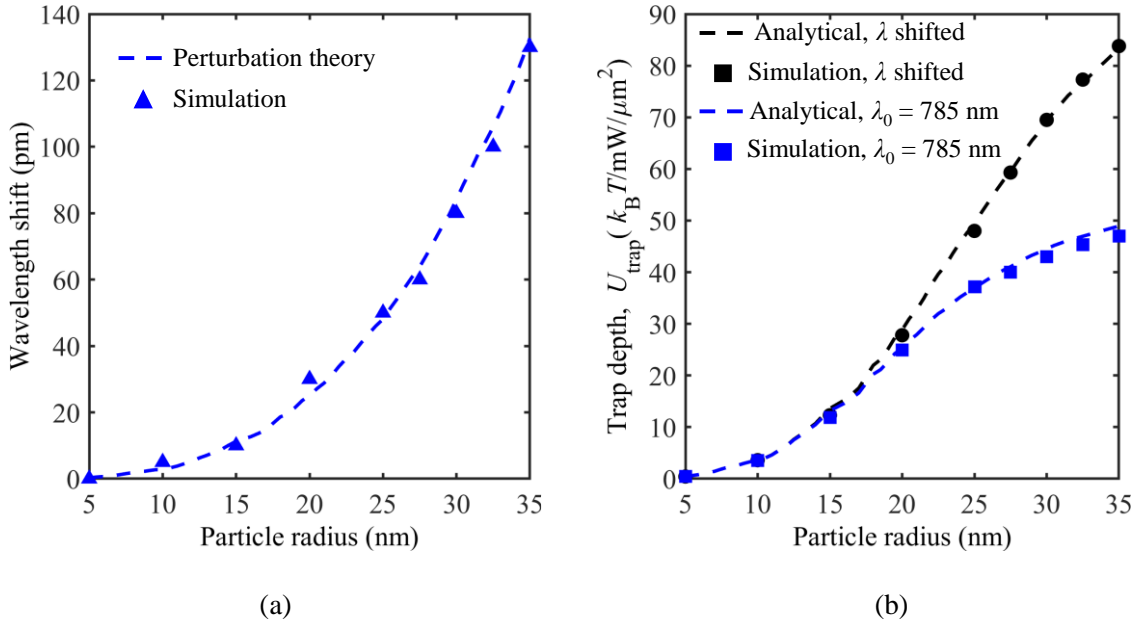


Figure 5.6: (a) Shift of resonance wavelength from empty cavity when a particle is trapped, as function of nanoparticle radius. Curve shown for perturbation theory and triangles for simulation of reflectance peak. (b) Trapping potential depth determined from analytical expression (dashed black line) and simulations (black filled circles) at the shifted resonance wavelengths from (a), and at the resonance λ_0 of the empty cavity (dashed blue and filled).

Paper III studies the influence of trapped EVs on the resonance wavelength using perturbation theory and simulations. In both cases, the resonance wavelength of the empty cavity ($\lambda_0 = 785$ nm) shifts towards a longer wavelength (red shift) with the radius of the trapped EVs, as shown in Figure 5.6(a). The trapped EVs also influence the trapping potential. The following analytical expression from [116] is used to show how the trap depth correlates with the radius of the EVs.

$$U_{\text{trap}} = 2\hbar N_p \frac{\kappa_{\text{ex}}}{\kappa} (\arctan[-\Delta] + \arctan[\eta + \Delta]) \quad (5.13)$$

The derivation and specific details of the parameters in equation (5.13) are skipped here and can be found in the supplementary material of paper III. Figure 5.6(b) shows depth of the trapping potential as a function of EV radius determined by 1) simulation of the field and analytical expression, and 2) simulation of the field and optical forces as function of position of the particle. The trap depth increases with the radius of the EVs, reaching a value of $84 k_B T / \text{mW} / \mu\text{m}^2$ for an EV radius of 35 nm. Note that this shifted resonance, and the corresponding potential occurs when all hotspots in the array are filled with identical particles. For the

unshifted wavelength, with an arbitrary number of trapped particles, the potential depth is approximately $50 k_B T / \text{mW} / \mu\text{m}^2$ for the EV radius of 35 nm. For stable trapping, a trap depth of $10 k_B T / \text{mW} / \mu\text{m}^2$ is considered sufficient. Thus, an input intensity of $1 \text{ mW} / \mu\text{m}^2$ is sufficient for stable trapping of EVs with a radius larger than 15 nm, shown in figure 5.6(b).

5.5 Dielectric quasi-BIC metasurface with parallel bars and a disk

This section presents the main findings from Paper IV. The metasurface with tilted bars, discussed in the previous section, shows a significant influence of variations in the design parameters on quasi-BICs. Moreover, it gives a small tip-to-tip gap of 81 nm, which is only suitable for the trapping of smaller EVs. Paper IV presents simulation of a quasi-BIC metasurface with parallel bars and a cylindrical disk. The design is optimized to achieve a larger tip-to-tip gap for trapping of larger EVs. Moreover, the influence of the ellipticity of the bars on the fabrication sensitivity is studied.

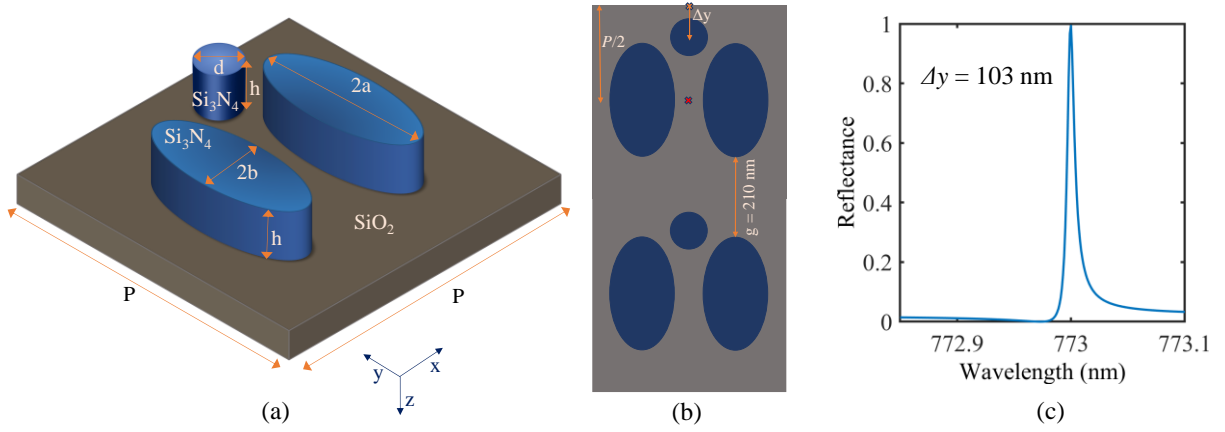


Figure 5.7: (a) Schematic of a unit cell with a pair of parallel bars and a cylindrical disk. (b) Illustration of symmetry breaking in the metasurface by introducing a cylindrical disk at a distance Δy from the upper edge of the unit cell. (c) Reflectance spectra showing a quasi-BIC resonance at $\lambda_0 = 773 \text{ nm}$ for the following design parameters: $P = 506 \text{ nm}$, $a = 148.5 \text{ nm}$, $b = 99 \text{ nm}$, $h = 230 \text{ nm}$, $r = 45 \text{ nm}$, and $\Delta y = 103 \text{ nm}$. With these parameters, the tip-to-tip gap is 209 nm, as shown in (b).

The unit cell of the metasurface is shown in figure 5.7(a), consisting of two identical elliptical bars and a cylindrical disk. Both the bars and the disk are taken to be silicon nitride and situated on a silica substrate. The bars are aligned vertically without being tilted, as opposed to the previous design. For this design, the symmetry is broken by placing the disk with a diameter d at a distance Δy from the upper edge of the unit cell, as shown in figure 5.7(b). The symmetry along the vertical axis is distorted, while the symmetry along the horizontal axis is maintained. The asymmetry parameter α is defined by $\alpha = \Delta y / (P/2)$, where P is the periodicity of the unit cell. The approach of creating asymmetry by adding a disk in the design can simplify the

fabrication compared to controlling a small tilt angle. The metasurface is excited by a plane wave polarized along the x -axis and propagating along the z -axis. Figure 5.7(c) shows a quasi-BIC resonance at $\lambda_0 = 773$ nm for the design parameters mentioned in the caption. This wavelength is chosen because it corresponds to the central wavelength of our tunable laser.

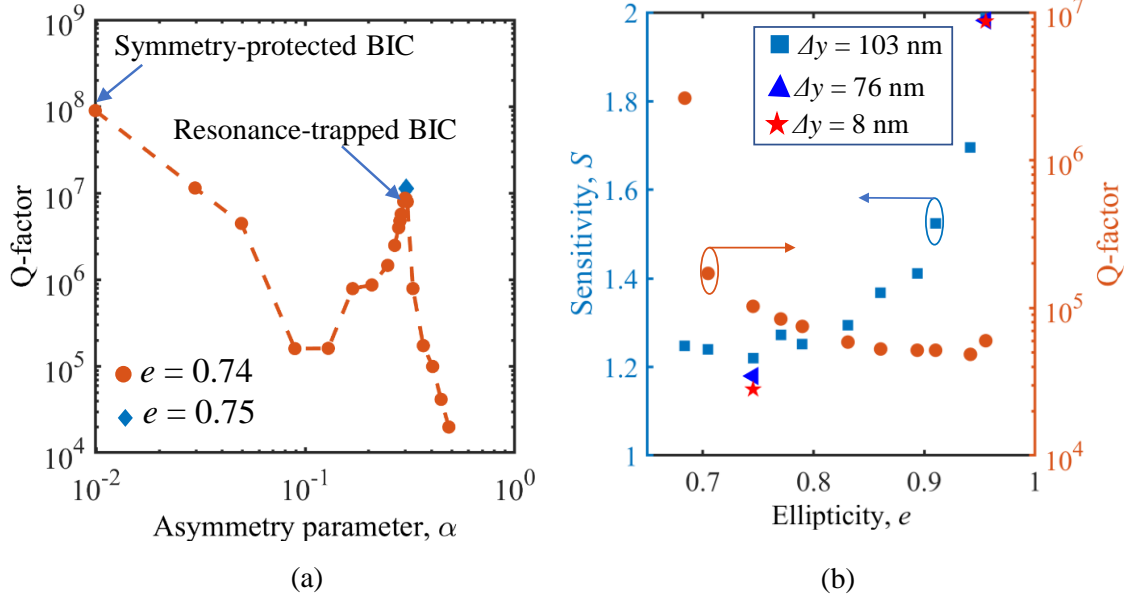


Figure 5.8: (a) Q-factor as a function of asymmetry parameter α for ellipticity of 0.74 (filled circles) and 0.75 (filled diamond). (b) Sensitivity of the wavelength, and the Q-factor, as a function of ellipticity e . The filled squares, triangles, and pentagons markers indicate the sensitivities for Δy of 103 nm, 76 nm, and 8 nm, respectively. The results shown for the triangle and pentagon markers are considered with ellipticities of 0.95 and 0.74, respectively.

Dependance of the Q-factor on the asymmetry parameter α is studied, which is shown in figure 5.8(a). When α is close to zero ($\Delta y = 3$ nm), the Q-factor reaches a very high value around 10^8 . This is due to a symmetry-protected BIC, as the structure becomes symmetric for $\Delta y = 0$. As the asymmetry increases slightly, the Q-factor decreases according to α^{-2} [107, 109]. For further increase in the asymmetry, the Q-factor increases again, reaching a peak for $\alpha = 0.3$. This corresponds to $\Delta y = 76$ nm. The increase of Q-factor is a result of resonance-trapped BIC. By changing the design parameters, the Q-factor of the resonance-trapped BIC will tend towards infinity. Paper IV also investigates how the ellipticity $e = \sqrt{1 - b^2/a^2}$ of the bars affects the sensitivity of the quasi-BIC to changes in design parameters. The sensitivity S is defined by $\Delta\lambda/\Delta r$ with $a' = a + \Delta r$, $b' = b + \Delta r$, and $r' = r + \Delta r$. To find the sensitivity, the design parameters a , b , and d are changed simultaneously for Δr within ± 10 nm. Fig. 5.8(b) shows the sensitivity (filled squares) and Q-factor (filled circles) as function of ellipticity e of the bars for $\Delta y = 103$ nm. The sensitivity decreases with decreasing ellipticity and reaches its minimum for an

ellipticity of 0.74. The sensitivity is approximately equal when the disk is moved closer to a symmetry-protected BIC ($\Delta y = 8$ nm) and close to a resonance-trapped BIC ($\Delta y = 76$ nm). Therefore, changing Δy has limited influence on the sensitivity. The Q-factor is also shown in figure 5.8(b) for varying ellipticity. The Q-factor increases sharply when the ellipticity approaches 0.7. Thus, a more circular shape of the bars is advantageous for achieving a higher Q-factor and a low sensitivity to fabrication.

The metasurface shows a high field enhancement around 4000 at the tips and decreases to 2400 in middle of the gap, as shown in figure 5.9(a) and (b), respectively, for $\Delta y = 76$ nm (resonance-trapped BIC) and ellipticity of 0.74. The high field enhancements, giving very confined hotspots, can be used for optical trapping of nanoparticles. An important feature of this design is the relatively large gap, which is 209 nm for $\Delta y = 103$ nm and ellipticity of 0.74. It is thus possible to trap EVs up to 200 nm diameter.

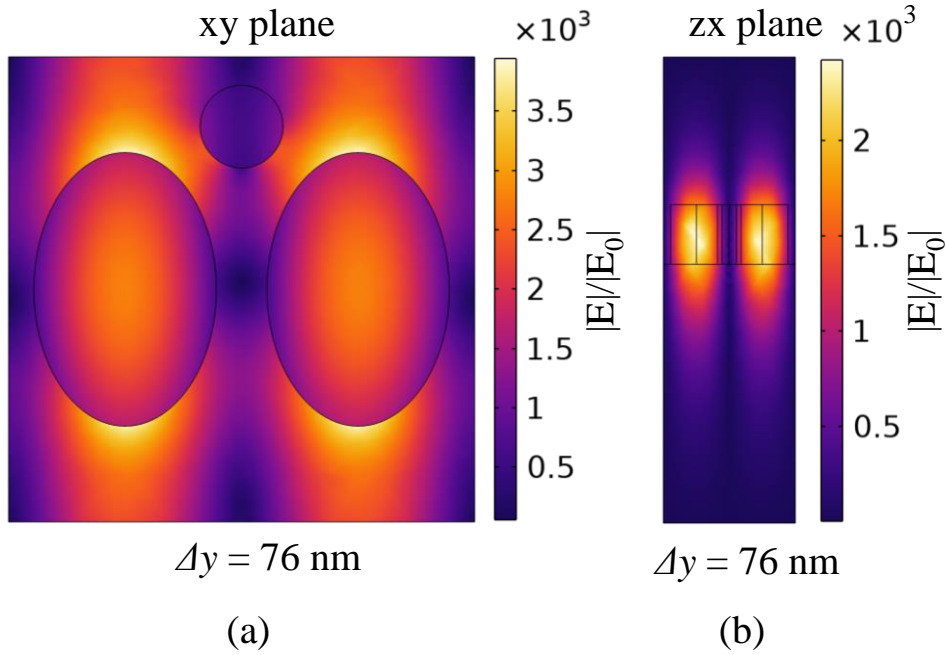


Figure 5.9: Electric field enhancement profiles at the quasi-BIC resonance in the (a) xy plane and (b) zx plane for $\Delta y = 76$ nm, $e = 0.74$ and $d = 90$ nm. The xy plane is taken at $z = h/2$ and the zx plane is taken at $y = P/2$.

The findings presented in paper III and IV are highly relevant to the goals of the RCN project. The quasi-BIC metasurfaces show high field enhancement in the gaps, enabling on-chip optical trapping of EVs at near-visible wavelengths. The metasurfaces does not heat up due to the transparency of silicon nitride and silica at these wavelengths. Furthermore, a modest intensity of $1 \text{ mW}/\mu\text{m}^2$ is sufficient for stable trapping (paper III). Using the trapping laser, Raman scattering can be excited from the trapped EVs and subsequently analyzed using a spectrometer.

The metasurface can have a number of hotspots, where multiple EVs can be trapped and analyzed simultaneously. A set-up similar to the one outlined in section 4.8 can be used, but with a tunable laser. The size of the gap between two adjacent unit cells determines the largest possible size of trapped EVs. With the quasi-BIC design studied in paper III, only EVs with a diameter up to 70 nm can be trapped, as the gap is limited to 81 nm. A different design, parallel bars with a cylindrical disk, is studied in paper IV. This design provides a larger gap of 209 nm, which can be used to trap EVs with a diameter up to 200 nm.

5.6 Fabrication of quasi-BIC metasurfaces

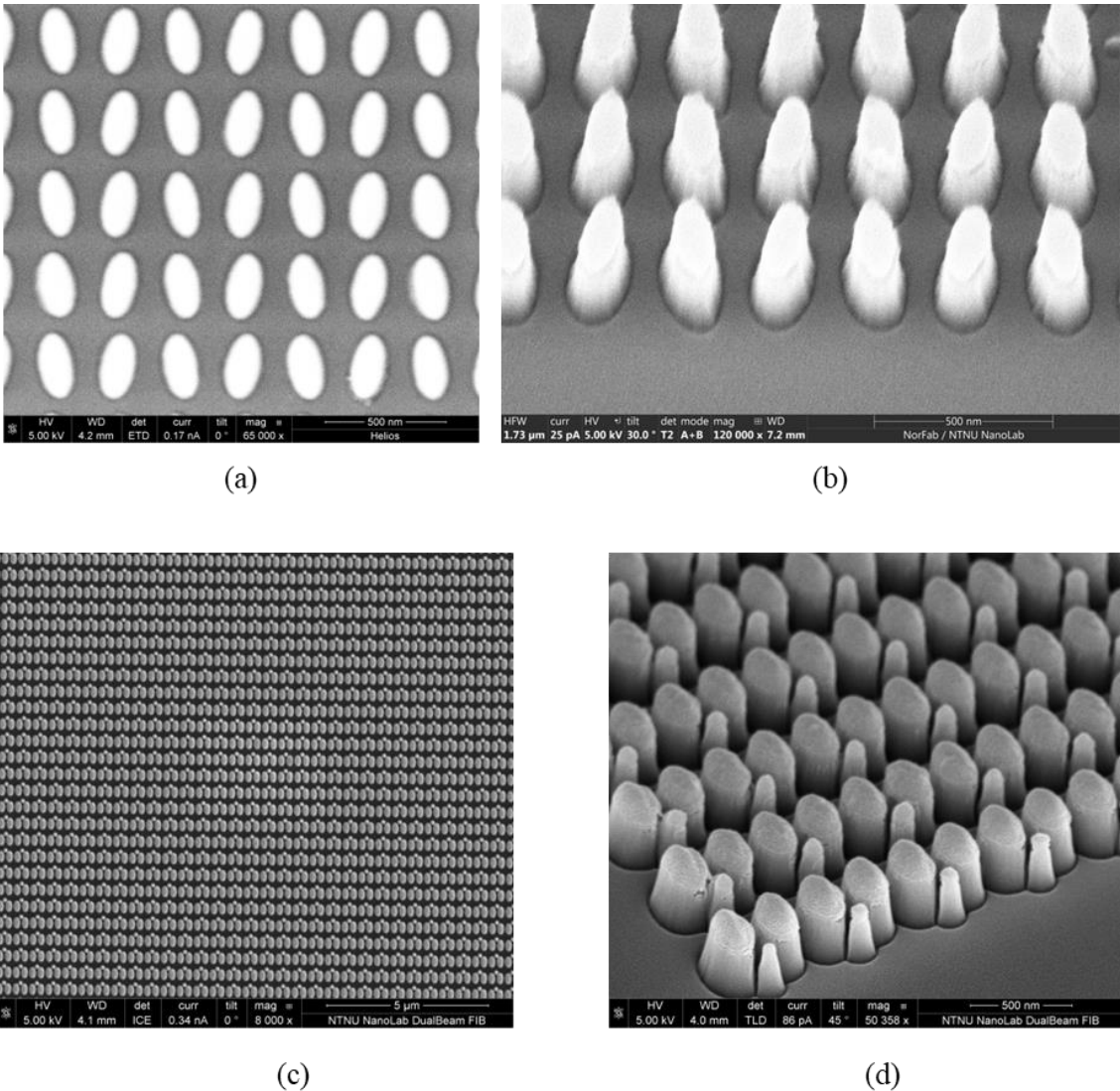


Figure 5.9: (a) Top view and (b) tilted view of the SEM images of the tilted bars metasurfaces. (c) Top view and (b) tilted view of the SEM images of the metasurfaces with parallel bars and cylindrical disks.

The metasurface designs presented in Paper III and IV were made during a test run by Dr. Marek Vlk. The metasurfaces were fabricated using electron beam lithography (EBL) and dry etching at NTNU Nanolab. Figure 5.9 shows some scanning electron microscope (SEM) images of the fabricated metasurfaces. The top and the tilted view of the tilted bars metasurface are shown in Figure 5.9 (a) and (b), respectively. Moreover, the top and the tilted view of the metasurface with parallel bars and cylindrical disks are shown in Figure 5.9 (c) and (d), respectively. As can be seen, the sidewalls are not vertical and there are large fabrication defects.

Future fabrication of the metasurfaces will be done in collaboration with Dr. Martin Møller Greve from the University of Bergen. Details of the fabrication steps are skipped here, as they fall outside the scope of this thesis.

5.7 Experimental setup for measurement of reflectance spectrum from metasurfaces

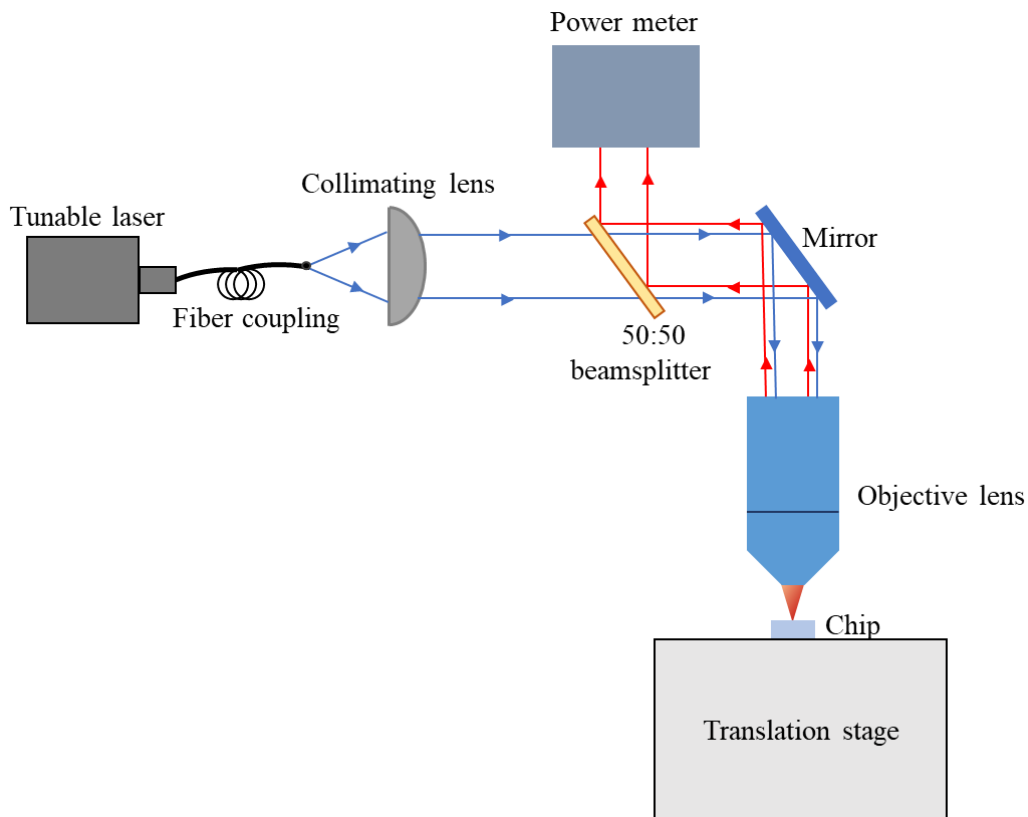


Figure 5.10: Schematic of the experimental setup for measurement of reflectance spectrum from metasurface.

An experimental setup has been built for characterization of quasi-BICs metasurfaces, together with Dr. Marek Vlk, which is shown in figure 5.10. Initially, a fiber-coupled laser is collimated by a lens. The beam is transmitted by a 50:50 beamsplitter and directed to the back aperture of a water dipping objective lens. The reflected light from the metasurface is captured by the

objective lens and returned along the same optical path. The beamsplitter subsequently reflects the beam to a power meter, which measures the power of the reflected beam. This setup was used to measure the reflectance spectrum of the fabricated chips shown in figure 5.9. However, no reflectance peak was identified within the range of the tunable laser in the reflectance spectra. This could potentially be attributed to imperfections in the fabrication process, as the dimensions and shapes of the fabricated metasurface diverged from those of the simulated metasurfaces, as shown in the tilted view of the SEM images in figure 5.9. With improved precision in the fabrication process, we hope to experimentally demonstrate quasi-BIC in the future.

CHAPTER 6

Conclusions and future work

6.1 Conclusions

This thesis studies high-throughput, on-chip methods for optical trapping and Raman spectroscopy of nanoparticles at near-visible wavelengths. Focus is given on dielectric nanostructures to minimize or avoid heating. Two different types of nanostructures, dielectric nanoantennas and quasi-BIC metasurfaces, are simulated using COMSOL Multiphysics. These nanostructures provide moderate to high electric field enhancement in their gaps, which act as hotspots for optical trapping of nanoparticles. Optical forces acting on the nanoparticles are studied using the rigorous Maxwell stress tensor method. Nanotweezers, based on these dielectric nanostructures, are considered potential alternatives to existing optical tweezers.

In paper I, a brief overview of current progress in dielectric nanoantennas is reviewed. This includes definitions and physics of important performance parameters of dielectric nanoantennas, which form the foundation of paper II. Paper I also presents some original simulation results for a spherical silicon dimer. It is shown that the nanoantenna provides a very small mode volume and a modest Q-factor. These two parameters are related to the Purcell factor, which is found to be high for a small dimer gap. The high Purcell factor in the nanoantenna contributes to enhance Raman intensity of a molecule when the molecule is placed nearby the nanoantenna.

In paper II, a dielectric bowtie nanoantenna is investigated. Four different dielectric materials are studied for the nanoantenna, and the design parameters are optimized to achieve maximum field enhancement in a 50 nm gap. The optimized designs are then numerically investigated for optical trapping of three different nanoparticles. The results show that nanoantennas with high

refractive indices (multilayer tungsten disulfide, silicon, and gallium phosphide) are only suitable for stable trapping of 40 nm QDs and PS beads using input intensities of $>10 \text{ mW}/\mu\text{m}^2$ and $>50 \text{ mW}/\mu\text{m}^2$, respectively. They require even higher input intensity for trapping of EVs. For multilayer tungsten disulfide, silicon, and gallium phosphide, the required intensities to trap 40 nm EVs are $121 \text{ mW}/\mu\text{m}^2$, $161 \text{ mW}/\mu\text{m}^2$, and $217 \text{ mW}/\mu\text{m}^2$, respectively. When using the tungsten disulfide and silicon nanoantennas to trap EVs with these intensities, the estimated temperature increase is very high, around 96 K and 22 K, respectively. Despite gallium phosphide being transparent at 785 nm, it is not a standard material for CMOS fabrication. Based on the simulation results in paper II, none of the investigated materials are suitable for trapping EVs.

In paper III, a tilted bars quasi-BIC metasurface is investigated. Transparent silicon nitride is used for the design to avoid absorption and heating at a near-visible wavelength of 785 nm. The design parameters are optimized to obtain a quasi-BIC resonance. At this wavelength, a high electric field enhancement is achieved in the middle of the tip-to-tip gap. The wavelength at the quasi-BIC resonance gives a significant field enhancement at the incident wavelength but there is no enhancement at the Raman emission wavelengths. The optimized dimensions of the unit cell are small, thus fabrication of the metasurface will be challenging. Fabrication tolerances are investigated, and it is shown that resonance wavelength is significantly influenced to variations of the design parameters. The interplay between the trapped nanoparticles (EVs) and the quasi-BIC cavity is investigated and their influence on the trapping performance is explored. Simulations show that an input intensity of $1 \text{ mW}/\mu\text{m}^2$ is sufficient for stable trapping of EVs using the quasi-BIC metasurface. The tip-to-tip gap is approximately 81 nm, which can be used to trap smaller EVs (30-70 nm) and many simultaneously, with one at each hotspot.

Finally, in paper IV, the tilted bars metasurface design is modified to obtain a large tip-to-tip gap for trapping of bigger EVs. The design consists of parallel bars with a cylindrical disk, possibly simplifying the fabrication process. The influence of ellipticity of the bars on the quasi-BIC is investigated. It is shown that the structure can be made less sensitive to fabrication errors by using less elliptical, more circular bars. The effect of varying the position of the disk on Q-factor and field enhancement is also studied. The design parameters are optimized to obtain a quasi-BIC resonance at 773 nm. A very high electric field enhancement of > 2000 can be achieved in the middle of the gap. The gap between the bars is approximately 209 nm. This can be used to trap EVs up to 200 nm diameter, which covers most EVs. This design is thus promising for optical trapping and Raman of EVs.

6.2 Future work

The findings of this thesis have brought new possibilities for on-chip optical trapping and Raman spectroscopy of biological nanoparticles such as EVs. The presented work is primarily based on extensive numerical simulations using COMSOL Multiphysics. Therefore, more work is necessary to realize a functional chip-based system. The immediate next step involves the fabrication of the metasurface. Among the designs considered, the metasurface with parallel bars and a cylindrical disk is recommended due to its larger dimensions compared to the tilted bar design. Reflectance measurements is the easiest method to demonstrate quasi-BICs in the fabricated chip.

As indicated in Papers III and IV, the metasurfaces are very sensitive to variations in design parameters, affecting the target resonance wavelength. Future work should involve further optimization of the design parameters to reduce this sensitivity. The goal is to develop a metasurface design that is more robust against fabrication defects and errors both systematic and random. It is suggested to use the COMSOL optimization module to find a suitable configuration.

The simulations performed for the metasurfaces assume an infinite array of unit cells. However, fabricated metasurfaces will necessarily have finite dimensions. Therefore, it would be useful to investigate the impact of the finite array size on the quasi-BIC and trapping performance. The development of a 2D equivalent model could be a useful direction for future studies, as the 3D simulation of finite array, but relatively large is computationally very costly.

Bibliography

- [1] H. M. Nussenzveig, "Cell membrane biophysics with optical tweezers," *Eur. Biophys. J.*, vol. 47, no. 5, pp. 499-514, 2017.
- [2] R. Smith, K. L. Wright, and L. Ashton, "Raman spectroscopy: an evolving technique for live cell studies," *The Analyst*, vol. 141, no. 12, pp. 3590-3600, 2016.
- [3] A. Ashkin, and J. M. Dziedzic, "Optical Trapping and Manipulation of Viruses and Bacteria," *Science*, vol. 235, no. 4795, pp. 1517-1520, 1987.
- [4] C. V. Raman, and K. S. Krishnan, "A New Type of Secondary Radiation," *Nature*, vol. 121, no. 3048, pp. 501-502, 1928.
- [5] S. Dochow, C. Krafft, U. Neugebauer *et al.*, "Tumour cell identification by means of Raman spectroscopy in combination with optical traps and microfluidic environments," *Lab on a Chip*, vol. 11, no. 8, pp. 1484-1490, 2011.
- [6] J. Lukose, M. N, G. Mohan *et al.*, "Normal saline-induced deoxygenation of red blood cells probed by optical tweezers combined with the micro-Raman technique," *RSC Adv.*, vol. 9, no. 14, pp. 7878-7884, 2019.
- [7] J. Lukose, M. N, G. Mohan *et al.*, "Optical tweezers combined with micro-Raman investigation of alcohol-induced changes on single, live red blood cells in blood plasma," *J. Raman Spectrosc.*, vol. 50, no. 10, pp. 1367-1374, 2019.
- [8] S. J. Webb, "Laser-Raman spectroscopy of living cells," *Phys. Rep.*, vol. 60, no. 4, pp. 201-224, 1980.
- [9] K. Kneipp, H. Kneipp, I. Itzkan *et al.*, "Ultrasensitive Chemical Analysis by Raman Spectroscopy," *Chem. Rev.*, vol. 99, no. 10, pp. 2957-2976, 1999.
- [10] P. Løvhaugen, B. S. Ahluwalia, T. R. Huser *et al.*, "Serial Raman spectroscopy of particles trapped on a waveguide," *Opt. Express*, vol. 21, no. 3, pp. 2964-2970, 2013.
- [11] Q. Zhang, P. Zhang, H. Gou *et al.*, "Towards high-throughput microfluidic Raman-activated cell sorting," *The Analyst*, vol. 140, no. 18, pp. 6163-6174, 2015.
- [12] A. Kotnala, Y. Zheng, J. Fu *et al.*, "Microfluidic-based high-throughput optical trapping of nanoparticles," *Lab on a Chip*, vol. 17, no. 12, pp. 2125-2134, 2017.
- [13] G. Karp, *Cell and molecular biology: concepts and experiments*: Wiley, 2009.
- [14] S. G. Kruglik, F. Royo, J.-M. Guigner *et al.*, "Raman tweezers microspectroscopy of circa 100 nm extracellular vesicles," *Nanoscale*, vol. 11, no. 4, pp. 1661-1679, 2019.
- [15] A. D. Grabarek, D. Weinbuch, W. Jiskoot *et al.*, "Critical Evaluation of Microfluidic Resistive Pulse Sensing for Quantification and Sizing of Nanometer- and Micrometer-

- Sized Particles in Biopharmaceutical Products,” *J. Pharm. Sci.*, vol. 108, no. 1, pp. 563-573, 2019.
- [16] H. Shao, H. Im, C. M. Castro *et al.*, “New Technologies for Analysis of Extracellular Vesicles,” *Chem. Rev.*, vol. 118, no. 4, pp. 1917-1950, 2018.
- [17] Y. Kwon, and J. Park, “Methods to analyze extracellular vesicles at single particle level,” *Micro Nano Syst. Lett.*, vol. 10, pp. 14, 2022.
- [18] H. Yan, Y. Li, S. Cheng *et al.*, “Advances in Analytical Technologies for Extracellular Vesicles,” *Anal. Chem.*, vol. 93, no. 11, pp. 4739-4774, 2021.
- [19] G. Raposo, and P. D. Stahl, “Extracellular vesicles: a new communication paradigm?,” *Nat. Rev. Mol. Cell Biol.*, vol. 20, no. 9, pp. 509-510, 2019.
- [20] G. van Niel, G. D'Angelo, and G. Raposo, “Shedding light on the cell biology of extracellular vesicles,” *Nat. Rev. Mol. Cell Biol.*, vol. 19, no. 4, pp. 213-228, 2018.
- [21] A. Bauwens, L. Kunsmann, H. Karch *et al.*, “Antibiotic-Mediated Modulations of Outer Membrane Vesicles in Enterohemorrhagic Escherichia coli O104:H4 and O157:H7,” *Antimicrob. Agents Chemother.*, vol. 61, no. 9, 2017.
- [22] A. L. Horstman, and M. J. Kuehn, “Enterotoxigenic Escherichia coli Secretes Active Heat-labile Enterotoxin via Outer Membrane Vesicles,” *J. Biol. Chem.*, vol. 275, no. 17, pp. 12489-12496, 2000.
- [23] P. A. Hassan, S. Rana, and G. Verma, “Making Sense of Brownian Motion: Colloid Characterization by Dynamic Light Scattering,” *Langmuir*, vol. 31, no. 1, pp. 3-12, 2014.
- [24] L. G. Rikkert, R. Nieuwland, L. W. M. M. Terstappen *et al.*, “Quality of extracellular vesicle images by transmission electron microscopy is operator and protocol dependent,” *J. Extracell. Vesicles*, vol. 8, no. 1, 2019.
- [25] J. P. Nolan, “Flow Cytometry of Extracellular Vesicles: Potential, Pitfalls, and Prospects,” *Curr. Protoc. Cytom.*, vol. 73, no. 1, 2015.
- [26] H. D. Roberts-Dalton, A. Cocks, J. M. Falcon-Perez *et al.*, “Fluorescence labelling of extracellular vesicles using a novel thiol-based strategy for quantitative analysis of cellular delivery and intracellular traffic,” *Nanoscale*, vol. 9, no. 36, pp. 13693-13706, 2017.
- [27] Y. Hisada, A. C. Auriemma, W. Alexander *et al.*, “Detection of tissue factor-positive extracellular vesicles by laser scanning confocal microscopy,” *Thromb. Res.*, vol. 150, pp. 65-72, 2017.
- [28] E. I. Buzás, C. Gardiner, C. Lee *et al.*, “Single particle analysis: Methods for detection of platelet extracellular vesicles in suspension (excluding flow cytometry),” *Platelets*, vol. 28, no. 3, pp. 249-255, 2016.
- [29] J. Stetefeld, S. A. McKenna, and T. R. Patel, “Dynamic light scattering: a practical guide and applications in biomedical sciences,” *Biophys. Rev.*, vol. 8, no. 4, pp. 409-427, 2016.

- [30] F. Caputo, R. Vogel, J. Savage *et al.*, “Measuring particle size distribution and mass concentration of nanoplastics and microplastics: addressing some analytical challenges in the sub-micron size range,” *J. Colloid Interface Sci.*, vol. 588, pp. 401-417, 2021.
- [31] M. Winey, J. B. Meehl, E. T. O'Toole *et al.*, “Conventional transmission electron microscopy,” *Mol. Biol. Cell.*, vol. 25, no. 3, pp. 319-323, 2014.
- [32] G. Boeck, “Current status of flow cytometry in cell and molecular biology,” *Int. Rev. Cytol.*, vol. 204, pp. 239-298, 2001.
- [33] A. A. Nawaz, R. H. Nissly, P. Li *et al.*, “Immunological Analyses of Whole Blood via “Microfluidic Drifting” Based Flow Cytometric Chip,” *Ann. Biomed. Eng.*, vol. 42, no. 11, pp. 2303-2313, 2014.
- [34] B. O. Leung, and K. C. Chou, “Review of Super-Resolution Fluorescence Microscopy for Biology,” *Appl. Spectrosc.*, vol. 65, no. 9, pp. 967-980, 2011.
- [35] H. Pollet, L. Conrard, A.-S. Cloos *et al.*, “Plasma Membrane Lipid Domains as Platforms for Vesicle Biogenesis and Shedding?,” *Biomolecules*, vol. 8, no. 3, pp. 94, 2018.
- [36] M. Z. Vardaki, C. G. Atkins, H. G. Schulze *et al.*, “Raman spectroscopy of stored red blood cell concentrate within sealed transfusion blood bags,” *The Analyst*, vol. 143, no. 24, pp. 6006-6013, 2018.
- [37] W. Lee, A. Nanou, L. Rikkert *et al.*, “Label-Free Prostate Cancer Detection by Characterization of Extracellular Vesicles Using Raman Spectroscopy,” *Anal. Chem.*, vol. 90, no. 19, pp. 11290-11296, 2018.
- [38] J. Langer, D. Jimenez de Aberasturi, J. Aizpurua *et al.*, “Present and Future of Surface-Enhanced Raman Scattering,” *ACS Nano*, vol. 14, no. 1, pp. 28-117, 2019.
- [39] K. Kneipp, Y. Wang, H. Kneipp *et al.*, “Single Molecule Detection Using Surface-Enhanced Raman Scattering (SERS),” *Phys. Rev. Lett.*, vol. 78, no. 9, pp. 1667-1670, 1997.
- [40] D. D. Galvan, and Q. Yu, “Surface-Enhanced Raman Scattering for Rapid Detection and Characterization of Antibiotic-Resistant Bacteria,” *Adv. Healthc. Mater.*, vol. 7, no. 13, pp. 1701335, 2018.
- [41] S. Liu, Q. Hu, C. Li *et al.*, “Wide-Range, Rapid, and Specific Identification of Pathogenic Bacteria by Surface-Enhanced Raman Spectroscopy,” *ACS Sensors*, vol. 6, no. 8, pp. 2911-2919, 2021.
- [42] D. Cialla, S. Pollok, C. Steinbrücker *et al.*, “SERS-based detection of biomolecules,” *Nanophotonics*, vol. 3, no. 6, pp. 383-411, 2014.
- [43] L. Ling, and Y.-q. Li, “Measurement of Raman spectra of single airborne absorbing particles trapped by a single laser beam,” *Opt. Lett.*, vol. 38, no. 4, pp. 416-418, 2013.

- [44] R. Gillibert, G. Balakrishnan, Q. Deshoules *et al.*, “Raman Tweezers for Small Microplastics and Nanoplastics Identification in Seawater,” *Environ. Sci. Technol.*, vol. 53, no. 15, pp. 9003-9013, 2019.
- [45] K. Ajito, and K. Torimitsu, “Single Nanoparticle Trapping Using a Raman Tweezers Microscope,” *Appl. Spectrosc.*, vol. 56, no. 4, pp. 541-544, 2002.
- [46] C. Xie, M. A. Dinno, and Y.-q. Li, “Near-infrared Raman spectroscopy of single optically trapped biological cells,” *Opt. Lett.*, vol. 27, no. 4, pp. 249-251, 2002.
- [47] A. Enciso-Martinez, E. van der Pol, A. T. M. Lenferink *et al.*, “Synchronized Rayleigh and Raman scattering for the characterization of single optically trapped extracellular vesicles,” *Nanotechnol. Biol. Med.*, vol. 24, pp. 102109, 2020.
- [48] S. Casabella, P. Scully, N. Goddard *et al.*, “Automated analysis of single cells using Laser Tweezers Raman Spectroscopy,” *The Analyst*, vol. 141, no. 2, pp. 689-696, 2016.
- [49] L. Rkiouak, M. J. Tang, J. C. J. Camp *et al.*, “Optical trapping and Raman spectroscopy of solid particles,” *Phys. Chem. Chem. Phys.*, vol. 16, no. 23, pp. 11426-11434, 2014.
- [50] Y. Ai, H. Alali, Y. Pan *et al.*, “Single-particle optical-trapping Raman spectroscopy for the detection and identification of aerosolized airborne biological particles,” *Meas. Sci. Technol.*, vol. 32, no. 5, pp. 055207, 2021.
- [51] Z. Gong, Y.-L. Pan, G. Videen *et al.*, “Optical trapping-Raman spectroscopy (OT-RS) with embedded microscopy imaging for concurrent characterization and monitoring of physical and chemical properties of single particles,” *Anal. Chim. Acta*, vol. 1020, pp. 86-94, 2018.
- [52] M. Boerkamp, T. van Leest, J. Heldens *et al.*, “On-chip optical trapping and Raman spectroscopy using a TripleX dual-waveguide trap,” *Opt. Express*, vol. 22, no. 25, pp. 30528-30537, 2014.
- [53] G. B. Loozen, A. Karuna, M. M. R. Fanood *et al.*, “Integrated photonics multi-waveguide devices for optical trapping and Raman spectroscopy: design, fabrication and performance demonstration,” *Beilstein J. Nanotechnol.*, vol. 11, pp. 829-842, 2020.
- [54] A. Ashkin, “Acceleration and Trapping of Particles by Radiation Pressure,” *Phys. Rev. Lett.*, vol. 24, no. 4, pp. 156-159, 1970.
- [55] J. R. Moffitt, Y. R. Chemla, S. B. Smith *et al.*, “Recent Advances in Optical Tweezers,” *Annu. Rev. Biochem.*, vol. 77, no. 1, pp. 205-228, 2008.
- [56] P. Polimeno, A. Magazzù, M. A. Iatì *et al.*, “Optical tweezers and their applications,” *J. Quant. Spectrosc. Radiat. Transf.*, vol. 218, pp. 131-150, 2018.
- [57] G. Pesce, P. H. Jones, O. M. Maragò *et al.*, “Optical tweezers: theory and practice,” *Eur. Phys. J. Plus*, vol. 135, no. 12, pp. 949, 2020.
- [58] C. J. Bustamante, Y. R. Chemla, S. Liu *et al.*, “Optical tweezers in single-molecule biophysics,” *Nat. Rev.*, vol. 1, no. 1, pp. 25, 2021.

- [59] C. Arbore, L. Perego, M. Sergides *et al.*, “Probing force in living cells with optical tweezers: from single-molecule mechanics to cell mechanotransduction,” *Biophys. Rev.*, vol. 11, no. 5, pp. 765-782, 2019.
- [60] J. D. Kolbow, N. C. Lindquist, C. T. Ertsgaard *et al.*, “Nano-Optical Tweezers: Methods and Applications for Trapping Single Molecules and Nanoparticles,” *Chem. Phys. Chem*, vol. 22, no. 14, pp. 1409-1420, 2021.
- [61] S. E. S. Spesyvtseva, and K. Dholakia, “Trapping in a Material World,” *ACS Photonics*, vol. 3, no. 5, pp. 719-736, 2016.
- [62] L. Novotny, and B. Hecht, *Principles of Nano-Optics*: Cambridge University Press, 2012.
- [63] S. Albaladejo, M. I. Marques, M. Laroche *et al.*, “Scattering forces from the curl of the spin angular momentum of a light field,” *Phys. Rev. Lett.*, vol. 102, no. 11, pp. 113602, Mar 20, 2009.
- [64] B. T. Draine, and J. Goodman, “Beyond Clausius-Mossotti - Wave-Propagation on a Polarizable Point Lattice and the Discrete Dipole Approximation,” *Astrophys. J.*, vol. 405, no. 2, pp. 685-697, Mar 10, 1993.
- [65] R. N. C. Pfeifer, T. A. Nieminen, N. R. Heckenberg *et al.*, “Colloquium: Momentum of an electromagnetic wave in dielectric media,” *Rev. Mod. Phys.*, vol. 79, no. 4, pp. 1197-1216, 2007.
- [66] M. Ploschner, “Optical forces near a nanoantenna,” *J. Nanophotonics*, vol. 4, no. 1, 2010.
- [67] K. Venkateswarlu, “Effect of temperature on the intensities of Raman lines,” *Proc. Indian National.*, vol. 14, no. 5, pp. 529-534, 1941.
- [68] A. H. J. Yang, S. D. Moore, B. S. Schmidt *et al.*, “Optical manipulation of nanoparticles and biomolecules in sub-wavelength slot waveguides,” *Nature*, vol. 457, no. 7225, pp. 71-75, 2009.
- [69] B. S. Ahluwalia, Ø. I. Helle, and O. G. Hellestø, “Rib waveguides for trapping and transport of particles,” *Opt. Express*, vol. 24, no. 5, pp. 4477-4487, 2016.
- [70] Ø. I. Helle, B. S. Ahluwalia, and O. G. Hellestø, “Optical transport, lifting and trapping of micro-particles by planar waveguides,” *Opt. Express*, vol. 23, no. 5, pp. 6601-6612, 2015.
- [71] S. Mandal, X. Serey, and D. Erickson, “Nanomanipulation Using Silicon Photonic Crystal Resonators,” *Nano Lett.*, vol. 10, no. 1, pp. 99-104, 2009.
- [72] Z. Xu, W. Song, and K. B. Crozier, “Direct Particle Tracking Observation and Brownian Dynamics Simulations of a Single Nanoparticle Optically Trapped by a Plasmonic Nanoaperture,” *ACS Photonics*, vol. 5, no. 7, pp. 2850-2859, 2018.

- [73] Q. Jiang, B. Rogez, J.-B. Claude *et al.*, “Temperature Measurement in Plasmonic Nanoapertures Used for Optical Trapping,” *ACS Photonics*, vol. 6, no. 7, pp. 1763-1773, 2019.
- [74] A. N. Koya, J. Cunha, T. L. Guo *et al.*, “Novel Plasmonic Nanocavities for Optical Trapping-Assisted Biosensing Applications,” *Adv. Opt. Mat.*, vol. 8, no. 7, pp. 1901481, 2020.
- [75] J.-H. Kang, K. Kim, H.-S. Ee *et al.*, “Low-power nano-optical vortex trapping via plasmonic diabolo nanoantennas,” *Nat. Commu.*, vol. 2, no. 1, pp. 582, 2011.
- [76] S. Kerman, C. Chen, Y. Li *et al.*, “Raman fingerprinting of single dielectric nanoparticles in plasmonic nanopores,” *Nanoscale*, vol. 7, no. 44, pp. 18612-18618, 2015.
- [77] S. Jones, A. A. Al Balushi, and R. Gordon, “Raman spectroscopy of single nanoparticles in a double-nanohole optical tweezer system,” *J. Opt.*, vol. 17, no. 10, 2015.
- [78] J.-M. Nam, J.-W. Oh, H. Lee *et al.*, “Plasmonic Nanogap-Enhanced Raman Scattering with Nanoparticles,” *Acc. Chem. Res.*, vol. 49, no. 12, pp. 2746-2755, 2016.
- [79] Z. Xu, W. Song, and K. B. Crozier, “Optical Trapping of Nanoparticles Using All-Silicon Nanoantennas,” *ACS Photonics*, vol. 5, no. 12, pp. 4993-5001, 2018.
- [80] Z. Xu, and K. B. Crozier, “All-dielectric nanotweezers for trapping and observation of a single quantum dot,” *Opt. Express*, vol. 27, no. 4, pp. 4034-4045, 2019.
- [81] M. Caldarola, P. Albella, E. Cortés *et al.*, “Non-plasmonic nanoantennas for surface enhanced spectroscopies with ultra-low heat conversion,” *Nat. Commu.*, vol. 6, no. 1, pp. 7915, 2015.
- [82] J. Cambiasso, M. König, E. Cortés *et al.*, “Surface-Enhanced Spectroscopies of a Molecular Monolayer in an All-Dielectric Nanoantenna,” *ACS Photonics*, vol. 5, no. 4, pp. 1546-1557, 2018.
- [83] A. I. Barreda, J. M. Saiz, F. González *et al.*, “Recent advances in high refractive index dielectric nanoantennas: Basics and applications,” *AIP Adv.*, vol. 9, no. 4, pp. 040701, 2019.
- [84] S. Bidault, M. Mivelle, and N. Bonod, “Dielectric nanoantennas to manipulate solid-state light emission,” *J. Appl. Phys.*, vol. 126, no. 9, pp. 094104, 2019.
- [85] B. Sain, C. Meier, and T. Zentgraf, “Nonlinear optics in all-dielectric nanoantennas and metasurfaces: a review,” *Adv. Photonics*, vol. 1, no. 2, pp. 024002, 2019.
- [86] A. Krasnok, M. Caldarola, N. Bonod *et al.*, “Spectroscopy and Biosensing with Optically Resonant Dielectric Nanostructures,” *Adv. Opt. Mat.*, vol. 6, no. 5, pp. 1701094, 2018.
- [87] D. G. Baranov, D. A. Zuev, S. I. Lepeshov *et al.*, “All-dielectric nanophotonics: the quest for better materials and fabrication techniques,” *Optica*, vol. 4, no. 7, pp. 814-825, 2017.

- [88] P. Albella, R. Alcaraz de la Osa, F. Moreno *et al.*, “Electric and Magnetic Field Enhancement with Ultralow Heat Radiation Dielectric Nanoantennas: Considerations for Surface-Enhanced Spectroscopies,” *ACS Photonics*, vol. 1, no. 6, pp. 524-529, 2014.
- [89] J. S. Donner, G. Baffou, D. McCloskey *et al.*, “Plasmon-Assisted Optofluidics,” *ACS Nano*, vol. 5, no. 7, pp. 5457-5462, 2011.
- [90] G. Baffou, and R. Quidant, “Thermo-plasmonics: using metallic nanostructures as nano-sources of heat,” *Laser Photonics Rev.*, vol. 7, no. 2, pp. 171-187, 2013.
- [91] P. Gresho, and R. Sani, *Incompressible Flow and the Finite Element Method*: Wiley, 1998.
- [92] B. J. Roxworthy, A. M. Bhuiya, S. P. Vanka *et al.*, “Understanding and controlling plasmon-induced convection,” *Nat. Commu.*, vol. 5, no. 1, pp. 3173, 2014.
- [93] J. Hu, S. Bandyopadhyay, Y.-h. Liu *et al.*, “A Review on Metasurface: From Principle to Smart Metadevices,” *Front. Phys.*, vol. 8, 2021.
- [94] H.-T. Chen, A. J. Taylor, and N. Yu, “A review of metasurfaces: physics and applications,” *Rep. Prog. Phys.*, vol. 79, no. 7, 2016.
- [95] S. M. Kamali, E. Arbabi, A. Arbabi *et al.*, “A review of dielectric optical metasurfaces for wavefront control,” *Nanophotonics*, vol. 7, no. 6, pp. 1041-1068, 2018.
- [96] L. Wan, D. Pan, T. Feng *et al.*, “A review of dielectric optical metasurfaces for spatial differentiation and edge detection,” *Front. Optoelectron.*, vol. 14, no. 2, pp. 187-200, 2021.
- [97] Y. He, G. Guo, T. Feng *et al.*, “Toroidal dipole bound states in the continuum,” *Phys. Rev. B* vol. 98, no. 16, pp. 161112(R), 2018.
- [98] D. Pan, L. Wan, M. Ouyang *et al.*, “Laplace metasurfaces for optical analog computing based on quasi-bound states in the continuum,” *Photonics Res.*, vol. 9, no. 9, pp. 1758-1766, 2021.
- [99] C. W. Hsu, B. Zhen, A. D. Stone *et al.*, “Bound states in the continuum,” *Nat. Rev. Mater.*, vol. 1, no. 9, pp. 16048, 2016.
- [100] J. v. Neumann, and E. Wigner, “Über merkwürdige diskrete Eigenwerte,” *Phys. Z.*, vol. 30, no. 524, pp. 291-293, 1929.
- [101] M. McIver, “An example of non-uniqueness in the two-dimensional linear water wave problem,” *J. Fluid Mech.*, vol. 315, pp. 257-266, 2006.
- [102] C. M. Linton, and P. McIver, “Embedded trapped modes in water waves and acoustics,” *Wave Motion*, vol. 45, no. 1-2, pp. 16-29, 2007.
- [103] D. C. Marinica, A. G. Borisov, and S. V. Shabanov, “Bound States in the Continuum in Photonics,” *Phys. Rev. Lett.*, vol. 100, no. 18, pp. 183902, 2008.

- [104] Y. Plotnik, O. Peleg, F. Dreisow *et al.*, “Experimental Observation of Optical Bound States in the Continuum,” *Phys. Rev. Lett.*, vol. 107, no. 18, pp. 183901, 2011.
- [105] S. Joseph, S. Pandey, S. Sarkar *et al.*, “Bound states in the continuum in resonant nanostructures: an overview of engineered materials for tailored applications,” *Nanophotonics*, vol. 10, no. 17, pp. 4175-4207, 2021.
- [106] R. Parker, “Resonance effects in wake shedding from parallel plates: Some experimental observations,” *J. Sound Vib.*, vol. 4, no. 1, pp. 62-72, 1966.
- [107] K. Koshelev, S. Lepeshov, M. Liu *et al.*, “Asymmetric Metasurfaces with High- Q Resonances Governed by Bound States in the Continuum,” *Phys. Rev. Lett.*, vol. 121, no. 19, pp. 193903, 2018.
- [108] C. W. Hsu, B. Zhen, J. Lee *et al.*, “Observation of trapped light within the radiation continuum,” *Nature*, vol. 499, no. 7457, pp. 188-191, 2013.
- [109] C. Fang, Q. Yang, Q. Yuan *et al.*, “High-Q resonances governed by the quasi-bound states in the continuum in all-dielectric metasurfaces,” *Opto-Electronic Adv.*, vol. 4, no. 6, pp. 200030, 2021.
- [110] K. Koshelev, Y. Tang, K. Li *et al.*, “Nonlinear Metasurfaces Governed by Bound States in the Continuum,” *ACS Photonics*, vol. 6, no. 7, pp. 1639-1644, 2019.
- [111] A. Tittl, A. Leitis, M. Liu *et al.*, “Imaging-based molecular barcoding with pixelated dielectric metasurfaces,” *Science*, vol. 360, no. 6393, pp. 1105-1109, 2018.
- [112] Y. Jahani, E. R. Arvelo, F. Yesilkoy *et al.*, “Imaging-based spectrometer-less optofluidic biosensors based on dielectric metasurfaces for detecting extracellular vesicles,” *Nat. Commun.*, vol. 12, no. 1, pp. 3246, 2021.
- [113] S. Li, C. Zhou, T. Liu *et al.*, “Symmetry-protected bound states in the continuum supported by all-dielectric metasurfaces,” *Phys. Rev. A*, vol. 100, pp. 063803, 2019.
- [114] M. R. Hasan, and O. G. Hellestø, “Metasurface supporting quasi-BIC for optical trapping and Raman-spectroscopy of biological nanoparticles,” *Opt. Express*, vol. 31, no. 4, 2023.
- [115] S. Yang, C. Hong, Y. Jiang *et al.*, “Nanoparticle Trapping in a Quasi-BIC System,” *ACS Photonics*, vol. 8, no. 7, pp. 1961-1971, 2021.
- [116] M. R. Hasan, and O. G. Hellestø, “Metasurface supporting quasi-BIC for optical trapping and Raman-spectroscopy of biological nanoparticles,” *Opt. Express*, vol. 31, no. 4, pp. 6782-6795, 2023.

Paper I: Dielectric optical nanoantennas

Published in Nanotechnology, February 2021.

Authors: Md Rabiul Hasan, and Olav Gaute Hellestø

Contribution notes: Md Rabiul Hasan performed the modelling, simulation, and data analysis. Md Rabiul Hasan wrote the initial draft and Olav Gaute Hellestø finalized it before submission. Both authors contributed to revise the manuscript.

Topical Review

Dielectric optical nanoantennas

Md Rabiul Hasan  and Olav Gaute Helleso 

Department of Physics and Technology, UiT—The Arctic University of Norway, Tromsø, Norway

E-mail: olav.gaute.helleso@uit.no

Received 15 September 2020, revised 11 November 2020

Accepted for publication 18 January 2021

Published 22 February 2021



CrossMark

Abstract

Nanophotonics allows the manipulation of light on the subwavelength scale. Optical nanoantennas are nanoscale elements that enable increased resolution in bioimaging, novel photon sources, solar cells with higher absorption, and the detection of fluorescence from a single molecule. While plasmonic nanoantennas have been extensively explored in the literature, dielectric nanoantennas have several advantages over their plasmonic counterparts, including low dissipative losses and near-field enhancement of both electric and magnetic fields. Nanoantennas increase the optical density of states, which increase the rate of spontaneous emission due to the Purcell effect. The increase is quantified by the Purcell factor, which depends on the mode volume and the quality factor. It is one of the main performance parameters for nanoantennas. One particularly interesting feature of dielectric nanoantennas is the possibility of integrating them into optical resonators with a high quality-factor, further improving the performance of the nanoantennas and giving very high Purcell factors. This review introduces the properties and parameters of dielectric optical nanoantennas, and gives a classification of the nanoantennas based on the number and shape of the nanoantenna elements. An overview of recent progress in the field is provided, and a simulation is included as an example. The simulated nanoantenna, a dimer consisting of two silicon nanospheres separated by a gap, is shown to have a very small mode volume, but a low quality-factor. Some recent works on photonic crystal resonators are reviewed, including one that includes a nanoantenna in the bowtie unit-cell. This results in an enormous increase in the calculated Purcell factor, from 200 for the example dimer, to 8×10^6 for the photonic crystal resonator. Some applications of dielectric nanoantennas are described. With current progress in the field, it is expected that the number of applications will grow and that nanoantennas will be incorporated into new commercial products. A list of relevant materials with high refractive indexes and low losses is presented and discussed. Finally, prospects and major challenges for dielectric nanoantennas are addressed.

Keywords: nanophotonics, dielectric materials, nanoantennas

(Some figures may appear in colour only in the online journal)

1. Introduction

Antennas for radio and microwave wavelengths are widely used as an integral part of wireless communications.

Compared to conventional antennas, optical nanoantennas are less common, mainly due to their small size. Advances in nanoscience and fabrication technologies have made it possible to realize structures down to nanometers [1], thus paving the way for new and improved designs of optical nanoantennas. The emergence of optical nanoantennas has opened new research directions and applications. Among the diverse applications are nanoparticle trapping [2–4], optical sensing [5–8], optical computing [9–12], and spectroscopy [13–17].



Original content from this work may be used under the terms of the [Creative Commons Attribution 4.0 licence](https://creativecommons.org/licenses/by/4.0/). Any further distribution of this work must maintain attribution to the author(s) and the title of the work, journal citation and DOI.

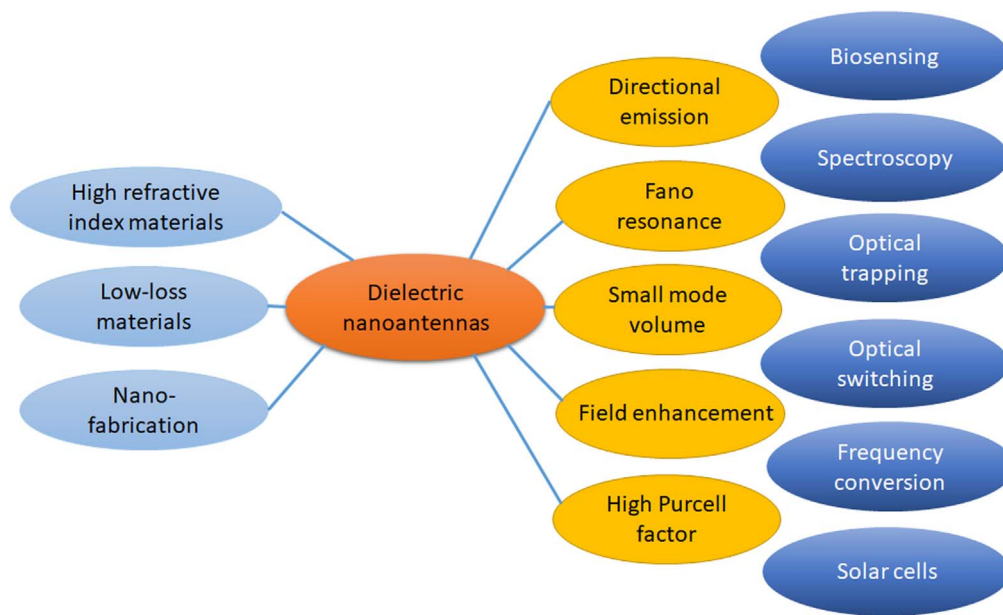


Figure 1. Schematic illustration of the factors necessary to realize dielectric optical nanoantennas, their main optical properties, and some applications.

Figure 1 illustrates the factors necessary to realize dielectric optical nanoantennas, their optical properties and some applications.

Optical nanoantennas can be categorized into three types: (a) plasmonic or metallic nanoantennas, (b) metal-dielectric nanoantennas, and (c) dielectric nanoantennas. Different configurations of plasmonic and metal-dielectric nanoantennas have been investigated and reviewed [18–27]. They include monopole nanoantennas, dimer nanoantennas, dipole nanoantennas, bowtie nanoantennas, core-shell nanospheres, Yagi-Uda nanoantennas, nanoflower arrays, directed scatterers, rhombic nanoantennas, and hybrid nanoantennas. Several metal-dielectric nanoantennas with active coatings have also been reported for enhanced scattering [27–30]. Active coatings have practical limitations, as the scattering becomes dependent on shape and polarization [27]. Plasmonic nanoantennas have two major drawbacks. First, they exhibit high optical loss due to the interband transitions of most commonly used plasmonic metals such as gold and silver [31, 32]. Therefore, they suffer from low antenna radiation efficiency. Second, the dissipative losses in metals generate heat in the nanoantenna structures and the surrounding environment [31, 32]. This is detrimental for several applications such as for heat-sensitive biological samples and optical trapping of nanoparticles, which are propelled out of the trap by thermally induced flows. In contrast, dielectric nanoantennas show considerably lower absorption loss and insignificant Joule heating, compared to their plasmonic counterparts. Therefore, they pave the way for new biological applications where negligible local heating is essential. Dielectric materials with a high refractive index offer enhancement of both electric and magnetic fields [33], which can be used to control the scattered radiation.

Dielectric optical nanoantennas can provide exceptionally small mode volumes, as demonstrated in several works

that will be reviewed. The review also includes the simulation of a dimer consisting of two silicon nanospheres separated by a small gap. This can be considered a basic example of an optical nanoantenna. The simulation shows that a very small gap also gives a very small mode volume. A notable advantage of dielectric nanoantennas is the possibility of integration with optical resonators. Optical resonators give added enhancement of the field by accumulating light on many roundtrips, and due to their low losses, nanoantennas can potentially be integrated in the resonator without reducing its quality factor. Such a combination can be realized by incorporating a nanoantenna in a photonic crystal resonator. Recent work and the state-of-the-art in this direction will be discussed and compared with the example dimer nanoantenna.

The fabrication technologies for dielectric materials are mature and allow us to realize compact, low-cost and integrated nanophotonic devices [1]. Over the last decade, several dielectric nanoantenna structures have been reported including microspheres [34–36], nanospheres [37–40], Yagi-Uda nanoantennas [41–45], core-shell nanoantennas [46–48], dimers [31, 32, 49–56], bowtie nanoantennas [57–59], nanodisks [60–62] and nanorods [63, 64]. The objective of this review is to (i) define the terminology and performance parameters, (ii) give an overview of recent progress in the field and compare some of the results, (iii) describe some potential applications, (iv) list and discuss suitable materials, and (v) discuss the future outlook and challenges for dielectric optical nanoantennas.

2. Definitions and performance parameters

In classical antenna theory, antennas are devices that transform alternating currents (electric and magnetic) to

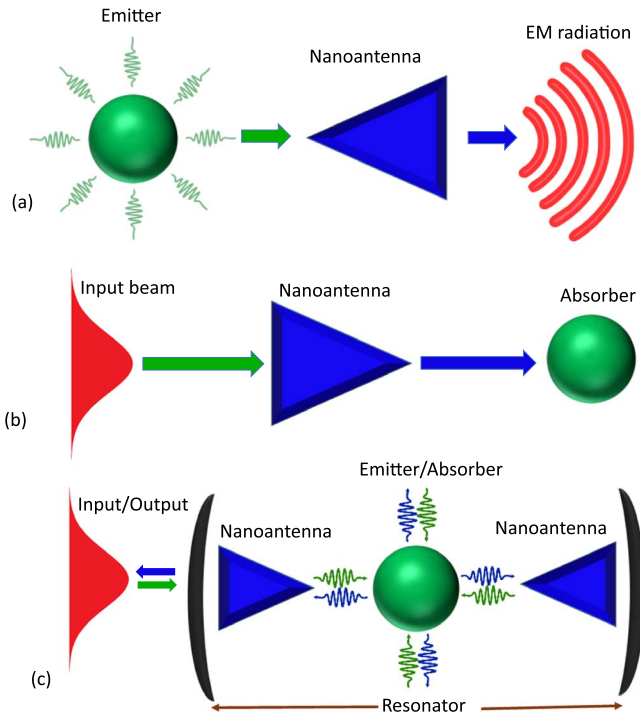


Figure 2. Outline of (a) a transmitting nanoantenna, (b) a receiving nanoantenna, and (c) a transmitting or receiving nanoantenna integrated in an optical resonator.

electromagnetic (EM) waves or EM waves to alternating currents. This definition is somewhat vague and inappropriate when it comes to defining optical nanoantennas. In general, optical nanoantennas serve as transducers between free EM radiation and localized energy [65]. Whereas an optical lens can focus a beam to a diffraction-limited spot, optical nanoantennas work with the near-field and, as a consequence, do not have a diffraction limit *per se*.

The interactions of a nanoantenna with an emitter or an absorber are illustrated in figures 2(a), (b). The emitter is taken as a point source that radiates isotropically, e.g. a fluorescent nanoparticle. Another example of an emitter can be an oscillating electric or magnetic dipole. The role of the transmitting nanoantenna is to enhance and pick up the emitted, highly diverging field, and transform it into a field that can be captured by a detector, e.g. a microscope. Similarly, a receiving nanoantenna transforms an incident field, e.g. a plane wave or a Gaussian beam, into a highly localized field, which is captured by an absorber [65]. As for the emitter, the absorber is much smaller than the operating wavelength. In principle, the two cases of transmitting and receiving nanoantennas are reversible and their respective output and input field-distributions can be of any shape depending on the application. However, as a detector only sees the amplitude of the field, the output field-distribution from a transmitting nanoantenna is often less critical than the input field for the receiving nanoantenna. To obtain high localized intensity on an absorber, a laser and thus a Gaussian field-distribution is most common. This is thus taken as the input beam for the absorber in figure 2(b). Alternatively, for simultaneous excitation of many receiving nanoantennas, a

wide beam or a plane wave can be used, which is the case for solar cells. A dielectric nanoantenna can be embedded inside an optical resonator in both transmitting and receiving modes as shown in figure 2(c). In transmitting mode, radiation from the emitter is captured by the nanoantenna and enhanced by the resonator, which produces an output beam. Reversely, in the receiving mode, the resonator builds up a strong field, which the nanoantenna transforms to a localized field, which in turn is captured by the absorber. In both cases, the resonator builds up the field over many cycles and enhances the energy density in the confined field, thus increasing the performance of the nanoantenna.

Optical nanoantennas resemble their classical counterparts. However, several important differences exist in terms of scaling and physical characteristics. In the following section, we will describe the most important performance parameters for nanoantennas, without giving a full theoretical treatment. Interested readers can follow [66, 67] for more extensive theory and definition of other parameters of dielectric nanoantennas.

2.1. Antenna efficiency and directivity

A nanoantenna experiences dissipative losses mostly by heat and absorption, which are low for dielectric materials, but must be accounted for. Antenna efficiency or radiation efficiency measures the degree of these losses. It is defined as the ratio of far-field radiated power to total power dissipated by the nanoantenna. Mathematically, the radiation efficiency of a nanoantenna is expressed by [68],

$$\epsilon_{\text{rad}} = \frac{P_{\text{rad}}}{P} = \frac{P_{\text{rad}}}{P_{\text{rad}} + P_{\text{loss}}}, \quad (1)$$

where P accounts for the total power dissipated by the nanoantenna, which consists of radiated power P_{rad} and total power loss P_{loss} of the nanoantenna. For a lossless hypothetical nanoantenna, the radiation efficiency is unity.

The directivity (D) of a nanoantenna measures the ability to concentrate radiated power in a particular direction. It is a comparative measure for how much the radiated power is enhanced if an isotropic antenna (an antenna that radiates power in all directions equally) is replaced by a directional antenna. In general, a narrow radiation pattern provides high directivity. The general expression for directivity is given by,

$$D(\theta, \phi) = \frac{4\pi}{P_{\text{rad}}} p(\theta, \phi), \quad (2)$$

where the angles θ and ϕ are measured in the spherical coordinate system and indicate the direction of observation. The normalized angular power density $p(\theta, \phi)$ defines the angular distribution of the radiated power, which is related to P_{rad} by the following expression,

$$P_{\text{rad}} = \int_0^\pi \int_0^{2\pi} p(\theta, \phi) \sin \theta d\phi d\theta \quad (3)$$

When the direction (θ, ϕ) is not clearly stated, the direction of maximum directivity (D_{max}) is often used. Mathematically,

D_{\max} is given by $D_{\max} = \frac{4\pi \text{Max}[p(\theta, \phi)]}{P_{\text{rad}}}$, where $\text{Max}[p(\theta, \phi)]$ is the radiation power transmitted by the main lobe.

2.2. Cross sections and field enhancement factors

Let us assume a spherical, dielectric nanoparticle with radius r and illuminated by a plane wave having intensity I_0 . Some of the power from the plane wave will be captured by the particle and concentrated in its near-field. The nanoparticle thus acts as a nanoantenna. A small fraction of the plane wave will be absorbed and scattered by the particle, and the plane wave will thus experience a small attenuation. For a plane wave, the intensity $I_0 = n_s |\mathbf{E}_{\text{in}}|^2 / 2Z_0$, where n_s is the refractive index of the surrounding medium, \mathbf{E}_{in} is the amplitude of the incident electric field and Z_0 is the impedance of free space. The net rate of EM energy passing across the surface of the nanoparticle is given by $\mathbf{S} \cdot \hat{\mathbf{e}}A$, where \mathbf{S} is the Poynting vector, and A is the area defined by the unit normal vector $\hat{\mathbf{e}}$. The scattering cross section is found by,

$$C_{\text{scat}} = \frac{1}{I_0} \iint (\mathbf{S}_s \cdot \hat{\mathbf{e}}) dA, \quad (4)$$

where \mathbf{S}_s is the Poynting vector for the scattered radiation. The integration is performed over the closed surface of the nanoparticle.

The absorption cross section is given by the following expression,

$$C_{\text{abs}} = \frac{1}{I_0} \iiint P_d dV, \quad (5)$$

where P_d is the power loss density in the nanoparticle and the integration must be performed over its volume V .

The extinction cross section, which is a measure of the attenuation experienced by the plane wave, is the sum of the scattering and absorption cross sections:

$$C_{\text{ext}} = C_{\text{abs}} + C_{\text{scat}} \quad (6)$$

The virtual scattering cross section of the nanoparticle is different from the physical scattering cross section. Three dimensionless parameters called efficiency factors, are used to relate the virtual and the physical scattering cross section. The efficiency factors for absorption, scattering and extinction are defined by

$$Q_{\text{abs}} = \frac{C_{\text{abs}}}{G}, \quad Q_{\text{scat}} = \frac{C_{\text{scat}}}{G}, \quad \text{and} \quad Q_{\text{ext}} = \frac{C_{\text{ext}}}{G}, \quad (7)$$

where G is the physical cross sectional area of the nanoparticle ($G = \pi r^2$ for a nanosphere). If the incident beam is totally absorbed or scattered by the nanoparticle, the efficiency factors for absorption and scattering cross-sections will be unity. However, some nanoparticles can absorb or scatter more light than what is given by the cross sectional area. Thus, the efficiency factors can be greater than unity.

The concentration of electric and magnetic fields by nanoantennas is measured by field enhancement factors. The electric field enhancement factor δ^e is defined as the ratio of

absolute electric field strength $|\mathbf{E}|$ at a given location in the presence of a nanoantenna, to the absolute electric field strength $|\mathbf{E}_0|$ in the absence of a nanoantenna. Depending on the value of $|\mathbf{E}|$ and $|\mathbf{E}_0|$, the electric field enhancement factor can be either greater or less than unity. Likewise, we can define the magnetic field enhancement factor δ^m , where electric fields $|\mathbf{E}|$ and $|\mathbf{E}_0|$ are replaced by magnetic fields $|\mathbf{H}|$ and $|\mathbf{H}_0|$, respectively.

2.3. Quality factor and mode volume

When a nanoantenna is placed inside an optical resonator, it produces an enhanced light-matter interaction. Moreover, dielectric nanoparticles with high refractive index behave as resonators on their own. The performance of such nanoantennas is characterized by two figures of merit: quality-factor and mode volume. The quality factor Q is a measure of photon cavity lifetime. The quality factor of an optical cavity mode can be defined by the following expression,

$$Q = 2\pi\nu_0 \left(\frac{E_{\text{stored}}}{P_{\text{loss}}} \right) \quad (8)$$

where ν_0 denotes the resonance frequency, E_{stored} is the stored EM energy in the cavity and P_{loss} is the power loss per cycle. Once the resonance profile is obtained, the quality factor can be determined from the resonance peak by fitting it to a Lorentzian lineshape function. In this case, the quality factor can be calculated from $Q = \nu_0 / \Delta\nu$, where $\Delta\nu$ refers to the full-width-at-half-maximum (FWHM) of the resonance peak. The cavity modes have a finite lifetime due to the dissipation of energy in the cavity. The lifetime is expressed by $1/\gamma_{\text{cav}} = 2\text{Im}[\omega_N]$, where γ_{cav} is the cavity decay rate and $\text{Im}[\omega_N]$ is the imaginary part of the complex resonance frequency. The cavity decay rate is related to the quality factor by $Q = \omega / 2\gamma_{\text{cav}}$. In practice, the cavity decay rate has contributions from both radiative and absorption components as given by $\gamma_{\text{cav}} = \gamma_{\text{cav}}^{\text{rad}} + \gamma_{\text{cav}}^{\text{loss}}$. The quality factor is then found from $Q^{-1} = Q_{\text{rad}}^{-1} + Q_{\text{loss}}^{-1}$, where Q_{rad}^{-1} is the decay rate due to radiation to air (or surrounding medium) and Q_{loss}^{-1} is the rate of loss due to absorption.

The mode volume V_m is a measure of the spatial spread and energy density of an optical mode. It represents the ability of a nanoantenna to concentrate the field into a tightly confined spot. For low losses, mode volume is given by [69],

$$V_m = \frac{\int \varepsilon(r) |\mathbf{E}(r)|^2 dV}{\text{Max}(\varepsilon(r) |\mathbf{E}(r)|^2)} \quad (9)$$

where E is the electric field and ε is the dielectric constant, which are both spatially dependent. In some cases, the mode volume can be significantly smaller than the physical volume of the nanocavity. For plasmonic nanostructures, a mode volume in the order of $10^{-3} (\lambda/n)^3$ has been reported [70]. Here, n is the refractive index of the surrounding material or in the nanocavity. Dielectric nanoantennas have been proposed with similar mode volumes, e.g. $5 \times 10^{-4} (\lambda/n)^3$ [71].

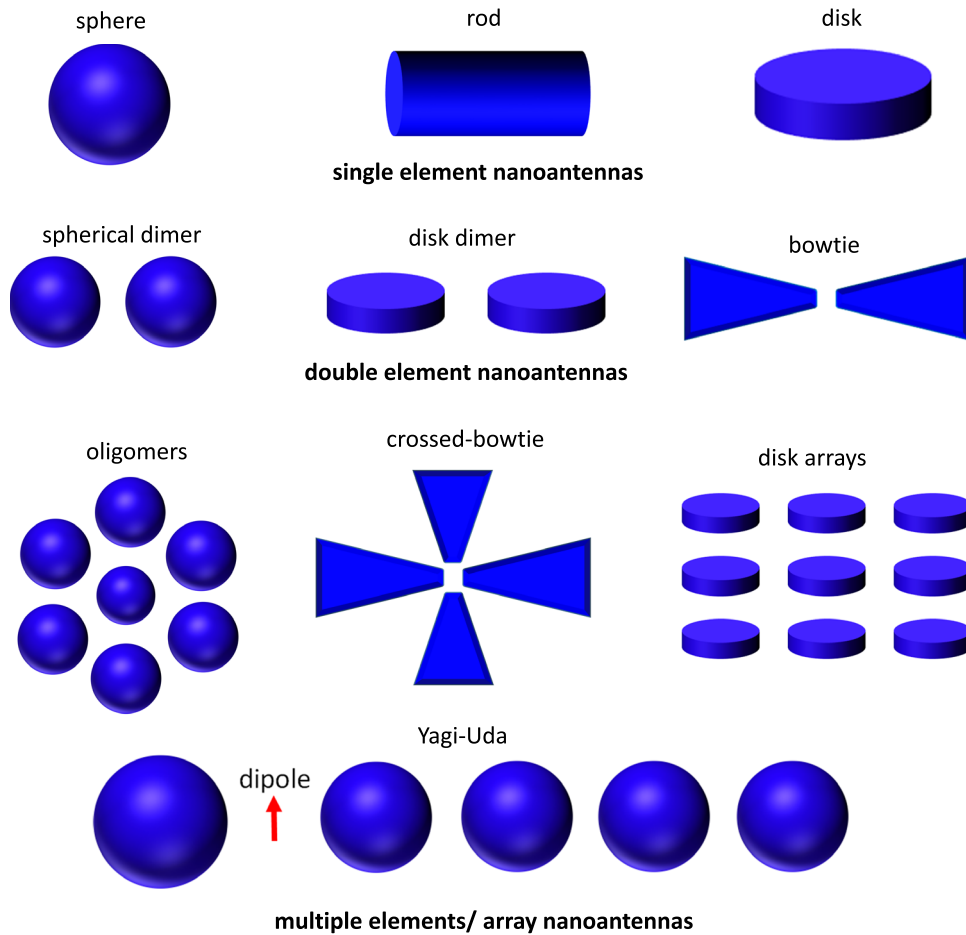


Figure 3. Classification of dielectric optical nanoantennas and illustration of their shapes.

The expression for mode volume must be modified if the nanocavity exhibits high dissipative rates, for which a complex mode volume is used.

2.4. Purcell effect and Purcell factor

As noted, when defining the various parameters, transmitting and receiving nanoantennas can enhance the efficiency of a quantum emitter and detector. The enhancement mechanism can be explained by the Purcell effect. Here, we will consider the Purcell effect for a nanoantenna in transmitting mode. It increases the efficiency of a quantum emitter, which has a finite number of discrete and stationary energy states [72]. When the emitter is excited, it should ideally stay in one of the energy states endlessly. However, the lifetime of the emitter's excited states is reduced because of interaction with the surrounding environment. Such interactions cause an emission of photons by spontaneous transition of the excited emitter into a lower energy state. Previously, it was thought that this spontaneous radiation occurs due to intrinsic characteristics of the atoms. This notion was proved wrong by the pioneering work of E. M. Purcell [73], who showed that the spontaneous relaxation rate of a magnetic dipole can be enhanced compared to the relaxation rate in free space, thus modifying the emission characteristics of the emitter. This phenomenon has been coined the Purcell effect. Based on this

effect, the spontaneous emission rate γ_{mol} can be increased using nanoantennas, and the increase is described by the Purcell factor F_p ,

$$F_p = \frac{\gamma_{\text{mol}}}{\gamma_{\text{mol}}^0} = \frac{2g^2}{\gamma_{\text{cav}}\gamma_{\text{mol}}^0} \quad (10)$$

where $\gamma_{\text{mol}} = 2g^2/\gamma_{\text{cav}}$ is the spontaneous emission rate of the emitter in the presence of a nanoantenna, g is the coupling constant, γ_{cav} is the cavity decay rate, $\gamma_{\text{mol}}^0 = \frac{nd^2\omega^3}{3\pi\hbar\epsilon_0c^3}$ is the decay rate into free space without the nanoantenna, d is the dipole moment, and \hbar is the reduced Planck constant. Equation (10) demonstrates that γ_{mol} of an emitter can be modified by the interplay with a nanocavity. The modification can be large when the resonant frequency of the nanocavity is tuned to the emission frequency of the emitter. Altering the emission lifetime of a quantum emitter with a nanoantenna has potential applications in spectroscopy and optical sensing.

The Purcell factor is related to the quality-factor and mode volume of the nanocavity by the following expression [74],

$$F_p = \frac{3}{4\pi^2} \left(\frac{\lambda}{n}\right)^3 \frac{Q}{V_m}. \quad (11)$$

Equation (11) indicates that the Purcell factor is directly proportional to the quality factor of the cavity and inversely

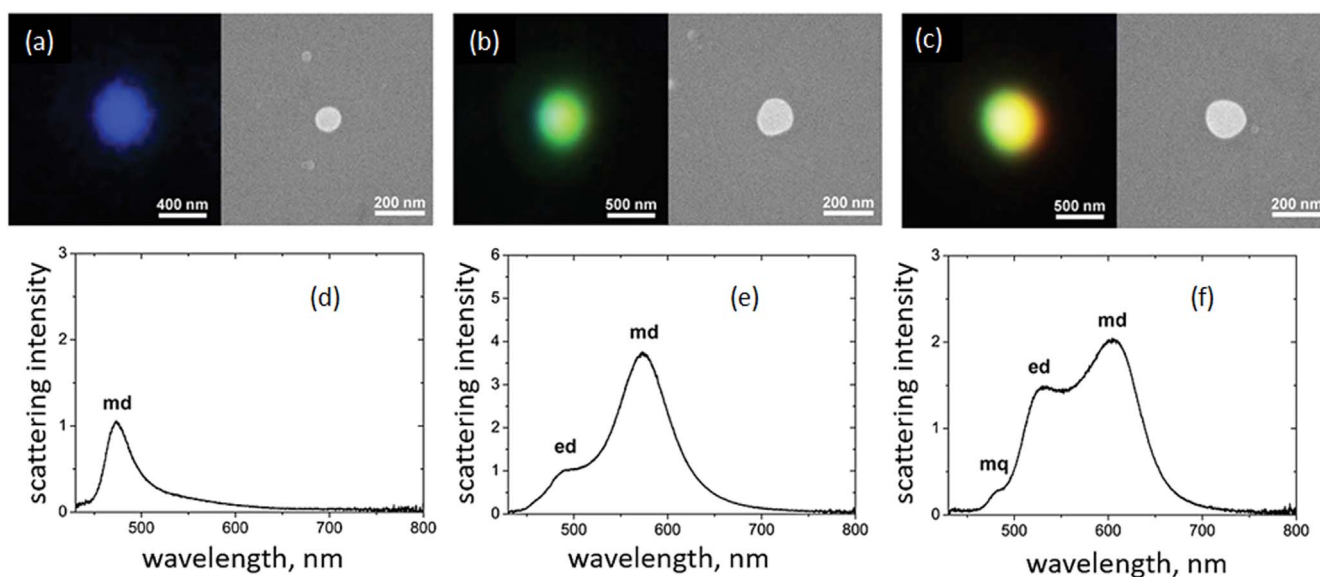


Figure 4. Illustration of Mie resonances in spherical Si nanoparticles. Dark-field microscope image (top left) and scanning electron microscope (SEM) image (top right) of spherical Si nanoparticles with (a) diameter $d = 100$ nm, (b) $d = 140$ nm, and (c) $d = 180$ nm, respectively. (d)–(f) Dark-field scattering spectra for (a), (b) and (c), respectively. Reproduced with permission from [107], © 2012, Nature Publishing Group.

proportional to the mode volume. To obtain a high Purcell factor, it is thus necessary to use a resonator with high quality factor and a nanocavity with a small mode volume.

The Purcell factor quantifies the enhancement of spontaneous emission for a perfect dipole [75]. The Purcell effect contributes to the enhancement of fluorescence and Raman scattering. These effects have been demonstrated for nanoantennas, as will be reported in the next section. For a discussion of the relationship between (theoretical) Purcell factor and (measured) fluorescence enhancement and Raman gain, see [76, 77].

3. Types of dielectric nanoantennas and their optical properties

High refractive index materials (e.g. silicon and germanium) have been used to make optical nanoantennas. These nanoantennas can have different shapes, including spheres [37–40], cylinders/disks [51, 78] and rods [63, 64]. Dielectric nanoantennas can be loosely grouped in three categories based on the number of nanoantenna elements: (i) single element nanoantennas, (ii) double element nanoantennas, and (iii) multiple elements or nanoantenna arrays. Single element nanoantennas include single nanospheres (monomers) [37–40, 79], single nanorods [63, 64] and single nanodisks [80–82]. Double element nanoantennas can consist of two dielectric nanoparticles or nanospheres (dimers) [55, 56, 83–88], two cylindrical nanodisks (nanodisk dimers) [51, 83, 89–93] or two tips as for bowtie nanoantennas [69, 71]. Multiple element or array nanoantennas are taken as any larger group of elements, such as two crossed-bowtie nanoantennas [57], Yagi-Uda nanoantennas [42, 45, 94], oligomers [95–99], and nanodisks arrays [100–102]. Figure 3

illustrates this classification of dielectric nanoantennas with their element types and schematic diagrams.

3.1. Scattering characteristics and resonances for single nanoparticles

Dielectric spherical nanoparticles with a characteristic dimension of a few hundred nanometers show unique scattering characteristics, as will be described in this section. The scattering characteristics are closely linked to the resonances of the particles. The resonances of spheres can be analytically predicted using Mie theory if the refractive index n and size parameter $q = \pi D/\lambda$ are specified [103], where D is the diameter and λ is the wavelength. Plasmonic nanoparticles usually show only electric-type resonances. Due to the absence of an EM field inside metallic nanoparticles, they do not show a magnetic response. However, both electric and magnetic resonances, known as the Mie resonances, can be observed in a dielectric spherical nanoparticle. The magnetic response is due to coupling of the incident light with circular displacement currents generated by the electric field inside the nanoparticle. This happens when the operating wavelength inside the particle becomes comparable to the particle's spatial dimensional $D = \lambda/n$. A dielectric nanosphere shows four dominant resonance modes, associated with magnetic dipole (MD), electric dipole (ED), magnetic quadrupole (MQ) and electric quadrupole (EQ) (for details see [103, 104]). Although higher-order multipoles can be excited, their contribution to scattering efficiency is considerably smaller than the magnetic dipole mode for nanoparticles, as will be shown in the next paragraph.

Theoretical investigations of electric and magnetic resonances for near-infrared (NIR) and visible wavelengths have been conducted for spherical silicon (Si) nanoparticles [105, 106]. It was demonstrated that nanoparticles with radii

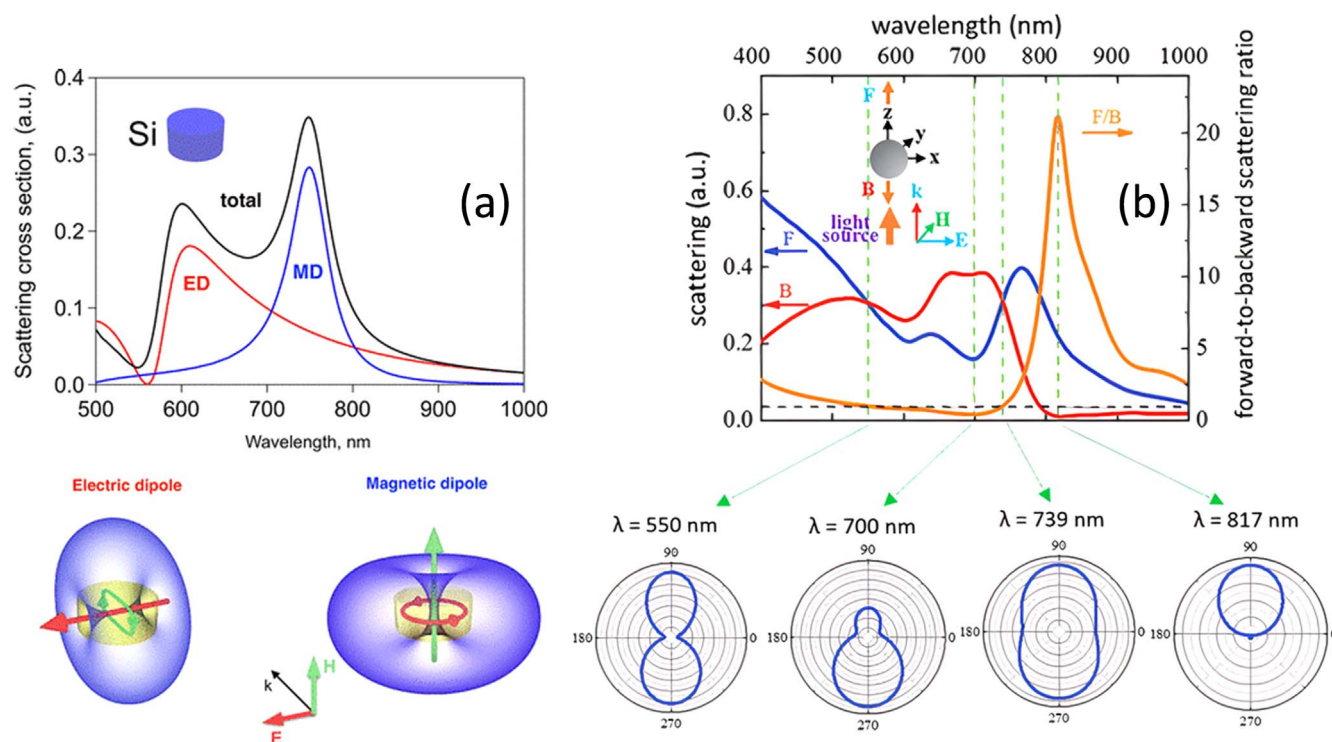


Figure 5. Scattering properties of cylindrical disk and spherical nanoparticles. (a) Numerically calculated scattering contributions for MD and ED resonances of a Si nanodisk with $h = 260$ nm and $d = 400$ nm. Schematic of the radiation patterns are shown in the bottom left. Reproduced with permission from [111], © 2017, ACS. (b) Forward and backward scattering cross-sections, and forward-to-backward scattering ratio of a spherical germanium (Ge) nanoparticle with $d = 150$ nm in free space. Far-field scattering radiation patterns at four different wavelengths are shown in bottom right. Reproduced with permission from [114], © 2017, John Wiley & Sons.

ranging from 65 to 330 nm exhibit electric and magnetic resonances. Experimentally, Mie resonances in spherical Si nanoparticles were reported for visible wavelengths in [107], and as shown in figure 4. Dark-field microscope images, figures 4(a)–(c), show magnetic dipole resonances at different wavelengths for nanoparticle sizes ranging from 100 to 200 nm. For the smallest size, the first resonance appears in the scattering spectra, which corresponds to an MD resonance (figure 4(d)). Increasing the particle size results in a red-shift of the MD resonance, and the appearance of ED (figure 4(e)) and MQ resonances (figure 4(f)). This shows the dominance of the dipole and quadrupole resonances, corresponding to the lower-order Mie resonances, for nanospheres. Mie resonances are not limited to nanospheres, but are also observed for other geometries such as cylindrical disks [108, 109] and rods [64, 110]. Mie resonances in disk-shaped nanoparticles at visible wavelengths have mostly been demonstrated in Si. Figure 5(a) shows electric and magnetic resonances in Si nanodisks with diameter and height of 400 and 260 nm, respectively [111]. As for nanospheres, in addition to the dominant MD and ED resonances, higher-order resonances can exist for larger diameter Si nanodisks, but with minor contributions to the scattering cross sections [80]. Apart from the theoretical investigations, Si nanodisks have been experimentally reported to demonstrate the Mie resonances [82, 108]. Electric and magnetic resonances of nanodisks have also been experimentally studied in other materials. Cylindrical disks of gallium arsenide (GaAs) [112] and

tellurium (Te) [113] were demonstrated at visible and mid-infrared (IR) wavelengths, respectively. Similar to nanospheres and nanodisks, dielectric nanorods can also support electric and magnetic resonances, as shown theoretically in [64] and experimentally in [110] for Si nanorods at visible wavelengths.

The coexistence and coherence of magnetic and electric dipolar resonances inside a dielectric nanoparticle can change the scattering properties and make them dependent on the phase between the magnetic and the electric dipole. Kerker *et al* [115] predicted the conditions necessary to control forward and backward scattering in dielectric particles, known as the Kerker conditions. When the electric and magnetic induced dipoles oscillate at similar magnitude and in-phase, the backward scattering can be made exactly zero (known as the first Kerker or zero backward condition). Correspondingly, near-zero forward scattering can be achieved when the induced dipoles are equal in magnitude but oscillate out-of-phase (the second Kerker or near-zero forward condition). Experimental investigations demonstrated that a dielectric sphere with a diameter of 18 nm and a refractive index of four can mimic the theoretical predictions of Kerker *et al* for microwave wavelengths [116]. Moving to the nano-range, a similar control over scattered radiation has been shown for visible wavelengths with Si nanospheres [117] and with germanium (Ge) nanospheres [114]. For a Ge nanosphere of 150 nm diameter, maximum and minimum forward-to-backward ratios of around 20 and 0.4 were achieved, as shown in

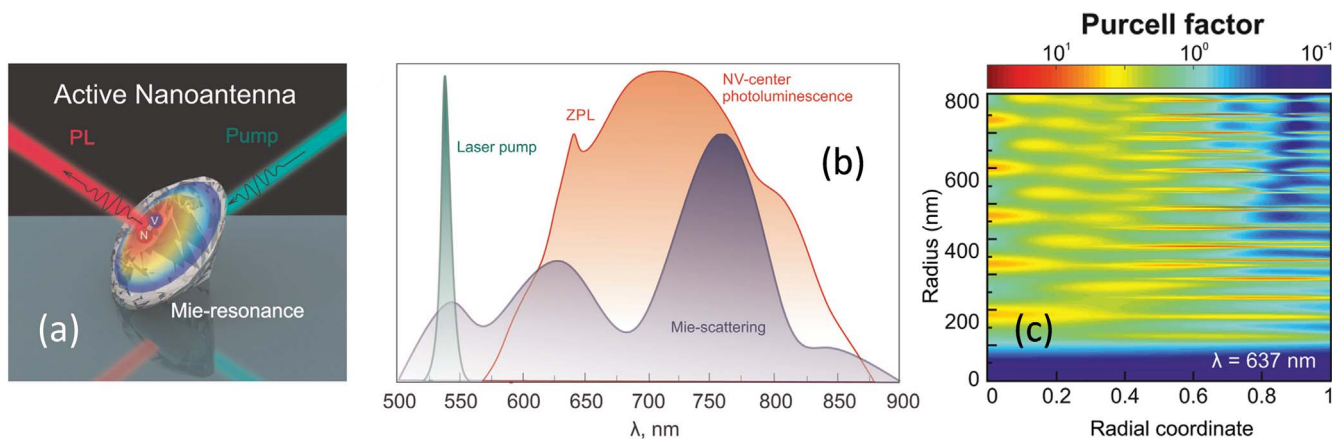


Figure 6. Purcell effect in active diamond nanoantennas. (a) Schematic of a diamond nanosphere with nitrogen vacancy (NV) centers. (b) Spectral overlap of laser pulse, NV-center photoluminescence (PL) spectrum and Mie scattering spectrum of diamond nanosphere. (c) Simulated Purcell factor as a function of radial position of NV-center along the nanosphere radius. Reproduced with permission from [124], © 2018, RSC.

figure 5(b). The scattering radiation patterns show zero backward and near-zero forward scattering at 817 and 700 nm, while an equal forward and backward scattering can be found at 550 and 739 nm, respectively (bottom of figure 5(b)). Similar forward and backward scattering patterns by Ge nanospheres have also been reported in the near-IR region [118]. Going one step further, multilayer nanospheres have been theoretically studied for simultaneously achieving zero backward and nearly-zero forward scattering [119]. As a consequence, the scattering is mainly sideways to the incoming light. Dielectric cylindrical disks can also be used for controlling scattered radiation, as realized in recent reports. Theoretical works demonstrating zero forward scattering can be found in [120, 121], while zero backward scattering was discussed in [112]. Moreover, dielectric nanorods have been investigated recently for achieving zero backward scattering [122]. Dielectric nanospheres can also be used to control the direction of scattering and provide a significant enhancement of directivity compared to the directivity of a point dipole. A Si nanosphere with a notch, and excited by a dipole placed within the notch, can induce higher-order magnetic multipoles, as shown by simulations in [38]. These multipoles contribute to increasing the directivity up to 10 times. Moreover, changing the source dipole position within the notch results in shifting the direction of the radiation, thus enabling a form of beam-steering.

Mie resonances in dielectric nanoparticles can enhance the spontaneous emission rate of an emitter, which is quantified by the Purcell factor (see section 2.4). Theoretically, a Purcell factor of 90 has been shown for a Si nanosphere (diameter 615 nm, NIR-wavelength) for a longitudinal MD excitation, while it was approximately 15 times for a transverse MD excitation [40]. A quantum emitter based on negatively charged nitrogen–vacancy (NV) centers in diamond can be used for the excitation of a Si nanosphere, giving a Purcell factor of up to 50 [123]. Recently, Purcell enhancement in an active diamond nanosphere with NV centers (figure 6(a)) has been studied through simulations and experiments [124]. By tuning the size of the diamond

nanosphere, magnetic and electric resonances can be overlapped with the pump wavelength and the photoluminescence (PL) spectrum of the NV-center (figure 6(b)). This process increases the Purcell factor due to reduction of the emission lifetime, thus enhancing the luminescence emission of NV-centers. The Purcell effect is suppressed for nanospheres with a radius of less than 150 nm and enhanced for larger nanospheres (figure 6(c)). By exciting higher-order Mie resonances in dielectric nanospheres, evanescent fields are produced, which can be utilized for enhancing the Raman signal from organic molecules attached to the nanospheres [37].

3.2. Dimers and field enhancement

The second category of nanoantennas according to figure 3 has two elements in a dimer or bowtie-configuration. A dielectric dimer consists of a pair of spherical or cylindrical nanoparticles and is a widely used configuration for nanoantennas. For dimers, our main focus will be on field enhancement, rather than on the scattering properties considered for single nanoantennas. A single dielectric nanosphere or disk can only provide low near-field enhancement [56]. In a dimer structure, the fields from two nanoparticles can interact in the gap between them, giving a significant enhancement of the near-field. Moreover, by adjusting the dimer gap, a smaller mode volume can be achieved [56, 83] than what is possible with a single nanoparticle. A metallic dimer only generates an electric hotspot when incident light is polarized along the dimer axis, as there is no magnetic hotspot for incident light polarized perpendicular to the dimer axis (figure 7(a)). On the other hand, a dielectric dimer produces both electric and magnetic hotspots in the dimer gap for incident light polarized, respectively, along and perpendicular to the dimer axis (figure 7(b)) [56].

Generation of electric and magnetic hotspots has been demonstrated for both spherical and disk dimers. A Si dimer, consisting of two nanospheres of radius 150 nm and separated by a narrow gap of 4 nm, gives nearly 30 and 13 times

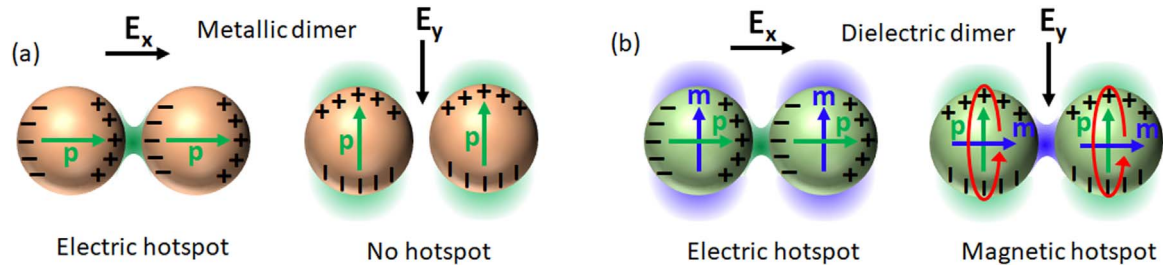


Figure 7. Comparison of hotspots generation in metallic and dielectric dimers. Electric and magnetic hotspots produced in (a) a metallic and (b) a dielectric dimer. The arrows indicate polarization direction of electric field. Here, \mathbf{p} and \mathbf{m} indicate electric and magnetic dipole moment. Reproduced with permission from [125] © 2015, ACS.

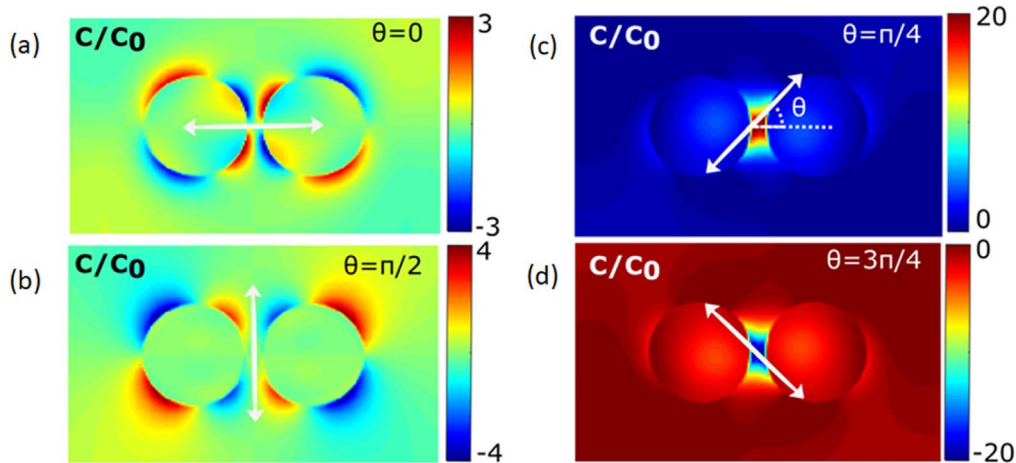


Figure 8. Enhancement of chiral density for a Si dimer for linear polarization relative to chiral density for circular polarization. For polarization (a) parallel and (b) perpendicular to the dimer axis, chiral density (and enhancement of it) is zero in the gap and low elsewhere. For off-axis polarization with (c) incident angle $\theta = \pi/4$ (d) and $3\pi/4$, the enhancement is considerable. Reproduced with permission from [78], © 2019, ACS.

enhancement of electric and magnetic fields in the center of the gap, according to simulations [56]. Field enhancement in hollow spherical Si dimers has also been simulated, showing an enhancement of ten times the magnetic near-field [126]. Electric and magnetic hotspots produced in Si cylindrical dimers were theoretically reported in [91]. Furthermore, the behavior of electric and magnetic resonances in AlGaAs nanopillar dimers has been demonstrated using simulations and cathodoluminescence imaging [127]. It was shown that coupling of adjacent nanopillars occurs due to the splitting of single pillar modes, thus generating symmetric and antisymmetric modes at different wavelengths.

Chirality is a measure of asymmetry. Two molecules are chiral if they are mirror images of each other, and the mirror images cannot be superimposed through translation or rotation. The two chiral molecules are referred to as enantiomers. Enantiomers can have very different chemical properties, making it important to distinguish between them. A difference in absorption for right- and left-handed circularly polarized light can be used to measure the chirality of a sample. A hotspot generated by a nanoantenna can increase the influence of the light–matter interaction on chirality, and thus make it easier to detect and distinguish enantiomers [57, 128, 129]. The influence of the field on chirality is given by the chiral

density of the field, $C = -\frac{\epsilon_0 \omega}{2} \text{Im}(\mathbf{E}^* \cdot \mathbf{B})$, where \mathbf{E} and \mathbf{B} are the electric and magnetic field vectors, and ω is the angular frequency.

Figure 8 shows a dimer and enhancement of the chirality of the field in the gap, for linear polarization (C) relative to the chiral density for circular polarization (C_0). For polarization along or perpendicular to the axis of the dimer, figures 8(a), (b), the field is not chiral in the gap, due to symmetry. On the other hand, for off-axis polarization, figures 8(c), (d), there is an enhancement of the chirality of up to ± 20 relative to circular polarization [78]. This shows that a dimer can be used for detection of chirality also using linear polarization, and that the sensitivity can be significantly larger than for circular polarization, which is normally used for detecting chirality. In addition to dimers, crossed-bowtie nanoantennas [57] and nanodisks with a slanted slot [130] have been demonstrated numerically for chirality enhancement.

Field enhancement and small mode volume in the dimer gap can increase fluorescence emission and Raman scattering due to the Purcell effect. The fluorescence enhancement in a dimer gap has been measured with fluorescence correlation spectroscopy, indicating that Si dimers provide somewhat higher fluorescence enhancement (around 270-fold) than Au dimers (around 200-fold) for similar configurations (figure 9(b)). Besides, a slightly

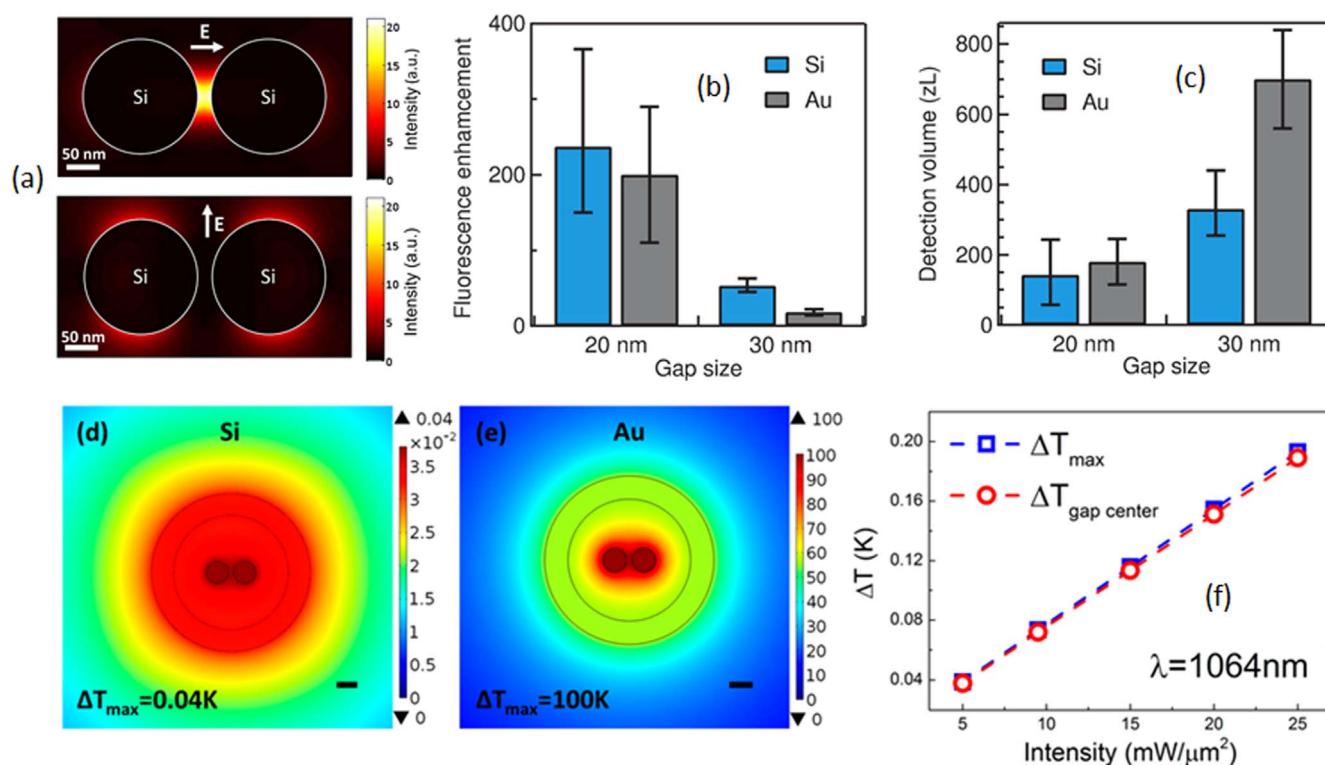


Figure 9. Comparison of fluorescence enhancement, detection volume and temperature rise for Si and Au dimers. (a) Simulated electric field enhancement in the gap of a cylindrical Si dimer with $h = 60$ nm, $g = 20$ nm and $d = 170$ nm. (b) Fluorescence enhancement for Si and Au dimers with gap of 20 and 30 nm. (c) Measured detection volume for Si and Au dimers with gap of 20 and 30 nm. Reproduced with permission from [83], © 2016, ACS. Simulated temperature increase around a (d) Si dimer and an (e) Au dimer with $d = 200$ nm, $h = 200$ nm, $g = 50$ nm and laser intensity of $5 mW/\mu m^2$. (f) Simulated temperature increase on the dimer surface (blue square) and in the dimer gap (red circle) for the Si dimer as a function of (trapping) laser intensity. Reproduced with permission from [132], © 2018, ACS.

reduced detection volume was found for the Si dimers for a 20 nm gap, and significantly reduced for a 30 nm gap, as compared to the Au dimers (figure 9(c)). Dielectric dimers enhance Raman scattering by utilizing the field enhancement in the gap. An enhancement of the Raman scattering of $\sim 10^3$ times has been demonstrated in Si dimers [32]. Additionally, surface fluorescence enhancement of ~ 1900 times was found with the same nanoantenna, and up to 3600 times with gallium phosphide (GaP) nanodisks separated by a 35 nm gap [131]. An important aspect of dielectric nanoantennas, and dielectric dimers in particular, is the low heat generation, which enables spectroscopic experiments at constant temperature. Simulation results indicate that the temperature increase around a Si dimer is very small, with a maximum of 0.04 K, while a Au dimer of similar configuration shows a dramatic temperature rise with a maximum of 100 K (figures 9(d), (e)) [32]. Moreover, increasing the laser intensity from 5 to $25 mW/\mu m^2$ results in a temperature rise from 0.04 to 0.2 K only, (figure 9(f)), thus demonstrating that high laser intensity can be used for nanoparticle trapping (which is the topic of [32]) and with dielectric nanoantennas in general.

The small mode volume and field enhancement of dimers increase the efficiency of quantum emitters and detectors. This increase is typically quantified by the Purcell factor as described in section 2.4. To complete this section, a simulation of a Si dimer is included and its Purcell factor calculated. The dimer, as proposed in [56], consists of two Si nanospheres with a radius 150 nm and separated by a gap. To find

the Purcell factor for the dimer, the quality factor must be known in addition to the mode volume. The finite-element method was used for the 3D simulations (COMSOL v.5.4). For a radius of 150 nm, the dimer shows three resonance peaks in the extinction spectra, which correspond to MD, ED and MQ resonances (see [56]). In the following, only the MD resonance is considered because it has the highest extinction efficiency and the sharpest resonance. The mode volume is calculated in air (i.e., in the dimer gap) using equation (9), and the quality factor is found from the extinction spectra as discussed in sections 2.2 and 2.3. The quality factor and mode volume as a function of the gap is shown in figure 10(a) for a plane wave with the electric field along the axis of the dimer. Enlarging the dimer gap results in a sharper MD resonance in the extinction spectrum (also shown in [56]), and consequently a higher quality factor. For a small dimer gap (e.g., 4 nm), the extinction spectrum becomes broad, showing a weak MD resonance, and thus a low quality factor. The dimer gap has a significant influence on the mode volume, with a small gap providing a tightly confined electric field in the gap (see [56]); therefore, an ultra-low mode volume. On the other hand, the electric field in the gap extends further out when the dimer gap is increased. This effect results in a significant increase in mode volume. To sum up, the quality factor is low to moderate (from 3 to 16), while the mode volume can be extremely small ($< 0.005 (\lambda/n)^3$). The Purcell factor is calculated by inserting the quality factor and mode volume in

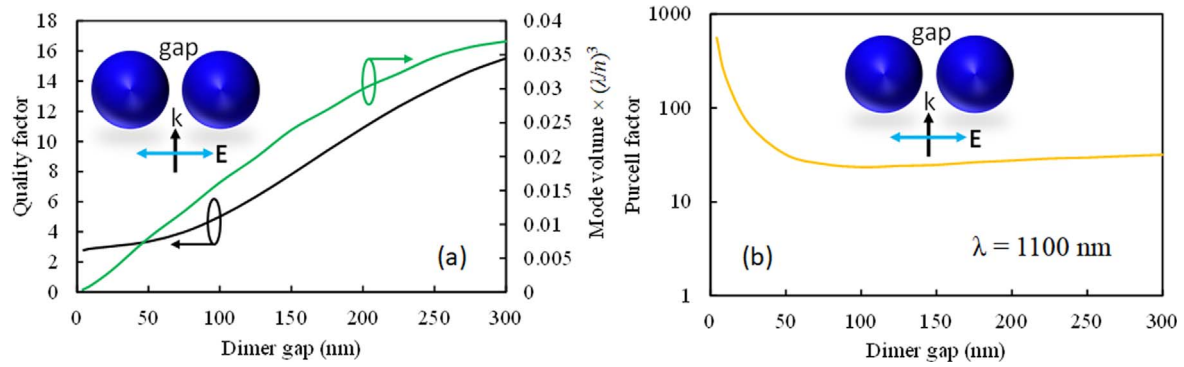


Figure 10. Simulation of a dimer to show the relationship between mode volume, quality factor and Purcell factor. The dimer consists of two Si nanospheres, radius 150 nm, separated by a gap. (a) Simulated quality-factor and mode volume as a function of dimer gap. (b) Calculated Purcell factor as a function of dimer gap at $\lambda = 1100$ nm. Schematic of the simulated dimer with excitation polarization is shown in the insets.

Table 1. Performance comparison of different dielectric nanoantennas.

Structure	λ (nm)	Enhancement factor			Purcell factor	Year	References
		Field (E/E_0)	Fluorescence	SERS			
Si disk dimer	860	5.5	2000	1000	—	2015	[32]
Si disk dimer	633	~ 4.6	270	—	~ 20	2016	[83]
Si disk dimer	633	—	470 ± 90	1720 ± 300	—	2018	[53]
GaP disk dimer	633	~ 5.5	3600	—	~ 22	2017	[131]
GaP disk dimer	532	~ 6.3	—	1000	~ 6	2019	[133]
Si particle arrays	600	—	—	—	65	2016	[134]
Si sphere	458	—	200	—	—	2017	[135]
GaP nanodisk	700	—	—	—	~ 800	2019	[136]

equation (11), as shown in figure 10(b) for $\lambda = 1100$ nm. For a gap larger than 50 nm, the Purcell factor is approximately constant around 25. As the gap decreases below 50 nm, the Purcell factor increases considerably, exceeding 200 for a gap of 10 nm.

Table 1 summarizes the performance of some dielectric nanoantennas, mostly Si and GaP disk dimers. The data is limited and the table thus sparse, as can be expected for a relatively new field. The selected performance parameters are most relevant for biological applications, e.g. fluorescence and Raman-spectroscopy. Therefore, the results are for visible and near-visible wavelengths. The comparison shows that disk dimers are the most widely implemented structures for fluorescence and SERS enhancement. Field enhancement in dimer gap depends mainly on physical separation between nanoparticles, operating wavelength and refractive index of the material. The results listed in the table have different values for these parameters, thus showing different field enhancements. Fluorescence enhancement in a dimer gap is due to increased radiative emission rates. A high absorption coefficient can make a route for nonradiative decay channels, which limits the fluorescence enhancement. The absorption coefficient of GaP is one order of magnitude smaller than that of Si [131] for 633 nm, giving a negligible contribution of nonradiative decay channels. Therefore, GaP dimers provide higher fluorescence enhancement than Si dimers, as shown in table 1.

3.3. Scattering characteristics of dimers and multiple element nanoantennas

Scattering from collections of nanoparticles and arrays is a large topic and only Fano resonance and Yagi-Uda nanoantennas will be considered here. For a general treatment of scattering by small particles, see e.g. [66, 67]. Arrays of nanoantennas are considered and demonstrated in [93, 100, 102, 137].

A resonance dip found in the scattering spectrum due to the destructive interference of broad and narrow spectral lines, is known as a Fano resonance. This unique dip is sensitive to the surroundings, and can thus be used for sensing applications [138]. One way to achieve Fano resonances is the use of complex oligomer structures [99]. However, simple configurations such as Si nanoparticle dimers can also be implemented for generating a Fano resonance. When two Si nanoparticles are in close proximity, coupling between ED resonances of the two nanoparticles produces a spectrally broadened mode, while two MD resonances produce a narrow mode (figure 11(a)). Therefore, the interaction of the broad electric and the narrow magnetic modes produces a dip, i.e. a Fano resonance in the backward scattering spectrum (figure 11(b)). The Fano resonances are modified when the diameter of the two Si nanoparticles is different. Simulation and measurement of a heterodimer with diameters of 115.2 and 129.8 nm shows two Fano resonances at 511 and 592 nm, respectively (figures 11(d), (e)). Fano resonances have been

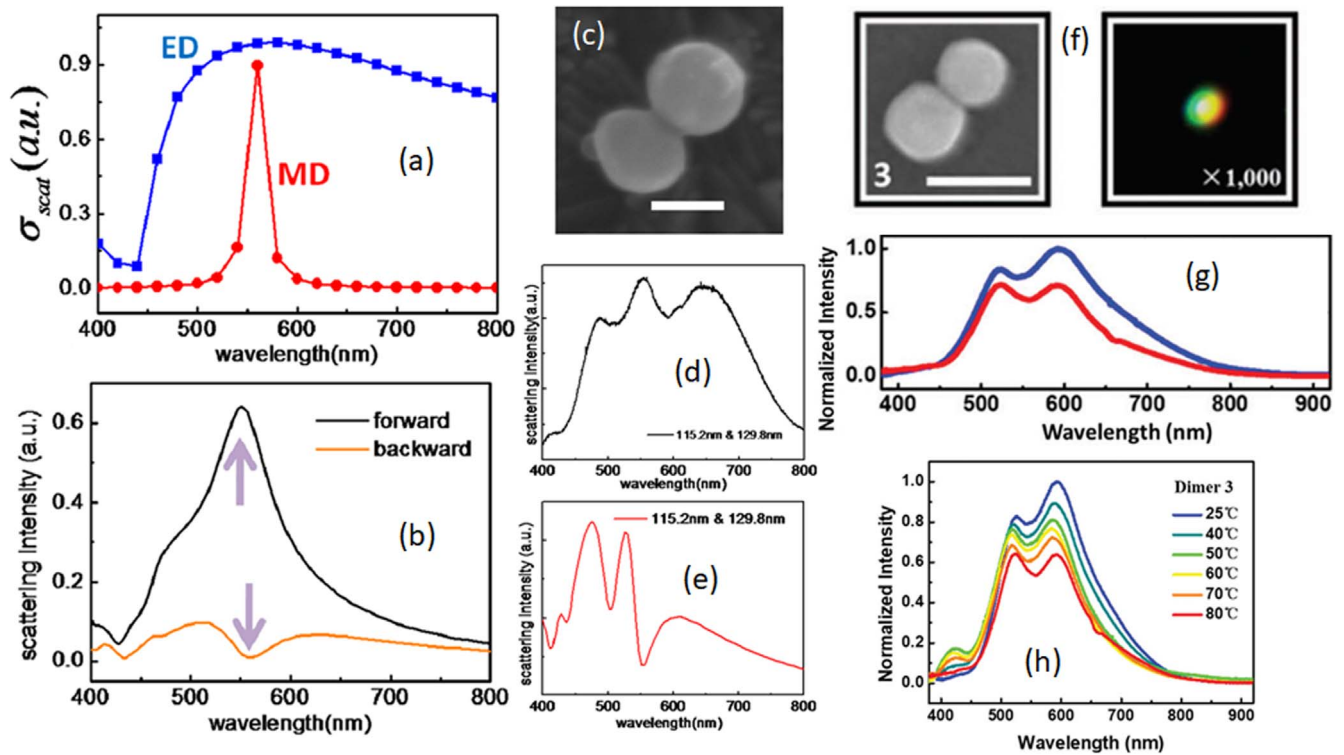


Figure 11. Fano resonances in dielectric dimers. (a) Simulated broad ED resonance and narrow MD resonance in a spherical homodimer with diameter of 130 nm. (b) Simulated forward and backward scattering cross-sections of the homodimer. (c) SEM image of the fabricated heterodimer with diameter of 115.2 and 129.8 nm. Backward scattering spectra found in (d) experiments and (e) numerical simulations. Reproduced with permission from [86], © 2015, ACS. (f) SEM and dark-field image of a dimer with diameter of 137.5 and 150.8 nm. (g) Experimental backward scattering intensity spectra obtained from the dimer deposited on a vanadium dioxide (VO_2) with an aluminum dioxide (Al_2O_3) substrate at 25 °C (violet curve) and 80 °C (red curve). (h) Continuous tuning of the Fano resonance by increasing temperature of the substrate. Reproduced with permission from [139], © 2019, RSC.

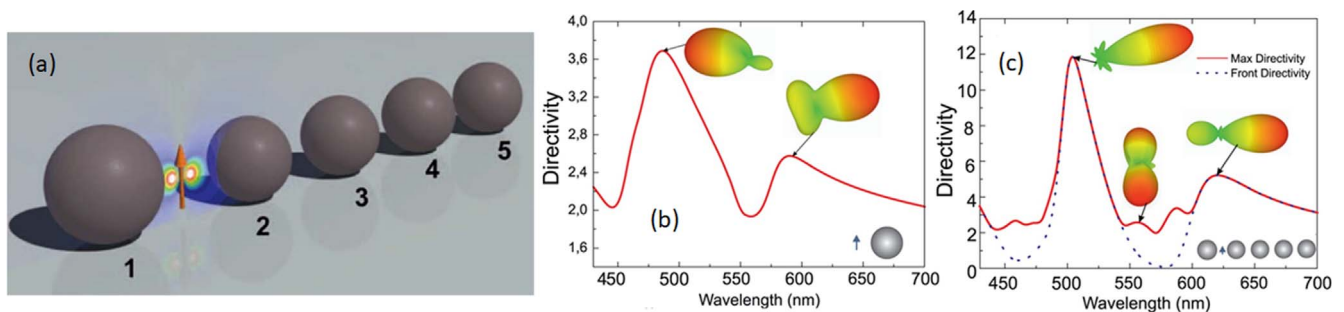


Figure 12. Yagi-Uda nanoantenna. (a) Schematic of a Si Yagi-Uda nanoantenna having a reflector with radius $R_r = 75$ nm, directors with radii $R_d = 70$ nm and excited by a point dipole. Comparison of directivity spectra for (b) a Si nanoparticle and (c) a Yagi-Uda nanoantenna. 3D radiation patterns at selected wavelengths are shown in the insets. Reproduced with permission from [44], © 2012, OSA.

demonstrated for visible wavelengths using Si dimers on a vanadium dioxide (VO_2) layer with an aluminum dioxide (Al_2O_3) substrate (figures 11(f), (g)) [139]. The resonance dips can be tuned by changing the phase transition of VO_2 , which is dependent on temperature (figure 11(h)). Conversely, the temperature sensitivity makes it possible to use the nanostructure as a temperature sensor. Apart from the spherical dimers, Fano resonances have been studied recently in nanoblock dimers [140].

As discussed earlier, the radiation pattern of a single Si nanoparticle can be switched from the backward to the forward direction by the Kerker effect. However, it shows low

directivity in the visible spectrum (figure 12(b)). The idea of using Yagi-Uda nanoantenna arrays (figure 12(a)) made of silicon nanoparticles, was first theoretically proposed in [44]. It was numerically shown that such nanoantennas can significantly enhance the directivity compared to a single nanoparticle (figure 12(c)). Moreover, the simulations showed enhanced radiation efficiency and a higher Purcell factor compared to an Au Yagi-Uda nanoantenna. Experimentally, a Si Yagi-Uda antenna has been demonstrated for microwave frequencies [42]. For visible wavelengths, enhanced directivity has been demonstrated using a square array of Si nanodisks [100]. Recently, arrays of gallium arsenide (GaAs)

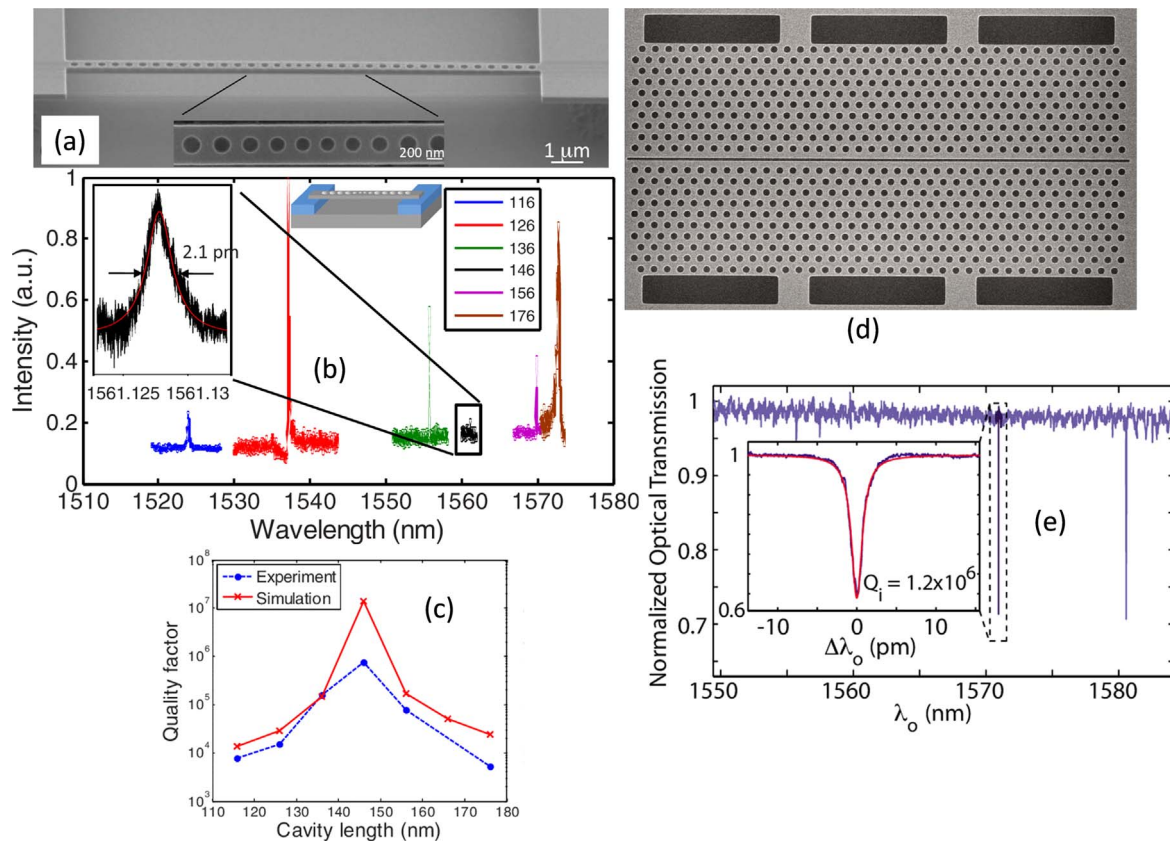


Figure 13. Optical microresonators. (a) SEM image of a fabricated photonic crystal nanobeam cavity. (b) Resonant scattering spectra for different cavity length. (c) Comparison of simulated and experimental quality-factor. Reproduced with permission from [146], © 2009, AIP. (d) SEM image of a fabricated two-dimensional slotted photonic crystal cavity. (e) Normalized optical transmission indicating the first and second order optical cavity modes. Quality-factor of the first order mode is shown in the inset. Reproduced with permission from [147], © 2010, AIP.

nanopillars have been experimentally studied for controlling the direction of emitted light, thus providing a new route for low-loss and directional lasing [93].

4. Combining dielectric optical nanoantennas and microresonators

Optical microresonators have been investigated extensively in the literature. Compared to optical nanoantennas, they provide much higher quality-factor, but at the cost of larger mode volume. A combination of microresonators and nanoantennas may thus be the ultimate combination, providing high quality-factor and small mode volume simultaneously. In this section, some recent results combining microresonators and nanoantennas will be reviewed.

Microsphere resonators have exceptionally high quality-factors, possibly the highest of any passive resonators, i.e. without amplification. As an example, a microsphere of fused silica has been demonstrated with a quality factor of 8×10^9 [141]. In addition to microspheres, a number of other designs for optical microresonators have been studied, e.g. microdisks, micropillars, microtoroids, Fabry–Perot microcavities and photonic crystal microcavities. For reviews of optical microresonators, see [74, 142, 143]. The mode volume of a

microsphere is typically $10^3 \times (\lambda/n)^3$ [144]. Some other designs give smaller mode volume at the cost of reduced quality-factor. One example of this is a micropillar cavity made by two distributed Bragg mirrors, with a reported quality factor and mode volume of 3×10^6 and $0.1 \times (\lambda/n)^3$, respectively [145]. Furthermore, various photonic crystal structures have achieved moderate to high quality-factors, combined with the smallest mode volume among all microresonators. Using a one-dimensional photonic crystal nanobeam cavity in Si (shown in figure 13(a)), a quality factor of 1.4×10^7 and a mode volume of $0.39 \times (\lambda/n)^3$ were demonstrated theoretically [146]. The reported experimental quality-factor was 7.5×10^5 measured from the scattered light (shown in figure 13(c)). A two-dimensional photonic crystal cavity has been experimentally reported using a slotted structure (SEM image is shown in figure 13(d)) [147]. The measured quality-factor and simulated mode volume for the cavity were 1.2×10^6 (shown in figure 13(e)) and $0.04 \times (\lambda)^3$, respectively. The mode volume is thus comparable to that of a Si dimer (see figure 10(a)), with a significantly higher quality factor. The calculated Purcell factor is $\sim 2.3 \times 10^6$, compared to maximum a few hundred for the Si dimer. The 2D photonic crystal cavity thus outperforms the Si dimer before taking special measures.

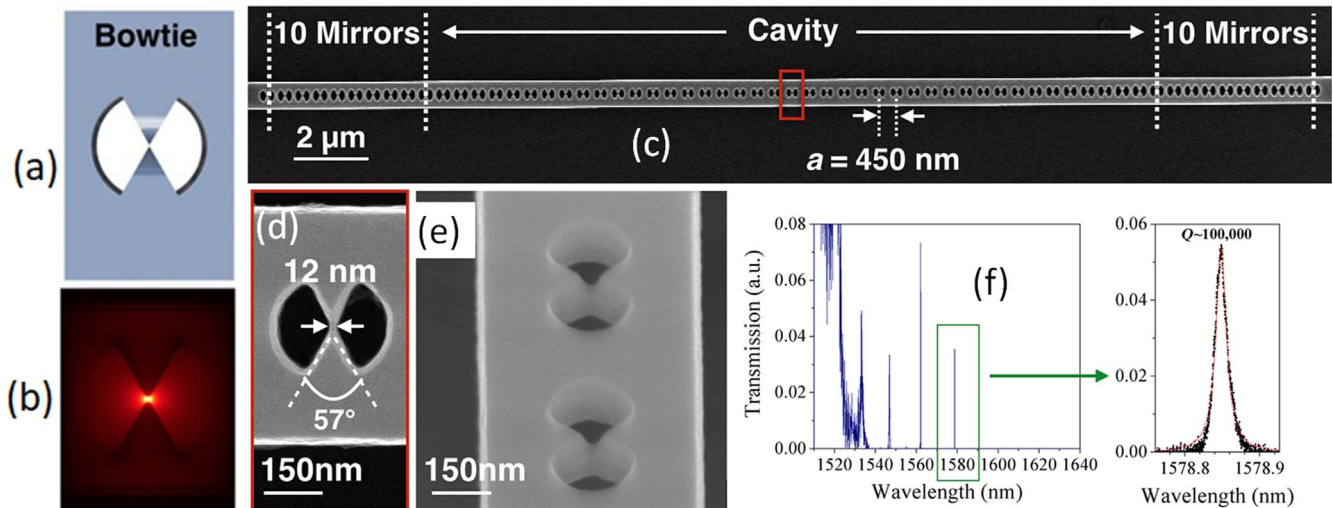


Figure 14. Photonic crystal Si nanobeam waveguide with bowtie unit cell. (a) Schematic of the bowtie unit cell, with (b) electric energy profile. SEM images of the fabricated (c) photonic crystal cavity, (d) enlarged view of a bowtie unit cell, and (e) tilted view of the bowtie showing the partial etching. (f) Experimental transmission spectra showing optical cavity modes, with enlarged view of the fundamental mode. Reprinted/adapted from [69]. © The Authors, some rights reserved; exclusive licensee American Association for the Advancement of Science. Distributed under a Creative Commons Attribution NonCommercial License 4.0 (CC BY-NC).

Microspheres have been combined with plasmonic nanoantennas [148–150]. In principle, several of the microresonator-designs can be combined with dielectric optical nanoantennas. Adding a nanoantenna to a microresonator will increase the loss if the nanoantenna is not perfectly matched to the mode of the microresonator, even if the nanoantenna does not have intrinsic losses. Perfect mode-matching is difficult to achieve for most microresonator-designs. As an example, fixing a Si dimer to the surface of a microsphere will give scattering and thus reduce the quality-factor of the microsphere. For waveguide ring resonators, an adiabatic transition to a nanoantenna etched into the waveguide core can be imagined. Going one step further, it has been proposed to embed a bowtie antenna in the unit cell of a photonic crystal waveguide [71]. This can give extreme light concentration at the bowtie tip as shown in figure 14(b) and thus provides an ultra-low mode volume. According to simulations, the bowtie unit cell provides 80 times enhancement of the peak electric field amplitude compared to a traditional circular unit cell [69]. The proposed design has been made and experimentally validated by S Hu *et al* [69], which is shown in figures 14(c)–(f). Note the small dimensions of the bowtie unit cell, with a minimum width of 12 nm (figure 14(d)). As the gap in the bowtie is not completely etched away (figure 14(e)), the mode volume is further reduced. The measured quality-factor was $\sim 10^5$, with a (simulated) mode volume of $10^{-3} \times (\lambda/n)^3$. This combination gives a Purcell factor of $\sim 8 \times 10^6$.

The combination of nanoantennas with resonators can thus give extremely high Purcell factors. This may result in significant improvements for applications such as optical trapping, as predicted in [151]. The combination may also find other applications, e.g. for single-molecule fluorescence and Raman-spectroscopy of nanoparticles. However, the wavelength of the emitter (or absorber) must be closely

matched to the resonance wavelength of the resonator. Also, the combination is suitable for one or a few nanoantennas, as opposed to single nanospheres, which can easily be multiplied to very large numbers. Combining nanoantennas and microresonators thus give very interesting results for applications where the wavelength can be adapted to the resonator and where a limited number of nanoantennas is required.

5. Applications of dielectric nanoantennas

Optical nanoantennas can be utilized in various applications including optical trapping [83, 132, 152], spectroscopy [31, 32, 131, 135], photovoltaics [153], directional lasing [93], nonlinear signal conversion [154–160] and optical sensing [161, 162]. A few of them have already been employed as operational devices (e.g. on-chip biosensing [101]), while others are expected to be implemented in devices soon (e.g. directional lasing [93]). In this section, we will discuss a few emerging applications.

5.1. Optical trapping

The application of dielectric optical nanoantennas to optical trapping is highly promising. The main reasons are low local heating and strong electric and magnetic resonances. Conventional optical tweezers can trap micrometer-sized particles by using the optical forces exerted from highly focused laser beams [163]. Their application to trapping of nanoparticles is limited because the trapping relies on the gradient force, which scales with the volume of the particle [164]. As lenses are used in the trapping system, the focal spot and thus the gradient forces are limited by the diffraction limit. Therefore, there is a lower limit for the size of a particle that can be trapped, depending on its refractive index, input power, and to some extent the shape of the particle. Dielectric nanoantennas

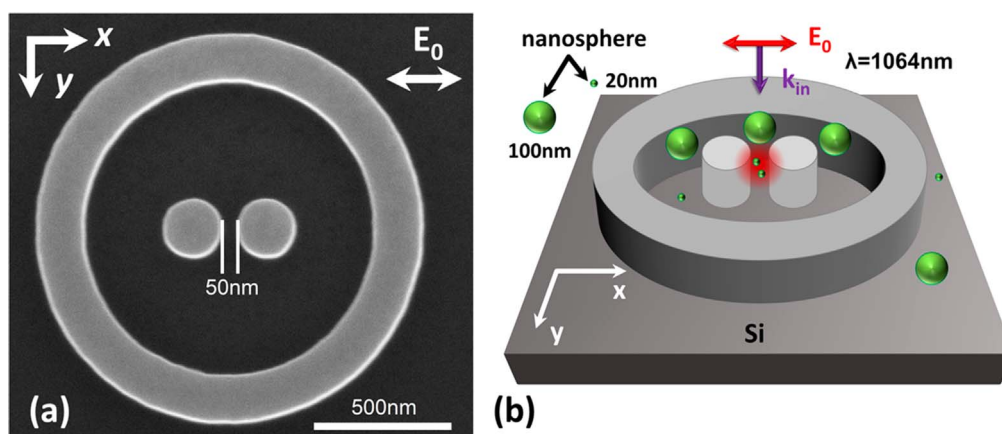


Figure 15. Si dimers for nanoparticle trapping. (a) SEM image of the fabricated silicon optical nanoantenna placed on a silicon substrate (top view) (b) Schematic of the optical trapping of nanospheres of diameter 20, while 100 nm nanospheres are not trapped. Reproduced with permission from [132], © 2018, ACS.

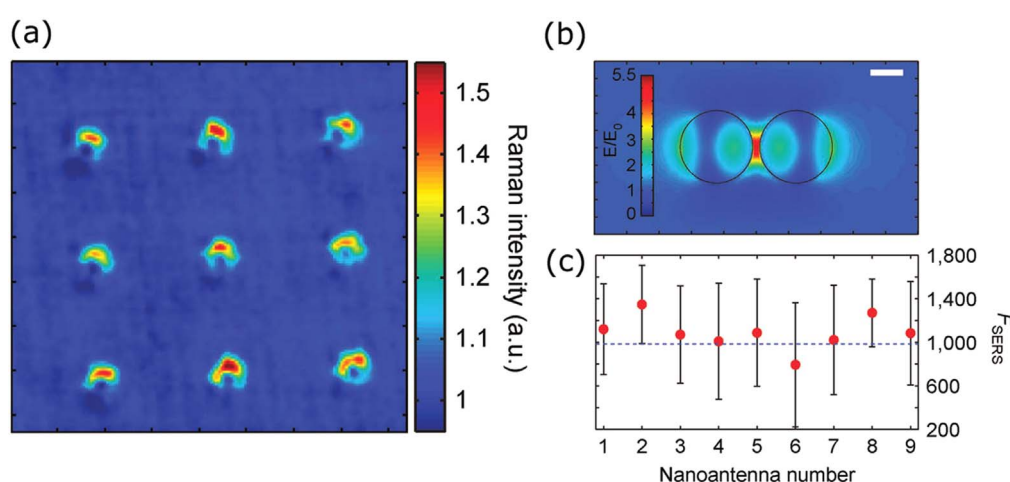


Figure 16. Surface-enhanced Raman scattering with silicon dimers. (a) Map of measured Raman-intensity for nine similar silicon dimers. (b) Simulated electric field enhancement for 20 nm gap between the silicon disks, and (c) SERS enhancement factors for the nine nanoantennas and the expected value (dotted line). Reproduced with permission from [32], © 2015, Nature Publishing Group.

can provide an effective solution to overcome this limit. Similarly to plasmonic nanoantennas, dielectric nanoantennas can be used to confine light to sub-wavelength mode volumes and thus enhance the gradient forces. This can be used for stable trapping of nanoparticles with low optical power. As dielectric nanoantennas produce less Joule heating than plasmonic ones, there is less thermally induced flow around the nanoantenna, which can push particles away. Also, avoiding heating is particularly important for some biological applications [165]. Recently, silicon optical nanoantennas have been reported for trapping of polystyrene nanospheres [132]. The authors used a pair of silicon nanocylinders having a gap of 50 nm and were able to trap multiple nanospheres with diameters of 20 nm (see figure 15). A single streptavidin-coated CdSe/ZnS quantum dot was trapped with similar dielectric nanoantennas in [152].

5.2. Surface-enhanced spectroscopy and fluorescence

Two other emerging applications of dielectric nanoantennas are surface-enhanced Raman spectroscopy (SERS) [32, 166, 167]

and surface-enhanced fluorescence emission [32, 131]. As for optical trapping, nanoantennas improve the light–matter interactions through tightly localizing the optical field. This increases the Purcell factor and improves excitation rates [40], which translates into larger Raman-scattering and increased fluorescence from material in the nanocavity. Due to less local heating, high Purcell factors, and improvement of the radiative decay rate, single-molecule sensitivity has been demonstrated with dielectric nanoantennas, as for plasmonic nanoantennas [83]. It has been shown that silicon nanoantennas provide better quantum efficiency than the plasmonic nanoantennas [56]. Dielectric dimer nanoantennas were used in [32] for producing surface-enhanced fluorescence and SERS. The measured Raman-intensity is shown in figure 16(a), where nine similar silicon dimers were demonstrated. Due to the enhancement of the near-field (figure 16(b)), the dimer nanoantennas showed an increase in the Raman scattering by a factor of 1000 (figure 16(c)).

Dielectric nanoantennas are free from quenching and charge carriers [165]. An emitter, in nanometer proximity of a

plasmonic structure, can be quenched due to nonradiative decay channels. This can be avoided by using dielectric spacers for plasmonic structures, while for dielectric nanoantennas, the problem is avoided entirely. This is a key benefit for dielectric nanoantennas as opposed to plasmonic nanoantennas. Using single silicon dielectric nanospheres, the fluorescence signal from a dye has been enhanced 200 times without a dielectric spacer [135]. Using a silicon dimer with a gap of 20 nm, 270-fold enhancement of a fluorescence signal has been demonstrated [131]. In another work on gallium phosphide (GaP) dimers [83], the authors reported 3600 times enhancement of the fluorescence signal.

5.3. Nonlinear photonics

Dielectric nanoantennas have gained attention for increasing photon–photon interactions. They are considered building blocks for exploring nonlinear effects because of low losses and the coexistence of both electric and magnetic resonances [154]. This is in contrast to plasmonic nanoantennas, which are dominated by electric resonances. Nonlinear optical effects can have very different properties depending on whether their origin is magnetic or electric. When the electric and magnetic resonances are mixed, nonlinear properties change considerably. This leads to new applications in nanophotonics such as nonlinear mode-mixing [168]. Recently, nonlinear effects have been studied, including second-harmonic generation (SHG) [155, 157, 160] and third-harmonic generation (THG) [154, 156, 158, 169], using dielectric nanoantennas. Such nonlinear effects find important applications in bioimaging and biosensing [170, 171]. Unfortunately, silicon nanoantennas for nonlinear effects are of limited use for optical communications, due to two-photon absorption. A practical solution is to use III-V materials, e.g. AlGaAs, which can be made transparent in the visible range. Thus, two-photon absorption is avoided and the materials are suitable for investigating nonlinear effects such as SHG. SHG based on AlGaAs nanodisks has been reported in [155, 160]. Additionally, germanium nanodisks have been explored for THG [154].

5.4. Solar cells

High-efficiency solar cells are required for sustainable and environmentally-friendly energy production. One of the key strategies to improve the efficiency of solar cells is to increase the solar absorption by light trapping [153]. Several nanoantenna structures have been demonstrated [153, 172, 173] for this application. An one dimensional (1D) dielectric core–shell nanoantennas made of absorbing amorphous silicon and nonabsorbing ZnO and Si₃N₄ have been reported to enhance the solar absorption [153]. Moreover, Si nanowires coated with dielectric shells and nanocrystalline Si nanoshells were also explored for enhanced light absorption [173, 174]. Additionally, submicron spherical Si arrays and Ge nanopillar arrays have been demonstrated for enhancement of the solar absorption [172, 175].

6. Dielectric materials and fabrication technologies

To obtain tight confinement of light in a nanoantenna, the material must have a high refractive index. The material should also have moderate or low losses from absorption, and preferably a low cost. As the size of the device is small, higher losses and cost can be accepted than for larger devices, e.g. a waveguide crossing a cm size chip. An extinction coefficient $k = 0.01$ can be used to demonstrate this difference. For a nanoantenna with dimensions similar to the wavelength (e.g. $\lambda_0 = 1 \mu\text{m}$), $k = 0.01$ corresponds to ~ 0.5 dB propagation loss, which might be an acceptable value. However, if the loss is due to absorption, the nanoantenna might heat up for a modest input power, and one of the main advantages of dielectrics over plasmonics is thus lost. Also, if the nanoantenna is to be combined with a resonator, the losses for the resonator material must be very low to get a high quality-factor. This can be done by combining two materials, a low-loss material for the resonator and a material with high refractive index for the nanoantenna. As losses depend on the wavelength, the choice of material depends on the wavelength required for the application. Finally, the availability of a suitable fabrication method can influence the choice of material for a nanoantenna.

Table 2 lists some relevant materials and includes both dielectrics and semiconductors. The properties of the materials depend strongly on wavelength, particularly close to absorption edges, and also depend on the fabrication method. Impurities can increase the extinction coefficient significantly and a porous structure can have a lower refractive index than a dense one. Values for the wavelength range are set to match the given (maximum) extinction coefficients. The values for the extinction coefficient are in several cases indicated as zero ($k \sim 0$), showing that the value is limited by the measurement range rather than the material. Some of the listed values have been measured for bulk materials and some are from models, and the values should thus be treated critically when used for designing nanostructures.

Silicon is a widely-used semiconductor material with low cost and mature fabrication technology [187]. It has a high refractive index and is very suitable for nanoantennas in the near-infrared, e.g. for telecommunications, and most of the examples in this review are on silicon nanoantennas. For biological applications, e.g. surface-enhanced Raman spectroscopy and fluorescence, visible light is mostly used. As silicon is partially absorbing for visible wavelengths, it can be used for small structures, i.e. the nanoantenna itself, operating in the visible. Some amorphous materials are transparent in the visible and have a moderately high refractive index, notably SiN/Si₃N₄, Ta₂O₅ and TiO₂. Amorphous materials can be deposited with common deposition methods, e.g. low pressure and plasma-enhanced chemical vapor deposition (LPCVD and PECVD), magnetron sputtering and atomic layer deposition. As the deposition is typically done on top of a silicon wafer, the cost is low compared to materials that need a crystalline wafer of the same material-type. For higher refractive index, a few crystalline semiconductor materials are transparent in the visible/NIR-range, e.g.

Table 2. Some relevant dielectric and semiconductor materials for optical nanoantennas. Most values have been accessed through [176].

Material	Spectral range (μm)	Refractive index (n)	Extinction coefficient (k)	References
TiO ₂	0.4–1.7	2.34–2.05	~ 0	[177]
Ta ₂ O ₅	0.5–1.8	2.2–2.1	~ 0	[178]
Si ₃ N ₄	0.5–2.5	2.1–2	~ 0	[179]
c-Si	0.5–1.1	4.3–3.5	$0.049\text{--}3 \times 10^{-5}$	[180]
	1.1–8.3	3.5–3.4	$< 3 \times 10^{-5}$	[181]
SiC	1–7.5	3.3–2.9	< 0.1	[182]
AlGaAs	0.75–12	3.6–3	< 0.02	[183, 184]
Ge	1.1–1.8	4.3–4.1	< 0.01	[185]
	1.8–11	4.1–4	~ 0	[185]
GaSb	1.5–12	4–3.7	< 0.1	[184]
Te	1.6–2	4.5–4.3	< 0.1	[186]
GaP	0.5–12	3.6–3.1	< 0.01	[184]

AlGaAs and GaP. For high refractive index in the mid- and far-IR, germanium, antimonides, tellurides, and silicon carbide are attractive and have low extinction coefficient. The cost would be high for a large wafer with these materials, but a wafer can contain a very large number of nanoantennas. Thus, the cost can be acceptable and even low for highly efficient devices, e.g. consisting of a few nanowires or nanospheres. For devices that can be separated from the crystalline wafer used for fabrication, hybrid integration on a silicon wafer with other optical devices is an option.

Fabrication techniques for optical nanoantennas include methods for thin-film deposition and patterning [188], growth of nanowires [189], and chemical methods for synthesis of nanoparticles [190]. A review of materials and fabrication methods for dielectric nanophotonics can be found in [1]. The choice of method is directly linked to the choice of material, and adapting and optimizing a technique for a new material can be a significant task. Passing from the research-stage to making components in a foundry is a big leap, and here silicon photonics has a large advantage. There are several foundries that make silicon photonics and compatible materials, e.g. S₃N₄ [191–194]. For nanoantennas made with non-standard materials, nanowires and nanoparticles, hybrid integration with silicon photonic circuits can be an alternative, as it is for quantum photonics [195]. Solar cells are an important, large-scale application of optical nanoantennas. Fabrication challenges and cost-issues are, due to the scale, very different from applications that focus on one or a few components, with a finite number of nanoantennas.

7. Discussion and outlook

This review provides a brief overview of recent advances regarding dielectric optical nanoantennas. It presents a broad classification based on the structural configuration of the nanoantennas and provides a review of selected works in each category. As an example, original simulation results are included for a spherical silicon dimer, quantifying parameters that are relevant for optical nanoantennas, such as mode volume, quality factor, and Purcell factor. The example shows



that the nanoantenna has a very small mode volume, but on its own it has a modest quality factor. This is a typical feature of optical nanoantennas as it is difficult to make a nano-size cavity with high quality-factor. There are a number of options for making high quality-factor optical resonators, both microresonators and larger, e.g. waveguide resonators. By combining nanoantennas with resonators, both very small mode volume and very high quality-factor can be obtained, as recently demonstrated [69]. The combination of dielectric optical nanoantennas and high quality-factor resonators is very promising, with performance set to improve and applications multiply in the future.

Low heat generation is one of the main advantages of dielectric optical nanoantennas, as compared to plasmonics. This is particularly important for applications with high power or when a nanoantenna is combined with a resonator, and also for some biological applications where temperature must be kept stable. Whereas plasmonics has established methods and designs to handle heating, the focus for dielectrics has mostly been on reducing dissipative loss in the materials. There are thus lessons to be learned from plasmonics, as for other topics related to the functioning of optical nanoantennas. Scattering losses are less important for nanostructures as they will not accumulate over a long structure, which is the case for e.g. optical waveguides. However, scattering and unintended hotspots might compromise the intended function of the nanoantenna and making perfectly smooth surfaces is a challenge. Whereas characterization of smoothness can readily be done with profilers and atomic force microscopes on the wafer- and chip-level, it is far from trivial to do the same for nanoantennas that have features in the nm range, and that can be very thin or have a spherical shape.

Silicon is dominating the field of dielectric nanoantennas, as can be expected from its excellent optical, thermal and mechanical properties, and its mature fabrication technology inherited from microelectronics. For near- to mid-IR, Si is highly transparent and has a high refractive index. For biological applications, e.g. Raman spectroscopy and fluorescence, visible wavelengths are preferable. Here, silicon has a disadvantage due to some absorption. Thus, other materials

can be good alternatives, both amorphous dielectrics (e.g. SiN, Ta₂O₅, TiO₂) with a lower refractive index, and other semiconductors (e.g. GaP, AlGaAs). Biology will probably be a major application for optical nanoantennas in the future, and many optical functions can be imagined, e.g. various types of super-resolution microscopy with nanoantennas. Thus, there is a need for new materials with a high refractive index and new designs of optical nanoantennas, suitable for biological applications in the visible range. The UV range has not been considered in this review. It is currently attracting attention, e.g. for nonlinear optics [196], and as the wavelength gets shorter, it might give an even smaller mode volume than for the visible range. For wavelengths approaching the UV-absorption edge of a material, the increased loss is accompanied by an increase in the refractive index. A compromise between refractive index and loss must thus be made, which can work well for nanoantennas. There is a limited number of suitable materials for the UV range, and new materials might become available if the interest increases. For existing materials, improving the purity, fabrication methods and characterization will be beneficial for the scientific community and for all wavelength ranges. The combination of optical functions, e.g. nanoantennas and microresonators, and further combination with nonoptical functions, e.g. microfluidics, thermal control and electric circuits, all on one chip, can open entirely new applications. Hybrid integration with detectors, lasers and other sources, is also of great interest, and can lead to highly efficient and cost-effective nanophotonic systems.

ORCID iDs

Md Rabiul Hasan  <https://orcid.org/0000-0002-9538-454X>
Olav Gaute Hellesø  <https://orcid.org/0000-0002-0494-8240>

References

- [1] Baranov D G *et al* 2017 All-dielectric nanophotonics: the quest for better materials and fabrication techniques *Optica* **4** 814–25
- [2] Kang J-H *et al* 2011 Low-power nano-optical vortex trapping via plasmonic diabolite nanoantennas *Nat. Commun.* **2** 582
- [3] Righini M *et al* 2009 Nano-optical trapping of Rayleigh particles and *Escherichia coli* bacteria with resonant optical antennas *Nano Lett.* **9** 3387–91
- [4] Roxworthy B J *et al* 2012 Application of plasmonic bowtie nanoantenna arrays for optical trapping, stacking, and sorting *Nano Lett.* **12** 796–801
- [5] Law S *et al* 2013 All-semiconductor plasmonic nanoantennas for infrared sensing *Nano Lett.* **13** 4569–74
- [6] Liu N *et al* 2011 Nanoantenna-enhanced gas sensing in a single tailored nanofocus *Nat. Mater.* **10** 631–6
- [7] Tittel A *et al* 2012 Spectral shifts in optical nanoantenna-enhanced hydrogen sensors *Opt. Mater. Express* **2** 111–8
- [8] Zundel L and Manjavacas A 2017 Spatially resolved optical sensing using graphene nanodisk arrays *ACS Photonics* **4** 1831–8
- [9] Pfeiffer M *et al* 2014 Eleven nanometer alignment precision of a plasmonic nanoantenna with a self-assembled GaAs quantum dot *Nano Lett.* **14** 197–201
- [10] Ridolfo A *et al* 2010 Quantum plasmonics with quantum dot-metal nanoparticle molecules: influence of the Fano effect on photon statistics *Phys. Rev. Lett.* **105** 263601
- [11] Hou J *et al* 2014 Dissipation-driven entanglement between qubits mediated by plasmonic nanoantennas *Phys. Rev. B* **89** 235413
- [12] Alù A and Engheta N 2010 Wireless at the nanoscale: optical interconnects using matched nanoantennas *Phys. Rev. Lett.* **104** 213902
- [13] Ahmed A and Gordon R 2011 Directivity enhanced Raman spectroscopy using nanoantennas *Nano Lett.* **11** 1800–3
- [14] Neubrech F *et al* 2017 Surface-enhanced infrared spectroscopy using resonant nanoantennas *Chem. Rev.* **117** 5110–45
- [15] Pucci A *et al* 2010 Surface enhanced infrared spectroscopy using gold nanoantennas *Phys. Status Solidi (B)* **247** 2071–4
- [16] D'Andrea C *et al* 2013 Optical nanoantennas for multiband surface-enhanced infrared and Raman spectroscopy *ACS Nano* **7** 3522–31
- [17] Estrada L C, Aramendía P F and Martínez O E 2008 10000 times volume reduction for fluorescence correlation spectroscopy using nano-antennas *Opt. Express* **16** 20597–602
- [18] Chen P-Y, Argyropoulos C and Alù A 2012 Enhanced nonlinearities using plasmonic nanoantennas *Nanophotonics* **1** 221–33
- [19] Biagioni P, Huang J-S and Hecht B 2012 Nanoantennas for visible and infrared radiation *Rep. Prog. Phys.* **75** 024402
- [20] Obermeier J, Schumacher T and Lippitz M 2018 Nonlinear spectroscopy of plasmonic nanoparticles *Adv. Phys. X* **3** 1454341
- [21] Giannini V *et al* 2011 Plasmonic nanoantennas: fundamentals and their use in controlling the radiative properties of nanoemitters *Chem. Rev.* **111** 3888–912
- [22] Berkovitch N, Ginzburg P and Orenstein M 2012 Nano-plasmonic antennas in the near infrared regime *J. Phys. Condens. Matter* **24** 073202
- [23] Christos A *et al* 2015 Plasmonic nanoantennas: enhancing light-matter interactions at the nanoscale *EPJ Appl. Metamater.* **2** 4
- [24] Krasnok A E *et al* 2013 Optical nanoantennas *Phys.-Usp.* **56** 539–64
- [25] Sheverdin A and Valagiannopoulos C 2019 core-shell nanospheres under visible light: optimal absorption, scattering, and cloaking *Phys. Rev. B* **99** 075305
- [26] Tzarouchis D C and Sihvola A 2018 General scattering characteristics of resonant core-shell spheres *IEEE Trans. Antennas Propag.* **66** 323–30
- [27] Arslanagić S and Jacobsen R E 2019 Active coated nano rod antennas for enhanced and directive scattering phenomena *EPJ Appl. Metamater.* **6** 19
- [28] Valagiannopoulos C A 2007 Single-series solution to the radiation of loop antenna in the presence of a conducting sphere *Prog. Electromagn. Res.* **71** 277–94
- [29] Thorsen R and Arslanagić S 2015 Eccentrically-layered active coated nano-particles for directive near- and far-field radiation *Photonics* **2** 773–94
- [30] Campbell S D and Ziolkowski R W 2015 Near-field directive beams from passive and active asymmetric optical nanoantennas *IEEE J. Sel. Top. Quantum Electron.* **21** 312–23
- [31] Albella P *et al* 2014 Electric and magnetic field enhancement with ultralow heat radiation dielectric nanoantennas: considerations for surface-enhanced spectroscopies *ACS Photonics* **1** 524–9

- [32] Caldarola M *et al* 2015 Non-plasmonic nanoantennas for surface enhanced spectroscopies with ultra-low heat conversion *Nat. Commun.* **6** 7915
- [33] Barreda A I *et al* 2019 Recent advances in high refractive index dielectric nanoantennas: basics and applications *AIP Adv.* **9** 040701
- [34] Guo H *et al* 2013 Near-field focusing of the dielectric microsphere with wavelength scale radius *Opt. Express* **21** 2434–43
- [35] Heifetz A *et al* 2007 Subdiffraction optical resolution of a gold nanosphere located within the nanojet of a Mie-resonant dielectric microsphere *Opt. Express* **15** 17334–42
- [36] Teraoka I, Arnold S and Vollmer F 2003 Perturbation approach to resonance shifts of whispering-gallery modes in a dielectric microsphere as a probe of a surrounding medium *J. Opt. Soc. Am. B* **20** 1937–46
- [37] Rodriguez I *et al* 2014 Silicon nanoparticles as Raman scattering enhancers *Nanoscale* **6** 5666–70
- [38] Krasnok A E *et al* 2014 Superdirective dielectric nanoantennas *Nanoscale* **6** 7354–61
- [39] Zywiets U *et al* 2014 Laser printing of silicon nanoparticles with resonant optical electric and magnetic responses *Nat. Commun.* **5** 3402
- [40] Rolly B *et al* 2012 Promoting magnetic dipolar transition in trivalent lanthanide ions with lossless Mie resonances *Phys. Rev. B* **85** 245432
- [41] Dregely D *et al* 2011 3D optical Yagi–Uda nanoantenna array *Nat. Commun.* **2** 267
- [42] Filonov D S *et al* 2012 Experimental verification of the concept of all-dielectric nanoantennas *Appl. Phys. Lett.* **100** 201113
- [43] Ghanim A M *et al* 2016 Highly directive hybrid yagi-uda nanoantenna for radiation emission enhancement *IEEE Photonics J.* **8** 5501712
- [44] Krasnok A E *et al* 2012 All-dielectric optical nanoantennas *Opt. Express* **20** 20599–604
- [45] Krasnok A E *et al* 2011 Huygens optical elements and Yagi–Uda nanoantennas based on dielectric nanoparticles *JETP Lett.* **94** 593–8
- [46] Tsuchimoto Y *et al* 2016 Fano resonant all-dielectric core/shell nanoparticles with ultrahigh scattering directionality in the visible region *Opt. Express* **24** 14451–62
- [47] Li R *et al* 2018 Broadband zero backward scattering by all-dielectric core–shell nanoparticles *Opt. Express* **26** 28891–901
- [48] de Sousa N *et al* 2016 Magneto-optical activity in high index dielectric nanoantennas *Sci. Rep.* **6** 30803
- [49] Baranov D G *et al* 2016 Tuning of near- and far-field properties of all-dielectric dimer nanoantennas via ultrafast electron-hole plasma photoexcitation *Laser Photonics Rev.* **10** 1009–15
- [50] Shibamura T, Albella P and Maier S A 2016 Unidirectional light scattering with high efficiency at optical frequencies based on low-loss dielectric nanoantennas *Nanoscale* **8** 14184–92
- [51] Shibamura T *et al* 2017 Experimental demonstration of tunable directional scattering of visible light from all-dielectric asymmetric dimers *ACS Photonics* **4** 489–94
- [52] Albella P, Shibamura T and Maier S A 2015 Switchable directional scattering of electromagnetic radiation with subwavelength asymmetric silicon dimers *Sci. Rep.* **5** 18322
- [53] Cambiasso J *et al* 2018 Surface-enhanced spectroscopies of a molecular monolayer in an all-dielectric nanoantenna *ACS Photonics* **5** 1546–57
- [54] Lapshina N, Noskov R and Kivshar Y 2012 Nanoradar based on nonlinear dimer nanoantenna *Opt. Lett.* **37** 3921–23
- [55] Zywiets U *et al* 2015 Electromagnetic resonances of silicon nanoparticle dimers in the visible *ACS Photonics* **2** 913–20
- [56] Albella P *et al* 2013 Low-loss electric and magnetic field-enhanced spectroscopy with subwavelength silicon dimers *J. Phys. Chem. C* **117** 13573–84
- [57] Gómez F R, Mejía-Salazar J R and Albella P 2019 All-dielectric chiral metasurfaces based on crossed-bowtie nanoantennas *ACS Omega* **4** 21041–7
- [58] Valagiannopoulos C A *et al* 2014 Hyperbolic-metamaterial antennas for broadband enhancement of dipole emission to free space *J. Appl. Phys.* **116** 163106
- [59] Valagiannopoulos C A and Sihvola A 2013 Improving the electrostatic field concentration in a negative-permittivity wedge with a grounded ‘bowtie’ configuration *Radio Sci.* **48** 316–25
- [60] Zhang X M *et al* 2018 Dual-band unidirectional forward scattering with all-dielectric hollow nanodisk in the visible *Opt. Lett.* **43** 1275–78
- [61] Visser D *et al* 2019 Optical properties and fabrication of dielectric metasurfaces based on amorphous silicon nanodisk arrays *Opt. Express* **27** 5353–67
- [62] Lv J *et al* 2018 Multi-wavelength unidirectional forward scattering in the visible range in an all-dielectric silicon hollow nanodisk *Appl. Opt.* **57** 4771–76
- [63] Frolov A Y *et al* 2017 Near-field mapping of optical Fabry–Pérot modes in all-dielectric nanoantennas *Nano Lett.* **17** 7629–37
- [64] Abujetas D R *et al* 2017 High-contrast Fano resonances in single semiconductor nanorods *ACS Photonics* **4** 1814–21
- [65] Novotny L and van Hulst N 2011 Antennas for light *Nat. Photonics* **5** 83–90
- [66] Mishchenko M I, Travis L D and Lacis A A 2002 *Scattering, Absorption, and Emission of Light by Small Particles* (Cambridge: Cambridge University Press)
- [67] Bohren C F and Huffman D R 1998 *Absorption and Scattering of Light by Small Particles* (New York: Wiley) (<https://doi.org/10.1002/9783527618156>)
- [68] Bharadwaj P, Deutsch B and Novotny L 2009 Optical antennas *Adv. Opt. Photonics* **1** 438–83
- [69] Hu S *et al* 2018 Experimental realization of deep-subwavelength confinement in dielectric optical resonators *Sci. Adv.* **4** eaat2355
- [70] Altug H, Englund D and Vučković J 2006 Ultrafast photonic crystal nanocavity laser *Nat. Phys.* **2** 484–8
- [71] Hu S and Weiss S M 2016 Design of photonic crystal cavities for extreme light concentration *ACS Photonics* **3** 1647–53
- [72] Landau L D and Lifshitz E M 1974 *Quantum Mechanics* (Pergamon) ch 4 116–35
- [73] Purcell E M, Torrey H C and Pound R V 1946 Resonance absorption by nuclear magnetic moments in a solid *Phys. Rev.* **69** 37–8
- [74] Vahala K J 2003 Optical microcavities *Nature* **424** 839–46
- [75] Jiao X and Blair S 2012 Optical antenna design for fluorescence enhancement in the ultraviolet *Opt. Express* **20** 29909–22
- [76] Sun G and Khurgin J B 2012 Origin of giant difference between fluorescence, resonance, and nonresonance Raman scattering enhancement by surface plasmons *Phys. Rev. A* **85** 063410
- [77] Maslovski S I and Simovski C R 2019 Purcell factor and local intensity enhancement in surface-enhanced Raman scattering *Nanophotonics* **8** 429–34
- [78] Zhao X and Reinhard B M 2019 Switchable chiroptical hotspots in silicon nanodisk dimers *ACS Photonics* **6** 1981–9
- [79] Rolly B *et al* 2013 Controllable emission of a dipolar source coupled with a magneto-dielectric resonant subwavelength scatterer *Sci. Rep.* **3** 3063
- [80] Todisco F *et al* 2020 Magnetic and electric Mie-exciton polaritons in silicon nanodisks *Nanophotonics* **9** 803–14
- [81] Feng T *et al* 2018 Unidirectional emission in an all-dielectric nanoantenna *J. Phys. Condens. Matter* **30** 124002

- [82] Habteyes T G *et al* 2014 Near-field mapping of optical modes on all-dielectric silicon nanodisks *ACS Photonics* **1** 794–8
- [83] Regmi R *et al* 2016 All-dielectric silicon nanogap antennas to enhance the fluorescence of single molecules *Nano Lett.* **16** 5143–51
- [84] Fu D *et al* 2017 Polarization-selective optical resonance with extremely narrow linewidth in Si dimers array for application in ultra-sensitive refractive sensing *Opt. Commun.* **390** 41–8
- [85] Wang H *et al* 2015 Janus Magneto–electric nanosphere dimers exhibiting unidirectional visible light scattering and strong electromagnetic field enhancement *ACS Nano* **9** 436–48
- [86] Yan J *et al* 2015 Directional fano resonance in a silicon nanosphere dimer *ACS Nano* **9** 2968–80
- [87] Deng F *et al* 2018 Sharp bending and power distribution of a focused radially polarized beam by using silicon nanoparticle dimers *Opt. Express* **26** 20051–62
- [88] Das T and Schuller J A 2017 Dark modes and field enhancements in dielectric dimers illuminated by cylindrical vector beams *Phys. Rev. B* **95** 201111(R)
- [89] Jia Z-Y *et al* 2016 Dipole coupling and dual Fano resonances in a silicon nanodimer *J. Appl. Phys.* **119** 074302
- [90] Wang L *et al* 2017 Shaping the third-harmonic radiation from silicon nanodimers *Nanoscale* **9** 2201–6
- [91] Mirzaei A and Miroshnichenko A E 2015 Electric and magnetic hotspots in dielectric nanowire dimers *Nanoscale* **7** 5963–8
- [92] Černigoj J *et al* 2018 Lattice resonances and local field enhancement in array of dielectric dimers for surface enhanced Raman spectroscopy *Sci. Rep.* **8** 15706
- [93] Ha S T *et al* 2018 Directional lasing in resonant semiconductor nanoantenna arrays *Nat. Nanotechnol.* **13** 1042–7
- [94] Liu Y G *et al* 2012 Unidirectional and wavelength-selective photonic sphere-array nanoantennas *Opt. Lett.* **37** 2112–4
- [95] Filonov D S *et al* 2014 Near-field mapping of Fano resonances in all-dielectric oligomers *Appl. Phys. Lett.* **104** 021104
- [96] Shcherbakov M R *et al* 2015 Nonlinear interference and tailorable third-harmonic generation from dielectric oligomers *ACS Photonics* **2** 578–82
- [97] Hopkins B *et al* 2015 Interplay of magnetic responses in all-dielectric oligomers to realize magnetic fano resonances *ACS Photonics* **2** 724–9
- [98] Yan J H *et al* 2015 Magnetically induced forward scattering at visible wavelengths in silicon nanosphere oligomers *Nat. Commun.* **6** 7042
- [99] Miroshnichenko A E and Kivshar Y S 2012 Fano resonances in all-dielectric oligomers *Nano Lett.* **12** 6459–63
- [100] Vaskin A *et al* 2018 Directional and spectral shaping of light emission with mie-resonant silicon nanoantenna arrays *ACS Photonics* **5** 1359–64
- [101] Yavas O *et al* 2017 On-a-chip biosensing based on all-dielectric nanoresonators *Nano Lett.* **17** 4421–6
- [102] Chong K E *et al* 2014 Observation of fano resonances in all-dielectric nanoparticle oligomers *Small* **10** 1985–90
- [103] Kuznetsov A I *et al* 2016 Optically resonant dielectric nanostructures *Science* **354** aag2472
- [104] Sain B, Meier C and Zentgraf T 2019 Nonlinear optics in all-dielectric nanoantennas and metasurfaces: a review *Adv. Photonics* **1** 024002
- [105] Evlyukhin A B *et al* 2010 Optical response features of Si-nanoparticle arrays *Phys. Rev. B* **82** 045404
- [106] García-Etxarri A *et al* 2011 Strong magnetic response of submicron Silicon particles in the infrared *Opt. Express* **19** 4815–26
- [107] Kuznetsov A I *et al* 2012 Magnetic light *Sci. Rep.* **2** 492
- [108] Evlyukhin A B *et al* 2014 Optical spectroscopy of single Si nanocylinders with magnetic and electric resonances *Sci. Rep.* **4** 4126
- [109] Coenen T, van de Groep J and Polman A 2013 Resonant modes of single silicon nanocavities excited by electron irradiation *ACS Nano* **7** 1689–98
- [110] Brönstrup G *et al* 2010 Optical properties of individual silicon nanowires for photonic devices *ACS Nano* **4** 7113–22
- [111] Kruk S and Kivshar Y 2017 Functional meta-optics and nanophotonics governed by mie resonances *ACS Photonics* **4** 2638–49
- [112] Person S *et al* 2013 Demonstration of zero optical backscattering from single nanoparticles *Nano Lett.* **13** 1806–9
- [113] Ginn J C *et al* 2012 Realizing optical magnetism from dielectric metamaterials *Phys. Rev. Lett.* **108** 097402
- [114] Ma C *et al* 2017 Directional scattering in a germanium nanosphere in the visible light region *Adv. Opt. Mater.* **5** 1700761
- [115] Kerker M, Wang D S and Giles C L 1983 Electromagnetic scattering by magnetic spheres *J. Opt. Soc. Am.* **73** 765–7
- [116] Geffrin J M *et al* 2012 Magnetic and electric coherence in forward- and back-scattered electromagnetic waves by a single dielectric subwavelength sphere *Nat. Commun.* **3** 1171
- [117] Fu Y H *et al* 2013 Directional visible light scattering by silicon nanoparticles *Nat. Commun.* **4** 1527
- [118] Gómez-Medina R 2011 Electric and magnetic dipolar response of germanium nanospheres: interference effects, scattering anisotropy, and optical forces *J. Nanophotonics* **5** 053512
- [119] Lee J Y, Miroshnichenko A E and Lee R-K 2018 Simultaneously nearly zero forward and nearly zero backward scattering objects *Opt. Express* **26** 30393–9
- [120] Staude I *et al* 2013 Tailoring directional scattering through magnetic and electric resonances in subwavelength silicon nanodisks *ACS Nano* **7** 7824–32
- [121] Terekhov P D *et al* 2017 Resonant forward scattering of light by high-refractive-index dielectric nanoparticles with toroidal dipole contribution *Opt. Lett.* **42** 835–8
- [122] Isro S D *et al* 2018 Engineering scattering patterns with asymmetric dielectric nanorods *Opt. Express* **26** 32624–30
- [123] Krasnok A E *et al* 2015 Enhanced emission extraction and selective excitation of NV centers with all-dielectric nanoantennas *Laser Photonics Rev.* **9** 385–91
- [124] Zalogina A S *et al* 2018 Purcell effect in active diamond nanoantennas *Nanoscale* **10** 8721–7
- [125] Bakker R M *et al* 2015 Magnetic and electric hotspots with silicon nanodimers *Nano Lett.* **15** 2137–42
- [126] Miri M and Sadra M 2017 Dimers and trimers of hollow silicon nanoparticles: manipulating the magnetic hotspots *J. Phys. Chem. C* **121** 11672–9
- [127] McPolin C P T *et al* 2018 Imaging electric and magnetic modes and their hybridization in single and dimer AlGaAs nanoantennas *Adv. Opt. Mater.* **6** 1800664
- [128] Yao K and Liu Y 2018 Enhancing circular dichroism by chiral hotspots in silicon nanocube dimers *Nanoscale* **10** 8779–86
- [129] Mohammadi E *et al* 2019 Accessible superchiral near-fields driven by tailored electric and magnetic resonances in all-dielectric nanostructures *ACS Photonics* **6** 1939–46
- [130] Reyes Gómez F *et al* 2020 Enhanced chiroptical activity with slotted high refractive index dielectric nanodisks *Phys. Rev. B* **101** 155403
- [131] Cambiasso J *et al* 2017 Bridging the gap between dielectric nanophotonics and the visible regime with effectively

- lossless gallium phosphide antennas *Nano Lett.* **17** 1219–25
- [132] Xu Z, Song W and Crozier K B 2018 Optical trapping of nanoparticles using all-silicon nanoantennas *ACS Photonics* **5** 4993–5001
- [133] Sortino L *et al* 2019 Enhanced light–matter interaction in an atomically thin semiconductor coupled with dielectric nanoantennas *Nat. Commun.* **10** 5119
- [134] Krasnok A *et al* 2016 Demonstration of the enhanced Purcell factor in all-dielectric structures *Appl. Phys. Lett.* **108** 211105
- [135] Sugimoto H and Fujii M 2017 Colloidal dispersion of subquarter micrometer silicon spheres for low-loss antenna in visible regime *Adv. Opt. Mater.* **5** 1700332
- [136] Mignuzzi S *et al* 2019 Nanoscale design of the local density of optical states *Nano Lett.* **19** 1613–7
- [137] Pellegrini G, Mattei G and Mazzoldi P 2009 Light extraction with dielectric nanoantenna arrays *ACS Nano* **3** 2715–21
- [138] Luk'yanchuk B *et al* 2010 The Fano resonance in plasmonic nanostructures and metamaterials *Nat. Mater.* **9** 707–15
- [139] Huang Y *et al* 2019 Active tuning of the Fano resonance from a Si nanosphere dimer by the substrate effect *Nanoscale Horiz.* **4** 148–57
- [140] Yang Z-J, Zhao Q and He J 2019 Fano interferences of electromagnetic modes in dielectric nanoblock dimers *J. Appl. Phys.* **125** 063103
- [141] Gorodetsky M L, Savchenkov A A and Ilchenko V S 1996 Ultimate Q of optical microsphere resonators *Opt. Lett.* **21** 453–5
- [142] Heylman K D *et al* 2017 Optical microresonators for sensing and transduction: a materials perspective *Adv. Mater.* **29** 1700037
- [143] Foreman M R, Swaim J D and Vollmer F 2015 Whispering gallery mode sensors *Adv. Opt. Photonics* **7** 168–240
- [144] Saleh B E and Teich M C 2019 *Fundamentals of Photonics* (New York: Wiley)
- [145] Zhang Y and Lončar M 2009 Submicrometer diameter micropillar cavities with high quality factor and ultrasmall mode volume *Opt. Lett.* **34** 902–4
- [146] Deotare P B *et al* 2009 High quality factor photonic crystal nanobeam cavities *Appl. Phys. Lett.* **94** 121106
- [147] Safavi-Naeini A H *et al* 2010 Optomechanics in an ultrahigh-Q two-dimensional photonic crystal cavity *Appl. Phys. Lett.* **97** 181106
- [148] Devilez A, Stout B and Bonod N 2010 Compact metallo-dielectric optical antenna for ultra directional and enhanced radiative emission *ACS Nano* **4** 3390–6
- [149] Tiwari S *et al* 2020 Dielectric microsphere coupled to a plasmonic nanowire: a self-assembled hybrid optical antenna *Adv. Opt. Mater.* **8** 1901672
- [150] Vasista A B, Tiwari S and Kumar G V P 2019 Wavevector distribution of metal photoluminescence from a gold film coupled microsphere antenna *J. Opt.* **21** 035002
- [151] Gao Y and Shi Y 2019 Design of a single nanoparticle trapping device based on bow-tie-shaped photonic crystal nanobeam cavities *IEEE Photonics J.* **11** 4500408
- [152] Xu Z and Crozier K B 2019 All-dielectric nanotweezers for trapping and observation of a single quantum dot *Opt. Express* **27** 4034–45
- [153] Yu Y *et al* 2012 Dielectric core–shell optical antennas for strong solar absorption enhancement *Nano Lett.* **12** 3674–81
- [154] Grinblat G *et al* 2016 Enhanced third harmonic generation in single germanium nanodisks excited at the anapole mode *Nano Lett.* **16** 4635–40
- [155] Camacho-Morales R *et al* 2016 Nonlinear generation of vector beams from AlGaAs nanoantennas *Nano Lett.* **16** 7191–7
- [156] Smirnova D A *et al* 2016 Multipolar third-harmonic generation driven by optically induced magnetic resonances *ACS Photonics* **3** 1468–76
- [157] Carletti L *et al* 2015 Enhanced second-harmonic generation from magnetic resonance in AlGaAs nanoantennas *Opt. Express* **23** 26544–50
- [158] Shcherbakov M R *et al* 2014 Enhanced third-harmonic generation in silicon nanoparticles driven by magnetic response *Nano Lett.* **14** 6488–92
- [159] Golla C, Weber N and Meier C 2019 Zinc oxide based dielectric nanoantennas for efficient nonlinear frequency conversion *J. Appl. Phys.* **125** 073103
- [160] Gili V F *et al* 2016 Monolithic AlGaAs second-harmonic nanoantennas *Opt. Express* **24** 15965–71
- [161] Sauvan C *et al* 2013 Theory of the spontaneous optical emission of nanosize photonic and plasmon resonators *Phys. Rev. Lett.* **110** 237401
- [162] Bogdanov S *et al* 2017 Electron spin contrast of Purcell-enhanced nitrogen-vacancy ensembles in nanodiamonds *Phys. Rev. B* **96** 035146
- [163] Grier D G 2003 A revolution in optical manipulation *Nature* **424** 810–6
- [164] Spesyvtseva S E S and Dholakia K 2016 Trapping in a material world *ACS Photonics* **3** 719–36
- [165] Krasnok A *et al* 2018 Spectroscopy and biosensing with optically resonant dielectric nanostructures *Adv. Opt. Mater.* **6** 1701094
- [166] Mannino G *et al* 2015 Octahedral faceted Si nanoparticles as optical traps with enormous yield amplification *Sci. Rep.* **5** 8354
- [167] Dmitriev P A *et al* 2016 Resonant Raman scattering from silicon nanoparticles enhanced by magnetic response *Nanoscale* **8** 9721–6
- [168] Rose A, Huang D and Smith D R 2013 Nonlinear interference and unidirectional wave mixing in metamaterials *Phys. Rev. Lett.* **110** 063901
- [169] Shibanuma T *et al* 2017 Efficient third harmonic generation from metal–dielectric hybrid nanoantennas *Nano Lett.* **17** 2647–51
- [170] Hao S, Chen G and Yang C 2013 Sensing using rare-earth-doped upconversion nanoparticles *Theranostics* **3** 331–45
- [171] Cai X *et al* 2017 Reduction of pulmonary toxicity of metal oxide nanoparticles by phosphonate-based surface passivation *Part. Fibre Toxicol.* **14** 13
- [172] Simovski C R *et al* 2013 Photovoltaic absorption enhancement in thin-film solar cells by non-resonant beam collimation by submicron dielectric particles *J. Appl. Phys.* **114** 103104
- [173] Yao Y *et al* 2012 Broadband light management using low-Q whispering gallery modes in spherical nanoshells *Nat. Commun.* **3** 664
- [174] Kim S-K *et al* 2014 Doubling absorption in nanowire solar cells with dielectric shell optical antennas *Nano Lett.* **15** 753–8
- [175] Fan Z *et al* 2010 Ordered arrays of dual-diameter nanopillars for maximized optical absorption *Nano Lett.* **10** 3823–7
- [176] <https://refractiveindex.info/>
- [177] Sarkar S *et al* 2019 Hybridized guided-mode resonances via colloidal plasmonic self-assembled grating *ACS Appl. Mater. Interfaces* **11** 13752–60
- [178] Gao L, Lemarchand F and Lequime M 2012 Exploitation of multiple incidences spectrometric measurements for thin film reverse engineering *Opt. Express* **20** 15734–51
- [179] Kischkat J *et al* 2012 Mid-infrared optical properties of thin films of aluminum oxide, titanium dioxide, silicon dioxide, aluminum nitride, and silicon nitride *Appl. Opt.* **51** 6789–98
- [180] Green M A and Keevers M J 1995 Optical properties of intrinsic silicon at 300 K *Prog. Photovoltaics Res. Appl.* **3** 189–92

- [181] Li H H 1980 Refractive index of silicon and germanium and its wavelength and temperature derivatives *J. Phys. Chem. Ref. Data* **9** 561–658
- [182] Larruquert J I *et al* 2011 Self-consistent optical constants of SiC thin films *J. Opt. Soc. Am. A* **28** 2340–45
- [183] Aspnes D E *et al* 1986 Optical properties of $\text{Al}_x\text{Ga}_{1-x}\text{As}$ *J. Appl. Phys.* **60** 754–67
- [184] Adachi S 1989 Optical dispersion relations for GaP, GaAs, GaSb, InP, InAs, InSb, $\text{Al}_x\text{Ga}_{1-x}\text{As}$, and $\text{In}_{1-x}\text{Ga}_x\text{As}_y\text{P}_{1-y}$ *J. Appl. Phys.* **66** 6030–40
- [185] Amotchkina T *et al* 2020 Characterization of e-beam evaporated Ge, YbF₃, ZnS, and LaF₃ thin films for laser-oriented coatings *Appl. Opt.* **59** A40–A47
- [186] Ciesielski A *et al* 2018 Permittivity of Ge, Te and Se thin films in the 200–1500 nm spectral range. Predicting the segregation effects in silver *Mater. Sci. Semicond. Process.* **81** 64–7
- [187] Staude I and Schilling J 2017 Metamaterial-inspired silicon nanophotonics *Nat. Photonics* **11** 274–84
- [188] Sarangan A 2016 Nanofabrication *Fundamentals and Applications of Nanophotonics* (Woodhead Publishing) ch 5 149–84
- [189] Shankar K S and Raychaudhuri A K 2005 Fabrication of nanowires of multicomponent oxides: review of recent advances *Materials Science and Engineering: C* **25** 738–51
- [190] Kalantar-zadeh K and Fry B 2008 Nano fabrication and patterning techniques *Nanotechnology-Enabled Sensors* (Boston, MA: Springer US) pp 135–210
- [191] Lim A E-J *et al* 2014 Review of silicon photonics foundry efforts *IEEE J. Sel. Top. Quantum Electron.* **20** 405–16
- [192] Thomson D *et al* 2016 Roadmap on silicon photonics *J. Opt.* **18** 073003
- [193] Bogaerts W and Chrostowski L 2018 Silicon photonics circuit design: methods, tools and challenges *Laser Photonics Rev.* **12** 1700237
- [194] Muñoz P *et al* 2017 Silicon nitride photonic integration platforms for visible, near-infrared and mid-infrared applications *Sensors* **17** 2088
- [195] Elshaari A W *et al* 2020 Hybrid integrated quantum photonic circuits *Nat. Photonics* **14** 285–98
- [196] He J *et al* 2020 Nonlinear nanophotonic devices in the ultraviolet to visible wavelength range *Nanophotonics* **9** 3781–804

Paper II: Materials for dielectric nanotweezers in the near-visible region

Published in ACS Applied Optical Materials, March 2023.

Authors: Md Rabiul Hasan, and Olav Gaute Hellestø

Contribution notes: Md Rabiul Hasan conceived the idea, performed all simulations and data analysis. Md Rabiul Hasan wrote the initial draft and Olav Gaute Hellestø finalized it before submission. Both authors contributed to revise the manuscript.

Materials for Dielectric Nanotweezers in the Near-Visible Region

Md Rabiul Hasan* and Olav Gaute Helleø

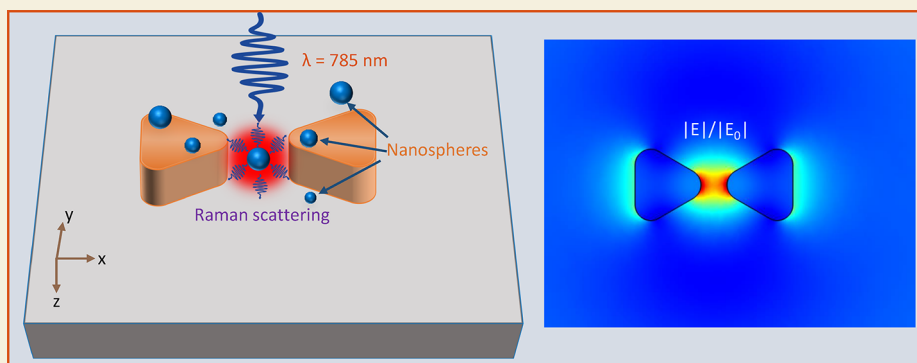
Cite This: *ACS Appl. Opt. Mater.* 2023, 1, 832–842

Read Online

ACCESS |

Metrics & More

Article Recommendations



ABSTRACT: Nanotweezers made of dielectric nanoantennas have enabled optical trapping and manipulation of nanoscale objects. Commonly used dielectric materials with a high refractive index, notably silicon (Si), suffer from absorption at visible wavelengths and thus Joule heating of the structure and the trapped object. They are thus normally considered unsuitable for trapping applications in this wavelength range. In this work, dielectric materials with low absorption at 785 nm are studied to minimize Joule heating. We consider a bowtie configuration, which is simulated for four different dielectric materials and optimized for maximum electric field enhancement. The results show a significant electric field enhancement in the bowtie gap, which can act as a “hotspot” for optical trapping and enhancement of Raman scattering of a single nanosphere. We numerically investigate optical trapping of nanospheres and compare the results with an analytical expression. Three nanospheres with different refractive indices are used as examples. We further study the temperature increase and the thermally induced flow around the bowtie nanoantenna to understand if and how the trapping is perturbed by Joule heating. We find that nanoantennas made by Si on a Si substrate, although absorbing, can be used for trapping quantum dots (QDs) and polystyrene (PS) beads. The required input intensities for stable trapping are approximately 10 and 50 mW/μm², for QDs and PS beads, respectively, inducing temperature increases of ~1.4 K and ~7 K, respectively. For transparent materials, the input intensity is the limiting factor, and gallium phosphide (GaP) requires the lowest input intensity due to its high refractive index. However, Si is a far more common and standard material and thus gives a significantly easier fabrication process.

KEYWORDS: dielectric nanotweezers, bowtie nanoantennas, finite element method, electric field enhancement, optical trapping, Raman enhancement factor, Joule heating

1. INTRODUCTION

Conventional optical tweezers combined with Raman spectroscopy is an effective tool to trap, transport, and analyze suspended microparticles.^{1–5} However, manipulation of nanometer-sized particles using this approach is difficult due to a weaker optical gradient force, as it scales with the third power of particle radius.⁶ Thus, a high laser power is required for stable trapping, which can cause optical damage to the trapped object.⁷ Besides, the spot size of the focused beam is restricted by the diffraction limit; thus, combining optical trapping and Raman spectroscopy of particles smaller than the focused beam spot is challenging.

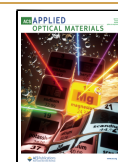
Plasmonic nanoantennas can confine light in the sub-wavelength scale and can give a moderate to high electric field

enhancement, depending on the geometry of the nanoantennas. The field enhancement by these nanostructures enables optical trapping of smaller objects, as reported in several works.^{8–12} Absorption losses of the plasmonic nanoantennas are the limiting factor for stable trapping, leading to thermophoresis and convection of fluid.¹³ As a result, the trapped nanoparticle tends to move away from the

Received: November 29, 2022

Accepted: March 15, 2023

Published: March 27, 2023



equilibrium position, thus making stable trapping difficult. Apart from plasmonic configurations, their dielectric counterparts^{14,15} are a promising platform for optical trapping of smaller nanoparticles. Dielectric structures such as waveguides,^{16,17} photonic crystal resonators,^{18,19} and nanoantennas^{20–22} made of high-refractive-index materials can produce a significant electric field enhancement, which is beneficial to obtain a higher gradient force. However, these benefits come at the cost of significant absorption losses for several of the materials, particularly at visible wavelengths. This is the case for silicon (Si),^{23–25} germanium (Ge),^{23–25} multilayer transition metal dichalcogenides, for example, tungsten disulfide (WS₂),²⁶ and so forth. Examples of materials with lower absorption and also lower refractive index are gallium phosphide (GaP),^{27–29} silicon nitride (Si₃N₄), and titanium dioxide (TiO₂). For these, heating is drastically reduced at the expense of a lower field enhancement.

One of the powerful applications of the nanometric-size “hotspots” in plasmonic nanostructures is surface-enhanced Raman scattering (SERS) for detection of single molecules. Several novel configurations including inter-particle nanogaps,³⁰ nanogap in electrode pairs,³¹ and nanoparticle-on-a-mirror (NPoM)³² have been investigated to obtain extremely high field enhancement in a small gap, giving a giant enhancement of the SERS signal. However, the spectra obtained with SERS can be influenced by chemical bonds between the molecule and the metal surface and tend to depend critically on the location of a particle relative to the plasmonic nanostructures.³³ Besides, due to different surface enhancements, the SERS spectrum of a nanoparticle captured at one location can differ from the spectrum of an identical particle trapped at another location. In this work, we focus on dielectric nanoantennas, as an alternative to SERS, to see if some of the drawbacks with plasmonic nanostructures can be mitigated. For optical spectrometers to have a sufficient signal-to-noise ratio for Raman spectroscopy, they must be based on the Si-photodetector, and their wavelength range is consequently limited to ≤ 1000 nm. A near-visible wavelength must thus be used for excitation to measure the Stokes-shifted Raman scattering using these spectrometers. Here, we consider a near-visible wavelength of 785 nm, commonly used for Raman spectroscopy, both for optical trapping and excitation of Raman scattering.

We mainly consider the bowtie configuration for the dielectric nanoantenna. Using numerical simulations, we optimize the dimensions of the nanoantenna for four dielectric materials (multilayer WS₂, Si, GaP, and Si₃N₄) to obtain maximum field enhancement and Raman enhancement at 785 nm. In addition, we consider the optical trapping of three nanospheres as examples, a quantum dot (QD), a polystyrene (PS) bead, and an extracellular vesicle (EV). Of the materials considered, GaP has a high refractive index ($n = 3.2$) and does not absorb at 785 nm. It is thus expected to perform better than the other materials, but it is not a standard semiconductor material. As Si and WS₂ are absorbing at 785 nm, it may appear counter-intuitive to study them as the absorption will cause heating. However, they also have high thermal conductivity, and the power absorbed by the nanoantenna is small. In this work, we explore if there is a window for using these materials, particularly Si, being the standard for semiconductor processing. All-Si and Si-on-glass nanoantennas have been reported in a few previous works, limited to optical trapping at 1064^{20,21,34} and 1550 nm,³⁵ respectively. These nanoantennas

are thus unsuitable for combining with Raman spectroscopy. The novelty of this article is to study all-dielectric bowtie nanoantennas for combining optical trapping with Raman spectroscopy at 785 nm, in particular, all-Si nanoantennas at this wavelength. The aim is to trap a single nanoparticle and collect the Raman spectrum from it, with limited input intensity and with low heating. The approach can be extended to an array of dielectric nanoantennas fabricated on a single chip, for parallel Raman spectroscopy of many individual nanoparticles. The limited attention to the use of Si at 785 nm is understandable due to the absorption. However, our investigation shows that the heat generated is effectively conducted away, giving limited heating even for relatively high input intensity. To use Si nanoantennas for a specific application, the nanoantenna structure, notably the gap, must be tailored to the nanoparticle size, and it must be ensured that the necessary intensity and the accompanying heating are acceptable. The results provided here can assist in the optimization of the structure and deciding if a Si nanoantenna is suitable. Furthermore, this systematic numerical study of two standard and two novel materials for nanoantennas at 785 nm can be valuable as a guide for future experimental investigations.

2. STRUCTURE DESIGN AND SIMULATION METHODS

The schematic of a bowtie nanoantenna is shown in Figure 1a, which consists of a pair of opposing triangles separated by a 50 nm gap g .

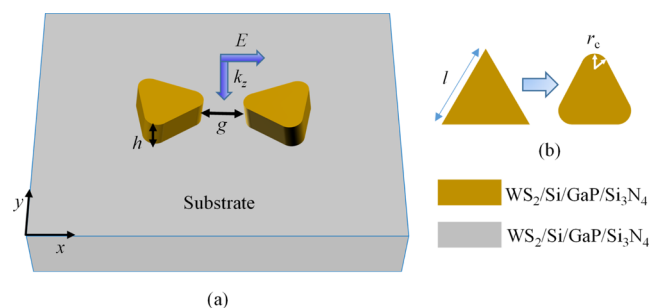


Figure 1. Schematic of a (a) bowtie nanoantenna, consisting of a pair of equilateral triangles separated by a gap $g = 50$ nm and placed on top of a substrate. (b) Rounded edges with a radius of curvature $r_c = 30$ nm. Excitation by a plane wave polarized along the x -axis and propagated along the z -axis is shown in the inset of (a).

The triangle has a side length l and height h . The tips of the triangles are slightly curved with a radius of curvature r_c , initially taken to be 30 nm (Figure 1b). The sharp tips of the triangles are rounded to avoid singularity problems and to approximate an actual fabricated design.^{36,37} Note that the substrate is the same material as the bowtie, unless otherwise stated. The nanoantenna is covered by water for optical trapping. Here, we consider four different dielectrics, which are multilayer WS₂, Si, GaP, and Si₃N₄ for the triangles and substrate. The complex refractive index of multilayer WS₂, Si, GaP, and Si₃N₄ has been taken from refs 26 and 38–3940, respectively. For water, only the real part of the refractive index ($n_w = 1.33$) is considered due to negligible absorption in near-visible wavelengths. We use COMSOL Multiphysics v.5.6 and a modified scattered field formulation for all simulations. The background field between the substrate and water cannot be directly defined in the scattered field formulation, as it will change due to the presence of the substrate. Therefore, the expression for the background field must be modified by incorporating the reflection and refraction at the interface. For this, we apply the Fresnel equations to compute the background field between the substrate and water, as demonstrated in ref 41. The

computed background field is then used in the scattered field formulation with the bowtie nanoantenna being a scatterer. For computing the background field, a plane wave is considered that propagates along the z -axis and polarizes along the x -axis (perpendicular to the mirror plane of the nanoantenna), as shown in Figure 1a. The wavelength used in the simulation is 785 nm, as stated previously. Perfectly matched layers are implemented around the computational domains to prevent the backscattering. The maximum mesh element size for the triangles and trapped nanosphere is 10 and 2 nm, respectively. The optical force exerted on the trapped nanosphere is found from the Maxwell stress tensor.^{21,34} In this work, we consider three refractive indices for the nanospheres, corresponding to a QD ($n_{\text{QD}} = 2.49$),⁴² a PS bead ($n_{\text{PS}} = 1.59$),⁴³ and an EV ($n_{\text{EV}} = 1.39$)⁴⁴ to study the optical trapping. The electromagnetic (EM) simulation provides a total power dissipation density, which is the sum of magnetic and resistive losses. The power dissipation density is integrated over the volume of the triangles and the substrate (for the absorbing materials), giving the absorbed power in these triangles and substrate. This absorbed power acts as a heat source, which is assumed to be uniformly distributed over the triangles and the substrate as the materials are good heat conductors. We use the COMSOL heat transfer module to calculate the temperature distribution around the nanoantenna. The temperature, in turn, creates flow, which is also simulated (with the COMSOL laminar flow module). No-slip boundary conditions are used at the boundaries between water and solids. Values for the fluidic properties of water have been taken from the COMSOL material library. The two different absorbing materials have thermal conductivities of $142 \text{ W K}^{-1} \text{ m}^{-1}$ for multilayer WS_2 ⁴⁵ and $148 \text{ W K}^{-1} \text{ m}^{-1}$ for Si.²¹ Note that the thermal conductivity of WS_2 and Si is high, which implies that heat is effectively transported away from the nanoantenna by the substrate. A thermally insulating layer between the substrate and the nanoantenna is detrimental to this heat transfer, as will be shown.

3. SIMULATION RESULTS AND DISCUSSION

We have divided this section into four subsections. In the first subsection, we optimize the dimensions of the bowtie nanoantenna to obtain maximum field enhancement and Raman enhancement in the middle of the gap. In the following two subsections, we study heating and thermally induced flow in the vicinity of absorbing nanoantennas. In the fourth subsection, we study optical trapping of nanospheres using the optimized nanoantenna dimensions.

3.1. Electric Field Enhancement and Raman Enhancement Factor

One of the key features of a dielectric nanoantenna is the enhancement $|E|/|E_0|$ of the electric field near the nanoantenna, where E is the local electric field with a nanoantenna and E_0 is the background electric field without the nanoantenna. The enhancement typically relies on nanoantenna shape, dimensions, and the refractive index of the nanoantenna material.^{24,46} For the studied bowtie nanoantenna, the field enhancement can be maximized by tuning its design parameters, which are side length l , height h , gap g , and radius of curvature r_c . We use an iterative approach, with optimization of one parameter at a time. We start by varying length l and keeping the other parameters fixed. The initial height is kept at $h = 100 \text{ nm}$, which provides sufficient retardation throughout the nanoantenna to support a current loop, as shown in previous works.^{47,48} Next, we put the value of l giving maximum enhancement into the simulation and vary h . Figure 2a shows the dependency of the field enhancement on l , where l is varied from 120 to 400 nm and the optimized h is kept at 330, 380, 370, and 400 nm for WS_2 , Si, GaP, and Si_3N_4 nanoantennas, respectively. Field enhancement in the middle

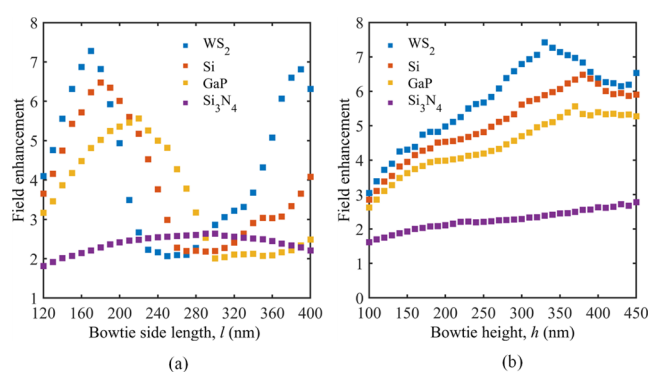


Figure 2. Electric field enhancement $|E|/|E_0|$ at the middle of the gap g as a function of (a) side length l and (b) height h at $\lambda = 785 \text{ nm}$ in WS_2 , Si, GaP, and Si_3N_4 nanoantennas with $g = 50 \text{ nm}$.

of the gap reaches the maximum at $l = 170, 180, 220,$ and 300 nm for WS_2 , Si, GaP, and Si_3N_4 nanoantennas, respectively. Figure 2b shows field enhancement in the middle of the gap as a function of h . We vary h from 100 to 450 nm while l is kept fixed at 170, 180, 220, and 300 nm for WS_2 , Si, GaP, and Si_3N_4 nanoantennas, respectively. The field enhancement increases with h , reaching a maximum at 330, 380, and 370 nm for WS_2 , Si, and GaP nanoantennas, respectively. The field enhancement for the Si_3N_4 nanoantenna goes up slowly throughout the entire range of h , without any clear peak. For the Si_3N_4 nanoantenna, we fix $h = 400 \text{ nm}$ for the rest of the study. For the other materials, we use the values of l and h giving the maximum field enhancement (not shown), unless otherwise noted.

Dielectric nanoantennas can store the EM field due to the displacement current inside the nanoantennas. They can support several resonance modes such as magnetic dipole (MD), electric dipole (ED), magnetic quadrupole (MQ), electric quadrupole (EQ), and other higher order multipoles, depending on the nanoantenna dimensions and excitation wavelength.^{24,48} For the optimized l and h of the bowtie Si nanoantenna, the z -component of the current density J_z is shown in Figure 3a, which illustrates the distribution of charges. The accumulation of positive and negative charges clearly reveals a dipole-like behavior. The x -polarized incident field excites an ED resonance in the Si bowtie nanoantenna. The ED resonance is identified by the circulating magnetic field loops inside the nanoantenna, shown by black arrows in Figure 3b, which extend outside the nanoantenna.²⁵ To find the scattering contributions of different resonance modes in the Si bowtie nanoantenna, we perform multipole decomposition analysis, implementing the procedures given in ref 49. The scattering efficiency at 785 nm (the vertical dotted line in Figure 3c) shows that ED and EQ give the highest contributions at this wavelength. For simplicity, the Si nanoantenna in air is considered here. Note that with the presence of a substrate, the scattering efficiency would increase slightly.⁴⁷

The electric and magnetic field enhancement at mid-height (xy plane) of the nanoantenna is shown in Figure 3b,d, respectively, for $\lambda = 785 \text{ nm}$. The field enhancement profile in the zx plane cutting the bowtie nanoantenna in its center is shown in Figure 3e. For the Si nanoantenna, the optimized height ($h = 380 \text{ nm}$) is sufficiently tall to fit two current loops inside the triangles (see Figure 3e and black arrows). This results in splitting of the hotspots, as described in ref 50. It is

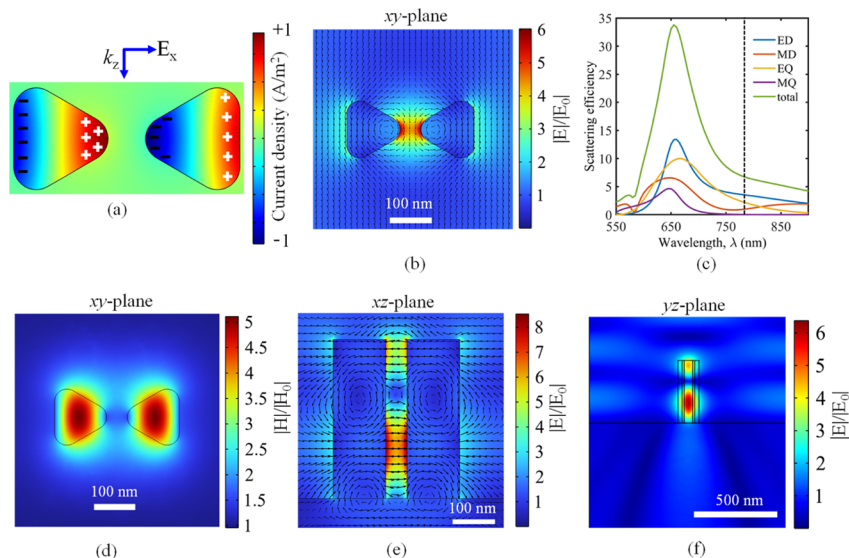


Figure 3. (a) Current density in the Si bowtie nanoantenna at 785 nm showing the distribution of positive and negative charges. (b) Illustration of ED resonance at $\lambda = 785$ nm (xy plane and mid-height of the nanoantenna), where the color bar indicates the field enhancement and black arrows indicate the orientation of the magnetic field vectors. (c) Multipolar contributions to the scattering efficiency of the Si nanoantenna in air, where ED = electric dipole, MD = magnetic dipole, EQ = electric quadrupole, and MQ = magnetic quadrupole. The vertical dotted line indicates multipolar contributions at 785 nm. (d) Magnetic field enhancement in the Si bowtie nanoantenna in the xy plane and mid-height of the nanoantenna. Electric field enhancement profile (e) in the xz plane cutting in the nanoantenna center and (f) in the yz plane (along the middle of the gap) for the Si nanoantenna. For all simulations, $g = 50$ nm.

worth noting that a smaller h would provide a single current loop, with reduced electric field enhancement in the middle of the gap. The field enhancement in the yz plane (at the middle of the gap) for the Si nanoantenna is shown in Figure 3f. The field profile and color bar show that the electric field localizes strongly in the narrow gap, thus making a hotspot for optical trapping. At the middle of the gap, a maximum field enhancement of ~ 6.5 can be achieved in the Si nanoantenna, as shown in Figure 3f. On the outer rims of the bowtie (Figure 3b), the field enhancement is significantly weaker than on the edges facing the gap. Due to two current loops inside the nanoantenna, two hotspots can be seen along the height (z -axis) (Figure 3e,f), as opposed to a single hotspot for smaller height in other works.^{20,21,27,51,52} The two hotspots are located around the mid-height and near the upper edges of the bowtie. The color bar in Figure 3e,f clearly indicates that the lower hotspot is more intense than the upper one. Similar field profiles were found for the other materials with a slightly different electric field enhancement (not shown).

Now, we investigate the impact of varying radius of curvature of the tips r_c and gap g on the field enhancement. A bowtie nanoantenna with sharp tips concentrates the electric field on the tips, giving a low field enhancement in the middle of the gap. The interaction in the gap can be increased by making the sharp tips into rounded corners with a radius of curvature r_c (see Figure 1b). With the optimized l and h obtained previously, field enhancement in the middle of the gap is plotted as a function of r_c , as shown in Figure 4a. The field enhancement has a rather weak dependency on r_c , reaching a maximum at $r_c = 30$ nm for WS_2 , Si, and GaP nanoantennas. For the Si_3N_4 nanoantenna, field enhancement goes up slowly with r_c and remains almost flat for the larger r_c . Therefore, we choose $r_c = 30$ nm in our simulation for all materials. Another crucial design parameter is the gap g between the two triangles. Figure 4b shows field enhancement in the middle of the gap as a function of g for WS_2 , Si, GaP,

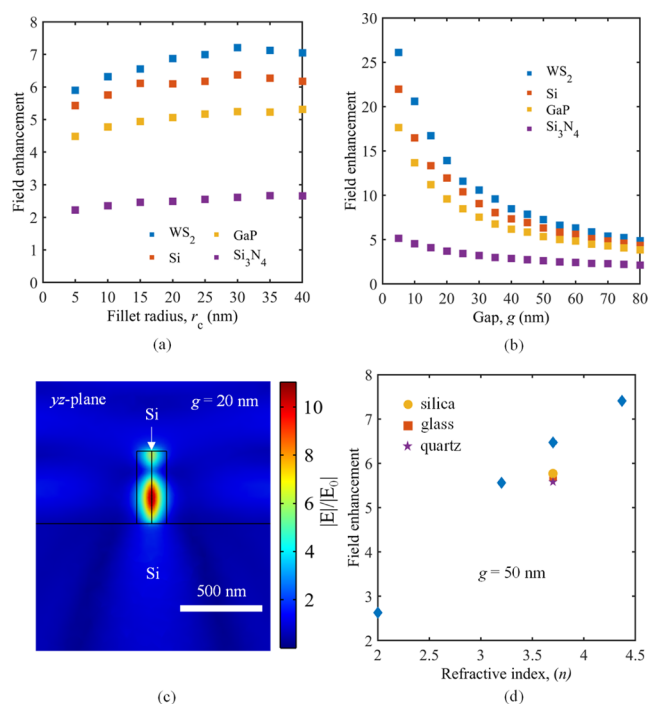


Figure 4. Dependency of electric field enhancement on (a) fillet radius r_c and (b) gap g in WS_2 , Si, GaP, and Si_3N_4 nanoantennas. In (a), $g = 50$ nm, and in (b), $r_c = 30$ nm. (c) Field enhancement profile in the yz plane (mid-height of the cylinder) of a Si cylindrical dimer with a Si substrate for $g = 20$ nm. (d) Field enhancement in the middle of the bowtie gap as a function of substrate refractive index with $g = 50$ nm.

and Si_3N_4 nanoantennas. As expected, a smaller gap g gives a higher field enhancement, due to the strong interaction in the gap. The field enhancement can be as high as ~ 10 , ~ 12 , and ~ 14 in the GaP, Si, and WS_2 nanoantennas for $g = 20$ nm. On

the other hand, field enhancement decreases monotonically with g , showing a value >5 for GaP, Si, and WS₂ nanoantennas with $g = 80$ nm. In fabrication point of view, obtaining a bowtie gap less than 10 nm is extremely challenging, as discussed in ref 32. Several novel nanostructures such as inter-particle nanogaps,⁵³ slit nanogaps,⁵⁴ and NPoMs⁵⁵ have been investigated to obtain more intense hotspots in a sub-5 nm gap. Table 1 shows a comparison between the novel

Table 1. Comparison between Sub-10 nm Nanostructures and Si Bowtie Nanoantennas

configuration	wavelength (nm)	type	gap (nm)	field enhancement
NPoM ⁵⁵	650	metal–dielectric	4	30
slit nanogap arrays ⁵⁴	515	plasmonic	5	13
inter-particle nanogap ⁵³	532	plasmonic	10	30
nanogap arrays ⁵⁸	633	plasmonic	9.2	40
bowtie nanoantenna (this work)	785	dielectric	10	16

nanostructures and the Si bowtie nanoantenna, with the former giving a significantly higher field enhancement. This is as expected due to the plasmonic effect. The field enhancement in different configurations of metallic and dielectric nanoantennas has been studied in refs 50 and 56. For comparison, we optimize the Si bowtie nanoantenna in air with $g = 20$ nm. We find that with $l = 230$ nm, $h = 260$ nm, and $r_c = 22$ nm, the simulated maximum field enhancement in the middle of the gap is ~ 11 . This value is lower than the reported field enhancement of ~ 26 ⁵⁰ for a Si cylindrical dimer in air for the same gap. To compare with our case of a nanoantenna on a substrate, we simulate the Si cylindrical dimer on a Si substrate, for a gap of 20 nm. The result is a maximum enhancement in the middle of the gap of ~ 11 (for $d = 130$ nm and $h = 320$ nm), as shown in Figure 4c. This is slightly lower than the value found for the Si bowtie nanoantenna (~ 12). This demonstrates that the addition of a substrate reduces the field enhancement in the Si cylindrical dimer. It also shows that the shape of the structure (triangles for the bowtie or cylindrical for the dimer) has limited influence on the field enhancement in the middle of the gap. This is in line with the weak dependency on fillet radius r_c , as shown in Figure 4a. For reference, field enhancements of ~ 5.5 and ~ 4.7 have been reported for cylindrical dimers with 20 nm gap, using silicon-on-insulator⁵² and silicon-on-glass substrates,⁵⁷ respectively.

Low-index materials such as silica ($n = 1.461$), glass ($n = 1.5$), and quartz ($n = 1.541$) are commonly used as substrates for dielectric nanoantennas.^{22,46} On the other hand, using a high-index material for both the nanoantenna and the substrate is less common but has been reported in some works.^{20,21,27,29} The maximum field enhancement is shown in Figure 4d (with diamonds) for the four materials considered and for the same material as the nanoantenna and the substrate. The gap here is taken to be $g = 50$ nm, and the enhancement is taken in the middle of the gap. As expected, field enhancement increases with the refractive index of the material. We also investigate the effect of a low-index substrate on the field enhancement. The Si bowtie nanoantenna is optimized for three substrate materials (silica, glass, and quartz) and $g = 50$ nm. The simulated field enhancements are ~ 5.6 , ~ 5.7 , and ~ 5.8 for

quartz, glass, and silica, respectively, as shown in Figure 4d. These values are slightly lower than for a Si substrate (~ 6.5) with the same gap. Apart from the small improvement of the field enhancement, the Si substrate provides significantly lower heating than the low-index and thermally insulating substrates, which will be discussed in Section 3.2.

The electric field enhancement $|E|/|E_0|$, that is, the hotspot, in the bowtie gap can be used to trap a nanoparticle and also to enhance Raman scattering from that particle. The excited Raman scattering extends over a wide range of wavelengths, depending on the chemical composition of the nanoparticle. The Raman enhancement factor EF_{Raman} can be determined using the following expression⁵⁹

$$EF_{\text{Raman}} = \left| \frac{E}{E_0} \right|^2 \times \left| \frac{E_{\text{emission}}}{E_0} \right|^2 \quad (1)$$

where $|E|^2/|E_0|^2$ is the intensity enhancement at the incident wavelength ($\lambda = 785$ nm) and $|E_{\text{emission}}|^2/|E_0|^2$ is the intensity enhancement at the Raman emission wavelength. To find the enhancement at the Raman emission wavelengths (here taken to be 785–900 nm), the simulation is carried out with a plane wave incident on the nanoantenna. Using eq 1, the Raman enhancement factor is plotted in Figure 5 as a function of

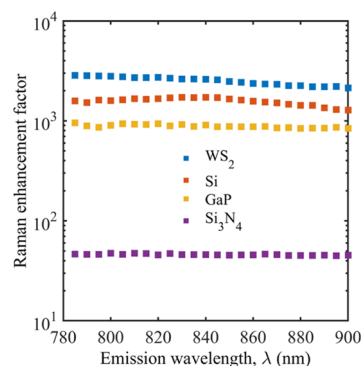


Figure 5. Raman enhancement as a function of Raman emission wavelength. The excitation wavelength is 785 nm. Optimized designed parameters of the nanoantennas are used in the simulations with $g = 50$ nm.

Raman emission wavelength. The calculated Raman enhancement factor exceeds 10^3 over a broad emission spectrum for WS₂, Si, and GaP nanoantennas. This enhancement is comparable to other works on dielectric nanoantennas.^{29,52} The Raman enhancement factor for the Si₃N₄ nanoantenna is considerably lower ($<10^2$), which is due to lower field enhancement, and, in turn, lower refractive index. A simplified approach to find the Raman enhancement is to use the fourth power of the field enhancement for the excitation wavelength (785 nm), as reported in refs 29, 52, and 60. This is a good approximation also for the cases considered here.

3.2. Temperature Increase around the Nanoantenna

The mechanism for heat generation in nanoantennas is simple: the incident light produces movement of mobile carriers inside the material, thus gaining kinetic energy.⁶¹ This energy turns into heat that diffuses away from the nanoantennas, leading to an increase in temperature of the surrounding medium. We next investigate the local temperature increase ΔT in the middle of the gap with respect to a reference temperature $T_0 = 293.15$ K. For the simulation of temperature increase, the

optimized dimensions of the WS₂ and Si nanoantennas are considered with an input intensity I_{in} of 1 mW/ μm^2 . A higher I_{in} is generally required for optical trapping (will be discussed later), and the temperature increase will thus be higher and can be calculated from a linear relationship between I_{in} and ΔT .²¹ Figure 6a,b shows the temperature increase distributions in the

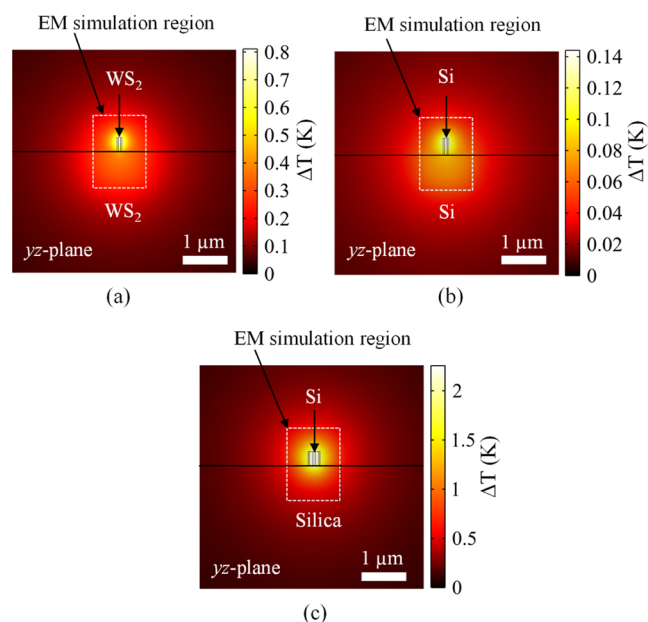


Figure 6. Distribution of temperature increase in the yz plane (middle of the gap) in (a) WS₂ and (b) Si nanoantenna for an intensity of 1 mW/ μm^2 , with the substrate and bowtie having the same material. (c) Effect on the temperature increase due to a low-index silica substrate in the Si bowtie nanoantenna. The white boxes in (a–c) indicate the region of EM simulation used for calculating absorbed power in the nanoantenna and substrate. For all simulations, $g = 50$ nm.

yz plane for WS₂ and Si nanoantennas, respectively. The distributions indicate that ΔT is the highest in the gap of the bowtie. This is due to absorption where high field enhancement overlaps with the inner edge of the bowtie, facing the gap. The color bars show a modest temperature increase of 0.8 and 0.15 K in the WS₂ and Si nanoantennas, respectively, for the relatively low input intensity considered here. As GaP and Si₃N₄ are transparent at 785 nm, they thus do not absorb light and there is no heating, unless there are fabrication defects or impurities.

The high-index Si substrate in the Si bowtie nanoantenna provides a slightly higher field enhancement than substrates with low refractive index, as discussed in Section 3.1. Now, we

investigate the temperature increase in the Si bowtie nanoantenna with silica as an example of a low-index, thermally insulating substrate. The result is a maximum ΔT of ~ 2.3 K (Figure 6c), which is 15 times higher than with a Si substrate ($I_{\text{in}} = 1$ mW/ μm^2). The high thermal conductivity of the Si substrate ($\kappa_{\text{Si}} \approx 148$ W K⁻¹ m⁻¹) serves as a good heat sink that minimizes the heating effect. On the other hand, the low thermal conductivity of silica ($\kappa_{\text{silica}} \approx 1.38$ W K⁻¹ m⁻¹) prevents heat diffusion through the substrate and the nanoantenna heats up. With glass ($\kappa_{\text{glass}} \approx 1$ W K⁻¹ m⁻¹)²¹ and quartz substrates ($\kappa_{\text{quartz}} \approx 3$ W K⁻¹ m⁻¹), ΔT is ~ 2.6 K and ~ 1.4 K, respectively (not shown).

3.3. Thermally Induced Flow

Temperature increase nearby a nanoantenna produces an upward convection of fluid due to reduction of the mass density of the fluid.¹³ We perform laminar flow simulations of this convective velocity field for $I_{\text{in}} = 1$ mW/ μm^2 and a water chamber height of 15 μm . Figure 7a shows the distribution of flow around a WS₂ nanoantenna, showing both magnitude and direction in the middle of the gap (yz plane). As expected, water moves upward and outward, showing a radially symmetric pattern with zero velocity near the nanoantenna surface. An identical flow pattern is obtained for a Si nanoantenna, but with a significantly reduced peak fluid velocity, as shown in Figure 7b, of 0.023 versus 0.12 nm/s for the WS₂ nanoantenna. As the fluid velocity is linearly related to the temperature increase, the small temperature increase in the Si nanoantenna results in a low fluid velocity. Increasing I_{in} will linearly increase temperature, which in turns linearly increases the fluid velocity. A small fluid velocity is highly desirable to maintain stable trapping.^{13,34} When a nanoparticle is trapped, the thermally induced flow gives a force on the particle that pushes it away from the equilibrium position. To find this force, we integrate the total fluid stress over the nanoparticle (here a PS bead) surface along the z -direction. We find that the induced fluid force for the Si nanoantenna is very weak ($\sim 10^{-19}$ N/mW/ μm^2). This is four orders of magnitude lower than the optical force (see the next section). Thus, the trapping itself will be unperturbed by the fluid force. However, a high input intensity will increase the fluid velocity around the nanoantenna and can obstruct particles from getting close to the nanoantenna and thus stop them from being trapped.

3.4. Optical Trapping of Single Nanospheres

In this section, the field enhancement found in Section 3.1 is used to study optical trapping. The bowtie gap is taken to be 50 nm wide, which poses an upper limit for the size of nanospheres that can be trapped. From this limit, the largest diameter considered here is 40 nm. A nanosphere will be

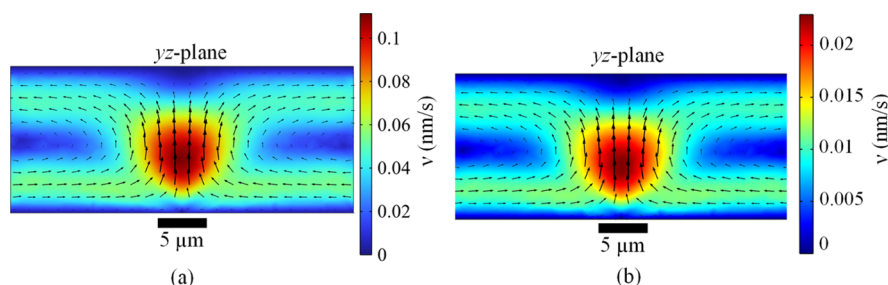


Figure 7. Distribution of thermally induced fluid velocity in the center of the yz plane for (a) WS₂ and (b) Si nanoantenna with an intensity of 1 mW/ μm^2 .

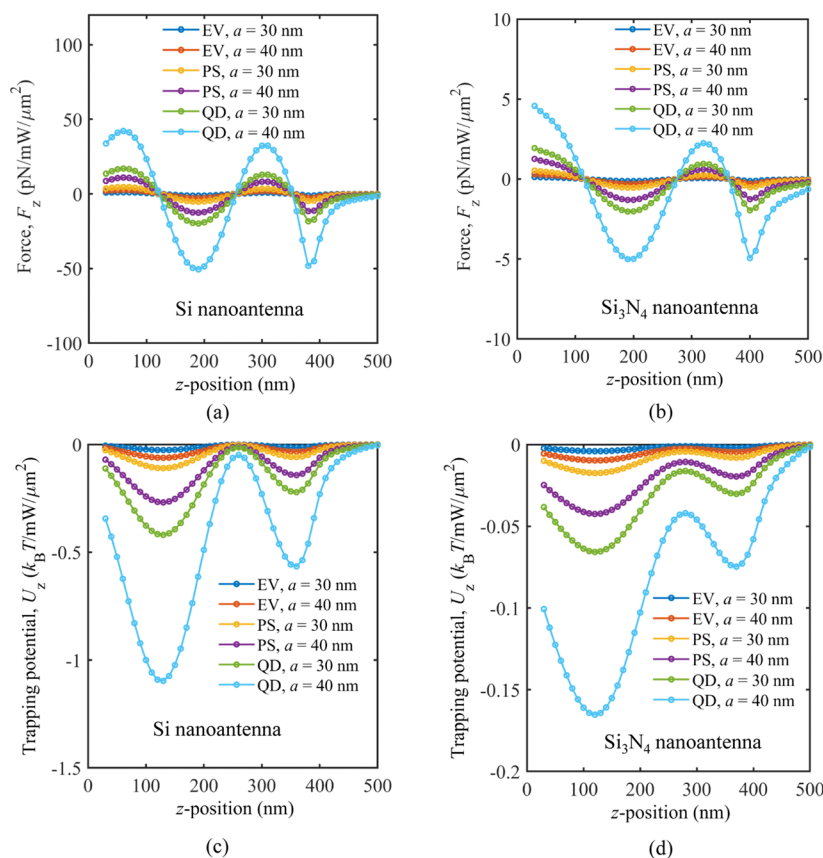


Figure 8. Optical force F_z (a,c) exerted on the trapped nanospheres and the corresponding trapping potential (b,d) for Si and Si_3N_4 nanoantennas, respectively, for $I_{\text{in}} = 1 \text{ mW}/\mu\text{m}^2$. The nanosphere is placed in the middle of the gap, at $x = 0$ and $y = 0$.

attracted to the point of the highest intensity of the hotspot due to gradient force and can be optically trapped.^{62,63} We find the field distribution with a nanosphere placed in the middle of the gap starting with $z = 30 \text{ nm}$. The time-averaged optical force F_z is computed by integrating the Maxwell stress tensor over the surface of the nanosphere. This procedure is repeated for increasing positions of the sphere up to a vertical position ($z = 500 \text{ nm}$) where the optical force approaches zero. The calculated F_z as a function of position z is plotted for Si (Figure 8a) and Si_3N_4 nanoantennas (Figure 8b) for nanospheres with 30 and 40 nm diameter. As discussed earlier, the optimized design shows two trapping hotspots; hence, the force spectra have two equilibrium positions. In Figure 8a, F_z is positive for $z < 120 \text{ nm}$ which pushes up the nanosphere toward the equilibrium position. For $120 \text{ nm} < z < 350 \text{ nm}$, the nanosphere is pulled down toward the equilibrium position, with F_z being negative. The force F_z is zero at $z = 120 \text{ nm}$, indicating the first equilibrium position. After the first equilibrium position, F_z crosses zero at $z = 255 \text{ nm}$, corresponding to a minimum for the field enhancement between the two hotspots, as shown in Figure 3e. Again, referring to Figure 8a, for $255 \text{ nm} < z < 350 \text{ nm}$ and $z > 350 \text{ nm}$, F_z is positive and negative, respectively, resulting in pushing up or pulling down the nanosphere toward the second equilibrium position at $z = 350 \text{ nm}$. To summarize, the equilibrium positions for the Si nanoantenna are $z = 120 \text{ nm}$ and $z = 350 \text{ nm}$. For WS_2 , GaP, and Si_3N_4 nanoantennas, the equilibrium positions are $z = 110$ and 320 nm , $z = 115$ and 340 nm , and $z = 120$ and 360 nm , respectively (not shown).

Next, the force F_z is integrated along a vertical path ($z = 30$ – 500 nm) to find the trapping potential U_z . Figure 8c,d shows U_z as a function of z -position for Si and Si_3N_4 nanoantennas, respectively. Two trapping potential wells can be seen, which is due to the two hotspots. For each trapping nanosphere, the trapping potential curve shows two potential minima at the equilibrium positions, that is, the positions with $F_z = 0$. The difference between the potential minima with respect to zero potential gives potential depth U_{depth} . The numerically calculated U_{depth} for WS_2 , Si, GaP, and Si_3N_4 nanoantennas is plotted as a function of nanosphere radius and shown by the square markers in Figure 9a–d.

The potential depth U_{depth} can also be found analytically from the intensity for a Rayleigh particle⁶⁴

$$U_{\text{depth}} = \frac{2\pi n_2 a^3}{c} \left(\frac{m^2 - 1}{m^2 + 2} \right) [I_{\text{max}} - I_{\text{min}}] \quad (2)$$

where a is the nanosphere radius, n_1 is the refractive index of the nanosphere, n_2 is the refractive index of the surrounding medium, c is the speed of light, $m = n_2/n_1$ is the relative refractive index, $I_{\text{max}} = |E|^2/|E_0|^2 \times I_{\text{in}}$ is the maximum enhancement of the field intensity, I_{min} is the minimum intensity, and I_{in} is the intensity of the input beam. Using eq 2, U_{depth} is plotted versus nanosphere radius for $I_{\text{in}} = 1 \text{ mW}/\mu\text{m}^2$, as shown by the solid lines in Figure 9a–d for WS_2 , Si, GaP, and Si_3N_4 nanoantennas, respectively. There is good agreement between the numerical results using the Maxwell stress tensor on a particle inserted in the gap and using the Rayleigh approximation on the field distribution without a particle. Thus, the Rayleigh approximation is valid for these particles,⁶⁵

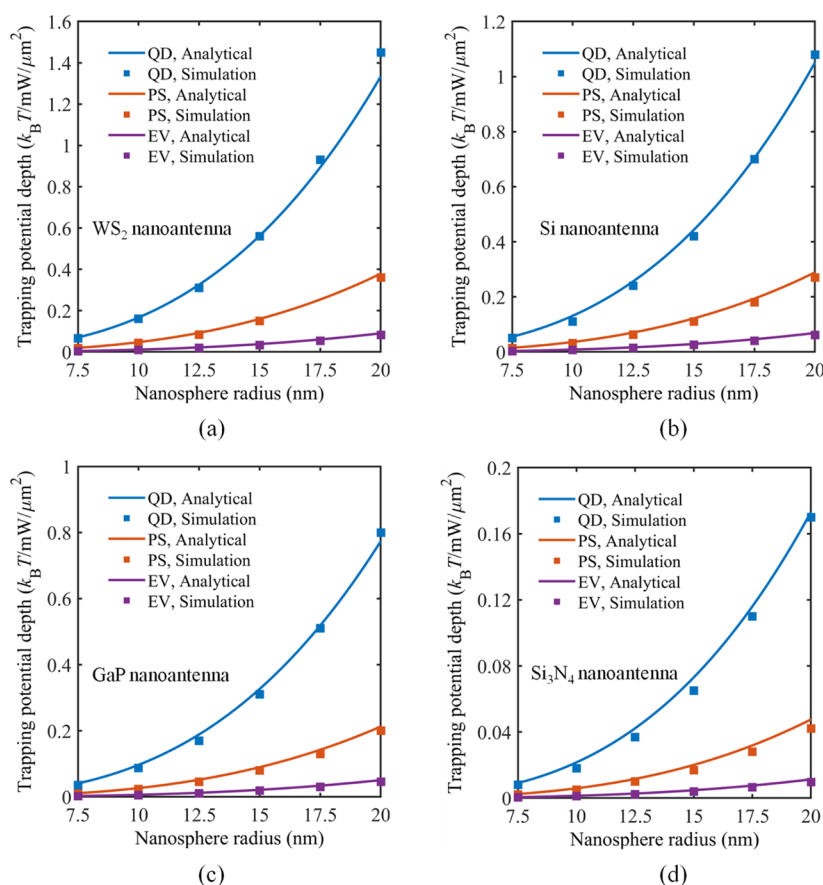


Figure 9. Trapping potential depth as a function of nanosphere radius using (a) WS₂, (b) Si, (c) GaP, and (d) Si₃N₄ nanoantennas with gap $g = 50$ nm. Analytical and simulated potential depths are shown by solid lines and square markers, respectively.

and, more noteworthy, the particles do not disturb the field distribution significantly. As expected, bigger nanospheres gives higher U_{depth} , as U_{depth} is proportional to the third power of nanosphere radius. In addition, a larger refractive index provides higher potential U_{depth} ($n_{\text{QD}} = 2.49$ vs $n_{\text{PS}} = 1.59$ and $n_{\text{EV}} = 1.39$), as expected.

To investigate how the optical trapping competes with Brownian motion, we now determine the input intensity I_{in} required for stable trapping in the presence of Brownian motion. The trapping potential produced by the gradient force must be strong enough to overcome the kinetic energy of the nanospheres. A trapping potential of $10 k_B T$ is commonly considered sufficient for stable trapping,^{1,64,66} where k_B is the Boltzmann constant and T is the room temperature. As optical forces have been found for $I_{\text{in}} = 1 \text{ mW}/\mu\text{m}^2$, the calculated trapping depth is expressed in $k_B T / mW / \mu\text{m}^2$. Thus, I_{in} required for $10 k_B T$ can be found simply by scaling up the potential found for $1 \text{ mW}/\mu\text{m}^2$. The potentials U_{trap} plotted in Figure 9 indicate that high intensity I_{in} is necessary to achieve $10 k_B T$ for the smallest nanospheres. As an example, WS₂ and QD with $r = 7.5$ nm give $0.066 k_B T$ for $1 \text{ mW}/\mu\text{m}^2$, thus obtaining $10 k_B T$ requires an I_{in} of $151 \text{ mW}/\mu\text{m}^2$. As the field enhancement increases with smaller gap, the potential depth also increases for smaller gap. Thus, the gap should be tailored to the size of the particles to be trapped, to achieve the necessary potential for the lowest possible input intensity.

For the Si nanoantenna and with a QD, the trapping potential depth is 0.05 and $1.1 \text{ mW}/\mu\text{m}^2$ for a radius of 7.5 and 20 nm, respectively. As the radius of the nanoparticle is small

and the field enhancement in the gap is moderate, the gradient force acting on the nanoparticle becomes small, resulting in a low trapping potential depth. Several geometries of the plasmonic nanostructure such as nanoapertures,^{67,68} double nanorods,⁶⁹ nanopyramids,⁷⁰ and bowtie nanoapertures⁷¹ have been investigated to trap smaller nanoparticles (10 – 50 nm in diameter). These configurations show a larger trapping potential depth compared to the proposed dielectric bowtie nanoantennas, with a low input intensity. Besides, dielectric nanoantenna-based optical trapping has been also reported in a few works,^{21,34} showing comparable trapping potential depths as found for the WS₂, Si, and GaP bowtie nanoantenna. To summarize, as shown in Figure 9, a bowtie nanoantenna made of a material with medium refractive index, taken to be Si₃N₄ here, is only suitable for trapping relatively large nanospheres (e.g., radius >15 nm) with high refractive index (here QDs). For materials with high refractive index, here WS₂, GaP, and Si, an intensity of $>10 \text{ mW}/\mu\text{m}^2$ is necessary to trap QDs, while $>50 \text{ mW}/\mu\text{m}^2$ is necessary for PS beads. EVs require even higher intensity.

For the case of a Si nanoantenna on a Si substrate, an input intensity of 10 and $50 \text{ mW}/\mu\text{m}^2$ gives a heating of ~ 1.4 and ~ 7 K, respectively, according to Figure 6b. These intensities are relatively high but can be obtained by focusing a high-power laser to a small spot. The resulting thermally induced flow and flow-induced forces on the particles will be limited, as shown in Section 3.3. Furthermore, the Si nanoantenna and substrate will have no problem withstanding this intensity and heating. A thin layer of thermal oxide will be formed on the

surface of crystalline Si, with a thickness of 1–2 nm.⁷² As the layer will be on the surface and silica is transparent, the heat conductivity and the absorption will not be affected. However, silica has a lower refractive index than Si. The layer will effectively increase the gap between the triangles, thus somewhat reducing the field enhancement. For an application, it is important that the nanoparticle can support the heating. In summary, Si nanoantennas on a Si substrate have some potential for use at 785 nm, depending on the size and type of particles to be trapped. As stated above, the gap of the nanoantenna must be tailored to the size of the particles.

4. CONCLUSIONS

We have numerically investigated all-dielectric bowtie nanoantennas for optical trapping and Raman spectroscopy of a single nanoparticle. The nanoantenna consists of a pair of triangles separated by a 50 nm gap, resting on a substrate made of the same material. This is typically the case for structures that are etched out of a substrate. We have considered four different dielectric materials (multilayer WS₂, Si, GaP, and Si₃N₄) for the nanoantennas. Using numerical simulations, we have optimized the design parameters of the nanoantennas for the highest electric field enhancement and Raman enhancement factor at 785 nm. We have shown a low to intermediate field enhancement in the bowtie gap, depending on the refractive index of the materials and dimensions of the nanoantennas. The calculated Raman enhancement factor varies with the choice of materials, showing >10³ for WS₂, Si, and GaP nanoantennas. We have presented temperature distributions around the WS₂ and Si nanoantennas, as these materials are absorbing at 785 nm. The maximum temperature increase was found to be ~0.80 and ~0.15 K, respectively, for a modest input intensity of 1 mW/μm². The good thermal conductivity limits the temperature increase, particularly for Si. We have also simulated the thermally induced flow for these two absorbing materials, which is found to be insignificant. For the materials that are transparent at 785 nm, GaP and Si₃N₄, the limiting factor is the available intensity, unless absorption in the fluid or the particle becomes a problem. Of the materials considered, GaP performs the best, as expected, due to high refractive index and transparency. Trapping of biological nanoparticles with any of the investigated materials, for example, EVs, will require a high intensity and will be challenging. The input intensity required for stable trapping is found to be >10 mW/μm² for QD and >50 mW/μm² for PS beads, for the three high-index materials considered (WS₂, GaP, and Si), and for 20 nm diameter particles in a 50 nm gap. These intensities are relatively high but can readily be obtained by focusing a high-power laser to a small spot. If illuminating an array of nanoantennas, the distance between the nanoantennas must be small and their number will be limited by the available laser power. Whereas monolayer WS₂ and GaP are not standard semiconductor materials, Si is indeed the standard. Using the intensities found together with the induced temperature increase, it is shown that a Si nanoantenna on a Si substrate will induce a temperature increase of ~1.4 and ~7 K for stable trapping of 20 nm QD and PS particles, respectively. For most applications, these values are acceptable and the structure itself will be inert with such temperatures and intensities. This allows for the use of an easily fabricated all-Si nanostructure for trapping and Raman spectroscopy. It is shown that the field enhancement only has a weak dependency on the fillet radius of the bowties and on the

geometrical structure (triangles for bowties or cylindrical for dimers). The shape of the nanoantenna is thus not critical, which relaxes fabrication tolerances. Note that this is for the field enhancement in the middle of the gap, and the dependency might be stronger on the tips of a bowtie. The main challenge regarding fabrication is to make the gap between the triangles. A gap $g = 50$ nm, as used in most of this work, can be readily made with electron beam lithography. Considering an application, with a given diameter and refractive index of the particles, the gap must be tailored to the particles, and it must be checked if the induced temperature increase is acceptable. If the values are acceptable, a straight-forward fabrication process with Si can be used, otherwise it is necessary to develop a suitable process for GaP or revert to different structures and materials than those considered in this work.

AUTHOR INFORMATION

Corresponding Author

Md Rabiul Hasan – Department of Physics and Technology, UiT The Arctic University of Norway, Tromsø 9037, Norway; orcid.org/0000-0002-9538-454X; Email: md.r.hasan@uit.no

Author

Olav Gaute Hellesø – Department of Physics and Technology, UiT The Arctic University of Norway, Tromsø 9037, Norway; orcid.org/0000-0002-0494-8240

Complete contact information is available at: <https://pubs.acs.org/10.1021/acsaoam.2c00171>

Notes

The authors declare no competing financial interest.

ACKNOWLEDGMENTS

The authors would like to thank the Research Council of Norway for supporting the research work through grant number 302333. The publication charge for this article is provided by UiT The Arctic University of Norway.

REFERENCES

- (1) Ashkin, A.; Dziedzic, J. M.; Bjorkholm, J. E.; Chu, S. Observation of a single-beam gradient force optical trap for dielectric particles. *Opt. Lett.* **1986**, *11*, 288–290.
- (2) Omori, R.; Kobayashi, T.; Suzuki, A. Observation of a single-beam gradient-force optical trap for dielectric particles in air. *Opt. Lett.* **1997**, *22*, 816–818.
- (3) Thurn, R.; Kiefer, W. Raman-Microsampling Technique Applying Optical Levitation by Radiation Pressure. *Appl. Spectrosc.* **1984**, *38*, 78–83.
- (4) Kaiser, T.; Roll, G.; Schweiger, G. Investigation of coated droplets in an optical trap: Raman-scattering, elastic-light-scattering, and evaporation characteristics. *Appl. Opt.* **1996**, *35*, 5918–5924.
- (5) Rkiouak, L.; Tang, M. J.; Camp, J. C. J.; McGregor, J.; Watson, I. M.; Cox, R. A.; Kalberer, M.; Ward, A. D.; Pope, F. D. Optical trapping and Raman spectroscopy of solid particles. *Phys. Chem. Chem. Phys.* **2014**, *16*, 11426–11434.
- (6) Spesyvtseva, S. E. S.; Dholakia, K. Trapping in a Material World. *ACS Photonics* **2016**, *3*, 719–736.
- (7) Bendix, P. M.; Reihani, S. N. S.; Oddershede, L. B. Direct measurements of heating by electromagnetically trapped gold nanoparticles on supported lipid bilayers. *ACS Nano* **2010**, *4*, 2256–2262.

- (8) Verschueren, D.; Shi, X.; Dekker, C. Nano-Optical Tweezing of Single Proteins in Plasmonic Nanopores. *Small Methods* **2019**, *3*, 1800465.
- (9) Zhang, J.; Lu, F.; Zhang, W.; Yu, W.; Zhu, W.; Premaratne, M.; Mei, T.; Xiao, F.; Zhao, J. Optical trapping of single nano-size particles using a plasmonic nanocavity. *J. Condens. Matter Phys.* **2020**, *32*, 475301.
- (10) Wu, B.; Lou, Y.; Wu, D.; Min, Q.; Wan, X.; Zhang, H.; Yu, Y.; Ma, J.; Si, G.; Pang, Y. Directivity-Enhanced Detection of a Single Nanoparticle Using a Plasmonic Slot Antenna. *Nano Lett.* **2022**, *22*, 2374–2380.
- (11) Pin, C.; Ishida, S.; Takahashi, G.; Sudo, K.; Fukaminato, T.; Sasaki, K. Trapping and Deposition of Dye–Molecule Nanoparticles in the Nanogap of a Plasmonic Antenna. *ACS Omega* **2018**, *3*, 4878–4883.
- (12) Tuna, Y.; Kim, J. T.; Liu, H.-W.; Sandoghdar, V. Levitated Plasmonic Nanoantennas in an Aqueous Environment. *ACS Nano* **2017**, *11*, 7674–7678.
- (13) Donner, J. S.; Baffou, G.; McCloskey, D.; Quidant, R. Plasmon-Assisted Optofluidics. *ACS Nano* **2011**, *5*, 5457–5462.
- (14) Barreda, A. I.; Sanz, J. M.; González, F. Using linear polarization for sensing and sizing dielectric nanoparticles. *Opt. Express* **2015**, *23*, 9157–9166.
- (15) García-Cámara, B.; Gómez-Medina, R.; Sáenz, J. J.; Sepúlveda, B. Sensing with magnetic dipolar resonances in semiconductor nanospheres. *Opt. Express* **2013**, *21*, 23007–23020.
- (16) Yang, A. H. J.; Moore, S. D.; Schmidt, B. S.; Klug, M.; Lipson, M.; Erickson, D. Optical manipulation of nanoparticles and biomolecules in sub-wavelength slot waveguides. *Nature* **2009**, *457*, 71–75.
- (17) Yang, A. H. J.; Lerdsuchatawanich, T.; Erickson, D. Forces and Transport Velocities for a Particle in a Slot Waveguide. *Nano Lett.* **2009**, *9*, 1182–1188.
- (18) Kang, P.; Serey, X.; Chen, Y. F.; Erickson, D. Angular orientation of nanorods using nanophotonic tweezers. *Nano Lett.* **2012**, *12*, 6400–6407.
- (19) Mandal, S.; Serey, X.; Erickson, D. Nanomanipulation using silicon photonic crystal resonators. *Nano Lett.* **2010**, *10*, 99–104.
- (20) Xu, Z.; Crozier, K. B. All-dielectric nanotweezers for trapping and observation of a single quantum dot. *Opt. Express* **2019**, *27*, 4034–4045.
- (21) Xu, Z.; Song, W.; Crozier, K. B. Optical Trapping of Nanoparticles Using All-Silicon Nanoantennas. *ACS Photonics* **2018**, *5*, 4993–5001.
- (22) Hasan, M. R.; Hellesø, O. G. Dielectric optical nanoantennas. *Nanotechnology* **2021**, *32*, 202001.
- (23) García-Etxarri, A.; Gómez-Medina, R.; Froufe-Pérez, L. S.; López, C.; Chantada, L.; Scheffold, F.; Aizpurua, J.; Nieto-Vesperinas, M.; Sáenz, J. J. Strong magnetic response of submicron Silicon particles in the infrared. *Opt. Express* **2011**, *19*, 4815–4826.
- (24) Rodríguez, I.; Shi, L.; Lu, X.; Korgel, B. A.; Alvarez-Puebla, R. A.; Meseguer, F. Silicon nanoparticles as Raman scattering enhancers. *Nanoscale* **2014**, *6*, S666–S670.
- (25) Todisco, F.; Malureanu, R.; Wolff, C.; Gonçalves, P. A. D.; Roberts, A. S.; Mortensen, N. A.; Tserkezis, C. Magnetic and electric Mie-exciton polaritons in silicon nanodisks. *Nanophotonics* **2020**, *9*, 803–814.
- (26) Verre, R.; Baranov, D. G.; Munkhbat, B.; Cuadra, J.; Kall, M.; Shegai, T. Transition metal dichalcogenide nanodisks as high-index dielectric Mie nanoresonators. *Nat. Nanotechnol.* **2019**, *14*, 679–683.
- (27) Cambiasso, J.; Grinblat, G.; Li, Y.; Rakovich, A.; Cortés, E.; Maier, S. A. Bridging the Gap between Dielectric Nanophotonics and the Visible Regime with Effectively Lossless Gallium Phosphide Antennas. *Nano Lett.* **2017**, *17*, 1219–1225.
- (28) Remesh, V.; Grinblat, G.; Li, Y.; Maier, S. A.; van Hulst, N. F. Coherent Multiphoton Control of Gallium Phosphide Nanodisk Resonances. *ACS Photonics* **2019**, *6*, 2487–2491.
- (29) Sortino, L.; Zotev, P. G.; Mignuzzi, S.; Cambiasso, J.; Schmidt, D.; Genco, A.; Afmann, M.; Bayer, M.; Maier, S. A.; Sapienza, R.; et al. Enhanced light-matter interaction in an atomically thin semiconductor coupled with dielectric nano-antennas. *Nat. Commun.* **2019**, *10*, 5119.
- (30) Masango, S. S.; Hackler, R. A.; Large, N.; Henry, A.-I.; McAnally, M. O.; Schatz, G. C.; Stair, P. C.; Van Duyne, R. P. High-Resolution Distance Dependence Study of Surface-Enhanced Raman Scattering Enabled by Atomic Layer Deposition. *Nano Lett.* **2016**, *16*, 4251–4259.
- (31) Tang, J.; Wang, Y.; Klare, J. E.; Tulevski, G. S.; Wind, S. J.; Nuckolls, C. Encoding Molecular-Wire Formation within Nanoscale Sockets. *Angew. Chem., Int. Ed.* **2007**, *46*, 3892–3895.
- (32) Barreda, A. I.; Zapata-Herrera, M.; Palstra, I. M.; Mercadé, L.; Aizpurua, J.; Koenderink, A. F.; Martínez, A. Hybrid photonic-plasmonic cavities based on the nanoparticle-on-a-mirror configuration. *Photonics Res.* **2021**, *9*, 2398–2419.
- (33) Ettabib, M. A.; Marti, A.; Liu, Z.; Bowden, B. M.; Zervas, M. N.; Bartlett, P. N.; Wilkinson, J. S. Waveguide Enhanced Raman Spectroscopy for Biosensing: A Review. *ACS Sensors* **2021**, *6*, 2025–2045.
- (34) Zhan, W.; Gao, K.; Zhu, C.; Song, W. Optical trapping using all silicon nanoantennas with ultra-high electric field enhancement. *Appl. Phys. Lett.* **2020**, *117*, 241102.
- (35) Yang, S.; Allen, J. A.; Hong, C.; Arnold, K. P.; Weiss, S. M.; Ndukaife, J. C. Multiplexed Long-Range Electrohydrodynamic Transport and Nano-Optical Trapping with Cascaded Bowtie Photonic Crystal Nanobeams. *Phys. Rev. Lett.* **2023**, *130*, 083802.
- (36) Kinkhabwala, A.; Yu, Z.; Fan, S.; Avlasevich, Y.; Müllen, K.; Moerner, W. E. Large single-molecule fluorescence enhancements produced by a bowtie nanoantenna. *Nat. Photonics* **2009**, *3*, 654–657.
- (37) Fromm, D. P.; Sundaramurthy, A.; Schuck, P. J.; Kino, G.; Moerner, W. E. Gap-dependent optical coupling of single “bowtie” nanoantennas resonant in the visible. *Nano Lett.* **2004**, *4*, 957–961.
- (38) Vuye, G.; Fisson, S.; Nguyen Van, V.; Wang, Y.; Rivory, J.; Abelès, F. Temperature dependence of the dielectric function of silicon using in situ spectroscopic ellipsometry. *Thin Solid Films* **1993**, *233*, 166–170.
- (39) Jellison, G. E. Optical functions of GaAs, GaP, and Ge determined by two-channel polarization modulation ellipsometry. *Opt. Mater.* **1992**, *1*, 151–160.
- (40) Luke, K.; Okawachi, Y.; Lamont, M. R. E.; Gaeta, A. L.; Lipson, M. Broadband mid-infrared frequency comb generation in a Si₃N₄ microresonator. *Opt. Lett.* **2015**, *40*, 4823–4826.
- (41) <https://www.comsol.com/blogs/modeling-the-scattering-of-light-off-of-an-object-on-a-substrate>. 10/03/2023
- (42) Leng, H. X.; Szychowski, B.; Daniel, M. C.; Pelton, M. Strong coupling and induced transparency at room temperature with single quantum dots and gap plasmons. *Nat. Commun.* **2018**, *9*, 4012.
- (43) Smart, C.; Willis, E. Determination of Refractive Indices of Polystyrene Latices by Light Scattering. *J. Colloid Interface Sci.* **1967**, *25*, 577–583.
- (44) Gardiner, C.; Shaw, M.; Hole, P.; Smith, J.; Tannetta, D.; Redman, C. W.; Sargent, I. L. Measurement of refractive index by nanoparticle tracking analysis reveals heterogeneity in extracellular vesicles. *J. Extracell. Vesicles* **2014**, *3*, 25361.
- (45) Peng, B.; Zhang, H.; Shao, H.; Xu, Y.; Zhang, X.; Zhu, H. Thermal conductivity of monolayer MoS₂, MoSe₂, and WS₂: interplay of mass effect, interatomic bonding and anharmonicity. *RSC Adv.* **2016**, *6*, 5767–5773.
- (46) Baranov, D. G.; Zuev, D. A.; Lepeshov, S. I.; Kotov, O. V.; Krasnok, A. E.; Evlyukhin, A. B.; Chichkov, B. N. All-dielectric nanophotonics: the quest for better materials and fabrication techniques. *Optica* **2017**, *4*, 814–825.
- (47) van de Groep, J.; Polman, A. Designing dielectric resonators on substrates: Combining magnetic and electric resonances. *Opt. Express* **2013**, *21*, 26285–26302.
- (48) van de Haar, M. A.; van de Groep, J.; Brenny, B. J.; Polman, A. Controlling magnetic and electric dipole modes in hollow silicon nanocylinders. *Opt. Express* **2016**, *24*, 2047–2064.

- (49) Alaei, R.; Rockstuhl, C.; Fernandez-Corbaton, I. An electromagnetic multipole expansion beyond the long-wavelength approximation. *Opt. Commun.* **2018**, *407*, 17–21.
- (50) Barreda, A.; Hell, S.; Weissflog, M. A.; Minovich, A.; Pertsch, T.; Staude, I. Metal, dielectric and hybrid nanoantennas for enhancing the emission of single quantum dots: A comparative study. *J. Quant. Spectrosc. Radiat. Transfer* **2021**, *276*, 107900.
- (51) Bakker, R. M.; Permyakov, D.; Yu, Y. F.; Markovich, D.; Paniagua-Domínguez, R.; Gonzaga, L.; Samusev, A.; Kivshar, Y.; Luk'yanchuk, B.; Kuznetsov, A. I. Magnetic and Electric Hotspots with Silicon Nanodimers. *Nano Lett.* **2015**, *15*, 2137–2142.
- (52) Caldarola, M.; Albella, P.; Cortés, E.; Rahmani, M.; Roschuk, T.; Grinblat, G.; Oulton, R. F.; Bragas, A. V.; Maier, S. A. Non-plasmonic nanoantennas for surface enhanced spectroscopies with ultra-low heat conversion. *Nat. Commun.* **2015**, *6*, 7915.
- (53) Shafi, M.; Liu, R.; Zha, Z.; Li, C.; Du, X.; Wali, S.; Jiang, S.; Man, B.; Liu, M. Highly efficient SERS substrates with different Ag interparticle nanogaps based on hyperbolic metamaterials. *Appl. Surf. Sci.* **2021**, *555*, 149729.
- (54) Im, H.; Bantz, K. C.; Lindquist, N. C.; Haynes, C. L.; Oh, S.-H. Vertically Oriented Sub-10-nm Plasmonic Nanogap Arrays. *Nano Lett.* **2010**, *10*, 2231–2236.
- (55) Sugimoto, H.; Fujii, M. Broadband Dielectric–Metal Hybrid Nanoantenna: Silicon Nanoparticle on a Mirror. *ACS Photonics* **2018**, *5*, 1986–1993.
- (56) Barreda, A.; Vitale, F.; Minovich, A. E.; Ronning, C.; Staude, I. Applications of Hybrid Metal-Dielectric Nanostructures: State of the Art. *Adv. Photonics Res.* **2022**, *3*, 2100286.
- (57) Regmi, R.; Berthelot, J.; Winkler, P. M.; Mivelle, M.; Proust, J.; Bedu, F.; Ozerov, I.; Begou, T.; Lumeau, J.; Rigneault, H.; et al. All-Dielectric Silicon Nanogap Antennas To Enhance the Fluorescence of Single Molecules. *Nano Lett.* **2016**, *16*, 5143–5151.
- (58) Jin, H. M.; Kim, J. Y.; Heo, M.; Jeong, S.-J.; Kim, B. H.; Cha, S. K.; Han, K. H.; Kim, J. H.; Yang, G. G.; Shin, J.; et al. Ultralarge Area Sub-10 nm Plasmonic Nanogap Array by Block Copolymer Self-Assembly for Reliable High-Sensitivity SERS. *ACS Appl. Mater. Interfaces* **2018**, *10*, 44660–44667.
- (59) Alonso-Gonzalez, P.; Albella, P.; Schnell, M.; Chen, J.; Huth, F.; Garcia-Etxarri, A.; Casanova, F.; Golmar, F.; Arzuabaga, L.; Hueso, L. E.; et al. Resolving the electromagnetic mechanism of surface-enhanced light scattering at single hot spots. *Nat. Commun.* **2012**, *3*, 684.
- (60) Cambiasso, J.; König, M.; Cortés, E.; Schlücker, S.; Maier, S. A. Surface-Enhanced Spectroscopies of a Molecular Monolayer in an All-Dielectric Nanoantenna. *ACS Photonics* **2018**, *5*, 1546–1557.
- (61) Albella, P.; Alcaraz de la Osa, R.; Moreno, F.; Maier, S. A. Electric and Magnetic Field Enhancement with Ultralow Heat Radiation Dielectric Nanoantennas: Considerations for Surface-Enhanced Spectroscopies. *ACS Photonics* **2014**, *1*, 524–529.
- (62) Moffitt, J. R.; Chemla, Y. R.; Smith, S. B.; Bustamante, C. Recent Advances in Optical Tweezers. *Annu. Rev. Biochem.* **2008**, *77*, 205–228.
- (63) Dogariu, A.; Sukhov, S.; Sáenz, J. Optically induced 'negative forces. *Nat. Photonics* **2012**, *7*, 24–27.
- (64) Zemánek, P.; Jonáš, A.; Šrámek, L.; Liška, M. Optical trapping of Rayleigh particles using a Gaussian standing wave. *Opt. Commun.* **1998**, *151*, 273–285.
- (65) Nieto-Vesperinas, M.; Sáenz, J. J.; Gómez-Medina, R.; Chantada, L. Optical forces on small magnetodielectric particle. *Opt. Express* **2010**, *18*, 11428–11443.
- (66) Maragò, O. M.; Jones, P. H.; Gucciardi, P. G.; Volpe, G.; Ferrari, A. C. Optical trapping and manipulation of nanostructures. *Nat. Nanotechnol.* **2013**, *8*, 807–819.
- (67) Juan, M. L.; Gordon, R.; Pang, Y.; Eftekhari, F.; Quidant, R. Self-induced back-action optical trapping of dielectric nanoparticles. *Nat. Phys.* **2009**, *5*, 915–919.
- (68) Pang, Y.; Gordon, R. Optical Trapping of 12 nm Dielectric Spheres Using Double-Nanoholes in a Gold Film. *Nano Lett.* **2011**, *11*, 3763–3767.
- (69) Zhang, W.; Huang, L.; Santschi, C.; Martin, O. J. F. Trapping and Sensing 10 nm Metal Nanoparticles Using Plasmonic Dipole Antennas. *Nano Lett.* **2010**, *10*, 1006–1011.
- (70) Tsuboi, Y.; Shoji, T.; Kitamura, N.; Takase, M.; Murakoshi, K.; Mizumoto, Y.; Ishihara, H. Optical Trapping of Quantum Dots Based on Gap-Mode-Excitation of Localized Surface Plasmon. *J. Phys. Chem. Lett.* **2010**, *1*, 2327–2333.
- (71) El Eter, A.; Hameed, N. M.; Baida, F. I.; Salut, R.; Filiatre, C.; Nedeljkovic, D.; Atie, E.; Bole, S.; Grosjean, T. Fiber-integrated optical nano-tweezer based on a bowtie-aperture nano-antenna at the apex of a SNOM tip. *Opt. Express* **2014**, *22*, 10072–10080.
- (72) Irene, E. A.; van der Meulen, Y. J. Silicon Oxidation Studies: Analysis of SiO₂ Film Growth Data. *J. Electrochem. Soc.* **1976**, *123*, 1380–1384.

Paper III: Metasurface supporting quasi-BIC for optical trapping and Raman-spectroscopy of biological nanoparticles

Published in Optics Express, February 2023.

Authors: Md Rabiul Hasan, and Olav Gaute Hellestø

Contribution notes: Md Rabiul Hasan conceived the idea, performed all simulations and data analysis. Olav Gaute Hellestø contributed to derive equations. Md Rabiul Hasan wrote the initial draft and Olav Gaute Hellestø finalized it before submission. Both authors contributed to revise the manuscript.



Metasurface supporting quasi-BIC for optical trapping and Raman-spectroscopy of biological nanoparticles

MD RABIUL HASAN  AND OLAV GAUTE HELLESØ* 

Department of Physics and Technology, UiT The Arctic University of Norway, Tromsø, Norway

**olav.gaute.helleso@uit.no*

Abstract: Optical trapping combined with Raman spectroscopy have opened new possibilities for analyzing biological nanoparticles. Conventional optical tweezers have proven successful for trapping of a single or a few particles. However, the method is slow and cannot be used for the smallest particles. Thus, it is not adapted to analyze a large number of nanoparticles, which is necessary to get statistically valid data. Here, we propose quasi-bound states in the continuum (quasi-BICs) in a silicon nitride (Si_3N_4) metasurface to trap smaller particles and many simultaneously. The quasi-BIC metasurface contains multiple zones with high field-enhancement ('hotspots') at a wavelength of 785 nm, where a single nanoparticle can be trapped at each hotspot. We numerically investigate the optical trapping of a type of biological nanoparticles, namely extracellular vesicles (EVs), and study how their presence influences the resonance behavior of the quasi-BIC. It is found that perturbation theory and a semi-analytical expression give good estimates for the resonance wavelength and minimum of the potential well, as a function of the particle radius. This wavelength is slightly shifted relative to the resonance of the metasurface without trapped particles. The simulations show that the Q-factor can be increased by using a thin metasurface. The thickness of the layer and the asymmetry of the unit cell can thus be used to get a high Q-factor. Our findings show the tight fabrication tolerances necessary to make the metasurface. If these can be overcome, the proposed metasurface can be used for a lab-on-a-chip for mass-analysis of biological nanoparticles.

© 2023 Optica Publishing Group under the terms of the [Optica Open Access Publishing Agreement](#)

1. Introduction

A blood-sample contains a vast number of biological nanoparticles of various types. One example is extracellular vesicles (EVs), which includes exosomes (diameter 30–100 nm) and microvesicles (diameter 100–1000 nm). EVs are considered a mechanism for intercellular communications, allowing cells to exchange proteins, lipids, and genetic material [1–3]. They can be important indicators of different conditions of a producing organism, and therefore can have applications in clinical settings. EVs are heterogeneous and exist in large numbers. Methods that analyse a sample of fluid, i.e., average over all the EVs in the sample, thus have limited usefulness as they do not capture the heterogeneous nature of the EVs and can hide important features present only for a few EVs in a population. Likewise, a method that analyses a limited number of EVs does not give statistically valid information about the population of EVs. By combining optical tweezers with Raman-spectroscopy to do 'Raman tweezers microspectroscopy', the composition of a single, suspended EV can be obtained [4–6]. However, the method is limited to particles that are larger than 100 nm in diameter and particles are analysed one at a time, and it thus takes time to build up statistics. The aim of this work is to investigate methods that can analyse biological nanoparticles one-by-one, but in parallel, with Raman-spectroscopy.

Nanophotonics offers several methods that can trap smaller particles, e.g., slit-waveguides [7,8] and photonic crystals [9–11]. But these methods typically rely on silicon, which is not transparent in the near-visible wavelengths and thus cannot be combined with Raman-spectroscopy. The

use of plasmonics and surface-enhanced Raman-scattering (SERS) [12–14] is problematic. The spectrum collected from one particle at one location can be different from that collected at another location due to different surface enhancement. In this paper, we propose to use a metasurface consisting of tilted elliptical bars, made of silicon nitride (Si_3N_4), to trap biological nanoparticles and analyse them with Raman-spectroscopy. Optical trapping using a silicon metasurface with elliptical bars has been proposed at a near-infrared (NIR) wavelength (1550 nm) [15]. Here, the metasurface dimensions are modified so that the operating wavelength can be moved from NIR to a near-visible wavelength, here 785 nm. As opposed to silicon, Si_3N_4 is transparent at 785 nm, making it suitable for combining optical trapping and Raman-spectroscopy. The fabrication technology for Si_3N_4 is mature and it has thus been chosen for the simulations in this work. There are also other suitable materials with comparable or higher refractive index, e.g., Ta_2O_5 and TiO_2 . The methods used and the overall results reported in this work will be valid for these materials too, but with the precise values depending on the refractive index.

A metasurface with elliptical bars can support quasi-bound states in the continuum (quasi-BICs) [15–18], which gives large electric field enhancement that we propose to use for trapping and excitation of Raman-scattering. True BICs are nonradiating states of light showing an infinite Q-factor [19], while quasi-BICs have a finite Q-factor. A metasurface with elliptical bars shows a true BIC for a perfectly symmetric structure (parallel elliptical bars), as previously shown in several works [15–18]. Introducing an in-plane asymmetry by rotating the bars results in a quasi-BIC [16], giving a finite Q-factor. Asymmetry can also be achieved by asymmetrically changing the ellipticity of the bars [17]. Even in a perfectly symmetry-protected system, the Q-factor is finite due to the finite size of the structure and material absorption [20]. Additionally, adding a perturbation element to a symmetric structure can also create a quasi-BIC, as demonstrated in [21].

To support a quasi-BIC at 785 nm wavelength, we find that the dimensions of the structure are small. Fabrication of the device will thus be challenging, and we numerically investigate the fabrication tolerances. Particular attention is given to the thickness of the metasurface, as it can influence the Q-factor significantly and it has not been studied previously (to the best of our knowledge). The size of the trapped particle influences the resonance wavelength, and we investigate this shift away from the resonance of the empty metasurface, i.e., without trapped nanoparticles. The influence of trapped nanoparticles on the resonance characteristics has been theoretically investigated in Refs. [15,22]. To reveal the influence on the trapping performance, we find semi-analytical expressions for the trapping potential and the wavelength giving the minimum of the potential well, which are both confirmed by numerical simulations. Whereas this work is based on extensive numerical simulations, it thus shows that limited simulations and semi-analytical expressions are sufficient for future analysis of the structure.

Raman scattering is extremely weak, with only one in 10^6 to 10^{10} photons stimulating vibrational modes [23]. Surface-enhanced Raman spectroscopy (SERS) is typically used to enhance the Raman scattering and enhancement factors of 10^7 to 10^{10} have been achieved, enabling single molecule detection [24]. We show that the high electric field enhancement in the metasurface can give an enhanced Raman scattering at multiple locations. The achievable Raman enhancement factor is generally lower than for SERS, but comparable enhancement values have previously been used for Raman spectroscopy of EVs [25] and single molecule detection [26]. By coupling each location to a channel of a multi-channel spectrometer, Raman-spectra of individual trapped particles can be acquired in parallel.

2. Metasurface design and simulation method

A unit cell of the metasurface investigated is shown in Fig. 1(a), consisting of two identical elliptical bars aligned with a tilt-angle $\pm\theta$. Periodic boundary conditions are used such that the simulated metasurface consists of an infinite array of unit cells. The design parameters of the unit

cell are also shown in Fig. 1(a), where P_x and P_y are the periodicities along x and y axis, a and b are the long and short axes of the bars, respectively, and h is the height of the bars. The design parameters (P_x , P_y , a , and b) are varied by a scaling factor S , using the relations $P_x \times S$, $P_y \times S$, $a \times S$, and $b \times S$, respectively. The unit cell is covered by water for the purpose of nanoparticle trapping. We use a software based on the finite element method (COMSOL Multiphysics v.5.6) to simulate the unit cell in an infinite array that forms a metasurface. We apply a port with an incident plane wave at the top and a receiving port on the bottom of the substrate. The plane wave is polarized along the x -axis (see Fig. 1(a)). Periodic boundary conditions are set on the faces of the unit cell in the x and y directions. For the simulation of the optical forces, we use an input intensity of $1 \text{ mW}/\mu\text{m}^2$ and integrate the Maxwell stress tensor over the surface of a nanosphere to find the forces. The refractive indices are set to $n_{\text{Si}_3\text{N}_4} = 2.02$ [27], $n_{\text{SiO}_2} = 1.461$ [28], and $n_{\text{water}} = 1.33$ [29]. A refractive index of $n_{\text{EV}} = 1.39$ [30] is used for the nanosphere to resemble an EV. A user defined mesh with a maximum element size of 12 nm is used for the elliptical bars. For the trapped nanospheres, the maximum element size is set to 3 nm. We use a step size of 0.25 pm for the wavelength sweep to resolve the spectral features.

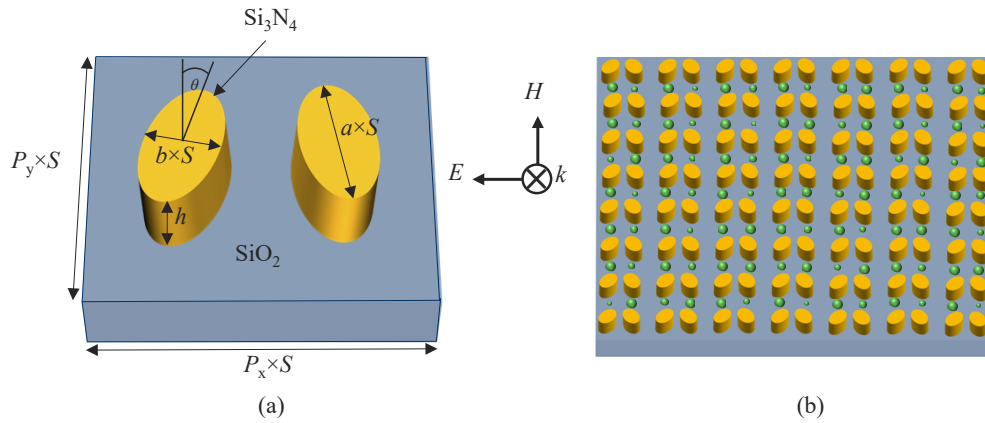


Fig. 1. (a) Schematic of the unit cell of the Si_3N_4 quasi-BIC metasurface with its geometrical parameters. (b) Schematic illustration of trapping of multiple nanospheres (green) using the proposed metasurface.

3. Results and discussion

For this work, the target resonance wavelength λ_0 of the quasi-BIC cavity is 785 nm, which is a wavelength commonly used for Raman-spectroscopy. To achieve this λ_0 , we systematically tune the scaling factor and height of the bars (see Supplement 1). The tilt angle for the bar is set to $\theta = \pm 10^\circ$ for all simulations. Figure 2(a) illustrates the reflectance spectrum with $P_x = 522.1 \text{ nm}$, $P_y = 336.1 \text{ nm}$, $a = 255.05 \text{ nm}$, $b = 125.03 \text{ nm}$, $S = 1$, and $h = 230 \text{ nm}$, showing a reflectance peak of unity at 785 nm. This corresponds to the resonance wavelength λ_0 of the quasi-BIC mode, without any particle in the unit cell (empty cavity). The symmetry of the proposed metasurface is broken by introducing the tilt angle ($\theta = \pm 10^\circ$), resulting in a finite Q-factor [16]. We fit the reflectance spectra in Fig. 2(a) with a Fano lineshape to extract the Q-factor using a Matlab curve fitting tool. The Fano lineshape formula is given by [15,31]:

$$R = \left| a_1 + ia_2 + \frac{b}{\omega - \omega_0 + i\gamma} \right|^2, \quad (1)$$

where a_1 , a_2 , and b are the fitting parameters, ω_0 is the central resonance frequency, and γ is the overall damping rate of the resonance. In Eq. (1), normalized ω and ω_0 are used, so that other

unknown parameters are within 0 to 1. The Q-factor is then computed by using $Q = \omega_0/2\gamma$. It is known that the Q-factor scales with $\sin^{-2} \theta$ [16,32,33] and this is not investigated further in this paper. Also, a thickness $h = 230$ nm is used initially and for the stated field-enhancement. The reflectance spectrum shown in Fig. 2(a) has a narrow linewidth, giving a high Q-factor of 1.3×10^4 .

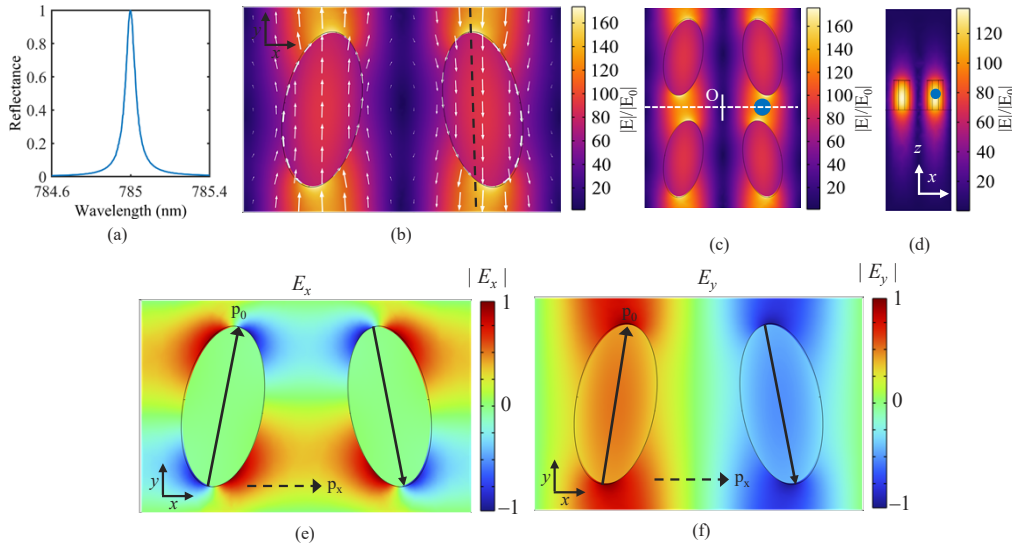


Fig. 2. (a) Simulated reflectance spectra showing $\lambda_0 = 785$ nm. Electric field enhancement profile in the xy plane at $z = 115$ nm (mid-height of the bar) for (b) an empty unit cell and (c) two unit cells with a 50 nm diameter trapped nanosphere. In (b), white arrows indicate the polarization vector of the near fields. The middle of the tip-to-tip gap is indicated with a horizontal dotted-line in (c), and the field enhancement along this line is shown in (d) in the zx plane. The trapped nanosphere is located at $x = P_x/4$, $y = 0$, and $z = 115$ nm, relative to the origin (marked by O in (c)). (e),(f) Electric field patterns with associated dipole moments shown by the black arrows, where p_0 is the dipole moment of a single elliptical bar and p_x is the net dipole moment of the unit cell.

One of the key advantages of BIC metasurfaces is the extreme field localization that results in a large electric field enhancement $|E|/|E_0|$, where $|E|$ is the absolute value of the local electric field with a metasurface and $|E_0|$ is the absolute value of the electric field without the metasurface. To investigate the field enhancement, we first consider an infinite array of empty unit cells, i.e., without trapped particles. The near-fields and the polarization vectors are plotted in Fig. 2(b) at $z = 115$ nm (half the height of the bars). The excited quasi-BIC mode originates from in-plane electric quadrupoles and out-of-plane magnetic dipoles, as also reported in [21,34]. The color bar indicates a maximum field enhancement of 177 on the tips of each elliptical bar. We also simulate a metasurface with two unit cells, including the gap between the bars (along z -axis), where a nanoparticle can be trapped. For the design parameters resulting in λ_0 at 785 nm, the gap size is 81 nm. This imposes an upper limit for the diameter of nanoparticles that can be trapped. In our study, we consider diameters up to 70 nm, which is comparable to small EVs or exosomes [35]. The proposed method will thus be complimentary to ‘Raman tweezers microscopy’, which is limited to particles larger than 100 nm. The field enhancement with a 50 nm diameter nanosphere in the center of the gap is shown in Fig. 2(c). Interestingly, the introduction of the nanosphere only has limited influence on the maximum field enhancement. This can be explained by the small refractive index difference between the particle ($n_{EV} = 1.39$) and the surrounding water

($n_{\text{water}} = 1.33$). The field enhancement is maximum on the tips of the bars (Fig. 2(c)), at 177 as previously stated, and decreases to 139 in the middle of the gap (Fig. 2(d)). The enhancement can be increased further by reducing the tilt angle θ [15] or reducing the thickness, as will be discussed below. Note that there are two hotspots per unit cell, and the case of Fig. 2(c) thus corresponds to 25% occupancy for the array. An array of unit cells can trap a large number of particles, possibly with only a single particle trapped at each hotspot (see Fig. 1(b)). A metasurface with quasi-BIC can thus be an efficient way to trap multiple nanoparticles simultaneously.

The high electric field enhancement in the gaps between the tips of the bars can be used to enhance Raman scattering. When a nanoparticle is trapped in the gap, the incident laser light can excite Raman scattering, which extends over a wide range of wavelengths, depending on the chemical composition of the particle. The Raman enhancement factor EF_{Raman} can be quantified by the following expression [36],

$$EF_{\text{Raman}} = \left| \frac{E}{E_0} \right|^2 \times \left| \frac{E_{\text{emission}}}{E_0} \right|^2, \quad (2)$$

where $|E|^2/|E_0|^2$ is the field intensity enhancement at the incident wavelength and $|E_{\text{emission}}|^2/|E_0|^2$ is the field intensity enhancement at the Raman emission wavelength. The Raman scattered light can have a different polarization than that of the incident light. Here, we assume that the polarization of the Raman scattered light is either parallel or perpendicular to the polarization of the incident light. To determine the field enhancement at the Raman emission wavelengths, we take the average field enhancement of the parallel and the perpendicular polarization. This simulation was carried out with a plane wave incident on the metasurface. An alternative approach would be to use a point dipole as an emitter at the equilibrium position in the gap. We have not considered the numerical aperture of any collecting optics. Figure 3(a) shows electric field enhancement for the parallel and perpendicular polarization as a function of Raman emission wavelengths ranging from 790 to 900 nm. The field enhancements for both polarizations are small, resulting in a low average field enhancement around ~ 1.05 over the whole spectrum. Using the maximum field enhancement in the middle of the gap ($|E|/|E_0| = 139$) and inserting the calculated average enhancement into Eq. (2), we find the Raman enhancement factor EF_{Raman} . This gives a significant enhancement of the obtained Raman-signal, with a calculated enhancement of $> 2 \times 10^4$ over the broad emission spectrum, for excitation at the resonance wavelength (Fig. 3(a)). Field enhancement profiles, at a randomly chosen Raman emission wavelength of $\lambda = 820$ nm, are shown in Figs. 3(b),(c) for parallel and perpendicular polarization, respectively. Enhancement at the emission wavelengths, in addition to enhancement at the excitation wavelength, would be an advantage if the enhancement is independent of wavelength. That is a difficult requirement to achieve.

Apart from the high field enhancement, the strong field localization in the gap provides a small mode volume V_m . We calculate mode volume V_m using the formula [37],

$$V_m = \frac{\iiint \epsilon(\mathbf{r}) |\mathbf{E}(\mathbf{r})|^2 d^3\mathbf{r}}{\max(\epsilon(\mathbf{r}) |\mathbf{E}(\mathbf{r})|^2)}, \quad (3)$$

where $\epsilon(\mathbf{r})$ is the dielectric function and $\mathbf{E}(\mathbf{r})$ is the electric field. The numerator indicates a volume integration performed over the unit cell, while the denominator indicates the maximum over the volume of the unit cell. For the empty cavity with one trapping location, the simulation predicts an extremely small V_m of $0.03 \times (\lambda/n_{\text{water}})^3$. The introduction of a nanosphere in the cavity leads to a minor change in the Q-factor and V_m (see Supplement 1). The high Q-factor and small V_m in this and other proposed metasurfaces may find applications in nonlinear photonics, e.g., for third harmonic generation (THG) [38,39]. As the intensity necessary for THG scales with the factor $(Q/V_m)^3$ [40], an enhanced nonlinear response can be achieved.

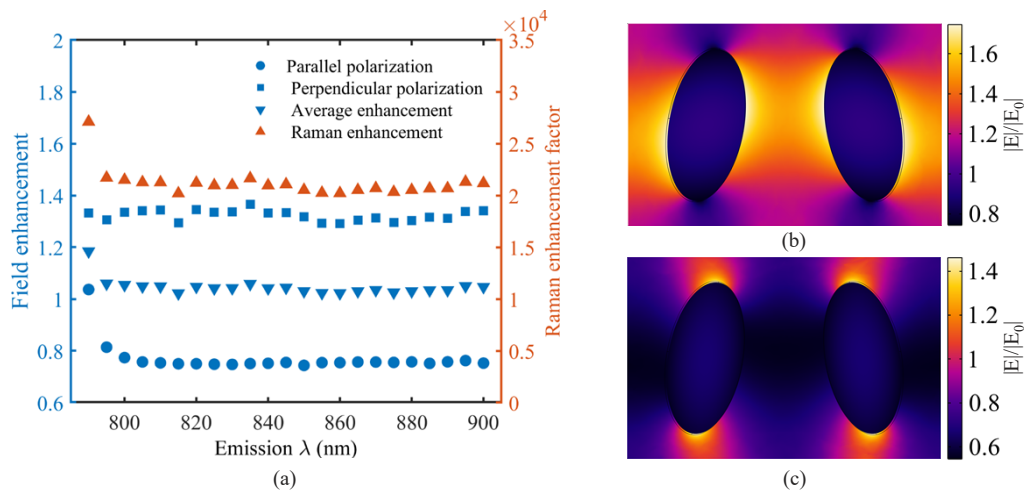


Fig. 3. (a) Field enhancement and Raman enhancement factor EF_{Raman} as a function of Raman emission wavelength. Field enhancement profile for (b) parallel and (c) perpendicular polarization at $\lambda = 820$ nm.

The mathematical definition of mode volume in Eq. (3) is widely used for resonance cavity but not applicable for plasmonic systems as the integrand becomes negative [41]. In addition, calculation of mode volume by this equation is not valid for an open cavity system where fields are not strictly confined [42]. Quasi-normal modes formalism [42,43] and finding local density of optical states with Q-factor [44] are two known approaches that can give an accurate mode volume. In our case, we have studied a dielectric system, which can be roughly treated as a closed cavity system as the fields are tightly confined to finite space with an extremely small leakage. Also, we note that the expression of mode volume in Eq. (3) has been used in other dielectric quasi-BIC systems [22,45].

The dimensions of a fabricated metasurface may deviate from the target dimensions, due to fabrication tolerances and defects. To quantify the impact of such deviations on the Q-factor and the resonance wavelength, we perform numerical simulations as function of the geometrical parameters S and h . The first relationship, between the scaling factor S and the resonance wavelength, is simply that λ_0 is linear with S . The graph in Fig. 4(a) confirms this, with a small difference in slope. Note that the linear relationship and the slope is irrespective of the refractive index of the material. The Q-factor is modestly affected by the change of S , as shown in the same figure. The effect of changing the height h of the bars is shown in Fig. 4(b). The resonance wavelength is approximately linear with h . A variation of h with $\pm 5\%$ gives ± 3 nm change of the resonance wavelength $\delta\lambda_0$, compared to ± 39 nm for a similar change of S . The sensitivity to h is thus significantly weaker than to the scaling factor S . This can be expected as h influences the resonance through the effective refractive index of the mode, whereas S affects the cavity-dimensions in the plane of the resonance. Finally, the Q-factor shows a higher sensitivity to changes of h , as opposed to the modest sensitivity to changes of S . In particular, the Q-factor increases drastically for small bar heights, for example $h = 40$ nm. To further investigate the dependence of the Q-factor on h , we fit the line $Q = a/(h-h_0)^2 + Q_0$ (dashed line in Fig. 4(b)). The values fitted to a , h_0 and Q_0 are $4.4 \times 10^8 \text{ nm}^2$, 18 nm and 2460, respectively. This is consistent with previous works, which have shown that the Q-factor generally varies with the inverse square of the asymmetry factor, as α^{-2} [16,39]. As the height h approaches h_0 , the mode stretches further into the substrate and is less affected by the asymmetry of the bars, giving an increase of the Q-factor and field enhancement. This is illustrated in Fig. 5, which shows electric

field distributions of the quasi-BIC for different bar heights. At $h = 230$ nm, the mode is mostly confined in water with a small part stretching into the underlying substrate. As the height is reduced, the mode extends further into the substrate region, as is clear for $h = 60$ nm. There are thus two factors that influence the Q-factor of our structure, namely the angle θ of the bars and their height h . To reach a high Q-factor for a fabricated structure, it can be advantageous to use a small h -value and a somewhat larger θ , as the thickness of a deposited layer can generally be tightly controlled, whereas a small angle θ can be masked by defects and topography changes during fabrication. We thus propose a thin metasurface as an alternative to small asymmetry in the xy -plane. As thickness is reduced, the dependency of the Q-factor on the thickness becomes more prominent, and generally the structure will be more prone to fabrication errors as the thickness is reduced.

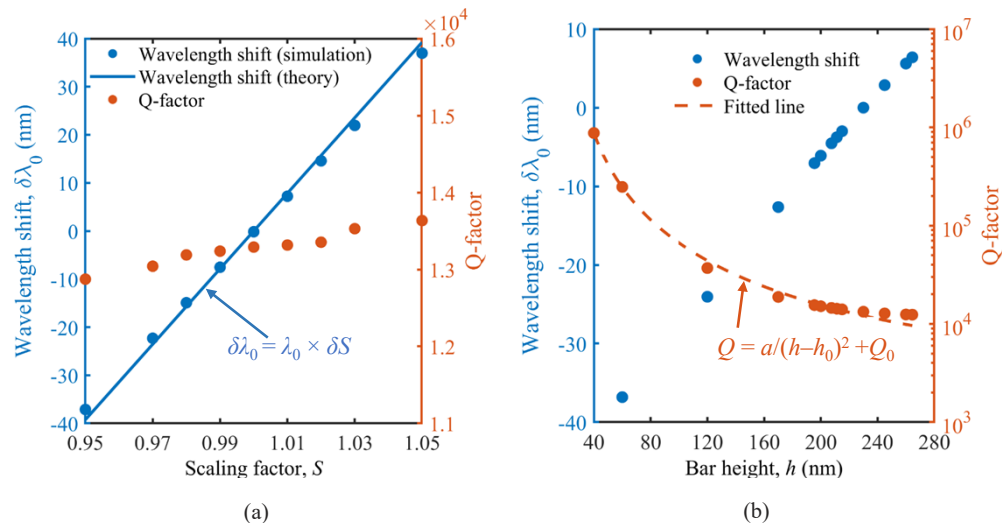


Fig. 4. Wavelength shift and Q-factor for deviations in (a) scaling factor S and (b) height h from the dimensions giving $\lambda_0 = 785$ nm ($S = 1$ and $h = 230$ nm). The straight blue line in (a) shows the linear prediction for S , while the dashed orange line in (b) is fitted to the Q-factors. An infinite array of the single unit cell is simulated for both (a) and (b).

In this work, we consider an ideal scenario by assuming an infinite array of perfect unit cells in a lossless material. For a fabricated metasurface with finite size, the resonance wavelength of the quasi-BIC may shift towards a shorter or longer wavelength [15]. In addition, the reflectance spectrum for a finite size metasurface is expected to be broadened, resulting in a reduced Q-factor [46]. The Q-factor of the quasi-BIC also depends on structural imperfections and material losses [20], and the Q-factor of a fabricated metasurface may thus have a different dependence on size than for a simulated array. Experimentally, the finite size of the metasurface will not significantly influence the Q-factor, and it will most likely be dominated by fabrication errors.

Before studying the forces on a trapped particle, we investigate the reflectance spectrum and how a quasi-BIC mode is influenced by a trapped nanosphere. The optimized dimensions found earlier were used, giving $\lambda_0 = 785$ nm for the empty cavity. We start by finding the shift in resonance wavelength $\delta\lambda_c$ when a nanosphere is introduced into the cavity (25% occupancy). A generalized approach to find $\delta\lambda_c$ is to apply cavity perturbation theory, which supposes a slight modification of the electromagnetic field inside the cavity due to the introduction of an external object. As a result, the resonant mode changes slightly, inducing a frequency shift $\delta\omega_c$ [47], that

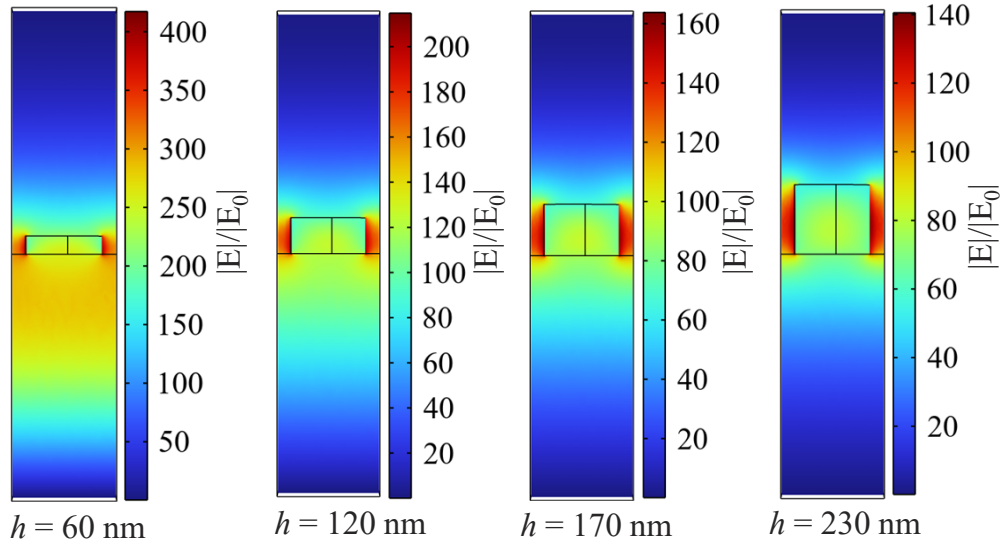


Fig. 5. Electric field distribution of the quasi-BIC for different bar heights. The fields are normalized to the incident electric field. An infinite array of single unit cells is simulated. The field distribution is taken along the yz plane with $x = P_x/4$ (see the black dashed line Fig. 2(b)).

can be expressed in terms of $\delta\lambda_c$ by:

$$\delta\lambda_c = \frac{\lambda_0}{2} \frac{\iiint d^3\mathbf{r} \Delta\varepsilon(\mathbf{r}) |\mathbf{E}(\mathbf{r})|^2}{\iiint d^3\mathbf{r} \varepsilon(\mathbf{r}) |\mathbf{E}(\mathbf{r})|^2}, \quad (4)$$

where λ_0 is the resonance wavelength of the unperturbed cavity, $\mathbf{E}(\mathbf{r})$ is the electric field of the unperturbed mode, $\varepsilon(\mathbf{r})$ is the dielectric function, and $\Delta\varepsilon(\mathbf{r})$ is the change of dielectric function due to the external object. Using Eq. (4), $\delta\lambda_c$ is calculated numerically and plotted in Fig. 6(a) (blue dashed line) as function of nanosphere radius. As expected, bigger nanospheres induce larger shifts $\delta\lambda_c$, with a $\delta\lambda_c$ of 132 pm for a nanosphere radius of 35 nm. To verify this result based on perturbation theory, we perform simulations of two unit cells with a trapped nanosphere positioned at the gap center and as function of wavelength. The nanosphere causes the reflectance peak to shift. Reflectance spectra for different radii of the nanosphere is shown in Fig. 6(b). Increasing the nanosphere radius results in a red shift, i.e., reflectance peak shifts towards a longer wavelength compared to the empty cavity wavelength of 785 nm. The $\delta\lambda_c$ calculated from the reflectance peak are plotted in Fig. 6(a) (filled triangles) together with the results of the perturbation theory. The close correspondence shows that the perturbation theory gives a good approximation for the wavelength shift of the peak in reflectivity. For an infinite array of identical unit cells, the integration in Eq. (4) is carried out over a unit cell, as was done here. However, Eq. (4) is also valid if integrating over the entire array. A small perturbation $\Delta\varepsilon(\mathbf{r})$, e.g., one trapped nanosphere in a large array, will thus give an insignificant change in the resonance wavelength. As the number of trapped particles increase, a linear increase of wavelength shift is expected with the number of trapped particles, as $\Delta\varepsilon(\mathbf{r})$ increases linearly. We verify this for two trapped nanospheres (50% filling of the array). In this case, $\delta\lambda_c$ increases by a factor 2.

The simulations reported here consider the ideal case of identical unit cells and identical particles. For an array with variations in the size of the unit cell, either intended or due to fabrication errors, and for variations in the size of the trapped particles, further simulations and development of the theory is necessary to give a quantitative description. However, a qualitative

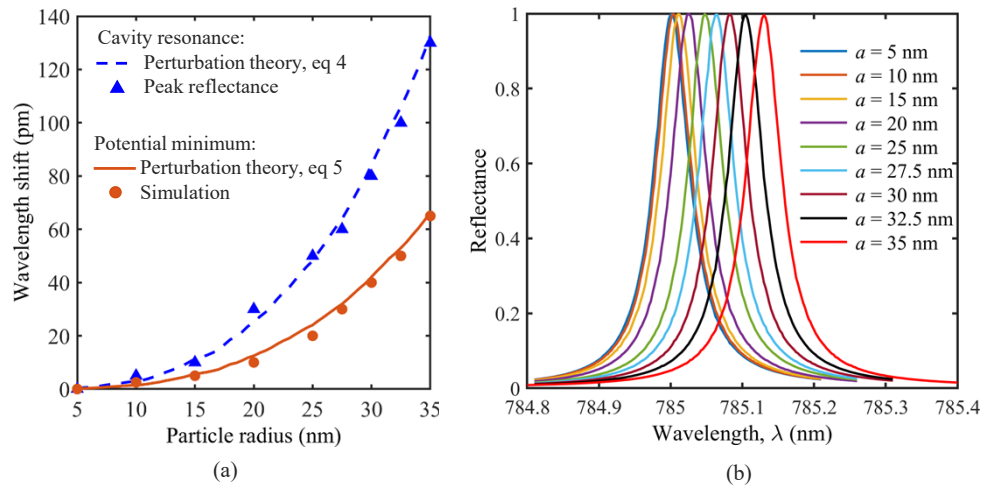


Fig. 6. (a) Resonance wavelength shift $\delta\lambda_c$ from perturbation theory (blue dashed line) and from numerical simulation for peak reflectance (blue triangles), and shift $\delta\lambda_L$ giving the minimum trapping potential, from Eq. (5) (orange solid line) and from numerical simulation (orange circles), all as function of nanosphere radius. (b) Reflectance spectra for different radii of the trapping nanosphere. The nanosphere is placed at $x = P_x/4$, $y = 0$, and $z = 100$ nm. For this study, an infinite array of two unit cells is simulated.

description of the influence on the reflection spectrum can be given. Both variations in the size of the unit cell and in the size of the particles will result in a reduction of the Q-factor related to the standard deviations of the distributions. There can also be a shift in the resonance wavelength related to the mean size of the unit cell and the mean size of the particles. In principle, it is thus possible to determine the size-distribution of the particles from the change in Q-factor and the resonance shift between an empty metasurface and a metasurface with particles. Note that the Q-factor and the wavelength shift also depend on the occupancy rate, and the relationship is thus complicated.

As discussed earlier, the metasurface shows localized near-field hotspots in the gaps between the bars. Due to the gradient of the localized field intensity, an optical gradient force is produced. This force attracts the trapping particles towards the middle of the gaps, while Brownian motion and unintended scattering from imperfect structures, will tend to push the trapped particles out of the trap. To study optical trapping, we again consider a two-unit cell that shares one trapped nanosphere in the middle of the gap. The two-unit cell is repeated, meaning that the trapped nanospheres are also repeated and located exactly at the same position in the gap in the infinite array. This is clearly not a realistic situation, and we will return to the case of one or few particles. The case of many particles at random positions in the gap will not be treated statistically.

To find the conditions for stable trapping of nanoparticles, we investigate the trapping potential and how it is influenced by the size of the trapped particle and the wavelength. The trapping potential U is a function of the wavelength, as was found for the reflectance, and this function is influenced by the radius of the nanosphere. We use numerical simulation of the field-distribution and the Maxwell stress tensor to find this dependency for the optimized metasurface ($S = 1$ and $h = 230$ nm). The optical force along the vertical axis F_z is found as function of z -position of the trapped nanosphere (see Supplement 1). The force F_z is then integrated along the vertical path from the equilibrium height in the gap ($F_z = 0$ for $z = 100$ nm) up to a position where F_z again approaches zero. This gives the potential U for a certain wavelength and nanosphere radius (see Supplement 1), as shown in Fig. 7(a). The potential for a given radius has a minimum for a

wavelength that is shifted $\delta\lambda_L$ from the resonance wavelength of the empty cavity. The shifts $\delta\lambda_L$ corresponding to the minima in Fig. 7(a) are plotted in Fig. 6(a) (orange circles). The relationship between this shift $\delta\lambda_L$ for the trapping potential and the shift in the resonance wavelength $\delta\lambda_L$ due to a trapped particle, is simply given by (see Supplement 1):

$$\delta\lambda_L = \delta\lambda_c/2, \quad (5)$$

where $\delta\lambda_c$ is found from perturbation theory, Eq. (4). The trapping potential is most influenced by the wavelength when the force on the particle is maximum. As the force is a gradient force, it is maximum when the field-gradient is maximum, which occurs when the nanosphere is, in qualitative terms, approximately half the way out of the well. Thus, this gives a simple explanation of Eq. (5) as the trapping potential is mostly influenced with the particle at the edge of the well, whereas the reflectance was calculated with the particle at the center of the well.

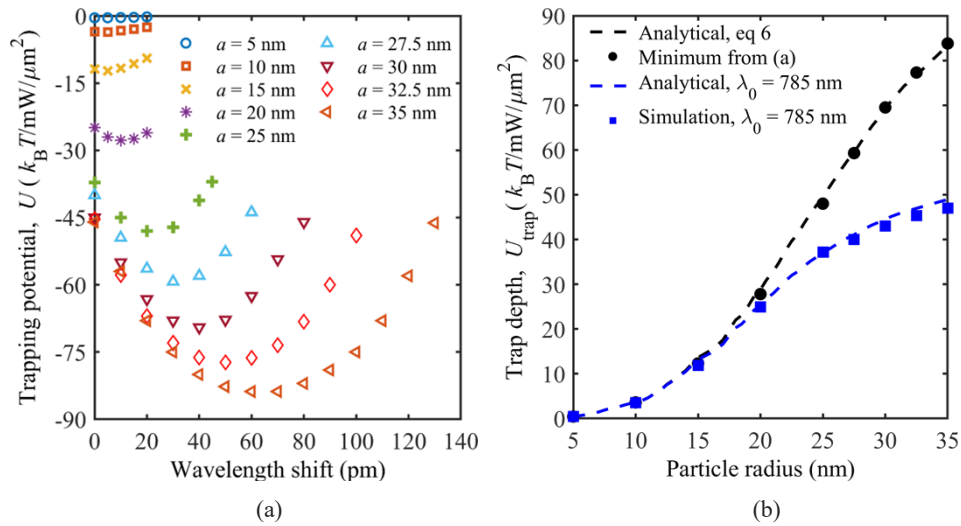


Fig. 7. (a) Trapping potential U as a function of wavelength shift away from the resonance of the empty cavity. (b) Maximum trapping potential depth U_{trap} from the semi-analytical expression (black dashed line) and as the minimum of the graphs in (a) (filled circles). Analytical trap depth (blue dashed line) is compared with simulated values (filled squares) for the empty cavity resonance wavelength of 785 nm.

The wavelength shift given by Eq. (5) is also plotted in Fig. 6(a) (orange solid line). The correspondence between this semi-analytical result and the numerical simulation is good. The numerical simulation involves finding the field-distribution at a number of positions as the nanosphere is moved out of the potential, and as function of wavelength. It is thus a computationally costly procedure. On the other hand, the semi-analytical expression only involves finding the field-distribution with the nanosphere at a single position (in the center of the well and the gap). It is thus significantly faster to perform.

Going one step further, we study in more detail the optical trapping potential and particularly the minima of the curves in Fig. 7(a), which gives the maximum trapping potential depth U_{trap} as function of nanosphere radius. An analytical expression for U_{trap} can be derived from [22] and is given by (see Supplement 1):

$$U_{\text{trap}} = 2\hbar N_p \frac{\kappa_{\text{ex}}}{\kappa} (\arctan[-\Delta] + \arctan[\eta + \Delta]), \quad (6)$$

where Δ is the (negative) dimensionless detuning between the laser and empty cavity frequencies, η is the dimensionless back-action parameter, and N_p is the number of photons injected into the

cavity for the input intensity. The mathematical definition of these parameters and details of other parameters in Eq. (6) can be found in [Supplement 1](#).

Using the analytical expression in Eq. (6), U_{trap} is plotted versus nanosphere radius, as shown by the dashed line in Fig. 7(b). The potential U_{trap} increases with nanosphere radius, reaching a value of $84 k_B T / \text{mW}/\mu\text{m}^2$ for a nanosphere radius of 35 nm. The relationship to radius is expected because the polarizability, and thus also the potential, is proportional to nanosphere volume [48]. The trapping time in a trap depends strongly on the trapping potential and the size of the trapped nanosphere [49]. A potential depth of $10 k_B T$ is generally considered sufficient for stable trapping [50]. We find that a somewhat deeper potential is necessary for the particles considered here, with $11 k_B T$ giving a trapping time of 10 seconds for a nanosphere with 15 nm radius (see [Supplement 1](#)). This is comparable to the integration times used for optical tweezers and Raman-spectroscopy [4]. To obtain this potential depth of $11 k_B T$, a relatively modest intensity of $1 \text{ mW}/\mu\text{m}^2$ is sufficient, and this intensity can thus be used to trap nanospheres with a radius of 15 nm or larger. Note that this is valid for a filling factor of 25%, with symmetric trapping of the nanospheres, and for a laser wavelength tuned to the resonance for this case. To verify the values of U_{trap} found from Eq. (6), we also find it from the simulations using the Maxwell stress tensor. This is simply taking the minima of the curves in Fig. 7(a) and converting them to potential depth relative to the zero potential. The graph with the semi-analytical results from Eq. (6) and from the fully numerical simulation is shown in Fig. 7(b), with dashed line and filled circles, respectively. Again, the results indicate a good agreement between the two approaches. For the metasurface studied in this work, it is thus sufficient to use the expression in Eq. (6) to fully characterize the trapping potential of the structure. The expression is semi-analytical as it depends on the wavelength shift $\delta\lambda_L$ that gives maximum potential depth, which in turn is found from perturbation theory, Eqs. (4), and (5).

For one or a few trapped particles, the resonance wavelength of an infinite (or large) array does not change, following Eq. (4), as pointed out previously. By consequence, $\lambda_L = \lambda_c = \lambda_0$ and $\Delta = 0$ in Eq. (6). For many particles trapped and a laser wavelength set to the resonance of the empty cavity, we again have $\lambda_L = \lambda_0$ and $\Delta = 0$. Thus, we find that for the laser wavelength set to the resonance of the empty cavity, the potential is independent of the number of trapped particles. This potential is also shown in Fig. 7(b). It is almost identical to the potential for periodic trapping with 25% filling for radii up to 20 nm, while for larger radii it is significantly lower. This implies that the conclusion in the previous paragraph, that an intensity of $1 \text{ mW}/\mu\text{m}^2$ is sufficient to trap nanospheres with a radius of 15 nm or larger, is valid for any number of trapped particles.

4. Conclusion

To conclude, we have proposed a new platform for optical trapping and Raman spectroscopy of multiple nanoparticles using a Si_3N_4 metasurface supporting quasi-BIC. The metasurface consists of an infinite array of unit cells where the unit cell consists of two identical Si_3N_4 elliptical bars deposited on a SiO_2 substrate. We have optimized the design parameters of the unit cell to obtain resonance at a wavelength of 785 nm and investigated how sensitive the resonance wavelength is to changes in these parameters. The sensitivity is high, particularly to the scaling factor S , implying that it will be challenging to fabricate a metasurface with resonance close to 785 nm. We find that the Q-factor increases significantly when the thickness of the metasurface is reduced. To achieve a high Q-factor, the thickness should thus be optimized, in addition to the asymmetry and geometry of the unit cell. We have shown a very high electric field enhancement in the gap center, allowing a means for nanoparticle trapping in the gap. The array of unit cells, with two trapping locations per unit cell, makes it possible to trap many nanoparticles simultaneously using a low input intensity. We have investigated the interplay between the quasi-BIC cavity and trapped nanoparticles, resulting in a shift in resonance wavelength, and we

have shown how this affects the trapping process. We have used biological nanoparticles, with a refractive index corresponding to small extracellular vesicles, in the simulations. Semi-analytical expressions for wavelength shift and maximum potential depth have been shown to agree well with the simulations, both for many and few trapped particles, and extensive simulations can thus be avoided in future work. We find that a relatively modest power can be used for trapping nanoparticles with diameters of 30–70 nm using near-visible light. The potential depth depends on the wavelength, the radius and the number of particles trapped. Experimentally, a tunable laser must be used, and the wavelength tuned to the peak in reflectance before trapping starts. With few particles trapped, the laser can remain at this wavelength. If the occupancy rate increases significantly, e.g., approaching 25%, it can be adjusted according to Eq. (5) and Fig. 7 to get a deeper potential well. Overall, the results are promising for using a metasurface with quasi-BIC as an on-chip platform for optical trapping of biological nanoparticles. A sufficient signal-to-noise ratio is necessary to combine optical trapping with Raman spectroscopy. The Raman signal increases with the acquisition time. A background signal can be expected due to Raman scattering by the metasurface, and this will also increase with the acquisition time. Consequently, the feasibility of combining trapping and Raman-spectroscopy using quasi-BIC depends partly on the Raman-background of the metasurface. This has not been considered here and will be explored in future experimental work.

Funding. Norges Forskningsråd (302333).

Acknowledgments. The publication charges for this article have been funded by a grant from the publication fund of UiT The Arctic University of Norway.

Disclosures. The authors declare no conflicts of interest.

Data availability. Data underlying the results presented in this paper are available in Ref. [51].

Supplemental document. See [Supplement 1](#) for supporting content.

References

1. J. M. Pitt, G. Kroemer, and L. Zitvogel, “Extracellular vesicles: masters of intercellular communication and potential clinical interventions,” *J. Clin. Investig.* **126**(4), 1139–1143 (2016).
2. G. Raposo and P. D. Stahl, “Extracellular vesicles: a new communication paradigm?” *Nat. Rev. Mol. Cell. Biol.* **20**(9), 509–510 (2019).
3. M. Yanez-Mo, P. R. Siljander, and Z. Andreu, *et al.*, “Biological properties of extracellular vesicles and their physiological functions,” *J. Extracell. Vesicles* **4**(1), 27066 (2015).
4. S. G. Kruglik, F. Royo, J. M. Guigner, L. Palomo, O. Seksek, P. Y. Turpin, I. Tatischeff, and J. M. Falcon-Perez, “Raman tweezers microspectroscopy of circa 100 nm extracellular vesicles,” *Nanoscale* **11**(4), 1661–1679 (2019).
5. W. Lee, A. Nanou, L. Rikkert, F. A. W. Coumans, C. Otto, L. Terstappen, and H. L. Offerhaus, “Label-Free Prostate Cancer Detection by Characterization of Extracellular Vesicles Using Raman Spectroscopy,” *Anal. Chem.* **90**(19), 11290–11296 (2018).
6. I. Tatischeff, E. Larquet, J. M. Falcon-Perez, P. Y. Turpin, and S. G. Kruglik, “Fast characterisation of cell-derived extracellular vesicles by nanoparticles tracking analysis, cryo-electron microscopy, and Raman tweezers microspectroscopy,” *J. Extracell. Vesicles* **1**(1), 19179 (2012).
7. A. H. Yang, S. D. Moore, B. S. Schmidt, M. Klug, M. Lipson, and D. Erickson, “Optical manipulation of nanoparticles and biomolecules in sub-wavelength slot waveguides,” *Nature* **457**(7225), 71–75 (2009).
8. A. H. Yang, T. Lertsuchatawanich, and D. Erickson, “Forces and transport velocities for a particle in a slot waveguide,” *Nano Lett.* **9**(3), 1182–1188 (2009).
9. S. Mandal, X. Serey, and D. Erickson, “Nanomanipulation using silicon photonic crystal resonators,” *Nano Lett.* **10**(1), 99–104 (2010).
10. T. van Leest and J. Caro, “Cavity-enhanced optical trapping of bacteria using a silicon photonic crystal,” *Lab Chip* **13**(22), 4358–4365 (2013).
11. C. Renaut, J. Dellinger, B. Cluzel, T. Honegger, D. Peyrade, E. Picard, F. de Fornel, and E. Hadji, “Assembly of microparticles by optical trapping with a photonic crystal nanocavity,” *Appl. Phys. Lett.* **100**(10), 101103 (2012).
12. J. M. Nam, J. W. Oh, H. Lee, and Y. D. Suh, “Plasmonic Nanogap-Enhanced Raman Scattering with Nanoparticles,” *Acc. Chem. Res.* **49**(12), 2746–2755 (2016).
13. H. Y. Wu, C. J. Choi, and B. T. Cunningham, “Plasmonic nanogap-enhanced Raman scattering using a resonant nanodome array,” *Small* **8**(18), 2878–2885 (2012).
14. C. Zhan, X. J. Chen, Y. F. Huang, D. Y. Wu, and Z. Q. Tian, “Plasmon-Mediated Chemical Reactions on Nanostructures Unveiled by Surface-Enhanced Raman Spectroscopy,” *Acc. Chem. Res.* **52**(10), 2784–2792 (2019).

15. S. Yang, C. Hong, Y. Jiang, and J. C. Ndukaife, "Nanoparticle Trapping in a Quasi-BIC System," *ACS Photonics* **8**(7), 1961–1971 (2021).
16. K. Koshelev, S. Lepeshov, M. Liu, A. Bogdanov, and Y. Kivshar, "Asymmetric Metasurfaces with High-Q Resonances Governed by Bound States in the Continuum," *Phys. Rev. Lett.* **121**(19), 193903 (2018).
17. Y. Jahani, E. R. Arvelo, F. Yesilkoy, K. Koshelev, C. Cianciaruso, M. De Palma, Y. Kivshar, and H. Altug, "Imaging-based spectrometer-less optofluidic biosensors based on dielectric metasurfaces for detecting extracellular vesicles," *Nat. Commun.* **12**, 3246 (2021).
18. F. Yesilkoy, E. R. Arvelo, Y. Jahani, M. K. Liu, A. Tittl, V. Cevher, Y. Kivshar, and H. Altug, "Ultrasensitive hyperspectral imaging and biodetection enabled by dielectric metasurfaces," *Nat. Photonics* **13**(6), 390–396 (2019).
19. C. W. Hsu, B. Zhen, A. D. Stone, J. D. Joannopoulos, and M. Soljačić, "Bound states in the continuum," *Nat. Rev. Mater.* **1**(9), 16048 (2016).
20. K. Koshelev, G. Favraud, A. Bogdanov, Y. Kivshar, and A. Fratallocchi, "Nonradiating photonics with resonant dielectric nanostructures," *Nanophotonics* **8**(5), 725–745 (2019).
21. G. Q. Moretti, A. Tittl, E. Cortés, S. A. Maier, A. V. Bragas, and G. Grinblat, "Introducing a Symmetry-Breaking Coupler into a Dielectric Metasurface Enables Robust High-Q Quasi-BICs," *Adv. Photonics Res.* **3**(12), 2200111 (2022).
22. L. Neumeier, R. Quidant, and D. E. Chang, "Self-induced back-action optical trapping in nanophotonic systems," *New J. Phys.* **17**(12), 123008 (2015).
23. C. F. Kenworthy, L. Pjotr Stoevelaar, A. J. Alexander, and G. Gerini, "Using the near field optical trapping effect of a dielectric metasurface to improve SERS enhancement for virus detection," *Sci. Rep.* **11**(1), 6873 (2021).
24. E. C. Le Ru, E. Blackie, M. Meyer, and P. G. Etchegoin, "Surface enhanced Raman scattering enhancement factors: a comprehensive study," *J. Phys. Chem. C* **111**(37), 13794–13803 (2007).
25. S. L. Dong, Y. H. Wang, Z. Q. Liu, W. W. Zhang, K. Z. Yi, X. G. Zhang, X. L. Zhang, C. Z. Jiang, S. K. Yang, F. B. Wang, and X. H. Xiao, "Beehive-Inspired Macroporous SERS Probe for Cancer Detection through Capturing and Analyzing Exosomes in Plasma," *ACS Appl. Mater. Interfaces* **12**(4), 5136–5146 (2020).
26. J. Cambiasso, M. König, E. Cortes, S. Schlucker, and S. A. Maier, "Surface-Enhanced Spectroscopies of a Molecular Monolayer in an All-Dielectric Nanoantenna," *ACS Photonics* **5**(4), 1546–1557 (2018).
27. K. Luke, Y. Okawachi, M. R. E. Lamont, A. L. Gaeta, and M. Lipson, "Broadband mid-infrared frequency comb generation in a Si₃N₄ microresonator," *Opt. Lett.* **40**(21), 4823–4826 (2015).
28. L. V. Rodríguez-de Marcos, J. I. Larruquert, J. A. Méndez, and J. A. Aznárez, "Self-consistent optical constants of SiO₂ and Ta₂O₅ films," *Opt. Mater. Express* **6**(11), 3622–3637 (2016).
29. M. Daimon and A. Masumura, "Measurement of the refractive index of distilled water from the near-infrared region to the ultraviolet region," *Appl. Opt.* **46**(18), 3811–3820 (2007).
30. C. Gardiner, M. Shaw, P. Hole, J. Smith, D. Tannetta, C. W. Redman, and I. L. Sargent, "Measurement of refractive index by nanoparticle tracking analysis reveals heterogeneity in extracellular vesicles," *J. Extracell. Vesicles* **3**(1), 25361 (2014).
31. S. Li, C. Zhou, T. Liu, and S. Xiao, "Symmetry-protected bound states in the continuum supported by all-dielectric metasurfaces," *Phys. Rev. A* **100**(6), 063803 (2019).
32. Z. Liu, Y. Xu, Y. Lin, J. Xiang, T. Feng, Q. Cao, J. Li, S. Lan, and J. Liu, "High-Q Quasibound States in the Continuum for Nonlinear Metasurfaces," *Phys. Rev. Lett.* **123**(25), 253901 (2019).
33. M. V. Rybin, K. L. Koshelev, Z. F. Sadrieva, K. B. Samusev, A. A. Bogdanov, M. F. Limonov, and Y. S. Kivshar, "High-Q Supercavity Modes in Subwavelength Dielectric Resonators," *Phys. Rev. Lett.* **119**(24), 243901 (2017).
34. M. K. Liu and D. Y. Choi, "Extreme Huygens' Metasurfaces Based on Quasi-Bound States in the Continuum," *Nano Lett.* **18**(12), 8062–8069 (2018).
35. L. M. Doyle and M. Z. Wang, "Overview of Extracellular Vesicles, Their Origin, Composition, Purpose, and Methods for Exosome Isolation and Analysis," *Cells* **8**(7), 727 (2019).
36. P. Alonso-Gonzalez, P. Albella, M. Schnell, J. Chen, F. Huth, A. Garcia-Etxarri, F. Casanova, F. Golmar, L. Arzubiaaga, L. E. Hueso, J. Aizpurua, and R. Hillenbrand, "Resolving the electromagnetic mechanism of surface-enhanced light scattering at single hot spots," *Nat. Commun.* **3**, 684 (2012).
37. S. Hu and S. M. Weiss, "Design of Photonic Crystal Cavities for Extreme Light Concentration," *ACS Photonics* **3**(9), 1647–1653 (2016).
38. L. Carletti, S. S. Kruk, A. A. Bogdanov, C. De Angelis, and Y. Kivshar, "High-harmonic generation at the nanoscale boosted by bound states in the continuum," *Phys. Rev. Res.* **1**(2), 023016 (2019).
39. K. Koshelev, Y. T. Tang, K. F. Li, D. Y. Choi, G. X. Li, and Y. Kivshar, "Nonlinear Metasurfaces Governed by Bound States in the Continuum," *ACS Photonics* **6**(7), 1639–1644 (2019).
40. M. Notomi, "Strong Light Confinement With Periodicity," *Proc. IEEE* **99**(10), 1768–1779 (2011).
41. A. F. Koenderink, "On the use of Purcell factors for plasmon antennas," *Opt. Lett.* **35**(24), 4208–4210 (2010).
42. P. Lalanne, W. Yan, K. Vynck, C. Sauvan, and J. P. Hugonin, "Light Interaction with Photonic and Plasmonic Resonances," *Laser Photonics Rev.* **12**(5), 1700113 (2018).
43. C. Tao, J. D. Zhu, Y. Zhong, and H. T. Liu, "Coupling theory of quasinormal modes for lossy and dispersive plasmonic nanoresonators," *Phys. Rev. B* **102**(4), 045430 (2020).
44. I. M. Palstra, H. M. Doeleman, and A. F. Koenderink, "Hybrid cavity-antenna systems for quantum optics outside the cryostat?" *Nanophotonics* **8**(9), 1513–1531 (2019).

45. W. Wang and X. D. Ma, "Achieving extreme light confinement in low-index dielectric resonators through quasi-bound states in the continuum," *Opt. Lett.* **46**(24), 6087–6090 (2021).
46. C. Z. Fang, Q. Y. Yang, Q. C. Yuan, X. T. Gan, J. L. Zhao, Y. Shao, Y. Liu, G. Q. Han, and Y. Hao, "High-Q resonances governed by the quasi-bound states in the continuum in all-dielectric metasurfaces," *Opto-Electron. Adv.* **4**(6), 200030 (2021).
47. J. D. J. Joannopoulos, G. Steven, Joshua N. Winn, and Robert D. Meade, *Photonic Crystals: Molding the Flow of Light (Second Edition)* (Princeton University Press, 2008).
48. P. Zemanek, A. Jonas, L. Sramek, and M. Liska, "Optical trapping of Rayleigh particles using a Gaussian standing wave," *Opt. Commun.* **151**(4-6), 273–285 (1998).
49. C. Hosokawa, H. Yoshikawa, and H. Masuhara, "Cluster formation of nanoparticles in an optical trap studied by fluorescence correlation spectroscopy," *Phys. Rev. E: Stat., Nonlinear, Soft Matter Phys.* **72**(2), 021408 (2005).
50. A. Ashkin, J. M. Dziedzic, J. E. Bjorkholm, and S. Chu, "Observation of a single-beam gradient force optical trap for dielectric particles," *Opt. Lett.* **11**(5), 288–290 (1986).
51. M. R. Hasan and O. G. Hellesø, "Replication data for : Metasurface supporting quasi-BIC for optical trapping and Raman-spectroscopy of biological nanoparticles," *DataverseNO*, V1 (2023), <https://doi.org/10.18710/VW1M5L>.

Metasurface supporting quasi-BIC for optical trapping and Raman-spectroscopy of biological nanoparticles: supplement

MD RABIUL HASAN  AND OLAV GAUTE HELLESØ* 

Department of Physics and Technology, UiT The Arctic University of Norway, Tromsø, Norway

**olav.gaute.helleso@uit.no*

This supplement published with Optica Publishing Group on 9 February 2023 by The Authors under the terms of the [Creative Commons Attribution 4.0 License](https://creativecommons.org/licenses/by/4.0/) in the format provided by the authors and unedited. Further distribution of this work must maintain attribution to the author(s) and the published article's title, journal citation, and DOI.

Supplement DOI: <https://doi.org/10.6084/m9.figshare.21921903>

Parent Article DOI: <https://doi.org/10.1364/OE.473064>

Supplementary information

Metasurface supporting quasi-BIC for optical trapping and Raman-spectroscopy of biological nanoparticles

MD RABIUL HASAN AND OLAV GAUTE HELLESØ*

Department of Physics and Technology, UiT The Arctic University of Norway, Tromsø, Norway

*olav.gaute.helleso@uit.no

S1. Optimization of scaling factor S and height h of elliptical bars for quasi-BIC at 785 nm

By varying the design parameters of the unit cell, a quasi-BIC can be tuned to a desired wavelength [1]. Here, we separately optimize scaling factor S and bar height h to obtain a resonance wavelength of 785 nm. As mentioned in the main text, the design parameters of the unit cell (P_x , P_y , a , and b) can be scaled by varying S . First, we vary S from 0.98 to 1.02 with a step size of 0.01 and the reflectance spectrum for each value of S is shown in Fig. S1a. Increasing the S values from 0.98 to 1.02 shows a shift of the resonance wavelength from 770.22 to 799.76 nm. With $S=1$, the design parameters are $P_x = 522.1$ nm, $P_y = 336.1$ nm, $a = 255.05$ nm, and $b = 125.03$ nm, giving a resonance wavelength at 785 nm. Second, we vary h from 200 to 260 nm with a step size of 15 nm. The resonance wavelength shows a red shift from 776.4 to 790.63 nm for increasing h from 200 to 260 nm, as shown by the reflectance spectra in Fig. S1b. At $h = 230$ nm, the resonance wavelength is 785 nm.

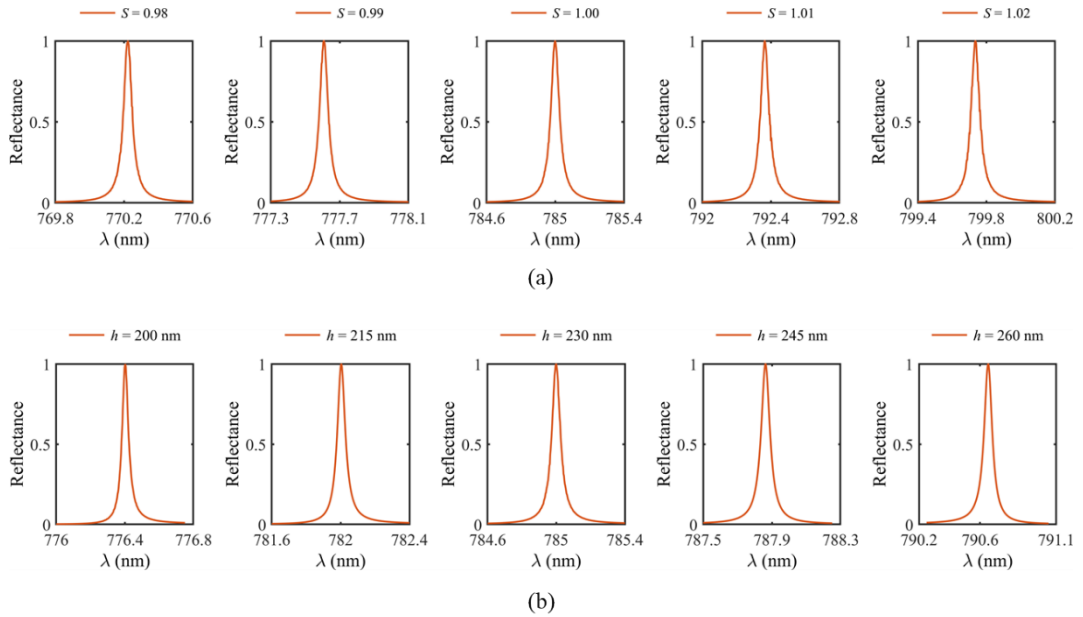


Fig. S1. Reflectance spectra for the variation of (a) scaling factor S and (b) height h . At $S = 1$ and $h = 230$ nm, the reflectance spectrum shows a resonance wavelength at 785 nm. For (a), S is varied with $h = 230$ nm and for (b), h is varied with $S = 1$. For optimization of S and h , an infinite array of one unit cell is simulated.

S2. Effect of size of trapped nanosphere on the Q-factor and mode volume.

The scattered field of the trapped nanosphere interfere with the quasi-BIC mode of the cavity, resulting in a slight modification of the intra-cavity electric field [2]. The influence on the Q-factor and the mode volume is shown in Fig. S2. The Q-factor increases slightly with the nanosphere radius. The extra dipole moment produced by the trapped nanoparticle increases the Q-factor, as explained in [2, 3]. Likewise, the mode volume is slightly influenced by the increase of the nanosphere radius, showing

a mode volume of $0.12 \times (\lambda/n_{\text{water}})^3$ for two unit cells. As two unit cells have four trapping locations, the mode volume for one location, i.e., a single gap between two bars, is $0.03 \times (\lambda/n_{\text{water}})^3$.

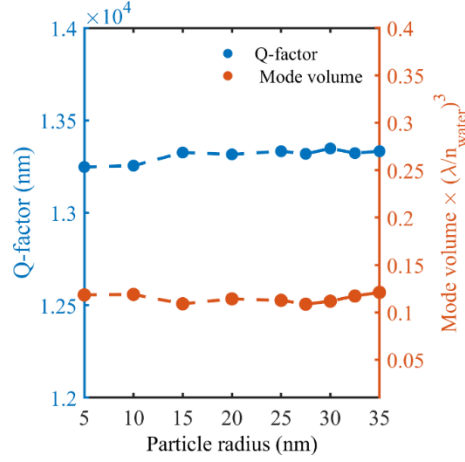


Fig. S2. Q-factor and mode volume of the cavity as a function of nanosphere radius. The trapping nanoparticle is placed at $x = P_x/4$, $y = 0$, and $z = 100$ nm. An infinite array of two unit cells is simulated, with one trapped particle (12.5% filling of the array).

S3. Determination of the equilibrium position and the vertical forces F_z .

To obtain the vertical force $F_z(z)$, the position of the trapped nanosphere is varied from $z = 40$ to 400 nm with a step size of 10 nm. For each position, F_z is computed by integrating the Maxwell stress tensor over the surface of the particle. F_z as a function of z -position for different radii of the nanosphere is shown in Fig. S3. Due to the high field enhancement, the nanosphere experiences strong optical forces, which increase with nanosphere radius. For $z < 100$ nm, F_z is positive and the trapped nanosphere is pushed up towards the equilibrium height. For $z > 100$ nm, F_z is negative and the nanosphere is pulled down towards the same equilibrium height. At the top of the elliptical bars ($z = 230$ nm), F_z is maximum, as this is where the field gradient is the largest. The force is zero at $z = 100$ nm, indicating the equilibrium height where the nanosphere can be stably trapped.

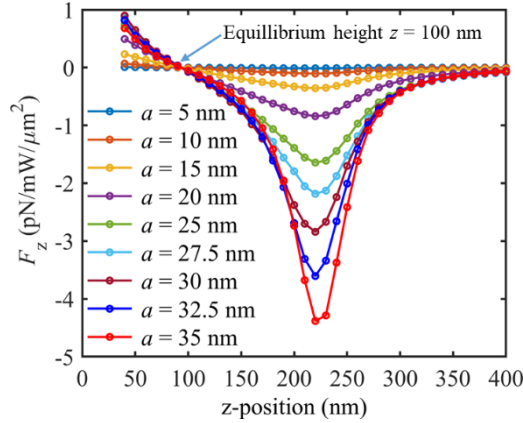


Fig. S3. Vertical force F_z as a function of z -position for different nanosphere radii. The z -positions of the trapping nanosphere are varied from 40 to 400 nm, while x and y positions are set to $P_x/4$ and 0 , respectively. The equilibrium position is close to mid-height of the bars, at $z = 100$ nm, where $F_z = 0$. The forces for each nanosphere radius are determined at the wavelength giving the maximum trapping potential depth, corresponding to the wavelength shift $\delta\lambda_L$.

S4. Determination of the trapping potential U_z .

The trapping potential U_z is calculated by the path integration of the force F_z found in Fig. S4 along the z -axis (from 40 to 400 nm). U_z as a function of z -position for different radii of the nanosphere is shown in Fig. S4. It can be noticed that the potential wells are broad compared to the case in the xy -plane, indicating a weaker confinement in the vertical direction. However, the large potential depths confirm strong pulling forces that bring back the nanosphere when it reaches the top of the metasurface. Besides, increasing the nanosphere radius gives a larger depth of the potential well, as expected. At the

equilibrium position ($F_z = 0$ and $z = 100$ nm), the deepest trapping potential is achieved for each nanosphere radius. The difference between the potential at $z = 400$ nm (zero potential) and $z = 100$ nm is defined as the maximum trapping potential depth U_{trap} . For the nanosphere with a radius of 35 nm, a U_{trap} of $84 k_B T$ can be obtained for a modest input intensity of $1 \text{ mW}/\mu\text{m}^2$, where k_B is the Boltzmann constant and T is the room temperature.

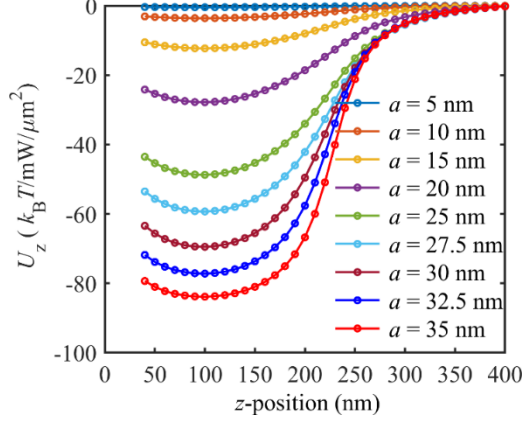


Fig. S4. Trapping potential U_z as a function of z -position for different radii of the nanosphere. The z -positions of the nanosphere are varied from 40 to 400 nm while x and y positions are set to $P_x/4$ and 0, respectively. Incident intensity for a unit cell is $1 \text{ mW}/\mu\text{m}^2$.

S5. Derivation of the wavelength shift giving the maximum trapping potential $\delta\lambda_L$ and maximum trapping potential depth U_{trap} .

A particle trapped in a nanoscale cavity can be described by the following Hamiltonian [3],

$$H = \hbar\omega_c(z)a^\dagger a + \hbar\sqrt{\kappa_{\text{ex}}}N_p(a^\dagger e^{i\omega_L t} + a e^{-i\omega_L t}) + \frac{p^2}{2m}, \quad (1)$$

where \hbar is the reduced Planck's constant, $\omega_c(z)$ is the z -position dependent resonance frequency, ω_L is the incident laser frequency, a is the annihilation operator, κ_{ex} is the loss rates due to external channels, p is the momentum of the particle, m is the mass of the particle, and N_p is the number of photons injected into the cavity, which is related to input intensity by: $N_p = \frac{I_0 A \lambda_0}{hc}$. Here, I_0 is the input intensity for the unit cell, A is the area of the unit cell, λ_0 is the resonance wavelength of the empty cavity, h is Planck's constant, and c is the velocity of light in vacuum. The total decay rate of the cavity κ can be written as: $\kappa = \kappa_{\text{ex}} + \kappa_{\text{int}} + \kappa_{\text{scat}}$, where κ_{int} is the intrinsic loss rates and κ_{scat} is the loss rates due to the scattering of the trapped particle. Ignoring mechanical damping and thermal effects, the equations of the particle motion read [3],

$$\frac{dz}{dt} = \frac{p}{m} \quad (2)$$

$$\frac{dp}{dt} = -n(z)\hbar \frac{d\omega_c(z)}{dz} \quad (3)$$

$$\frac{d\beta}{dt} = i(\omega_L - \omega_c(z))\beta - \frac{\kappa}{2}\beta + i\sqrt{\kappa_{\text{ex}}}N_p \quad (4)$$

where $\beta = \langle a \rangle$ is the expectation value of the photon amplitude and $n(z) = |\beta|^2$ is the expectation value of the intra-cavity photon number. The value of $n(z)$ is given by [2, 3],

$$n(z) = \frac{4N_p\kappa_{\text{ex}}}{\kappa^2} \frac{1}{1 + (\eta f(z) + \Delta)^2} \quad (5)$$

where η is the dimensionless back action parameter, which in turn is defined by $\eta = \frac{\alpha(\omega)}{\varepsilon_r \varepsilon_0 V_m} Q$. Here, $\alpha(\omega)$ is the polarizability of the trapped particle, V_m is the mode volume of the empty cavity, Q is the quality factor the cavity, ε_0 is the permittivity of free space, and ε_r is the relative permittivity of the surrounding medium of the particle. The term Δ in eq (5) is defined as the dimensionless detuning between the laser frequency ω_L and empty cavity frequency ω_0 and is given by $\Delta = \frac{2(\omega_L - \omega_0)}{\kappa}$. Note

that a nanosphere in the gap results in $\omega_0 > \omega_L$, thus Δ becomes a negative quantity. By putting eq (5) into eq (3) and integrating the negative force with respect to z , we obtain an equation of the general trapping potential [3],

$$U(z) = -2\hbar N_p \frac{\kappa_{\text{ex}}}{\kappa} \arctan[\eta f(z) + \Delta]. \quad (6)$$

In eq (5) and (6), $f(z)$ is defined as a dimensionless spatial intensity profile of the empty cavity, which is normalized to be 0 and 1 at the intensity minimum and maximum, respectively. For the fundamental mode of a Fabry-Perot cavity, the intensity profile is $f(z) = \cos^2(kz)$, where $f(z) = 1$ for at $z = 0$ and $f(z) = 0$ at $z = \pm \pi/2$ (see Fig. S5a). To find a corresponding intensity function for the quasi-BIC of an empty cavity, the simulated intensity as a function of z -position is fitted onto $f(z) = \cos^2(kz+a)$ using the Matlab curve fitting toolbox, where k and a are fitting parameters. Here, intensity is rescaled into 0 to 1, while the position is rescaled into $-\pi/2$ to $\pi/2$. The intensity profile of the cavity fits well into $f(z) = \cos^2(kz)$ with an R^2 value larger than 99%, as shown in Fig. S5b. The intensity function of the quasi-BIC is thus the same as for the fundamental mode of a Fabry-Perot cavity.

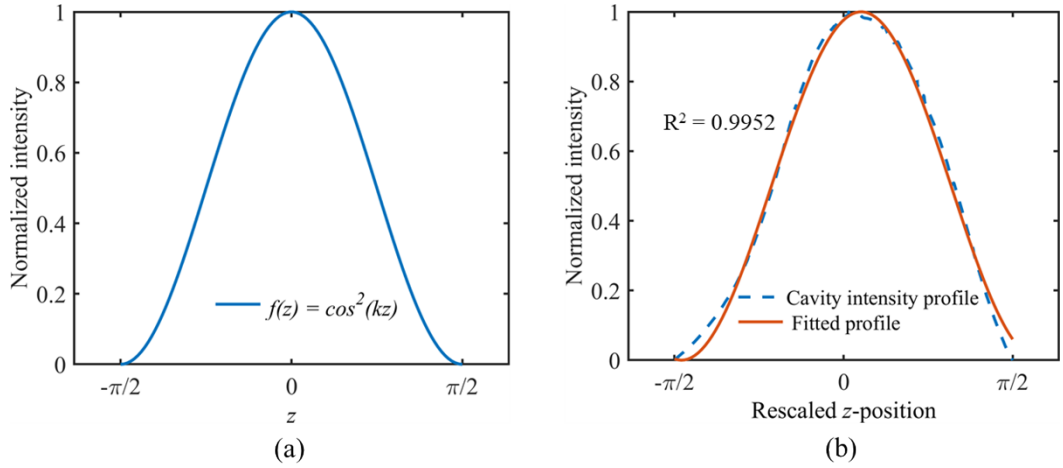


Fig. S5. (a) Intensity profile of the fundamental mode of a Fabry-Perot cavity, $f(z) = \cos^2(kz)$. (b) Intensity profile of the empty quasi-BIC is fitted to the fundamental mode profile of the Fabry-Perot cavity. Intensity and position values are rescaled. The intensity profile of the cavity and the corresponding fitted profile are shown by the dotted and the solid lines, respectively. The intensity of the quasi-BIC mode is taken along the z -axis with $x = P_x/4$ and $y = 0$.

The position with the minimum intensity z_{max} provides a maximum trapping potential U_{max} from eq (6),

$$U_{\text{max}}(z_{\text{max}}) = -2\hbar N_p \frac{\kappa_{\text{ex}}}{\kappa} \arctan[\Delta]. \quad (7)$$

Likewise, the position with the maximum intensity z_{min} gives a minimum trapping potential U_{min} , again from eq (6):

$$U_{\text{min}}(z_{\text{min}}) = -2\hbar N_p \frac{\kappa_{\text{ex}}}{\kappa} \arctan[\eta + \Delta]. \quad (8)$$

The trapping potential depth dU is then given by,

$$dU = U_{\text{max}}(z_{\text{max}}) - U_{\text{min}}(z_{\text{min}}) \quad (9)$$

$$= 2\hbar N_p \frac{\kappa_{\text{ex}}}{\kappa} (\arctan[-\Delta] + \arctan[\eta + \Delta]). \quad (10)$$

Using trigonometric identities and taking the derivative of dU with respect to Δ gives the maximum trapping potential depth U_{trap} . It follows that dU is maximized, i.e., $dU = U_{\text{trap}}$, when $\Delta = -\eta/2$.

Using perturbation theory, the particle induced frequency shift can be expressed as [3],

$$\delta\omega_c(z) = -\frac{\kappa}{2}\eta f(z). \quad (11)$$

Rearranging $\Delta = \frac{2(\omega_L - \omega_0)}{\kappa}$ and putting $\Delta = -\eta/2$, we can write $\omega_L = \omega_0 - \frac{1}{4}\kappa\eta$. At the position of the maximum intensity profile, i.e. $f(z) = 1$, we insert $\kappa = \omega_c/Q$ into eq (11) and finally obtain,

$$\delta\omega_L(z) = \frac{\delta\omega_c(z)}{2} \quad (12)$$

Now using the relation $\frac{\delta\omega}{\omega} = \frac{\delta\lambda}{\lambda}$, eq (13) can be written in terms of wavelength by,

$$\delta\lambda_L(z) = \frac{\delta\lambda_c(z)}{2}, \quad (13)$$

where $\delta\lambda_L(z)$ is the wavelength shift giving the maximum trapping potential depth and $\delta\lambda_c(z)$ is the resonance wavelength shift due to the introduction of a nanosphere in the cavity. $\delta\lambda_c(z)$ can be determined using either perturbation theory or from the shift of the reflectance peak.

S6. Requirement of a minimum trapping potential for a trapping time $\tau_{\text{trap}} = 10$ seconds.

The nanosphere trapped by the quasi-BIC stays a certain period before leaving the cavity, which is known as the trapping time τ_{trap} . A long τ_{trap} is highly desirable as the recorded Raman signal increases with τ_{trap} . τ_{trap} can be calculated using the following equation [4],

$$\tau_{\text{trap}} = \tau_0 \exp\left(\frac{|U_{\text{trap}}|}{k_B T}\right) \quad (14)$$

where $|U_{\text{trap}}|$ is the absolute value of the optical trapping potential and τ_0 is the transit time of the trapped particle in the laser focal spot without optical trapping. The transit time can be expressed as $\tau_0 = w_0^2/6D$, where w_0 is the beam waist and D is the diffusion coefficient, which in turn is given by $D = k_B T/6\pi\eta_w a$. Here, k_B is the Boltzmann constant, T is the room temperature ($T = 298$ K), η_w is the viscosity of water ($\eta_w = 1.0518 \times 10^{-3}$ N.s/m²), and a is the radius of the trapped nanoparticle. To find the waist w_0 , we fit a gaussian profile to the intensity distribution of the quasi-BIC. The curve fitting is shown in Fig. S6a, giving an estimated w_0 of 138 nm. In passing, we note that the \cos^2 -fit in S5 gave almost the same goodness (R^2 of 0.9917 vs. 0.9952). Next, we calculate the minimum trapping potential U_{trap} required to obtain a given τ_{trap} . Fig. S6b shows the U_{trap} , as a function of nanosphere radius, required minimum for $\tau_{\text{trap}} = 10$ seconds. To trap the smallest particle ($a = 5$ nm) for 10 seconds, the required minimum U_{trap} is $12 k_B T/\text{mW}/\mu\text{m}^2$, whereas for the largest particle ($a = 35$ nm), the value is $10 k_B T/\text{mW}/\mu\text{m}^2$. To obtain a reliable Raman-signal, a longer exposure time must be used for the smallest particles, thus increasing the necessary trapping time, and in turn further increasing the required trapping potential for the smallest particles. The values given here for the minimum U_{trap} are included as an indication only, as the required trapping time depends on several factors, e.g., input power, numerical aperture of microscope objective, transmission of the optical system and sensitivity of the spectrometer used.

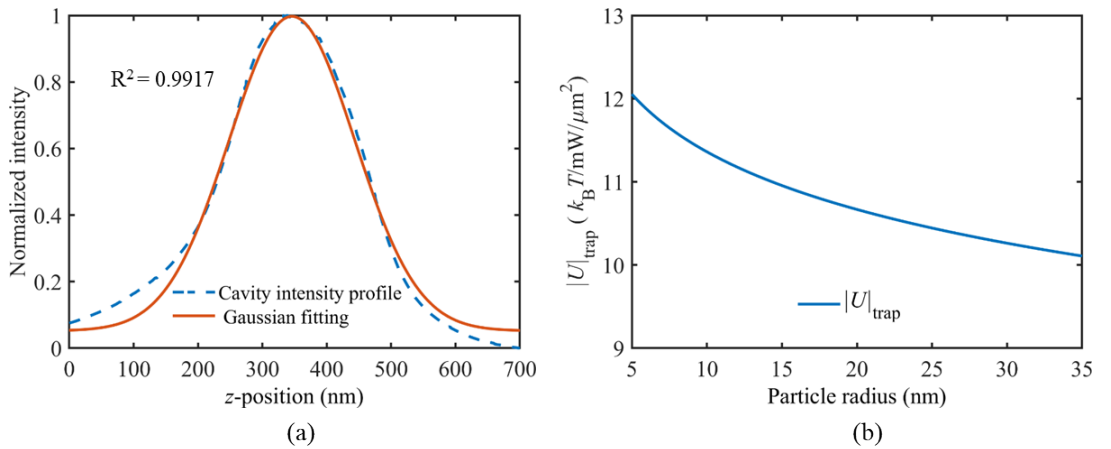


Fig. S6. (a) A gaussian profile (solid line) is fitted to the intensity profile of the quasi-BIC (dotted line). (b) Minimum trapping potential required for $\tau_{\text{trap}} = 10$ seconds as function of nanosphere radius.

References

1. A. Tittl, A. Leitis, M. Liu, F. Yesilkoy, D. Y. Choi, D. N. Neshev, Y. S. Kivshar, and H. Altug, "Imaging-based molecular barcoding with pixelated dielectric metasurfaces," *Science* **360**(6393), 1105-1109 (2018).
2. S. Yang, C. Hong, Y. Jiang, and J. C. Ndukaiife, "Nanoparticle Trapping in a Quasi-BIC System," *ACS Photonics* **8**(7), 1961-1971 (2021).
3. L. Neumeier, R. Quidant, and D. E. Chang, "Self-induced back-action optical trapping in nanophotonic systems," *New Journal of Physics* **17**(12), (2015).
4. C. Hosokawa, H. Yoshikawa, and H. Masuhara, "Cluster formation of nanoparticles in an optical trap studied by fluorescence correlation spectroscopy," *Phys. Rev. E Stat. Nonlin. Soft Matter Phys.* **72**(2), 021408 (2005).

Paper IV: Influence of ellipticity on quasi-BIC in metasurface with parallel bars and a disk

Manuscript submitted to IEEE Photonics Technology Letters.

Authors: Md Rabiul Hasan, and Olav Gaute Hellestø

Contribution notes: Md Rabiul Hasan conceived the idea, performed all simulations and data analysis. Both authors contributed to the initial draft and finalized it before submission.

Influence of Ellipticity on Quasi-BIC in Metasurface with Parallel Bars and a Disk

Md Rabiul Hasan and Olav Gaute Hellesø

Abstract— Dielectric metasurfaces can support quasi-bound states in the continuum (quasi-BICs), which show high Q-factor and electric field enhancement, enabling various applications in nanophotonics. At optical wavelengths, and particularly when moving towards the visible range, the dimensions of the structure are small. Optimizing the design to reduce the sensitivity to fabrication imperfections is thus important. In this letter, a structure with two elliptic, parallel bars and a cylindrical disk is considered. The ellipticity of the bars influences the sensitivity of the resonance wavelength to changes in the radii of the bars and the disk, and it is found that smaller ellipticity, i.e., more circular bars, give reduced sensitivity. Smaller ellipticity also increases the gap between the tips of the bars, making it possible to optically trap nanoparticles with a diameter up to 200 nm. The structure can support both symmetry-protected and resonance-trapped BIC for different sets of design parameters, with a similar sensitivity of resonance wavelength to radii found for both types of BIC.

Index Terms—Bound states in the continuum, metasurfaces, Q-factor, field enhancement

I. INTRODUCTION

Bound states in the continuum (BICs) have been explored theoretically and experimentally in several works [1-5]. A true BIC refers to an electromagnetic state perfectly localized in, e.g., an optical metasurface, without outgoing radiation, thus showing an infinite Q-factor. Material losses and fabrication imperfections limit the Q-factor obtainable in reality [6], thus a quasi-BIC with high, but finite, Q-factor is the real-world alternative to a true BIC. The two main types of BIC are symmetry protected and resonance trapped (also called accidental) BICs [1, 7]. The latter type will be further described in the Results-section. A symmetry protected BIC can be transformed into a quasi-BIC by breaking the symmetry, which is useful for investigating the behavior of the BIC and to control the Q-factor by design, rather than relying on fabrication imperfections. Metasurfaces with elliptical bars have been shown to support quasi-BICs [6], for applications in optical trapping [8, 9] and biosensing

[10, 11]. For these metasurfaces, the symmetry can be broken by tilting the elliptical bars [6, 12] or, for parallel bars, by introducing an asymmetrically positioned disk [13]. The dimensions of the bars and the gaps between them are small, particularly when moving towards the visible range. To be able to take full advantage of quasi-BICs, a high Q-factor is solicited within a specified wavelength range. This implies that fabrication tolerances are tight. The aim of this work is to find design parameters that gives a robust behavior in the presence of fabrication imperfections. We focus on the resonance wavelength, and the sensitivity of the resonance wavelength to changes in the radii of the structures. There are several reasons for this. The periodicity of a structure, i.e., width and length of the unit cell, can be accurately controlled by e-beam lithography and the resonance wavelength will typically be linear with the size of the unit cell [9]. Furthermore, the influence of the height of the structure is also limited [9]. On the other hand, when (elliptical) bars and disks are made with lithography and etching, it is notoriously difficult to control over- and under-exposure and -etching at the level required here. Thus, it is difficult to control the radius of thin cylinders precisely and deviations from the design will occur. Finding a design that has limited sensitivity to these variations is thus important. As the Q-factor will depend on absorption, scattering and variations from one unit cell to the other, while the resonance wavelength is directly influenced by these variations in radius, even if the structure is perfectly transparent, smooth, and periodic. Although Q-factors are included here, our main focus is on the resonance wavelength. We explore the sensitivity of the resonance to the radii for various positions of a disk, the radius of this disk and, most importantly, the ellipticity of the parallel bars, as defined in the next section.

II. METASURFACE DESIGN AND SIMULATION METHODS

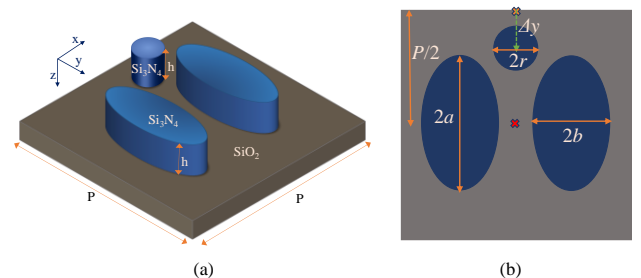


Fig. 1. (a) Schematic diagram of the unit cell, which contains two identical elliptical bars and a cylindrical disk. (b) An asymmetry is introduced by shifting the disk a distance Δy from the upper edge, which is a symmetry point. The red cross in the center shows the second symmetry point.

This work was supported by Research Council of Norway under Grant number 302333. (Corresponding author: O. G. Hellesø).

M. R. Hasan is with Department of Physics and Technology, UiT The Arctic University of Norway, Tromsø 9037, Norway (e-mail: md.r.hasan@uit.no).

O.G. Hellesø is with Department of Physics and Technology, UiT The Arctic University of Norway, Tromsø 9037, Norway (e-mail: olav.gaute.helleso@uit.no).

For this work, we have chosen to study a metasurface with a unit cell consisting of two elliptical parallel bars and a disk, as shown in Fig. 1(a). The unit cell is square, with periodicity P along the x -axis and the y -axis. The array of unit cells is considered to be infinite. The unit cell contains a cylindrical disk with radius r and a pair of parallel ellipses with major radius a , minor radius b , and height h . The ellipticity e can be defined as $e = \sqrt{1 - b^2/a^2}$. This design gives a relatively large gap ($g = P - 2a$) between the tips of the bars, with high field-enhancement, making it suitable for optical trapping of nanoparticles with a diameter up to 200 nm. The unit cell is always symmetric along the x -axis. It is also symmetric along the y -axis for two positions of the disk, on the edge and in the center of the unit cell, as shown in Fig. 1(b). As disks with diameters $2r$ larger than the separation between the ellipses are considered, only the symmetry point on the edge is considered here. For this case, the asymmetry parameter is $\alpha = \Delta y / (P/2)$, with Δy the distance from the edge to the disk.

COMSOL Multiphysics v.6 is used to simulate the unit cell. It is excited by a plane wave polarized along the x -axis and propagating along the z -axis using an incident port on the top and a receiving port at the bottom. Periodic boundary conditions are imposed on the faces in the x and y directions. The unit cell is submerged in a water medium ($n = 1.33$) to make it suitable for optical trapping. The structures are taken to be made of Si_3N_4 ($n = 2.02$) as it is transparent in the visible range [14]. The under-cladding is taken to be SiO_2 ($n = 1.46$) [15]. The maximum mesh size used for the bars and the disk is 12 nm. The initial design parameters are $P = 506$ nm, $a = 148.5$ nm, $b = 99$ nm, $h = 230$ nm, $r = 45$ nm, and $\Delta y = 103$ nm. Wavelength scans are performed, in this case giving a quasi-BIC at 773 nm, as shown in Fig. 2(a). A Fano lineshape function is fitted to the reflection, and the Q-factor for the quasi-BIC is found from the width of the fitted lineshape.

III. RESULTS AND DISCUSSIONS

We start by considering a fixed ellipticity $e = 0.74$ and study the Q-factor as function of the asymmetry parameter α , as shown in Fig. 2(b). As α approaches zero, the Q-factor tends to infinity. This shows that a symmetric structure supports a true, symmetry-protected BIC, as expected. As the asymmetry increases slightly, the Q-factor decreases according to $1/\alpha^2$, as also found in previous works [4, 6]. For a further increase in the asymmetry, the Q-factor increases again, reaching a peak for $\alpha = 0.3$. The Q-factor is indeed high around this peak value, but it is continuous, not tending towards infinity. It is thus not a true BIC. A resonance-trapped BIC can be pictured as a resonance trapped between two resonators, each with 100% reflectivity at the resonance wavelength, and with a separation giving 2π phase-shift [7, 16, 17]. To achieve this, it is normally necessary to tune several parameters. In our case, changing just Δy is not sufficient. By also changing the ellipticity, a higher Q-factor is obtained (shown in the zoomed-in view in Fig. 2b), indicating that there is a resonance-trapped BIC in the vicinity of this point. Finally, when further increasing the asymmetry, the Q-factor is again reduced.

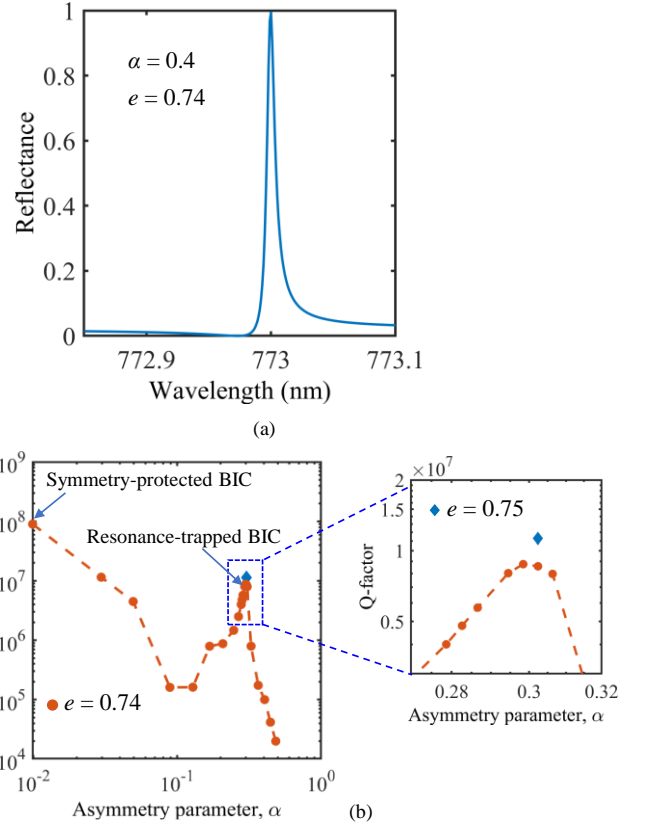


Fig. 2. (a) Reflectance spectra showing a quasi-BIC resonance at 773 nm. (b) Q-factor as a function of asymmetry parameter α for the $e = 0.74$ and $r = 45$ nm. The zoomed-in view showing the increase of Q-factor when $e = 0.75$ (filled diamond). A symmetry-protected BIC and a resonance-trapped BIC are shown in arrows for different values of α .

The main aim of this work is to study the sensitivity of the resonance wavelength to changes in design parameters. As fabrication process are likely to change radii in the same way, e.g., by over-etching, a common sensitivity is defined as $S = \Delta\lambda/\Delta r$, with $a' = a + \Delta r$, $b' = b + \Delta r$, and $r' = r + \Delta r$. Rather than changing the design parameters one-by-one, a , b , and r are thus changed simultaneously for Δr within ± 10 nm to find the sensitivity S . The wavelength is expected to be less sensitive to disk radius r than to a and b of the ellipses if these are considered individually.

To study the sensitivity as function of ellipticity, the minor radius b is increased, but with some adjustment also of the major radius a to keep the resonance wavelength close to the initial value ($\lambda = 773$ nm). Fig. 3 shows the sensitivity S as function of ellipticity for an offset of the disk $\Delta y = 103$ nm. The sensitivity decreases with decreasing ellipticity, to the limit where the two elliptical bars touch each other. The sensitivity of the resonance wavelength to radius is thus smaller for rather round bars, rather than elongated bars. However, the sensitivity is still high, with changes of just 10 nm in the radii giving a shift of the resonance of 12 nm. Inserted in Fig. 3 are also sensitivities for disk offsets $\Delta y = 8$ nm and $\Delta y = 76$ nm for two values of the ellipticity. For an ellipticity of 0.95, the three values for the disk offset give the same sensitivity, and for an ellipticity of 0.74, the sensitivity is approximately the same. Based on this, it can be concluded that the disk offset has limited influence on the sensitivity.

This implies that the sensitivity is similar close to a symmetry-protected BIC ($\Delta y = 8$ nm) and close to a resonance-trapped BIC ($\Delta y = 76$ nm). Changing the radius of the disk also has limited influence on the sensitivity ($r = 45, 50$ and 55 nm tested).

The Q-factor is also shown in Fig. 3 for varying ellipticity. It increases sharply as the ellipticity approaches 0.7. For the right combination of design parameters, there may be a resonance-trapped BIC as the two ellipses almost touch. In general, resonance-trapped BIC can exist for various disk offsets Δy , whereas a symmetry-protected BIC only exists for $\Delta y = 0$ and $\Delta y = P/2$, with the latter only possible for disks smaller than the separation between the bars.

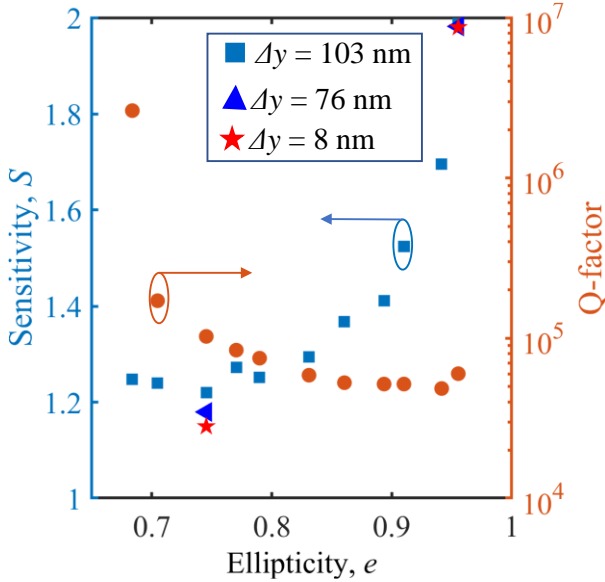


Fig. 3. Sensitivity of the wavelength to changes of radii, and the Q-factor, as a function of ellipticity. The filled squares, triangles, and pentagons markers indicate the sensitivities for Δy of 103 nm, 76 nm, and 8 nm, respectively. The results shown for the triangle and pentagon markers are considered with ellipticities of 0.95 and 0.74, respectively.

A key feature of quasi-BIC is their ability to provide a high electric field enhancement at the resonance. The field enhancement is the ratio $|E|/|E_0|$ between the total electric field E and the incident electric field E_0 . Fig. 4 shows, as an example, the field enhancement for $e = 0.74$, $r = 45$ nm and $\Delta y = 76$ nm. This is thus close to a resonance-trapped BIC and the Q-factor is high, at 10^7 . The field enhancement in the xy plane, at mid-height $z = h/2$, reaches approximately 4000 at the tips of the elliptical bars and decreases to 2400 in the middle of the gap between them i.e., on the edge of the unit cell. The high field enhancements, giving confined hotspots, can be used for optical trapping of nanoparticles, as studied in previous works [8, 9]. The Q-factor obtained in simulations, and thus the field-enhancement, can be increased further by optimizing the parameters further or moving the disk towards symmetry. However, as material and fabrication imperfections will limit the real Q-factor, simulation of this is of limited interest. A more interesting feature is the relatively large gap for this design. For the case considered here ($a = 148.5$ nm, $b = 99$ nm, giving $e = 0.74$), the tip-to-tip gap between the ellipses is 209 nm. It is thus possible to trap nanoparticles with a

diameter up to 200 nm. This is relevant for trapping exosome, which typically has a diameter of 30–150 nm. Previous studies were limited to smaller gaps, such as 70 nm in ref. [9] and 81 nm in ref. [8].

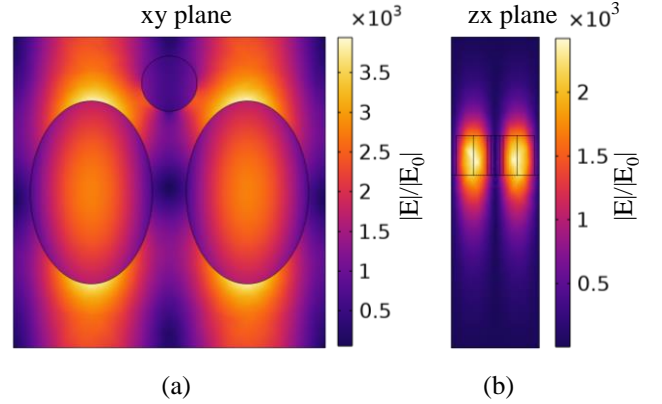


Fig. 4. Electric field enhancement profiles at the quasi-BIC resonance in the (a) xy plane and (b) zx plane for $\Delta y = 76$ nm, $e = 0.74$ and $r = 45$ nm. The xy plane is taken at $z = h/2$ and the zx plane is taken at $y = P/2$.

V. CONCLUSION

Metasurfaces supporting quasi-bound states in the continuum can offer high Q-factor resonances and intense hotspots as shown by simulations in this letter, e.g., for optical trapping of nanoparticles. The design studied here, with two elliptical bars and a cylindrical disk, can support both symmetry-protected and resonance-trapped BIC, depending on the position of the disk.

To obtain a resonance wavelength within a predetermined range, the dimensions of the fabricated structure must match the design very closely, to within a few nm or, at best, 10s of nm. It was shown in a previous work [9] that the height of the structure is less critical, while the resonance wavelength is proportional to the size of the unit cell. In this letter, the influence of the ellipticity of the bars is studied, and it is found that smaller ellipticity, i.e., more circular bars, are favorable. This can reduce the sensitivity of the resonance wavelength to changes in radii from 2 to 1.2. This is still a high sensitivity and further studies to reduce it are solicited. For different values of asymmetry α and disk radius r , similar sensitivities are obtained (but different Q-factors). An interesting result is that the sensitivity is approximately the same close to symmetry-protected and close to resonance-trapped BIC.

For this design, the tip-to-tip gap between the elliptical bars changes with the ellipticity. A lower ellipticity gives a larger gap, and as stated above, simultaneously reduces the sensitivity of the resonance wavelength to changes of the radii. The smallest ellipticity results when the two bars are almost in contact (along y -axis) and gives a gap of 209 nm (along x -axis). This, combined with the high field-enhancement at resonance, makes the structure suitable for trapping nanoparticles with a diameter up to 200 nm.

REFERENCES

- [1] C. W. Hsu, B. Zhen, A. D. Stone, J. D. Joannopoulos, and M. Soljačić, “Bound states in the continuum,” *Nat. Rev. Mater.*, vol. 1, no. 9, 2016.
- [2] S. Joseph, S. Pandey, S. Sarkar, and J. Joseph, “Bound states in the continuum in resonant nanostructures: an overview of engineered materials for tailored applications,” *Nanophotonics*, vol. 10, no. 17, pp. 4175-4207, 2021.
- [3] D. C. Marinica, A. G. Borisov, and S. V. Shabanov, “Bound States in the Continuum in Photonics,” *Phys. Rev. Lett.*, vol. 100, no. 18, 2008.
- [4] K. Koshelev, Y. Tang, K. Li, D.-Y. Choi, G. Li, and Y. Kivshar, “Nonlinear Metasurfaces Governed by Bound States in the Continuum,” *ACS Photonics*, vol. 6, no. 7, pp. 1639-1644, 2019.
- [5] H. Zhao, X. Cao, Q. Dong, C. Song, L. Wang, and L. Gao, “Large-area silicon photonic crystal supporting bound states in the continuum and optical sensing formed by nanoimprint lithography,” *Nanoscale Advances*, vol. 5, no. 5, pp. 1291-1298, 2023.
- [6] K. Koshelev, S. Lepeshov, M. Liu, A. Bogdanov, and Y. Kivshar, “Asymmetric Metasurfaces with High-Q Resonances Governed by Bound States in the Continuum,” *Physical Review Letters*, vol. 121, no. 19, 2018.
- [7] A. Kodigala, T. Lepetit, Q. Gu, B. Bahari, Y. Fainman, and B. Kanté, “Lasing action from photonic bound states in continuum,” *Nature*, vol. 541, no. 7636, pp. 196-199, 2017.
- [8] S. Yang, C. Hong, Y. Jiang, and J. C. Ndukaiife, “Nanoparticle Trapping in a Quasi-BIC System,” *ACS Photonics*, vol. 8, no. 7, pp. 1961-1971, 2021.
- [9] M. R. Hasan, and O. G. Hellesø, “Metasurface supporting quasi-BIC for optical trapping and Raman-spectroscopy of biological nanoparticles,” *Opt. Express*, vol. 31, no. 4, 2023.
- [10] F. Yesilkoy, E. R. Arvelo, Y. Jahani, M. Liu, A. Tittl, V. Cevher, Y. Kivshar, and H. Altug, “Ultrasensitive hyperspectral imaging and biodetection enabled by dielectric metasurfaces,” *Nat. Photon.*, vol. 13, no. 6, pp. 390-396, 2019.
- [11] M. L. Tseng, Y. Jahani, A. Leitis, and H. Altug, “Dielectric Metasurfaces Enabling Advanced Optical Biosensors,” *ACS Photonics*, vol. 8, no. 1, pp. 47-60, 2020.
- [12] A. Tittl, A. Leitis, M. Liu, F. Yesilkoy, D.-Y. Choi, D. N. Neshev, Y. S. Kivshar, and H. Altug, “Imaging-based molecular barcoding with pixelated dielectric metasurfaces,” *Science*, vol. 360, no. 6393, pp. 1105-1109, 2018.
- [13] G. Q. Moretti, A. Tittl, E. Cortés, S. A. Maier, A. V. Bragas, and G. Grinblat, “Introducing a Symmetry-Breaking Coupler into a Dielectric Metasurface Enables Robust High-Q Quasi-BICs,” *Adv. Photon. Res.*, vol. 3, no. 12, 2022.
- [14] K. Luke, Y. Okawachi, M. R. E. Lamont, A. L. Gaeta, and M. Lipson, “Broadband mid-infrared frequency comb generation in a Si₃N₄ microresonator,” *Opt. Lett.*, vol. 40, no. 21, pp. 4823-4826, 2015.
- [15] L. V. Rodríguez-de Marcos, J. I. Larruquert, J. A. Méndez, and J. A. Aznárez, “Self-consistent optical constants of SiO₂ and Ta₂O₅ films,” *Opt. Mater. Exp.*, vol. 6, no. 11, 2016.
- [16] C. W. Hsu, B. Zhen, J. Lee, S.-L. Chua, S. G. Johnson, J. D. Joannopoulos, and M. Soljačić, “Observation of trapped light within the radiation continuum,” *Nature*, vol. 499, no. 7457, pp. 188-191, 2013.
- [17] S. Han, L. Cong, Y. K. Srivastava, B. Qiang, M. V. Rybin, A. Kumar, R. Jain, W. X. Lim, V. G. Achanta, S. S. Prabhu, Q. J. Wang, Y. S. Kivshar, and R. Singh, “All-Dielectric Active Terahertz Photonics Driven by Bound States in the Continuum,” *Advanced Materials*, vol. 31, no. 37, 2019.

